

Sheffield Hallam University

Cathodic protection of steel framed masonry structures.

WU, Yu-You.

Available from the Sheffield Hallam University Research Archive (SHURA) at:

<http://shura.shu.ac.uk/20575/>

A Sheffield Hallam University thesis

This thesis is protected by copyright which belongs to the author.

The content must not be changed in any way or sold commercially in any format or medium without the formal permission of the author.

When referring to this work, full bibliographic details including the author, title, awarding institution and date of the thesis must be given.

Please visit <http://shura.shu.ac.uk/20575/> and <http://shura.shu.ac.uk/information.html> for further details about copyright and re-use permissions.

CITY CAMPUS, HOWARD STREET
SHEFFIELD S1 1WB



REFERENCE

ProQuest Number: 10701222

All rights reserved

INFORMATION TO ALL USERS

The quality of this reproduction is dependent upon the quality of the copy submitted.

In the unlikely event that the author did not send a complete manuscript and there are missing pages, these will be noted. Also, if material had to be removed, a note will indicate the deletion.



ProQuest 10701222

Published by ProQuest LLC (2017). Copyright of the Dissertation is held by the Author.

All rights reserved.

This work is protected against unauthorized copying under Title 17, United States Code
Microform Edition © ProQuest LLC.

ProQuest LLC.
789 East Eisenhower Parkway
P.O. Box 1346
Ann Arbor, MI 48106 – 1346

Cathodic Protection of Steel Framed Masonry Structures

Yu-You Wu

A thesis submitted in partial fulfilment of the requirements of
Sheffield Hallam University for the degree of Doctor of Philosophy



August 2005

Abstract

The identification of "Regent Street Disease" in the United Kingdom in the late 1970's highlighted the problems of the corrosion of iron and steel frames and other structural components in historically sensitive buildings. This has resulted in serious consequences with respect to serviceability, safety, aesthetics and heritage.

Cathodic protection is a proven method for preventing and protecting buried and submerged steel and reinforced concrete structures from corrosion. More recently, the method has been introduced to prevent and control corrosion in steel-framed masonry structures. However, with several sizeable installations in the UK, there are no formal guidelines for the design, installation and operation of such systems and much of the knowledge is based on empirical observations.

The work presented in the thesis investigates the polarisation of structural steel sections in masonry environments; the distribution of current and potential in representative cathodic protection systems for steel-framed masonry structures; the effect of masonry type and joints width on protective current and potential distribution and stray current corrosion. These studies are considered essential in the understanding of the mechanisms of cathodic protection and the design of optimised cathodic protection systems for such structures.

The study has involved both experimental measurements and boundary element modelling. The results have identified how the several key factors, such as the electrolyte resistivity, anode locations, masonry types and joint width, influence the distribution of the protective current and potential on the steel surface.

Furthermore, the work has confirmed that boundary element modelling can provide a powerful technique for analysing and optimising the design of cathodic protection systems for steel framed masonry structures. The technique also generates valuable information about the level of interference in terms of current density on the surface of stray current affected components and is therefore a valuable tool for the analysis of possible CP interference in steel-framed masonry buildings.

It is hoped that the output from this work will help progress the development of this technology and contribute to the development of formal guidelines and standards for the cathodic protection of steel-framed masonry buildings.

Acknowledgement

The author would like to thank the following people who have assisted in its completion.

The research presented in this thesis would not have been possible without the insight, advice and patience offered by Professor Paul Lambert. I am equally indebted to Professor Pal Mangat for his encouragement and support.

Excellent technical support was provided throughout the period by Geoff Harwood and Bob Skelton. I would also like to thank Ann Wilson and Sue Biggins for all their assistance and the help of Dr Lufeng Yang in programming.

I could not have studied at SHU without the funding provided by the University. I am also grateful to the Mott MacDonald Group Limited for providing me with further funding to complete the thesis.

Over the course of my PhD study, Mr Song Chen, Mr Yuxiang Meng, Dr Guiyi Tang and Mr Shanfang Xiao have provided support to my family in China. Dr Nelson Chilengwe has been a wonderful and consistent friend and often provided the motivation with my study.

My older brother Shengfeng Wu and my school teacher Mr Ruizheng Yu gave me the initial instruction and advice in China. This is a memory which will be everlasting.

Finally, I would like to express my deepest gratitude to my wife Ling-Ling for her continuous understanding and patience which has been a source of inspiration during the course of my study.

**To: My wife, my parents, my
parents-in-law and my
older brother.**

TABLE OF CONTENTS

Chapter 1: Introduction	1
1.1 Research Background.....	2
1.2 Aims and Objectives.....	3
1.3 Scope of Current Research	3
1.4 Methodology.....	4
1.5 Structure of Thesis	4
Chapter 2: Literature Review	7
2.1 Electrochemistry of Steel Corrosion	8
2.1.1 The Process of Steel Corrosion.....	8
2.1.2 Effect Factors	11
2.1.3 Forms of Corrosion.....	11
2.2 Corrosion of Steel Framed Masonry Buildings	11
2.2.1 Construction of Steel Framed Masonry Buildings.....	12
2.2.2 Steel Frame Corrosion and the Damage Mechanism.....	13
2.3 Electrochemical Testing Methods.....	18
2.3.1 Measurements of Half-Cell Potential	19
2.3.2 Resistivity Measurement	19
2.3.3 Linear Polarisation Resistance	20
2.3.4 Potentiodynamic and Potentiostatic Polarisation Curves.....	21
2.3.5 Other Techniques	21
2.4 Principles of Cathodic Protection.....	22
2.4.1 Theoretical Basis	22
2.4.2 Impressed Current System.....	23
2.4.3 Sacrificial Anode System.....	24
2.5 The History of Cathodic Protection.....	25
2.5.1 Cathodic Protection of Buried Pipelines	26
2.5.2 Cathodic Protection of Reinforced Concrete	27
2.5.3 Cathodic Protection of Steel-framed Masonry Buildings.....	28
2.6 The Existing Standards and Test Methods.....	29
2.7 Development of Numerical Methods for Predicting Current and Potential Distribution of Cathodic Protection Systems.....	30
2.7.1 Introduction.....	30
2.7.2 Mathematical Theory	31
2.7.3 Analytical Methods	32
2.7.4 Finite Difference Method	33
2.7.5 Finite Element Method.....	34
2.7.6 Boundary Element Method	35
2.7.7 Comparison of Numerical Methods	37
2.8 Stray Current Corrosion.....	39
2.8.1 The Sources of Stray Current and Corrosion	39
2.8.2 Measurement of Stray Current Corrosion Potential.....	40
2.8.3 Boundary Element Method for Analysis of Stray Current Corrosion.....	40
2.9 Conclusions from the Literature Review	41

Chapter 3:	Introduction to the Experimental Work	43
3.1	Introduction.....	44
3.2	The Components of the Impressed Current Cathodic Protection Systems.....	44
3.3	Experimental Programme	46
3.4	Test Materials	47
Chapter 4:	Boundary Element Method for the Modelling of Cathodic Protection Systems	49
4.1	Introduction.....	50
4.2	Basic Equations.....	51
4.2.1	Governing Equation.....	51
4.2.2	Boundary Integral Equation	52
4.3	The Boundary Element Method.....	54
4.3.1	Discretisation of Boundary Integral Equation and Numerical Solutions.....	54
4.3.2	Types and Interpolations of Elements	58
4.3.3	The Internal Solutions.....	63
4.4	Boundary Conditions	64
4.5	Methods and Procedure of Solution	66
4.6	Multi-regional Problems.....	68
4.7	Implementation of Computer Programs.....	72
4.8	Conclusions.....	72
Chapter 5:	Measurement of Steel Polarization Data in Sand and Mortar	74
5.1	Introduction.....	75
5.2	Materials and Test Specimens	76
5.2.1	Materials.....	76
5.2.2	Test Specimens.....	76
5.2.2.1	Specimens for Measuring Polarization Data of Steel in Sand ..	76
5.2.2.2	Specimens for Measuring Polarization Data of Steel in Mortar	77
5.3	Test Method and Procedure	79
5.3.1	Resistivity	79
5.3.2	Apparatus and Procedure of Measurements	82
5.4	Results	85
5.4.1	The Polarization Data of Steel in Sand.....	85
5.4.2	Polarization Data for Steel in Mortar.....	85
5.5.1	Discussion and Conclusion	92
Chapter 6:	Distribution of Current/Potential of Impressed Current Cathodic Protection Systems	95
6.1	Introduction.....	96
6.2	Experimental Procedure	96
6.2.1	Test Design of Impressed Current Cathodic Protection Systems	96

6.2.2	Measurement of Protective Potential.....	101
6.3	Modelling of Boundary Element of ICCP System A and B.....	104
6.3.1	Discussion of Boundary Conditions.....	104
6.3.2	Boundary Element Analysis of ICCP System A.....	105
6.3.3	Boundary Element Analysis of ICCP System B.....	126
6.4	Modelling Results and Discussion.....	144
6.4.1	The Effect of Resistivity on Potential & Current Density Distribution	144
6.4.2	Relationship between Potential Distribution and Anode Location	144
6.4.3	Comparison of Boundary Element Modelling with the Experiments and Discussion	145
6.5	Conclusions.....	146
 Chapter 7: Effect of Brick Type and Joints Width on CP Current and Potential Distribution		
147		
7.1	Introduction.....	148
7.2	Test Set-up.....	149
7.2.1	Basic Components	149
7.2.2	Test Specimen.....	150
7.2.3	Resistivity of Test Specimen	152
7.2.4	Installation of CP System and Power Supply	153
7.2.5	Measurement of Protective Potential.....	154
7.3	Monitoring of the CP System.....	156
7.3.1	Modelling of Boundary Element of ICCP System	156
7.4	Discussion of Boundary Conditions.....	157
7.4.1	Boundary Element Analysis.....	159
7.4.2	Modelling Results and Discussion.....	161
7.4.3	Further Discussion of Modelling Results.....	182
7.5	Comparison of Boundary Element Modelling with the Experiments	195
7.6	Conclusions.....	196
 Chapter 8: Analysis of Stray Current Corrosion.....		
198		
8.1	Introduction.....	199
8.2	Experimental Configuration	200
8.2.1	Specimen Design	200
8.2.2	Measurement of Potential.....	201
8.3	Boundary Element Modelling.....	203
8.3.1	Boundary Conditions	203
8.3.2	Description of the Boundary Element Modelling.....	205
8.3.3	Weight Loss of Steel.....	207
8.3.4	Modelling Results and Discussion.....	208
8.4	Discussion of Boundary Element Modelling with Experimentally Obtained Values.....	217
8.5	Conclusions.....	217

Chapter 9: General Conclusions & Recommendations for Further Research	218
9.1 Introduction.....	219
9.2 General Conclusions	219
9.2.1 Introduction of Boundary Element Technique to the Modelling Cathodic Protection of Steel Framed Masonry Structures.....	219
9.2.2 Measurement of Steel Polarization Data in Sand and Mortar.	220
9.2.3 Distribution of Impressed Current & Potential of Cathodic Protection Systems.....	221
9.2.4 Effects of Brick Type and Joint Widths on Distributions of Impressed Current and Potential	222
9.2.5 Analysis of Stray Current Corrosion	223
9.3 Recommendations for Further Research.....	223
9.3.1 Boundary Element Modelling.....	224
9.3.2 Protection of Non-structural Metalwork.....	224
9.4 Conclusion.....	225
Chapter 10: References	226
Appendix I: FORTRAN Modelling Program Developed for this Study	237
Appendix II: Reprint of Peer-Reviewed Paper from the Proceedings of the Second International Conference on Maritime Heritage, April 2005, Barcelona, Spain	249

LIST OF FIGURES

Figure 2.1: Corrosion reactions on steel	10
Figure 2.2: Construction of steel-framed masonry buildings (1)	12
Figure 2.3: Construction of steel-framed masonry buildings (2)	13
Figure 2.4: Corrosion of a steel-framed beam	15
Figure 2.5: Corrosion of a steel-framed stanchion or column	15
Figure 2.6: Portland stone cracking resulting from corrosion of a steel column	17
Figure 2.7: Brick cracking resulting from corrosion of a steel column	18
Figure 2.8: Evans diagram illustrating the increasing CP current requirements as potential of the structure is depressed	22
Figure 2.9: Impressed current cathodic protection	24
Figure 2.10: Sacrificial anode cathodic protections	25
Figure 4.1: The discretation of boundary into elements	54
Figure 4.2: One-dimensional elements for two dimensional problems	58
Figure 4.3: Two dimensional elements for three dimensional problems	64
Figure 4.4: Flow chart of the general iteration procedure	68
Figure 4.5: A model consisting of two zones	70
Figure 5.1: Test specimen for measuring polarization data of steel in sand	77

Figure 5.2:	Test specimen for measuring polarization data of steel in mortar	78
Figure 5.3:	Schematic illustration two probe resistivity measurement	80
Figure 5.4:	Relationship between resistivity and exposure time	82
Figure 5.5:	Schematic illustration of test facility	83
Figure 5.6:	Test apparatus - potentiostat and ramp generator	84
Figure 5.7:	Polarization curves of steel in sand	86
Figure 5.8:	Polarization curves of steel in mortar (Specimen D)	86
Figure 5.9:	Polarization curves of steel in mortar (Specimen D)	87
Figure 5.10:	Polarization curves of steel in mortar (Specimen D)	87
Figure 5.11:	Polarization curves of steel in mortar (Specimen D)	88
Figure 5.12:	Polarization curves of steel in mortar (Specimen D)	88
Figure 5.13:	Polarization curves of steel in mortar (Specimen D)	89
Figure 5.14:	Polarization curves of steel in mortar (Specimen E)	89
Figure 5.15:	Polarization curves of steel in mortar (Specimen F)	90
Figure 5.16:	Polarization curves of steel in mortar (Specimen F)	90
Figure 5.17:	Polarization curves of steel in mortar (Specimen F)	91
Figure 5.18:	Polarization curves of steel in mortar (Specimen F)	91
Figure 5.19:	Polarization curves of steel in mortar (Specimen F)	92
Figure 6.1:	Steel Section A (unit: mm)	98
Figure 6.2:	Steel Section B (unit: mm)	98
Figure 6.3:	Dimensions of the large sandbox	98
Figure 6.4:	Schematic illustration of test facility (ICCP System A)	99
Figure 6.5:	Components of ICCP System A	99
Figure 6.6:	Buried steel section B and the Anodes A and B	100
Figure 6.7:	Components of ICCP System B	100
Figure 6.8:	Distribution of Protective Potential (mV, vs CSE) on the free surface of the sandbox, Z=22.0cm, ICCP System A.	102
Figure 6.9:	Distribution of Protective Potential (mV vs. CSE) on the free surface of sandbox, Z=22.0cm, of ICCP System B	103
Figure 6.10:	Schematic representation of the total boundary element mesh for ICCP System A	107
Figure 6.11:	Schematic representation of the boundary element mesh on the surface of sandbox for ICCP System A	107
Figure 6.12:	Schematic representation of the boundary element mesh on the surface of Steel Section A of ICCP System A	108
Figure 6.13:	Potential distribution on the surface of sandbox of ICCP System A (mV, vs CSE)	108
Figure 6.14:	Potential distribution at Z=11.0cm of ICCP System A (mV, vs SCE)	109
Figure 6.15:	Potential distribution on the surface of Steel Section A of ICCP System A (mV, vs CSE)	110
Figure 6.16:	Current distribution on the surface of Steel Section A of ICCP System (mA)	111
Figure 6.17:	Potential distribution at the free surface of sandbox of ICCP System A (mV, vs CSE)	112
Figure 6.18:	Potential distribution at Z=11.0cm of ICCP System A (mV, vs SCE)	113

Figure 6.19:	Potential distribution on the surface of Steel Section A of ICCP System A (mV, vs SCE)	114
Figure 6.20:	Current distribution on the surface of Steel Section A of ICCP System A (mA)	115
Figure 6.21:	Potential distribution on the surface of sandbox of ICCP System A (mV, vs CSE)	116
Figure 6.22:	Potential distribution at Z=11.0cm of ICCP System A (mV, vs CSE)	117
Figure 6.23:	Potential distribution on the surface of Steel Section A of ICCP System A (mV, vs CSE)	118
Figure 6.24:	Current distribution on the surface of Steel Section A of ICCP System A (mA)	119
Figure 6.25:	Potential distribution on the surface of sandbox of ICCP System A (mV, vs CSE)	120
Figure 6.26:	Potential distribution on the surface of Steel Section A of ICCP System A (mV, vs CSE)	121
Figure 6.27:	Current distribution on the surface of Steel Section A of ICCP System A (mA)	122
Figure 6.28:	Potential distribution on the surface of sandbox of ICCP System A (mV, vs CSE)	123
Figure 6.29:	Potential distribution on the surface of Steel Section A of ICCP System A (mV, vs CSE)	124
Figure 6.30:	Current distribution on the surface of Steel Section A of ICCP System A (mA)	125
Figure 6.31:	Schematic representation of the total boundary element mesh for ICCP System B	127
Figure 6.32:	Schematic representation of the boundary element mesh on the surface of sandbox for ICCP System B	128
Figure 6.33:	Schematic representation of the boundary element mesh on the surface of Steel Section B of ICCP System B	128
Figure 6.34:	Potential distribution on the surface of sandbox of ICCP System B (mV, vs CSE)	129
Figure 6.35:	Potential distribution at Z=11.0cm of ICCP System B (mV, vs SCE)	130
Figure 6.36:	Potential distribution on the surface of Steel Section A of ICCP System A (mV, vs CSE)	131
Figure 6.37:	Details of potential distribution on ZY plane of steel (mV)	131
Figure 6.38:	Current distributions on the surface of Steel Section B of ICCP System B (mA)	132
Figure 6.39:	Potential distribution on the surface of sandbox of ICCP System B (mV, vs CSE)	133
Figure 6.40:	Potential distribution at Z=11.0cm of ICCP System B (mV, vs CSE)	134
Figure 6.41:	Potential distribution on the surface of Steel Section B of ICCP System B (mV, vs CSE)	135
Figure 6.42:	Details of the potential distribution on ZY plane of steel of ICCP System B (mV)	135
Figure 6.43:	Current distribution on the surface of Steel Section B of ICCP System B (mA)	136

Figure 6.44 :	Potential distribution on the surface of sandbox of ICCP System B (mV, vs CSE)	137
Figure 6.45:	Potential distribution at Z=11.0cm of ICCP System B (mV, vs CSE)	138
Figure 6.46:	Potential distribution on the surface of Steel Section B of ICCP System B (mV, vs CSE)	139
Figure 6.47:	Details of potential distribution on ZY plane of steel of ICCP System B (mV)	139
Figure 6.48:	Current distribution on the surface of Steel Section B of ICCP System B (mA)	140
Figure 6.49:	Potential distribution on the surface of sandbox of ICCP System B (mV, vs. CSE)	141
Figure 6.50:	Potential distribution on the surface of Steel Section B of ICCP System B (mV, vs. CSE)	142
Figure 6.51:	Current distribution on the surface of Steel Section B ICCP System B (mA)	143
Figure 7.1	Non-uniform current distribution	148
Figure 7.2:	Steel section (unit: mm)	150
Figure 7.3:	Layout of brick and dimension of test specimen (unit: mm)	151
Figure 7.4:	Plane view of position of the anodes (a) and embedded probe (b)	152
Figure 7.5:	Experimental set-up of ICCP system	153
Figure 7.6:	Test specimen plan view of ICCP system	154
Figure 7.7:	Schematic representation of the total boundary element mesh on the surface of the encased specimen (Case 1 and Case 2)	162
Figure 7.8	Schematic representation of the boundary element mesh for the mortar beds (Case 1 and Case 2)	163
Figure 7.9:	Schematic representation of the boundary element mesh on the surface of each brick (Case 1 and Case 2)	164
Figure 7.10:	Schematic representation of the boundary element mesh on the surface of steel section (Case 1 and Case 2, symmetric in plane X=0)	164
Figure 7.11:	Potential distribution on the surface of mortar (mV vs CSE, symmetric in plane X=0, Case 1)	165
Figure 7.12:	Potential distribution on the surface of brick (mV vs CSE, symmetric in plane X=0, Case 1)	166
Figure 7.13:	Potential distribution on the surface of steel (mV vs CSE, symmetric in plane X=0, Case 1)	167
Figure 7.14:	Normal current distribution on the surface of steel (mA/cm^2 , - current in, + current out, symmetric in plane X=0, Case 1)	168
Figure 7.15:	Potential distribution on the plane which is closed by X=0.0cm, Y1=18.425cm, Y2=24.05cm, Z1=0 and Z2=45cm (mV vs CSE)	169
Figure 7.16:	Potential distribution on the plane, Y=0.00, (mV vs CSE, symmetric in plane X=0, Case 1)	170
Figure 7.17:	Potential distribution on the surface of mortar (mV vs CSE, symmetric in plane X=0, Case 2)	171

Figure 7.18:	Potential distribution on the surface of brick (mV vs CSE, symmetric in plane X=0, Case 2)	172
Figure 7.19:	Potential distribution on the surface of steel (mV vs CSE, symmetric in plane X=0, Case 2)	173
Figure 7.20:	Normal current distribution on the surface of steel (mA/cm ² , - current in, + current out, symmetric in plane X=0, Case 2)	174
Figure 7.21:	Potential distribution on the plane which is closed by the lines X=0.0cm, Y1=18.425cm, Y2=24.05cm, Z1=0 and Z2=45cm (mV vs CSE, symmetric in plane X=0, Case 2)	175
Figure 7.22:	Potential distribution on the plane which is closed by the lines X1=0.3cm, X2=22.0, Y=0.0, Z1=0 and Z2=45cm (mV vs CSE, symmetric in plane X=0, Case 2)	176
Figure 7.23:	Schematic representation of the total boundary element mesh on the surface of specimen (Case 3)	177
Figure 7.24:	Schematic representation of the boundary element mesh on the mortar bed (Case 3)	177
Figure 7.25:	Schematic representation of details of the boundary element mesh on the surface of each brick (Case 3)	178
Figure 7.26:	Schematic representation of the boundary element mesh on the surface of steel piece (Case 3, symmetric in plane Y=0)	178
Figure 7.27:	Potential distribution on the surface of mortar (mV vs CSE, symmetric in plane Y=0, Case 3)	179
Figure 7.28:	Potential distribution on the surface of brick (mV vs CSE, symmetric in plane Y=0, Case 3)	179
Figure 7.29:	Potential distribution on the surface of steel (mV vs CSE, symmetric in plane Y=0, Case 3)	180
Figure 7.30:	Normal current distribution on the surface of steel (mA/cm ² , - current in, + current out, symmetric in plane Y=0, Case 3)	180
Figure 7.31:	Potential distribution on the plane Z=20.0cm, (mV vs CSE, symmetric in plane Y=0, Case 3)	181
Figure 7.32:	Potential distribution on the plane which is closed by the lines X=0.0cm, Y1=18.425cm, Y2=24.05cm, Z1=0 and Z2=45cm (mV vs CSE, symmetric in plane X=0, Case 3)	181
Figure 7.33:	Schematic representation of the total boundary element mesh (Case 4, symmetric in plane X=0)	185
Figure 7.34:	Schematic representation of details of boundary element mesh on the surface of mortar (Case 4, symmetric in plane X=0)	185
Figure 7.35:	Schematic representation of the boundary element mesh on the surface of steel piece (symmetric in plane X=0, Case 4)	186
Figure 7.36:	Potential distribution on the surface of mortar (mV vs CSE, symmetric in plane X=0, Case 4)	186
Figure 7.37:	Potential distribution on the surface of steel (mV vs CSE, symmetric in plane X=0, Case 4)	187

Figure 7.38:	Normal current distribution on the surface of steel (mA/cm ² , - current in, + current out, symmetric in plane X=0, Case 4)	188
Figure 7.39:	Potential distribution on the plane which is closed by the lines X=0.0cm, Y1=18.425cm, Y2=24.05cm, Z1=0 and Z2=45cm (mV vs CSE symmetric in plane X=0, Case 4)	189
Figure 7.40:	Potential distribution on the plane which is closed by the lines X1=0.3cm, X2=22.0, Y=0.0, Z1=0 and Z2=45cm (mV vs CSE, symmetric in plane X=0, Case 4)	190
Figure 7.41:	Schematic representations of the total boundary element mesh (symmetric in plane Y=0, Case 5)	191
Figure 7.42:	Schematic representation of boundary element mesh on the surface of mortar (Case 5, symmetric in the plane Y=0)	191
Figure 7.43:	Schematic representation of the boundary element mesh on the surface of steel section (symmetric in plane Y=0, Case 5)	192
Figure 7.44:	Potential distribution on the surface of mortar (mV vs CSE, symmetric in plane Y=0, Case 5)	192
Figure 7.45:	Potential distribution on the surface of steel (mV vs CSE, symmetric in plane Y=0, Case 5)	193
Figure 7.46:	Normal current distribution on the surface of steel (mA/cm ² , - current in, + current out, symmetric in plane Y=0, Case 5)	193
Figure 7.47:	Potential distribution on the plane Z=20.0 cm, (mV vs CSE, symmetric in plane Y=0, Case 5)	194
Figure 7.48:	Potential distribution on the plane which is closed by the lines X=0.0cm, Y1=18.425cm, Y2=24.05cm, Z1=0 and Z2=45cm (mV vs CSE, symmetric in plane X=0, Case 5)	194
Figure 7.49:	Comparison of experimental measurement of potential with boundary element solutions on the steel surface (Case 1)	195
Figure 8.1:	CP inducing corrosion on discontinuous metal fixings	200
Figure 8.2:	Steel Section (unit: mm)	200
Figure 8.3:	Schematic illustration of test facility	202
Figure 8.4:	Sandbox and ICCP components	202
Figure 8.5:	Schematic representation of the total boundary element mesh on the surface of sandbox	206
Figure 8.6:	Schematic representation of the element mesh on the surface of steel piece and steel bar	207
Figure 8.7:	Potential distribution on the surface of sandbox (mV vs CSE, Case 1)	209
Figure 8.8:	Potential distribution on the surface of the steel section and steel bars (mV vs CSE, Case 1)	209
Figure 8.9:	Potential distribution on the surface of Steel Bar 1 (mV vs CSE, Case 1)	210
Figure 8.10:	Potential distribution on the surface of Steel Bar 2 (mV vs CSE, Case 1)	210

Figure 8.11:	Normal current distribution on the surface of steel and steel bars (mA/cm ² , - current in, + current out, Case 1)	211
Figure 8.12:	Normal current distribution on the surface of Steel Bar 1 (mA/cm ² , - current in, + current out, Case 1)	211
Figure 8.13:	Normal current distribution on the surface of Steel Bar 2 (mA/cm ² , - current in, + current out, Case 1)	212
Figure 8.14:	Potential distribution on the surface of the sandbox (mV vs CSE, Case 2)	212
Figure 8.15:	Potential distribution on the surface of steel section and steel bars (mV vs CSE, Case 2)	213
Figure 8.16:	Potential distribution on the surface of Steel Bar 1 (mV vs CSE, Case 2)	213
Figure 8.17:	Potential distribution on the surface of Steel Bar 2 (mV vs CSE, Case 2)	214
Figure 8.18:	Normal current distribution on the surface of steel section and bars (mA/cm ² , - current in, + current out, Case 2)	214
Figure 8.19:	Normal current distribution on the surface of Steel Bar 1 (mA/cm ² , - current in, + current out, Case 2)	215
Figure 8.20:	Normal current distribution on the surface of Steel Bar 2 (mA/cm ² , - current in, + current out, Case 2)	215
Figure 8.21	Comparison of experimental measurement of potential with boundary element solutions (Case 2)	216

LIST OF TABLES

Table 2.1:	Boundary Conditions	32
Table 5.1:	Resistivity of Sand	80
Table 5.2:	Resistivity of Mortar (Specimens D, E and F)	81
Table 7.1:	Protective potential on steel surface	155
Table 8.1:	Protective potential on the free surface of sandbox	203

NOTATION

E	Potential at any point of domain (electrolyte)
E^*	Fundamental solution of Laplace equation
\mathbf{E}	Nodal potential vectors
E_a	Potential on the anode surface
E_c	Potential on the cathode surface
\mathbf{i}	Nodal normal current density vectors
K	Conductivity of electrolyte
i	Normal current density at the electrode surface
i_0	Initial normal current density at the electrode surface
i_a	Normal current density at the anode surface
i_c	Normal current density at the cathode surface
Ω	Problem domain
Γ	Boundary or surface of the domain Ω
Γ_{elem}	An element boundary
n	Normal vector to the electrode surface
r	Distance between the source point and field point in space

r_x	The component of r in the x direction
r_y	The component of r in the y direction
r_z	The component of r in the z direction
n_x	The components in the x direction of unit normal to boundary surface
n_y	The components in the y direction of unit normal to boundary surface
n_z	The components in the z direction of unit normal to boundary surface
$\int_{\Gamma_{elem}}$	Integration over an element
ϕ_n	Interpolation functions
f	A function which represents the electrode kinetics and polarization on the anodic or cathodic surface
J	Jacobian matrix
$ J $	Determininant of the Jacobian matrix

1.1 Research Background

The identification of “Regent Street Disease” in the United Kingdom in the 1970’s first highlighted the problems of steel framed corrosion occurring on a significant number of the grand and often listed structures in the centres of many cities. This form of steel-frame building construction, initially employed in Chicago and subsequently used in most western cities in the first two decades of the 20th century, has resulted in serious consequences with respect to serviceability, safety and aesthetics.

Cathodic protection, originally developed by Humphry Davy in 1824 and later employed widely on buried and submerged structures, was first considered for reinforced concrete in the late 1950’s but it was not until the development of improved anode systems in the early 1980’s that it became a serious commercial solution.

The transfer to steel-framed buildings was somewhat slower and it was not until 1997 that the first full structure was protected by such a system (Gloucester Road Underground Station, London). Even now, with several sizeable installations in the United Kingdom, there are no formal guidelines for the design, installation and operation of such systems. Most of the knowledge is based on empirical observation and is in the hands of a very small number of specialists.

One of the major problems in understanding the mechanisms of cathodic protection in steel-framed construction is the relatively complex geometry of the systems under consideration. No information exists with respect to current

throw onto typical steel sections, yet this is fundamental to the design of such systems.

1.2 Aims and Objectives

The overall aim of the research project is to better identify the factors associated with the correct performance of cathode protection systems for steel-framed masonry structures with respect to design, installation and operation.

The specific objectives are as follows:

1. To identify the theoretical basis for design of cathodic protection systems.
2. To model the operation of cathodic protection in steel-framed buildings.
3. To validate the model with laboratory-based experiments.
4. To generate design and operation criteria based on theoretical, computer modelled and experimentally validated criteria

1.3 Scope of Current Research

The project mainly concentrates on the following key work:

1. The Distributions of Current/Potential of Cathodic Protection System of Steel-Framed Masonry Structures
2. The Effects of Joint Widths on the Distribution of Current/Potential of Cathodic Protection Systems
3. The Analysis of Stray Current Corrosion by Cathodic Protection Systems

The above works are essential to understand the mechanisms of cathodic protection in steel-framed masonry structures. At present, there are few publications in these areas; the study will therefore will be novel and challenging.

1.4 Methodology

Initial studies have been carried out on a range of steel and anode geometries employing a sandbox to represent the surrounding masonry. This technique has previously been employed to study the throw of current from ground-beds to pipeline sections in conventional cathodic protection applications but has not been used in this context. This also allows the risk and magnitude of stray current effects on discontinuous metallic components, e.g. cramps and wall-ties, to be formally evaluated for the first time.

On completion of the sandbox work, a number of geometries have been selected for further testing with mortar and brick encasement.

In parallel with the laboratory work, the boundary element method has been used to model and analyse the cathodic protection system to improve the design and optimisation of such systems capable of extending the life of these structures with the minimum of disruption to the fabric of the buildings.

1.5 Structure of Thesis

The thesis is composed of ten chapters:

Chapter 1 is an introduction.

Chapter 2 presents a detailed review of literature on corrosion of steel in steel-framed masonry buildings, cathodic protection and related subjects. It covers aspects of the electrochemistry of steel corrosion, corrosion of steel-framed buildings, electrochemical test methods, principles and history of cathodic protection, the existing criteria and standards relating to cathodic protection, development of numerical methods for modelling of cathodic protection, stray current corrosion and conclusions from the literature review.

Chapter 3 is an introduction to the experimental work undertaken in the study.

Chapter 4 describes the basic theory of the boundary element method and its application in the analysis of cathodic protection systems, especially in homogeneous electrolytes and inhomogeneous or multiregional electrolytes.

Chapter 5 presents the measurement of polarisation data. It describes the details of the test facility and components and the measurement procedures. Finally, cathodic polarisation data for steel in sand and mortar are listed respectively.

Chapter 6 applies the theories and knowledge derived in Chapters 2 to 5 to the analysis of two constructed cathodic protection systems. The work includes experimental measurement and boundary element modelling. Furthermore, the experimental data is compared with computational results. A discussion is also included.

Chapter 7 investigates the effects of brick type and joint width on the distribution of the protective current and potential of cathodic protection

systems. The experimental work is in parallel with boundary element modelling. Both results are compared and discussed.

Chapter 8 analyses the corrosion of stray current. In the present study, the boundary element technique is used to model a laboratory evaluation. The objective is to minimise the risk and extent of cathodic protection interference.

Chapter 9 discusses the main conclusions from the work and suggests the areas that would benefit from further work.

Chapter 10 is the list of references employed in the main chapters.

2.1 Electrochemistry of Steel Corrosion

Metallic corrosion is the destructive result of chemical or electrochemical reaction between a metal or metal alloy and its environment. In past years, the theory of corrosion electrochemistry has been well established by many researchers [Fontana 1978, Jones 1996, Kelly et al 2003, Uhlig & Winston Revie 1985].

The process of steel corrosion, the effect factors and the forms of corrosion are discussed below.

2.1.1 The Process of Steel Corrosion

The steel corrosion process involves the transfer of an electronic charge in an aqueous solution plus other factors. Its electrochemical nature and mechanism have been described by many authors for a range of commonly encountered exposure environments [Atkins et al 2002, Fontana 1978, Jones 1996, Lambert 2001, Uhlig & Winston Revie, 1985].

When moisture and oxygen are present, steel rusts. In its simplest form, the corrosion process can be represented by two dissimilar metals in an aqueous electrolyte, joined to allow electrons to pass from anode to cathode. In reality, when a metal corrodes, anodic and cathodic areas can be formed on a single metal surface in contact with the aggressive aqueous environment. As a result, corrosion can occur at a large number of sites over the surface of the metal. Dissolved ions react with hydroxyl and other ions to form characteristic corrosion products [Atkins et al 2002, Lambert 2001].

The reactions occurring at anodic and cathodic sites can be represented as follows:

Anode

At anodic areas the following oxidation reaction (anodic reaction) takes place:



(iron dissolves and forms iron ion and electrons)

{Iron → iron ion + electrons}

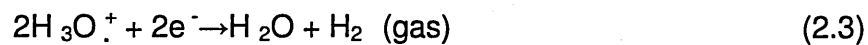
Cathode

In well-aerated neutral and alkaline environments, the following reduction reaction (cathodic reaction) takes place at cathodic areas:

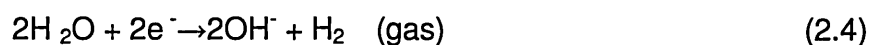


{Oxygen + water + electrons → Hydroxyl ion}

In some cases, especially in acidic conditions, the following reduction reactions can occur:

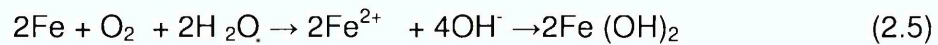


(acidic condition)

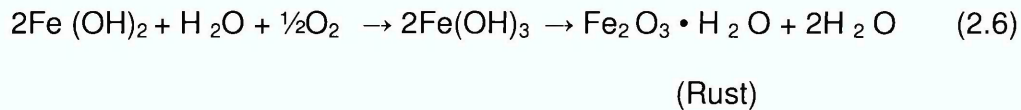


(neutral condition)

Dissolved iron ions react with hydroxyl ions to form corrosion products. The reaction can be obtained by adding (2.1) and (2.2):



Ferrous hydroxide precipitates from solution. However, this compound is unstable in oxygenated solutions and is oxidized to the ferric salt:



The final product is rust. The full corrosion process on steel is illustrated in Figure 2.1.

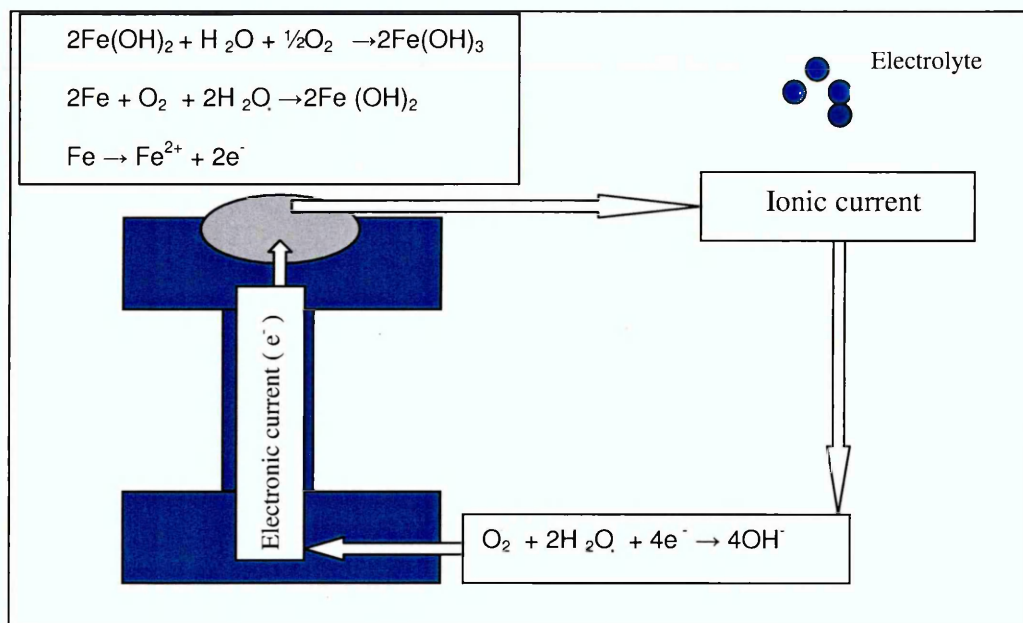


Figure 2.1: Corrosion reactions on steel

Production of hydrogen at the cathode can lead to failure in some materials, e.g. high strength low alloy steels, due to hydrogen embrittlement in areas that are stressed.

2.1.2 Effect Factors

The rate and nature of the corrosion process mainly depends on the following factors:

1. Alloy composition;
2. Environmental factors;
3. Design and nature of additional factors.

The relative humidity of an environment in particular has a profound effect on the rate of corrosion of steel [Atkins et al 2002].

2.1.3 Forms of Corrosion

Corrosion may be classified into eight forms [Fontana 1978]. These are: uniform or general attack; galvanic or two-metal corrosion; crevice corrosion; pitting; intergranular corrosion; selective leaching; erosion corrosion and stress corrosion.

In aqueous environments, the forms of metal corrosion are mainly as follows :

- (1) Uniform or general attack;
- (2) Galvanic, or bi-metallic corrosion;
- (3) Crevice corrosion;
- (4) Pitting

2.2 Corrosion of Steel Framed Masonry Buildings

There has been increasing awareness over the last 25 years that many high-profile steel-framed masonry buildings in many city centres may be prone to extensive damage as a result of corrosion of the steel frame, typically

constructed pre-1930 [Jones et al 1999]. Construction of these buildings, the steel frame corrosion, damage mechanism and types of corrosion are described below.

2.2.1 Construction of Steel Framed Masonry Buildings

The problems of corrosion of the steel-framed masonry buildings are related to the original designs and the form of construction in the first quarter of the 20th century at a time when the technology of corrosion protection was still largely undeveloped.

The external masonry of the buildings was tightly placed around the steel frame and cavities infilled with mortar, brick, or other porous rubble [Warland 1924]. These are illustrated in Figure 2.2 and Figure 2.3.

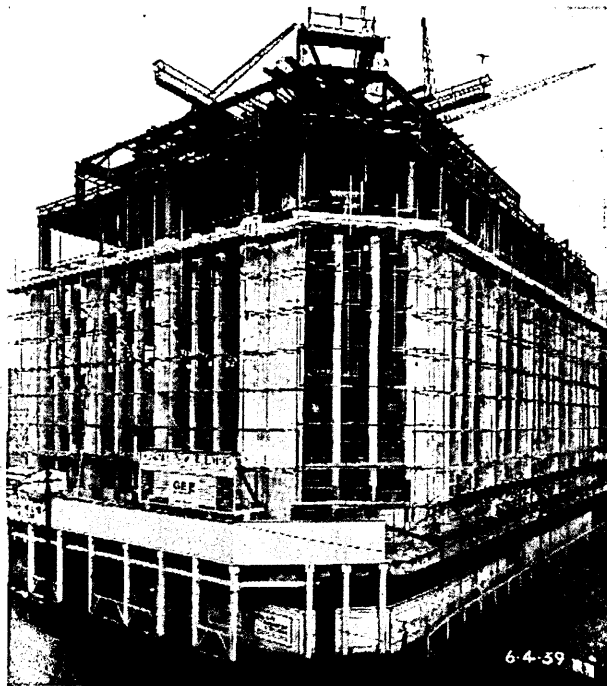


Figure 2.2: Construction of steel-framed masonry buildings (1)

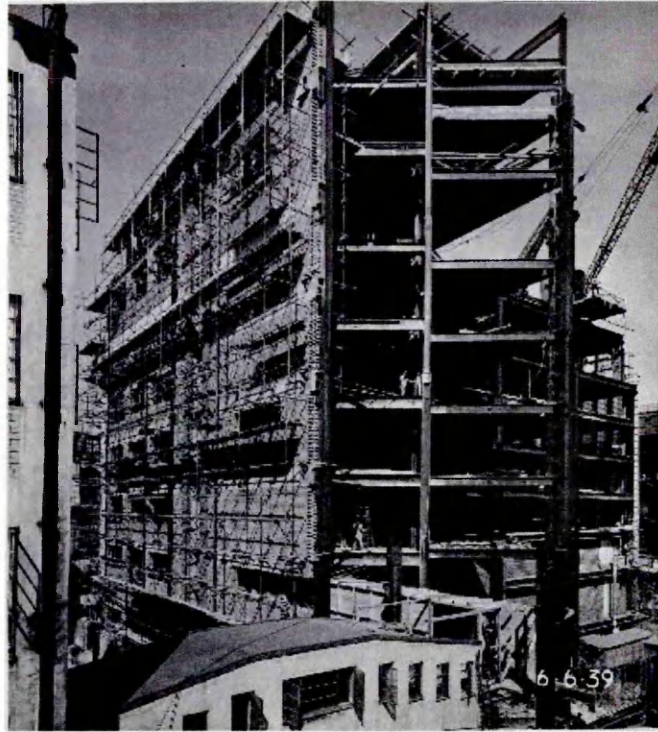


Figure 2.3: Construction of steel-framed masonry buildings (2)

2.2.2 Steel Frame Corrosion and the Damage Mechanism

The most common mechanism of failure in steel framed masonry buildings is corrosion of metals that support these buildings. This includes corrosion of small section lateral anchors, steel shelf angles and the steel frame of the building [Rewerts 2000]. Figure 2.4 and Figure 2.5 show the corrosion of a steel-framed beam and column respectively.

Atkins, Lambert and Coull [2002] described the mechanism of damage in steel-framed structure. It can be summarized as follows:

- The porous masonry and in-fill materials allow moisture entering the structures to come into contact with steelwork. Besides, moisture can also enter the structures through a variety of routes including open

joints, cracks or through poorly maintained gutters and pipework. As a result, corrosion becomes inevitable.

- As expansive corrosion products are formed, the tremendous stresses act on the surrounding mortar and masonry. These results in cracking, spalling and displacement of masonry, further opening up joints and cracks and permitting greater access to water. Thus, the rate of degradation tends to accelerate.

Thermal movements that aggravate the opening of joints will also lead to an acceleration of the damage, as typically observed on the weather-exposed corners of such buildings.

The rate at which the damage to the cladding occurs is governed by a number of factors:

- The time at which corrosion initiates—largely depends upon location, aspect and level of previous maintenance.
- The rate at which corrosion progresses—largely depends upon availability to moisture and oxygen, the type of environment, and the variability of the environment.
- The intimacy of the contact between the corroding steel and the cladding—gaps between steel and cladding can accommodate extensive corrosion with no visible damage.

Atkins, Lambert and Coull [2002] also described the location and severity of damage on a typical building in the UK.

Corrosion damage not only destroys the integrity of these buildings, but also could pose a serious public hazard and liability issue for the owner. The damage due to corrosion is shown in Figure 2.4 and Figure 2.5 respectively.



Figure 2.4: Corrosion of a steel - framed beam



Figure 2.5: Corrosion of a steel - framed stanchion or column

There are two major types of corrosion that can affect masonry clad steel frame buildings [Gibbs 2000, Daily & Somerville 2002]:

Uniform or General Corrosion

Uniform attack appears as an even layer of rust on the steel surface. This is the most common form of corrosion that is found in perimeter steel of masonry clad steel framed building. Uniform corrosion is generally due to electrochemical reaction, which occurs from the presence of oxygen and moisture. Under certain conditions the water or moisture that is in contact with the steel, may have extremely low values of pH due to acidic pollutants from rainfall (acid rain).

In fact, acid rain pH surveys have shown that acid precipitation at PH of 2 is not uncommon, especially during the initial period of snow or rain [Baboian 1995]. Carbonation, another contributor to corrosion, is a process by which carbon dioxide enter into the masonry. Carbon dioxide combines with the pore water in the mortar to form carbonic acid, which reduces the pH of the mortar to approximately 8 or 9. At these levels the protective oxide film at steel surface is no longer stable and, with adequate supply of oxygen and moisture, corrosion will start.

The penetration of masonry by carbonation is a slow process, the rate of which is determined by the porosity, permeability and moisture content of mortar.

Pitting Corrosion

Pitting corrosion, which is a localized form of attack, can lead to significant loss of steel section. Although this form of corrosion is uncommon in masonry clad steel-framed buildings, it can be found in coastal buildings where air borne salts have penetrated through the porous cladding to the steel surface.

The role of chloride ion in inducing corrosion of steel in concrete is well documented. If chlorides are present in sufficient quantity, they disrupt the passive film and subject the steel members to corrosion even when the steel is encased in good quality mortar or concrete.

Gibbs detailed steel corrosion in concrete and mortar, stone and other masonry [Gibbs 2000]. The corrosion of interior steelwork is also described.

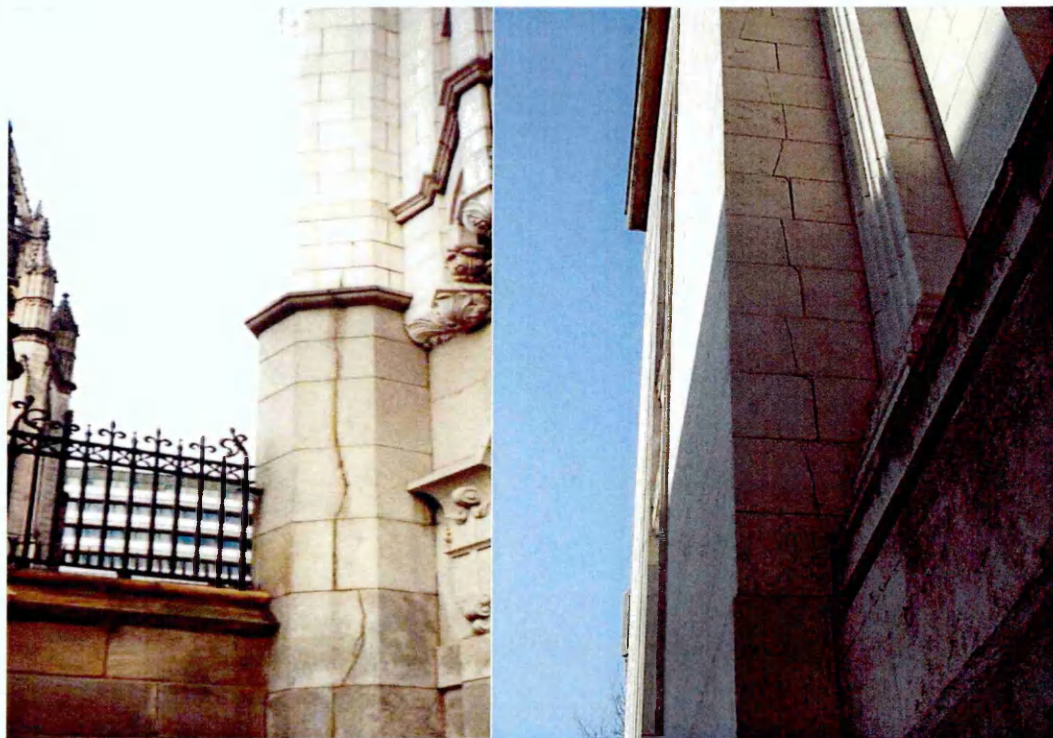


Figure 2.6: Portland stone cracking resulting from corrosion of a steel column



Figure 2.7: Brick cracking resulting from corrosion of a steel column

2.3 Electrochemical Testing Methods

Electrochemical techniques have been widely employed to investigate and identify corrosion. The most commonly used methods are half-cell potential, resistivity measurement, linear polarisation resistance, and potentiodynamic and potentiostatic polarisation curves.

The theory and principles of these methods have been well described by a number of authors [Fontana 1978, Jones 1996, Kelly et al 2003, Uhlig & Winston Revie 1985]. The applications and limitations of these techniques are given below.

2.3.1 Measurements of Half-Cell Potential

The half-cell potential is one of the most widely recognised and used non-destructive methods for assessing the corrosion state of buried pipelines [Parker 1984], reinforcement concrete structures [Berkley 1990, Bertolini et al 2004, Broomfield 1997, Chess 1998], and steel-framed masonry buildings [Gibbs 2000].

Care must be taken in the interpretation of readings. The readings are affected by the electrolyte and are dependent on the form of structures, their resistivity and the actual corrosion potential of the steel. Furthermore, this method is not applicable to structures in concrete containing corrosion inhibitors and structures subjected to electrical fields produced by stray current that induce current exchange between reinforcement and concrete [Bertolini et al 2004].

It should be noted that half-cell potential measurement cannot be correlated directly with the corrosion rate of the steel [Bertolini et al 2004]. It only gives an indication of the corrosion risk of the steel. The measurement is linked by empirical comparisons to the probability of corrosion [Broomfield 1997].

2.3.2 Resistivity Measurement

The resistivity of the electrolyte may be useful for monitoring and inspecting steel corrosion in various environments. The equipments used, the procedures and interpretation of the measurement in buried pipelines [Parker 1984], reinforcement concrete structures [Berkley 1990, Bertolini et al 2004, Broomfield 1997, Chess 1998], and steel-framed masonry buildings [Gibbs 2000] have been discussed by various authors.

It should be pointed out that temperature changes have a significant influence on electrolyte resistivity. In a similar manner to half-cell potential, the resistivity is only an indication of corrosion risk. The resistivity measurement is an additional measurement to aid identification of the problem areas. The readings can only be considered alongside other measurements.

2.3.3 Linear Polarisation Resistance

As discussed above, the measurements of half-cell potential and resistivity are not correlated directly with the corrosion rates. They are only indications of corrosion risk and probability of corrosion. Alternatively, the linear polarisation resistance technique can measure the corrosion current density and then the mass of steel consumed can be obtained by Faraday's law [Fontana 1978, Jones 1996]. Its basic principles, the instruments used and experimental procedures are described by the above authors.

This technique has inherent advantages [Jones 1996] as follows:

- The non-destructive nature of the test.
- The ability to measure a quantifiable corrosion rate.
- Speed of making corrosion rate measurements.
- Very high resolution of corrosion rate can be determined using Faraday's law.

Therefore, It has become one of the most common electrochemical techniques and has been widely employed in corrosion monitoring, for example, the corrosion of steel in concrete [Bertolini et al 2004, Broomfield 1997] and in the corrosion of steel-framed masonry buildings [Gibbs 2000].

It should be noted that the main problem of the technique is that it is, at best, an approximation of the corrosion rate rather than an accurate measurement. Furthermore, if corrosion is occurring at a few pits, it will tend to underestimate the corrosion rate in pits and overestimate the general corrosion rate.

2.3.4 Potentiodynamic and Potentiostatic Polarisation Curves

Potentiodynamic and potentiostatic polarisation curves are commonly used for assessing the kinetics of a corroding system. Its principles, instruments used and the experimental procedures have been described elsewhere [Fontana 1978, Jones 1996, Uhlig & Winston Revie 1985].

The results of the measurement are typically plotted in the form of potential versus log current density curves. The curves are used to study the mechanisms of corrosion and measure the corrosion rate. Scully & Bundy (1985) studied the steel pipe corrosion rates in soil. Hack (1995) measured the polarisation curves of a series of metal materials in seawater. Page and Treadaway (1982) discussed the mechanism of corrosion of steel in concrete. Cigna et al (1992) investigated the effect of different concrete mixes on the polarisation curves.

However, the measured curves are not only dependent on the environment condition but also the position of the anode and cathode.

2.3.5 Other Techniques

Other electrochemical techniques are also available, including AC impedance spectroscopy [Jones 1996] and electrochemical noise [Dawson 1983].

However, these techniques are not suitable for use in the field for application to the corrosion of steel in concrete and the corrosion of steel-framed in masonry buildings so they are not discussed herein.

2.4 Principles of Cathodic Protection

2.4.1 Theoretical Basis

Cathodic protection is one of the most widely used methods of corrosion control. The electrochemical basis of cathodic protection has been described by various authors [Fontana 1978, Jones 1996, Uhlig & Revie 1985].

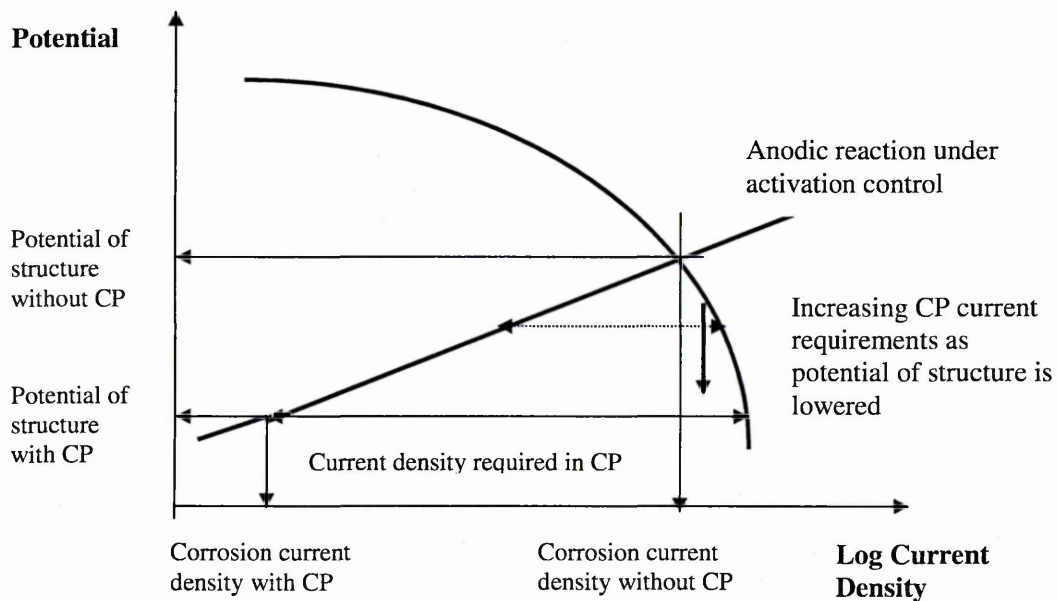


Figure 2.8: Evans diagram illustrating the increasing CP current requirements as potential of the structure is depressed.

An Evans diagram can provide the theoretical basis of cathodic protection. Such a diagram is shown schematically in Fig. 2.8 [Roberge 1999].

In principle, it can reduce or prevent the corrosion of any metal or alloy exposed to any aqueous electrolyte. Corrosion can be reduced to virtually

zero, and a properly maintained system will provide protection indefinitely. Cathodic protection reduces the corrosion rate by cathodic polarization of a corroding metal surface that relies on shifting the potential of the steel to more negative values.

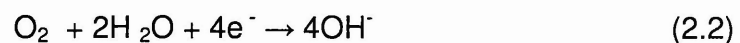
There are two basic types of cathodic protection systems commonly used. They are discussed below [Berkley 1990, Broomfield 1997, Chess 1998, Morgan 1959].

2.4.2 Impressed Current System

Consider iron corroding in well aerated neutral and alkaline environments. Impressed current cathodic protection works by a small direct current (DC) from a permanent anode fixed on to the surface or placed into the electrolyte of the protected steel. The power supply passes sufficient current from the anode to the protected steel to force the anodic reaction (2.1) to stop:



And make the cathodic reaction (2.2) to be the only one occurring on the protected steel surface. The cathodic reaction will then occur across the protected steel network:



The system is illustrated schematically in Figure 2.9.

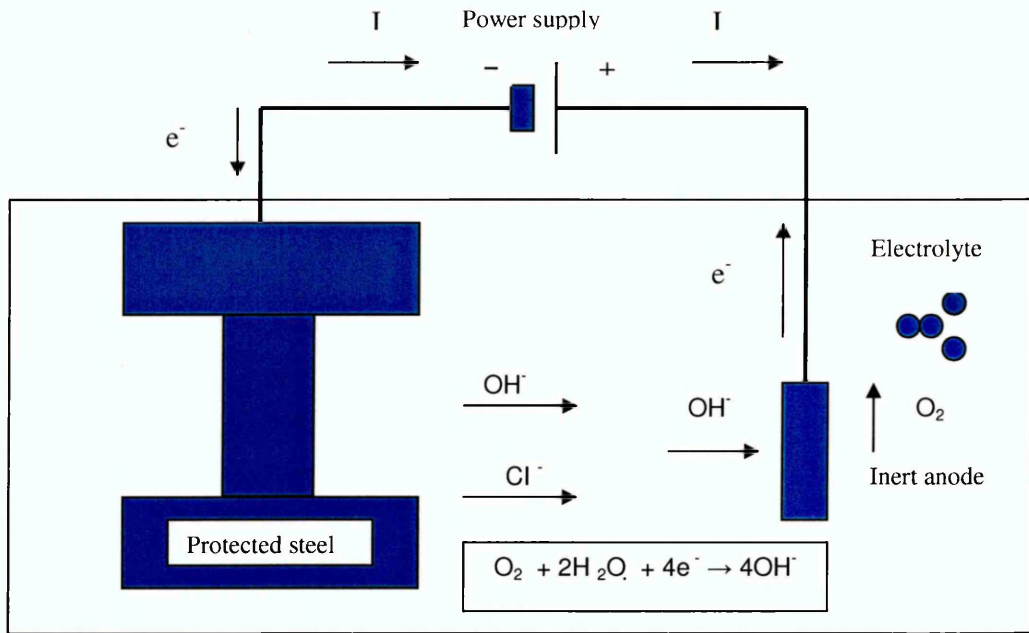


Figure 2.9: Impressed current cathodic protection

2.4.3 Sacrificial Anode System

Sacrificial Anode System is to directly connect the protected steel to a sacrificial or galvanic anode such as zinc without using a power supply. This anode corrodes preferentially, liberating electrons with the same effect as the impressed current system, e.g.



The system is illustrated schematically in Figure 2.10.

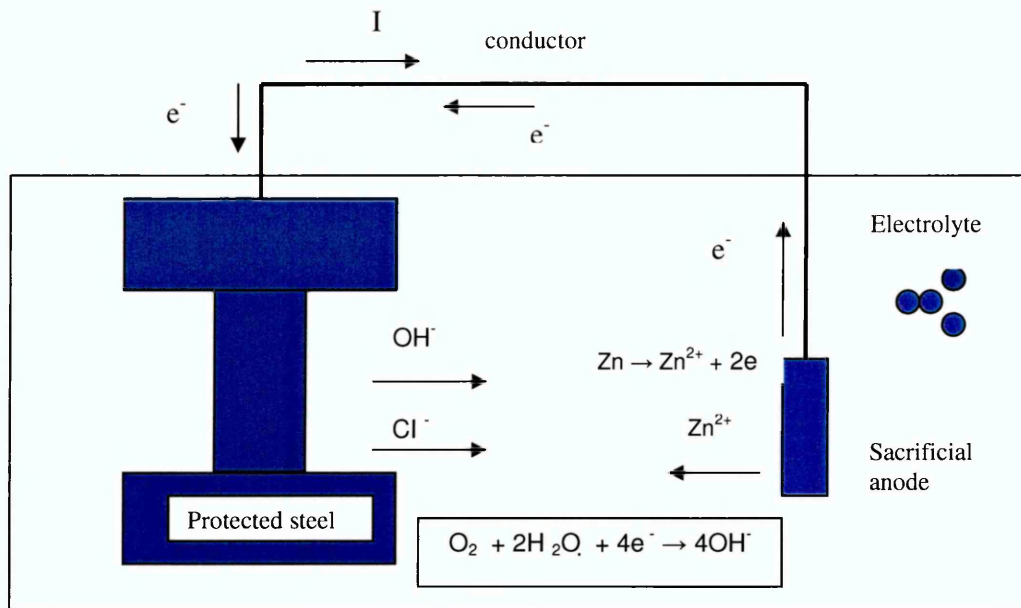


Figure 2.10: Sacrificial anode cathodic protections

2.5 The History of Cathodic Protection

The principles of sacrificial anode cathodic protection were first expounded by Sir Humphry Davy in 1824. His findings were used over the next century to protect the submerged metallic parts of ships from corrosion.

After Davy's discovery, Faraday examined the corrosion of cast iron in sea water and found that it corrodes faster near the water surface than deeper down. In 1834 he discovered the quantitative connection between corrosion weight loss and electric current. With this discovery he laid the scientific foundation of electrolysis and cathodic protection.

2.5.1 Cathodic Protection of Buried Pipelines

In the early decades of the 20th century cathodic protection technology was applied to underground pipelines. When it was found that the soil resistance was too high, impressed current cathodic protection was developed. It is little known that Thomas Alva Edison tried to achieve cathodic protection of ships with impressed current in 1890 [Baeckmann 1997]; however, the sources of current and anodic materials available to him were inadequate.

In 1902, K. Cohen achieved practical cathodic protection using impressed direct current. The German Herbert Geppert constructed the first cathodic protection installations for pipelines in 1906. This was a direct current generator of 10V 12A capacity protecting 300m of gas and water pipelines within the electrical field of a tramline.

To protect steam boilers and their tubes from corrosion, E. Cumberland used cathodic impressed current in America in 1905. From 1928 onward cathodic protection of pipelines was applied in United States. Robert J. Kuhn was called the "Father of Cathodic Protection" in America. He installed the first cathodic protection rectifier in 1928 on a long-distance gas pipeline in New Orleans, and thus inaugurated the first practical application of cathodic protection of pipelines.

As early as 1923, E. R. Shepard in New Orleans had diverted powerful tramline stray currents with an electrical drainage system. The protection range of plain cast pipes with poorly conducting joints did not extend to the ends of pipeline, so Kuhn put additional protective rectifiers in. He found by experiments that a protective potential of -0.85V against a saturated

copper/copper-sulphate electrode provided sufficient protection against any form of corrosion. At the Washington Conference for Corrosion Protection held by the National Bureau of Standards in 1928, Kuhn reported on the significant value of his experiments, on which the entire modern technology of cathodic protection is founded [Kuhn 1928].

Publications on the cathodic protection of pipelines became known in Europe at the end of the 1920s. In Belgium the drainage of streetcar stray currents was widely practiced. L. de Brouwer applied protection to gas supply lines in Brussels from 1932 onward and in 1939 the base plates of a gasholder were also protected with impressed current. In Germany the following report was made in 1939 on the cathodic protection of pipelines.

From former Soviet publications on cathodic protection, it appears that by about 1939 more than 500 cathodically protected installations existed in the USSR and judging by their numbers, these utilised sacrificial anodes. Cathodic protection of pipelines by sacrificial anodes appeared in Great Britain after 1940 [Morgan 1959]. In Germany cathodic protection technology was in use by 1949. Today cathodic protection for pipelines has become standard practice in many countries.

2.5.2 Cathodic Protection of Reinforced Concrete

The first reference of cathodic protection of reinforced concrete is in the 1950's [Heuze 1965]. The work that had been carried out up to the late 1970's emphasized the limitations of the techniques and materials then available but the last few years have seen major anode developments which allowed a

significant expansion of these methods of corrosion prevention [Berkley 1990].

In 1973 and 1974 the first commercial cathodic protection system for reinforced concrete was applied to the top deck of Sly Park Crossing Bridge Deck in California, USA [Stratful]. This coke/asphalt anode system operated for 11 years. CP applications to parking structures in USA did not appear until 1984.

In 1984 the first UK trial was designed and installed on Melbury House above Marylebone Station in London for British Rail. This included remote control and monitoring by modem link [Broomfield 1987]. Following this a large number of cathodic protection systems for reinforced concrete were designed and installed in UK.

Since those first systems were applied in the 1970's systems have been developed and applied to bridge decks, substructures and other elements, buildings, wharves, and every conceivable type of reinforced steel.

Anodes have been developed in the form of conductive coatings, metal embedded in concrete overlays, conductive concrete overlays and probes drilled into concrete.

2.5.3 Cathodic Protection of Steel-framed Masonry Buildings

The cathodic protection system for steel-framed Masonry Buildings [Gibbs 2000, Lambert 2001] is most recent application for this technology. The first cathodic protection system for the prevention of steel corrosion in a masonry structure was installed in 1991. The system protects the entrance colonnade

at Royal College of Science, Dublin; a limestone structure containing two parallel structural 'I' beam members. Regular remote monitoring and annual visual inspections have confirmed corrosion has been arrested.

Further applications in the early 1990s induced two Grade I Listed sites with the protection of iron cramps in the Inigo Jones Gateway, Chiswick House, London, and iron staircase supports embedded in the brickwork of Kenwood House, Hampstead.

It was not until 1997 that the first full steel-framed structure was protected by a cathodic protection system (Gloucester Road Underground Station). To date over twenty systems have been completed. Examples include: Lloyds Bank, Lombard Street London; Arkwright House and House of Fraser in Manchester; St Andrew House, Edinburgh and Putney Boathouse.

However, despite several sizeable installations in the United Kingdom and considerable overseas interest, there remain no formal guidelines for the design, installation and operation of such systems.

2.6 The Existing Standards and Test Methods

The existing standards and test methods for cathodic protection design such as NACE (2000), "Standard RP0290-2000, Impressed Current Cathodic Protection of Reinforcing Steel in Atmospherically Exposed Concrete Structures", European Standards (2000), "EN 12696:2000, Cathodic Protection of Steel in Concrete" and British Standards Institution, 2000 are not specific for steel-framed masonry structure. Historic Scotland Technical Advice Note 20 is based on empirical guidelines and various papers have also

been published based on practical experience [Atkins et al 2002, Gibbs 2000, Gibbs 2001].

At present no formal design guidelines, test methods or standards are available specifically for the cathodic protection of steel-framed masonry structures. In their absence it has become common practice for pilot schemes or trial installation to be employed in determining the suitability and design of CP systems for such applications.

2.7 Development of Numerical Methods for Predicting Current and Potential Distribution of Cathodic Protection Systems.

2.7.1 Introduction

An adequate and effective current and potential distribution is one of the important parameters determining the effectiveness of cathodic protection systems. Both under-protection and over-protection are undesirable. Under-protection of a structure does not completely prevent corrosion and over-protection can significantly reduce the life of the components and result in other undesirable side effects such as acid generation and hydrogen evolution. To avoid these problems, proper anode location to produce uniform current and potential distributions is important. This can also help minimise the current required to achieve the protection criterion, thus reducing the cost and improving the life of the system components.

To determine the optimum anode distributions, the current and potential distributions of cathodically protected structures need to be calculated. Traditionally, these have mainly relied on empirical methods and experience.

These methods have been used for a long time and have been an adequate tool for most conventional applications. However, for new applications of cathodic protection, the accuracy of these methods becomes uncertain. Hence, the current and potential distribution prediction of cathodic protection systems is not only useful but necessary when extending the technique to more sensitive or technically challenging applications.

2.7.2 Mathematical Theory

For a uniform, isotropic medium, the flow of current and distribution of potential can be shown to obey the Laplace equation [Adey et al 1985].

$$k\nabla^2 E=0 \quad (2.4)$$

where: E =potential and k =conductivity,

together with the relationship between the current density and potential

$$i = -k \frac{\partial E}{\partial n} \quad (2.5)$$

where i is current density at the electrode surface, n is the normal vector to the electrode surface. This is the governing partial differential equation for potential distributions in electrochemical cells. In order to solve this equation the boundary conditions must be defined. The boundary conditions are presented in Table 2.1 [Zamani et al 1986].

Combining the associated boundary conditions, the Laplace equation is solved and the potential distributions in electrochemical cells are given.

Table 2.1: Boundary Conditions

Type	Boundary Condition	Comment
Anodically polarized electrode	$-k \frac{\partial E}{\partial n} = i_0 f(E-E_{eq})$	Anodic branch if experimental polarization curve used
Cathodically polarized electrode	$-k \frac{\partial E}{\partial n} = i_0 f(E-E_{eq})$	Cathodic branch if experimental polarization curve used
Painted surface	$\frac{\partial E}{\partial n} = 0$	
Non-polarized	$E = \text{fixed value}$	For E consult EMF series
Impressed current	$-k \frac{\partial E}{\partial n} = \text{fixed value}$	Current density output

2.7.3 Analytical Methods

During the early 1950s, Wagner [1951, 1952] and Waber and co-workers [1954, 1955, 1956] discussed the analytical formulation of the cathodic protection systems with tools such as conformal mapping, perturbation techniques and the singularity distribution methods. Owing to the limitation of an analytical approach, only linear polarization behaviours were considered.

In 1977, McCafferty tried related problems in an axisymmetric geometry with linear boundary conditions. However, in practice, for the cathodic protection systems, there are two areas.

Firstly, the boundary or interface between the anode/cathode and the electrolyte (seawater, soil, concrete or mortar), which may have a complex geometry.

Secondly, the boundary condition or the relationship between potential and current density at the boundary (polarization behaviour) which can be both non-linear and time dependent.

It is widely accepted that such a system cannot be solved solely by analytical methods, and numerical methods have been used. The three major numerical approaches used for cathodic protection analyses are the finite difference method (FDM), finite element method (FEM) and boundary element method (BEM).

2.7.4 Finite Difference Method

The Laplace equation can be solved by the finite difference method. This method was first introduced in corrosion engineering in 1964 by Klingert [1964] and by Fleck [1964], separately. Smyrl and Newmann [1976] and Doig and Flewitt [1979] independently performed finite difference solutions for the potential distributions in particular galvanic cells.

Strommen and Rodland performed another attempt at a finite difference solution to the optimisation of anode distribution of an offshore platform protected by sacrificial anodes [Strommen & Rodland, 1981,1983]. Munn and Clark used this method to analyse current distribution of buried pipelines with impressed current CP systems [Munn et al 1983]. More recently, Glass and Buenfeld [1997] used this method to analyse the current and distribution of an atmospherically exposed concrete structure protected by impressed current CP systems.

As one of the numerical techniques, the finite difference method played an important part in corrosion engineering and has its own significant disadvantages. This method requires the sub-division or 'discretization' of the entire electrolyte domain and structure surface into a large number of elements. An equal number of simultaneous equations have to be solved to calculate the potential at each element, and a commensurate size of storage space is required in the computer memory.

With increasing geometrical complexity, the CPU time, and the memory size requirements may easily become prohibitive. Furthermore, this method has been mostly limited to an orthogonal mesh structure with little flexibility in varying the element shape, For this reason, the applications of finite difference method in corrosion engineering are restricted to simple geometry, two-dimensional and axisymmetric problems such as pipelines and tubular joints on offshore structures [Nisancioglu 1993].

2.7.5 Finite Element Method

The finite element method allows much great flexibility in the modelling of complex geometries because of the possibility of varying the element size and geometry. This method was introduced in cathodic protection system analysis in 1980 by Forest and Wu [1980].

Subsequently, several cathodic protection systems have been solved by this method such as two-dimensional/axisymmetric ships [Helle1980], ship's propeller [Forest & Bicicci 1981], a steel plate [Munn 1982], offshore structure [Decarlo 1982], submerged pipelines [Kasper & April 1983] and the tubes [Holser et al 1992].

Munn and Devereux [1991] used the finite element method to analyse galvanic corrosion systems and Hassanein, Glass and Buenfeld [2002] used this method to analyse the current and distribution of atmospherically exposed concrete structures protected by impressed current CP systems .

There are numerous commercial packages such as NASTRAN, MARC, ANSYS and WECAN [Zamani 1986]. Most of these are capable of solving potential problems in two and three dimension.

A prominent advantage of the finite element method is the ability to handle complicated geometries. As with the finite difference method, the finite element method utilizes a discretization of the bulk of the electrolyte into finite elements and solve Laplace equation (1) numerically in this discretized electrolyte. Hence, there are a number of unknowns, long calculating time and a commensurate size of storage space is required in the computer memory.

2.7.6 Boundary Element Method

The disadvantages of FDM and FEM can be overcome by the boundary element method [Brebbia 1978, Brebbia & Dominguez 1989]. With the BEM the Laplace equation is first transformed into an integral equation valid at the boundary. In order to solve this equation only the boundary surface has to be discretized into finite (surface) elements.

Using this method, the model of a structure surrounded by an electrolyte will, in general, be much simpler than FDM and FEM. This is a tremendous advantage in the design process where numerous anode configurations along

with a complex geometry may require evaluation before a final CP design is determined.

The first papers describing the application of boundary element techniques to cathodic protection analysis were published by Fu and Chen [1982], and Danson and Warne [1983], separately. The former analysed the potential distribution of the cathodically protected storage tank bottom with impressed current system. The latter described the application of the boundary elements to the cathodically protected Conoco Hutton Tension Leg Platform installed in the North Sea.

Gartland and Johnsen carried out modelling of an offshore test rig and tubular joint cathodic protection system [Gartland & Johnsen 1985]. Zamani [1986, 1988] used this method to simulate a cathodic protection system in a prototype ship.

Other work is described by Adey et al [1985], Niku and Adey [1985], Adey and Niku [1985], Niku et al [1986], Brebbia and Niku [1988], Adey and Niku [1992], Strommen [1981,1987,1992], Munn [1982], Telles [1985], Giorgi [1992] and Nisancioglu [1993], Amaya & Aoki [2003]. It is noticeable that the boundary element method has been mainly used in the modelling of cathodically protected offshore structures and marine structures.

Optimisation methods combined with the Boundary Elements Technology have become a useful techniques to analyse the optimisation of the cathodic protection systems. The study includes the optimisation of the anode current and position. Aoki and Amaya [1992] determined the optimum impressed

current density and optimum location of the electrode in 2D cathodic protection system. In 1997, they also presented an effective sensitivity analysis method for 3D problems and a cylindrical domain was studied.

Hang and Adey [1999] presented an approach to the global optimisation of a ship's ICCP system coupling the boundary element method with the global optimisation method. More recently, the study has been further developed by Santana Diaz and Adey [2002, 2003].

It should be pointed out that the most of works in optimisation analysis are limited to the analysis of the flat surface structures. When the surface of the protected structures are complex and irregular, the problems have not been well sorted out.

Some commercial packages such as COMCAPS [Gartland & Johsen 1985] and BEASY-CP [Niku et al 1986] have been developed and used in CP design.

It is worth mentioning that, although non-homogeneous electrolytes can be modelled by the boundary element method, the implementation is tedious [Brebbia et al 1984].

2.7.7 Comparison of Numerical Methods

The choice of numerical methods requires careful consideration. Each method has its advantages and disadvantages. These are discussed below [Zamanni 1986].

The finite difference method has a well established theory and it is very simple for code purposes. The resulting system of linear equations is well structured and sparse; therefore, it can be solved with efficient algorithms. Another feature of the finite difference method is the ability to handle a non-homogeneous electrolyte.

The major drawback of finite differences is their restriction due to irregular boundaries. This can be corrected to some extent by employing a body-fitted co-ordinate system. This is not an easy task in three dimensions. Another drawback which arises in corrosion problems is that the information generated in the body of the electrolyte may not be useful for corrosion analysis.

The finite element method also has a sound mathematical foundation. The implementation of the finite element is not as straightforward as that of the finite difference method, but it can easily handle irregular geometries. Like the finite difference method, the finite element method has well structured and sparse matrices, and has the ability to handle a non-homogeneous electrolyte. In corrosion applications, the resulting matrix is symmetric and positive definite.

In general, even in finite elements, three dimensional mesh generations can be difficult and time consuming. Furthermore, finite elements (also finite differences) have difficulties with infinite regions. This means that to analyse a structure in an infinite medium, the structure has to be enclosed in a box which could simulate the boundary conditions at infinity. As in finite differences, the information generated in the body of the electrolyte cannot be used for corrosion analysis.

The last method to be discussed is the boundary element method. This method is a relatively new method. A major feature of the boundary element method is that only the boundary of the domain under consideration has to be discretized. An attractive feature is that it can easily handle infinite domains. As far as corrosion calculations are concerned, the potentials and current densities are calculated on the structure to be protected.

There are two major drawbacks to the boundary element method. Firstly, an inhomogeneous electrolyte can be handled by sub-structuring, but it requires additional effort and is quite tedious. Secondly, the system of linear equations associated with the boundary element method is full and non-symmetric.

2.8 Stray Current Corrosion

Stray currents are currents flowing in the electrolyte from external sources. Stray current corrosion is the corrosion induced by stray current. The relevant background knowledge is reviewed as follows.

2.8.1 The Sources of Stray Current and Corrosion

There are a number of sources of undesirable stray current, including adjacent cathodic protection installations; DC transit systems such as electrified railways, subway systems, and streetcars; welding operations; and electrical power transmission systems. Stray currents can be classified into three categories:

- Direct currents
- Alternating currents
- Telluric currents.

Corrosion induced by these currents, its effects on buried pipelines and reinforced concrete have been well documented [Bertolini et al 2004, Roberge 1999]. Control of stray current corrosion is also discussed.

2.8.2 Measurement of Stray Current Corrosion Potential

Inspection of structures subjected to stray current can be based on potential measurement [Bertolini et al 2004]. The authors detailed the procedures of measurement and interpretation of potential. The correlation between the potential and the state of corrosion of carbon steel reinforcement affected by stray current is discussed.

Measurement is often influenced by the different factors, including ohmic drop and interference from external currents. In the case of stray current from cathodic protection systems the interfering current can be momentarily interrupted by turning off the source of current at the time of measurement. This is known as the "on-off" technique. In the case of stray current caused by DC traction systems this technique cannot be applied.

2.8.3 Boundary Element Method for Analysis of Stray Current Corrosion

Trevelyan and Hack [1994] firstly described the stray current corrosion modelling of ship structures and pipelines by the boundary element method. Strong et al [1997] used this method to predict the likelihood of cathodic protection interference on steel structures located in proximity to large cathodically protected chemical storage tanks. Adey and Pei Yuan Pang [1999] analyzed the stray current corrosion between ships and steel piles.

The results of the various pieces of research indicate that the application of the boundary element method allows cathodic protection interference to be assessed in term of current density, which is directly proportional to the corrosion rate, rather than having to use the qualitative approach of measuring the potential shift of the electrolyte.

Furthermore, the computer modelling approach enables results to be obtained at the design stage, allowing cathodic protection systems to be optimised so that interference is minimised.

2.9 Conclusions from the Literature Review

Cathodic protection is one of the most widely used methods of corrosion control. Its beneficial effects were recognised in the early part of the eighteenth century. Since the second half of the last century the technique has been increasingly employed in the protection of pipelines, ships, oil structures and reinforced concrete structures.

More recently, the technology has been applied to the protection of steel-framed masonry structures. In the UK, the first full steel-framed structure protected by such system was Gloucester Road Underground Station. To date over twenty CP systems have been completed and commissioned in such structures. However, the systems employed for such structures have been developed from the extensive experience gained in the cathodic protection of reinforced concrete.

Design guidelines, standards and test methods for steel-framed masonry structures currently do not exist. The existing standards and test methods for

cathodic protection design such as NACE (2000), "Standard RP0290-2000, Impressed Current Cathodic Protection of Reinforcing Steel in Atmospherically Exposed Concrete Structures", European Standards (2000), "EN 12696:2000, Cathodic Protection of Steel in Concrete" and British Standards Institution, 2000 are not specific for steel-framed masonry structures and are not directly applicable.

In the absence of formal design guidelines, test methods or standards specifically for the cathodic protection of steel-framed masonry structures, it has become common practice for pilot schemes or trial installations to be employed in determining the suitability and design of CP systems for such applications.

Numerical methods have not been employed on modelling the current and potential distribution of cathodic protection for steel-framed masonry structures. They have also not been used for the analysis of stray current corrosion resulting from cathodic protection interference in such structures.

It is therefore apparent that considerable development is required in order to obtain an appropriate numerical system for modelling the current and potential distributions of such systems and analyzing the stray current corrosion in steel-framed masonry structures.

3.1 Introduction

The overall aim of the project is to more accurately identify the factors associated with the optimum performance of cathode protection systems for steel-framed masonry structures with respect to the design, installation and operation. This requires a thorough understanding of the mechanisms of cathodic protection in such structures. The experimental work has principally concentrated on the following key topics:

1. Measuring the cathodic polarisation response of steel in representative environments.
2. Investigating the distribution of current and potential for cathodic protection systems designed for steel-framed masonry structures.
3. Determining the influence of brick type and joint width on the distribution of current and potential in cathodic protection systems.
4. Analysing corrosion due to stray current effects resulting from cathodic protection systems in steel-framed masonry buildings.

As the overall study involves both laboratory work and numerical modelling, this part of the work represents one of the two key tasks in the present project. An overview of the experimental programme is given below.

3.2 The Components of the Impressed Current Cathodic Protection Systems

A series of impressed current cathodic protection (ICCP) systems need to be assembled and constructed in laboratory conditions. The essential elements of such systems include the cathode, impressed current anodes, the electrolyte and the transformer/rectifier plus monitoring system [Broomfield

1997]. These components, as employed in the experimental work, are described below:

The Cathode: In these circumstances this is the beam or column (stanchion) of the steel frame that is to be protected. A variety of different sized "I" section low carbon steel sections are employed for this purpose.

Impressed Current Anodes: The two most widely used forms of anode currently employed for steel framed masonry structures are ribbons and discrete anodes. The ribbons are fine expanded meshes of mixed metal oxide (MMO) coated titanium and lend themselves for embedment in joints. This has the advantage of relatively simple installation and a very clean finished appearance, but can result in a number technical and operational concerns due to the restricted geometry. For these reasons the majority of commercial installations to date are understood to have employed discrete anodes.

Discrete anodes, in the form of MMO coated titanium rods or tubes or titanium ceramic tubes, are grouted into drilled holes into the body of masonry and fixed in place, usually with a cementitious grout. This allows much greater control over the distribution of current and can also overcome concerns over stray current effects to cramps and surface fixings by avoiding discontinuous items being interposed between the anodes and the steel. For these reasons, discrete anodes have been employed for the majority of the experiments.

The electrolyte: This is the medium through which the ionic current flows between anode to cathode. In the cathodic protection of steel framed masonry structures, direct current can pass through the mortar fill or masonry in contact with the steel frame. The masonry and mortar fill is therefore acting as the electrolyte. In the case of these experiments, damp sand may be employed to represent porous, fully carbonated masonry fill of neutral pH.

The transformer/rectifier: This is the direct current power supply system that transforms standard alternating current to a lower voltage and rectifies it to direct current. The positive terminal is connected to the anode and negative to the cathode (in this case, the steel). For this study, a CPI manual power supply system, manufactured and supplied by Cathodic Protection International Aps, has been employed.

Two different forms of experimental arrangement have been employed, using either sand or mortar and brick masonry as the electrolyte. Further details of the individual experiments are provided in Chapter 6 and Chapter 7.

3.3 Experimental Programme

The experimental programme can be sub-divided into the following four sections:

1. The investigation of the cathodic polarisation response of encased steel, involving:
 - Measurement of cathodic polarisation data for steel in damp sand with a range of resistivities.

- Measurement of cathodic polarisation data for steel in lime and cement-lime mortar of varying composition and resistivity.

The experimentally determined polarisation data and curves describe the relationship between the potential and current density on the surface of the anode and the cathode.

2. Experimental work carried out on the ICCP system employing a sandbox to represent the surrounding masonry. The aim is to study of distribution of CP potentials and currents. The potential distribution is measured under a range of test conditions by moving a hand-held reference (potential measurement) electrode.
3. Experimental work carried out on the ICCP system with mortar and brick encasement. The aim is to investigate the effect of brick type and joint width on the distribution of CP potentials and currents.
4. Set up an ICCP system employing a sandbox to represent the encasing masonry for studying the corrosion of structures subject to stray current. The corrosion potential of stray current will be measured in this section.

The test set-ups and experimental procedures are detailed in Chapters 5 to 8.

The experimental data obtained from these experiments will be compared with the results of the numerical modelling.

3.4 Test Materials

Five classes of structural material are used in this experimental work. They are low carbon (mild) steel, medium grain sand, ordinary Portland cement,

slaked lime and brick masonry. All these materials are easily sourced and commercially available.

More specific details of the materials and how individual test specimens are constructed will be described separately in the following chapters.

Chapter 4:
Boundary Element Method for the
Modelling of Cathodic Protection Systems

4.1 Introduction

Over the past decade computer modelling has become a significant tool in the analysis and design of cathodic protection systems. Amongst the techniques that can be employed are the finite difference method, finite element method, and boundary element method. They have been widely used to model the cathodic protection systems for buried pipelines, ship structures, offshore structures, and reinforced concrete structures.

However, the review of previous work (Chapter 2) revealed that none of these techniques have been employed on modelling the current and potential distribution of cathodic protection for steel-framed masonry structures. They have also not been used for the analysis of stray current corrosion resulting from cathodic protection interference in such structures. It is therefore apparent that considerable development is required in order to use an appropriate numerical technique for modelling the current and potential distributions of such systems and analyzing the stray current corrosion in steel-framed masonry structures.

When compared to the finite difference method and the finite element method, the boundary element methods for the analysis of cathodic protection shows the following advantages [Adey and Niku 1992]:

- The meshes are only on the surface; hence only one or two-dimensional elements are required. It therefore reduces the number of nodes required to model a particular system and minimises data preparation.

- Boundary element methods give the solutions on the boundary and, only if required, at specified internal points. Since for analysis of cathodic protection the solution is only required on the surfaces, it is far easier to analyze the results than the finite element method which automatically gives results for all nodes (internal or boundary).
- Boundary element methods are very effective and accurate for modelling infinite domains.

With these advantages in mind, boundary element methods have therefore been employed for the modelling of cathodic protection systems for steel-framed masonry structures in this project. In the following sections the theory of the boundary element method and its applications in analysis of cathodic protection systems are discussed and developed.

4.2 Basic Equations

4.2.1 Governing Equation

For a uniform homogeneous electrolyte, the flow of current can be shown to obey the Laplace equation. The equation is written in terms of the electrical potential [Fu & Chow 1982, Danson & Warne 1983, Adey & Niku 1992]:

$$k\nabla^2 E(p) = 0 \quad p \in \Omega \quad (4.1)$$

where E is the potential at any $p(x, y, z)$ of domain

k is the conductivity of electrolyte

Ω is the problem domain

together with the following relationship between the current density and potential:

$$i = -k \frac{\partial E}{\partial n} \quad (4.2)$$

where i is current density at the electrode surface and n is the normal vector to the electrode surface. This is the governing partial differential equation for potential distributions in electrochemical cells.

The problem in cathodic protection is to solve the above Laplace equation subject to certain boundary conditions. These boundary conditions will be described in Section 4.4.

4.2.2 Boundary Integral Equation

Equation (4.1) can be written in terms of boundary values only. By starting from Green's second identity or weighted residual statement and following standard procedure, its boundary integral equation is derived. This equation can be expressed as follows [Brebbia 1978, Danson & Warne 1983, Adey & Niku 1992, Brebbia & Dominguez 1989]:

$$c(p) E(p) + \int_{\Gamma} i^* E d\Gamma = \int_{\Gamma} E^* i d\Gamma \quad (4.3)$$

where Γ is the boundary or surface of the domain Ω . i is the component of current density normal to boundary.

$c(p)$ is the multiplier. $c(p) = 1$ when the point p is completely inside the domain Ω . If the point p is completely outside the domain Ω , $c(p) = 0$. On the smooth boundary $c(p) = 0.5$. At sharp corners:

$$c(p) = \frac{\theta}{2\pi} \quad (4.4)$$

where θ is the angle subtended by the domain at the source point's immediately geometry.

E^* and i^* are the fundamental solutions. For homogeneous electrolyte in two dimensional (2D) analysis:

$$E^* = \frac{1}{2\pi\kappa} \ln\left(\frac{1}{r}\right) \quad (4.5)$$

and:

$$i^* = -\frac{1}{2\pi r^2} (r_x n_x + r_y n_y) \quad (4.6)$$

where r is the distance in space. r_x and r_y are the component of r in the x and y direction respectively, and n_x and n_y are likewise the components in the x and y direction of unit normal to boundary surface.

For three dimensional analysis:

$$E^* = \frac{1}{4\pi\kappa r} \quad (4.7)$$

and:

$$i^* = -\frac{1}{4\pi r^3} (r_x n_x + r_y n_y + r_z n_z) \quad (4.8)$$

Thus it can be seen that the boundary integral equation (4.3) gives the potential at any point p , inside the domain or on the boundary, as a function of the potential and normal current density components around the boundary surface. The next section discusses how this equation may be expressed in a discrete form, leading to the boundary element method.

4.3 The Boundary Element Method

4.3.1 Discretisation of Boundary Integral Equation and Numerical Solutions

It is clear that the boundary integral equation (4.3) completely describes the distributions of potential and normal current density around the boundary in terms of the integrals around the boundary surface Γ of the fundamental solutions E^* and i^* .

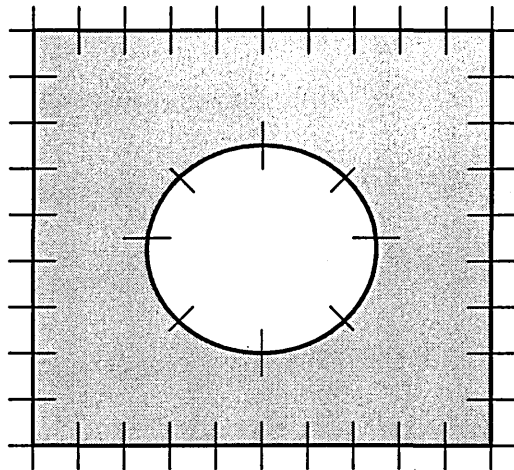


Figure 4.1 The discretation of boundary into elements

It should be noted for engineering analysis that the integrations needed to solve the boundary integral equation cannot be performed completely analytically except for special cases. Therefore, it is needed to use numerical integration for general problems. To integrate numerically the functions E^* and

i^* , the surface Γ is divided into many small segments or boundary elements, for example in a two dimensional analysis (Figure 4.1).

The integrations are then performed over small sections of the boundary surface Γ , and their contributions added together to complete the surface integrals in equation (4.3).

Thus the boundary integral equation (4.3) becomes:

$$c(\rho) E(\rho) + \sum_{elem} \int_{\Gamma_{elem}} i^* E d\Gamma_{elem} = \sum_{elem} \int_{\Gamma_{elem}} E^* i d\Gamma_{elem} \quad (4.9)$$

where $\int_{\Gamma_{elem}}$ denotes integration over an element and Γ_{elem} an element boundary.

The distributions of potential E and normal current density i with any one element in equation (4.9) can be expressed in term of the values of these variables at discrete points on the boundary, called nodes. The potential at any point can be found by using some method of interpolation between the values of potential at the anodes. Similarly, the normal current density at a boundary point may be found by interpolating the values of normal current density from the nodes.

By using pre-assigned node positions, a set of interpolation functions, which define the values of potential and normal current density at any point on the element in terms of the values at the nodes on the element can be written. So for an element having n nodes, the values of potential E at any point on the

element can be defined in term of the values of potential (E_1, E_2, \dots, E_n) at the nodes and interpolation functions:

$$E = \phi_1 E_1 + \phi_2 E_2 + \dots + \phi_n E_n = [\phi_1, \phi_2, \dots, \phi_n] \begin{Bmatrix} E_1 \\ E_2 \\ \cdot \\ \cdot \\ E_n \end{Bmatrix} \quad (4.10)$$

where the ϕ terms are the interpolation functions. Equation (4.10) can also be written conveniently in the vector form:

$$E = \Phi^T \mathbf{E} \quad (4.11)$$

where $\Phi^T = [\phi_1, \phi_2, \dots, \phi_n]$ and $\mathbf{E}^T = [E_1, E_2, \dots, E_n]$. Similarly, an equation can be defined for the normal current density, in which the values of i at ant point can be expressed:

$$i = \Phi^T \mathbf{i} \quad (4.12)$$

where \mathbf{i} is a vector of normal current density values at the n nodes on the element. Substituting equation (4.11) and (4.12) into equation (4.9) and taking the vector \mathbf{E} and \mathbf{i} outside the integrals since they can be considered to be constants, the following equation is obtained:

$$c(\rho) E(\rho) + \sum_{elem} \int_{\Gamma_{elem}} i^* \Phi^T d\Gamma_{elem} \mathbf{E} = \sum_{elem} \int_{\Gamma_{elem}} E^* \Phi^T d\Gamma_{elem} \mathbf{i} \quad (4.13)$$

This is the general discrete form of the boundary integral equation.

By setting up an equation such as equation (4.13) for point p corresponding to each node in turn, a series of linear algebraic equations are formed which may be written in matrix notation:

$$\mathbf{HE}=\mathbf{Gi} \quad (4.14)$$

where:

\mathbf{H} and \mathbf{G} are the $(n \times n)$ square matrices, called the influence matrices.

The detailed expressions are given by Brebbia [1978], \mathbf{E} contains the nodal potential vectors, \mathbf{i} contain the nodal normal current density vectors.

Equation (4.14) cannot be solved immediately since for each node there is one equation and as seen in equation (4.14), one value of potential and one current density which are both unknown. However, when applying the technique to real geometries additional information will be known which will enable the equation to be solved. For example, the potential may be known on the anode but the current density unknown. Alternatively the current density may be known on some anodes but the potential unknown.

By rearranging equation (4.14) to get all known values on the right-hand side, and all unknown values on the left-hand side, the following equation is obtained:

$$\mathbf{AX}=\mathbf{BY} \quad (4.15)$$

The right-hand side is multiplied out to obtain

$$\mathbf{AX}=\mathbf{F} \quad (4.16)$$

For the linear boundary conditions, the above equation can be solved by Gauss Elimination or LU Decomposition [Press et al 1992]. However, in practice the boundary conditions on the anodes and cathodes are represented by the non-linear polarisation curves. Equation (4.16) is therefore solved by an interactive procedure. More details will be discussed in Section 5.5.

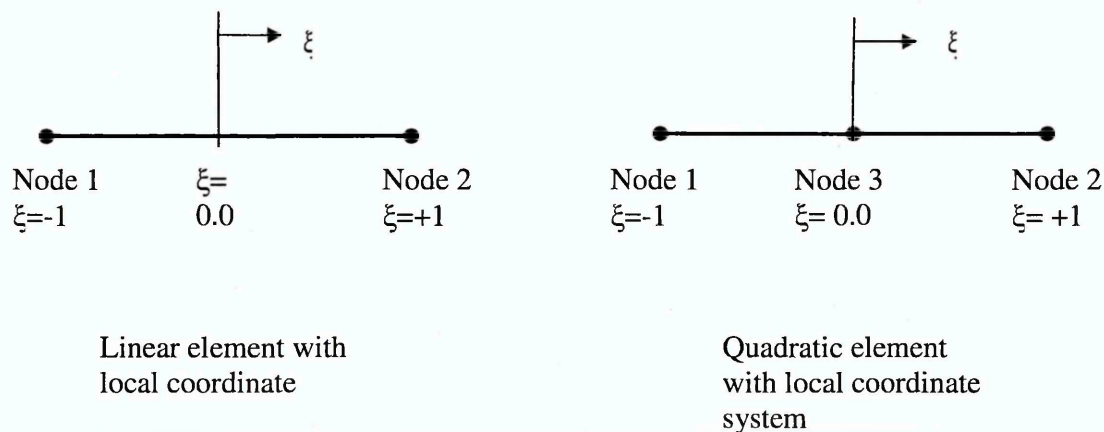


Figure 4.2: One-dimensional elements for two dimensional problems

4.3.2 Types and Interpolations of Elements

In the previous section the procedure for the boundary element method has been discussed. The types and interpolations of elements which can be used are described below.

For 2D problems typical boundary elements are one-dimensional elements, shown in Figure 4.2. The order of the element may vary, e.g. linear, quadratic by using different numbers of nodes.

For a one-dimensional linear and quadratic isoparametric elements for which the geometrical shape of the element is defined in the same way as the

potential E and normal current density i , the following interpolations are introduced by using the local coordinate system ξ in the definition:

$$u(\xi) = \sum_{n=1}^L \phi_n(\xi) \mathbf{u}_n^e \quad \text{Geometry}$$

$$E(\xi) = \sum_{n=1}^L \phi_n(\xi) \mathbf{E}_n^e \quad \text{Potential}$$

$$i(\xi) = \sum_{n=1}^L \phi_n(\xi) \mathbf{i}_n^e \quad \text{Current density}$$

where L is the number of element nodes, ϕ_n is the interpolation functions and $\mathbf{u}_n^e = [u_1^e, u_2^e, \dots, u_n^e]^T$ are the values of the nodal coordinate.

For Linear elements ($L=2$):

$$\phi_1 = \frac{1}{2} (1 - \xi); \quad \phi_2 = \frac{1}{2} (1 + \xi)$$

For Quadratic elements ($L=3$):

$$\phi_1 = \frac{1}{2} \xi (1 - \xi); \quad \phi_2 = \frac{1}{2} \xi (1 + \xi); \quad \phi_3 = \frac{1}{2} \xi (1 + \xi) (1 - \xi)$$

Elements of a higher order than quadratic, for example cubic elements, are seldom used in practice and are therefore not discussed here.

For three dimensional problems, surface elements are used which cover the boundary of the domain. They are usually two types; triangular or quadrilateral, and both can be flat or curved as shown in Figure 4.3.

Their interpolations, using the local coordinate system (ξ, η) , may be defined as follows:

$$u(\xi, \eta) = \sum_{n=1}^L \phi_n(\xi, \eta) \mathbf{u}_n^e \quad \text{Geometry}$$

$$E(\xi, \eta) = \sum_{n=1}^L \phi_n(\xi, \eta) \mathbf{E}_n^e \quad \text{Potential}$$

$$i(\xi, \eta) = \sum_{n=1}^L \phi_n(\xi, \eta) \mathbf{i}_n^e \quad \text{Current density}$$

For continuous quadrilateral elements a set of interpolation functions are as follows:

Bilinear elements:

$$\phi_1(\xi, \eta) = \frac{1}{4} (1 + \xi) (1 + \eta); \quad \phi_2(\xi, \eta) = \frac{1}{4} (1 - \xi) (1 + \eta)$$

$$\phi_3(\xi, \eta) = \frac{1}{4} (1 - \xi) (1 - \eta); \quad \phi_4(\xi, \eta) = \frac{1}{4} (1 + \xi) (1 - \eta)$$

Biquadratic elements:

$$\phi_1(\xi, \eta) = \frac{1}{4} \xi \eta (1 + \xi) (1 + \eta); \quad \phi_2(\xi, \eta) = \frac{1}{4} \xi \eta (1 - \xi) (1 + \eta)$$

$$\phi_3(\xi, \eta) = \frac{1}{4} \xi \eta (1 - \xi) (1 - \eta); \quad \phi_4(\xi, \eta) = \frac{1}{4} \xi \eta (1 + \xi) (1 - \eta)$$

$$\phi_5(\xi, \eta) = \frac{1}{2} \eta (1 - \xi) (1 + \xi) (1 + \eta); \quad \phi_6(\xi, \eta) = \frac{1}{2} \xi (1 - \xi) (1 - \eta) (1 + \eta)$$

$$\phi_7(\xi, \eta) = \frac{1}{2} \eta (1 - \xi) (1 + \xi) (1 - \eta); \quad \phi_8(\xi, \eta) = \frac{1}{2} \xi (1 + \xi) (1 - \eta) (1 + \eta)$$

$$\phi_9(\xi, \eta) = (1 - \xi) (1 + \xi) (1 - \eta) (1 + \eta)$$

Similarly, a set of interpolation functions for triangular elements may be written below:

Linear elements:

$$\phi_1(\xi, \eta) = \xi; \quad \phi_2(\xi, \eta) = \eta; \quad \phi_3(\xi, \eta) = 1 - \xi - \eta$$

Quadratic elements:

$$\phi_1(\xi, \eta) = \xi (2\xi - 1); \quad \phi_2(\xi, \eta) = \eta (2\eta - 1)$$

$$\phi_3(\xi, \eta) = (1 - \xi - \eta)[2(1 - \xi - \eta) - 1]; \quad \phi_4(\xi, \eta) = 4\xi\eta$$

$$\phi_5(\xi, \eta) = 4\eta(1 - \xi - \eta); \quad \phi_6(\xi, \eta) = 4\xi(1 - \xi - \eta)$$

To avoid the problem of having two unknown current densities at a corner node, the discontinuous elements are introduced. Further details are referenced elsewhere [Brebbia 1989].

It should be noted that equation (4.13) gives the general discrete form of boundary integral equation as solved by boundary elements of any order, by introducing the interpolation functions. The integrals which have to be performed over each element have to be solved by a numerical integration procedure. This type of procedure involves changing the variables of the

integration, which are ξ for two dimensional problems and ξ, η for three dimensional problems.

As this involves the use of a new coordinate system for performing the integration over an element length (2D analysis) or area (3D analysis), there is a need to include a coordinate transformation term in the integral equation. Use of these Jacobian matrices is well documented [Hayami & Brebbia 1989].

For example, in a 3D problem the current density components in a local coordinate system (ξ, η, ζ) may be related by a Jacobian matrix to the current density components in the global Cartesian system (x, y, z) as follows:

$$\begin{pmatrix} \frac{\partial u}{\partial \xi} \\ \frac{\partial u}{\partial \eta} \\ \frac{\partial u}{\partial \zeta} \end{pmatrix} = \begin{pmatrix} \frac{\partial x}{\partial \xi} & \frac{\partial y}{\partial \xi} & \frac{\partial z}{\partial \xi} \\ \frac{\partial x}{\partial \eta} & \frac{\partial y}{\partial \eta} & \frac{\partial z}{\partial \eta} \\ \frac{\partial x}{\partial \zeta} & \frac{\partial y}{\partial \zeta} & \frac{\partial z}{\partial \zeta} \end{pmatrix} \begin{pmatrix} \frac{\partial u}{\partial x} \\ \frac{\partial u}{\partial y} \\ \frac{\partial u}{\partial z} \end{pmatrix} \quad (4.17)$$

or

$$\begin{pmatrix} \frac{\partial u}{\partial \xi} \\ \frac{\partial u}{\partial \eta} \\ \frac{\partial u}{\partial \zeta} \end{pmatrix} = \mathbf{J} \begin{pmatrix} \frac{\partial u}{\partial x} \\ \frac{\partial u}{\partial y} \\ \frac{\partial u}{\partial z} \end{pmatrix} \quad (4.18)$$

In order to transform the coordinates of the integration, the determinant of the Jacobian matrix, $|J|$, is included in the function to be integrated. Thus equation (4.13) can be written as follows.

For two dimensional problem:

$$c(p) E(p) + \sum_{elem} \int_{\Gamma_{elem}} i^* \Phi^T |J| d\xi E = \sum_{elem} \int_{\Gamma_{elem}} E^* \Phi^T |J| d\xi i \quad (4.19)$$

For three dimensional problem:

$$c(p) E(p) + \sum_{elem} \int_{\Gamma_{elem}} i^* \Phi^T |J| d\xi d\eta E = \sum_{elem} \int_{\Gamma_{elem}} E^* \Phi^T |J| d\xi d\eta i \quad (4.20)$$

Equations (4.19) and (4.20) show that equation (4.13) can be completely integrated in the local coordinate systems of the boundary elements.

4.3.3 The Internal Solutions

After all values of the potentials and normal current densities in equation (4.16) are solved, the solutions of the internal point in domain can be easily calculated. When the point p is completely inside the domain Ω , $c(p) = 1$ in equation (4.3). So it becomes:

$$E(p) + \int i^* E d\Gamma = \int E^* i d\Gamma \quad (4.21)$$

Where $E(p)$ is the values of potential in the internal domain and the boundary potential and the normal current density terms E and i are known. Equation (4.21) therefore gives the potentials $E(p)$ at the internal point in terms of completely known functions, and it can therefore be evaluated.

By differentiating equation (4.21) with respect to x, y, z direction another equation which gives the current density components in the directions at the internal points can be obtained.

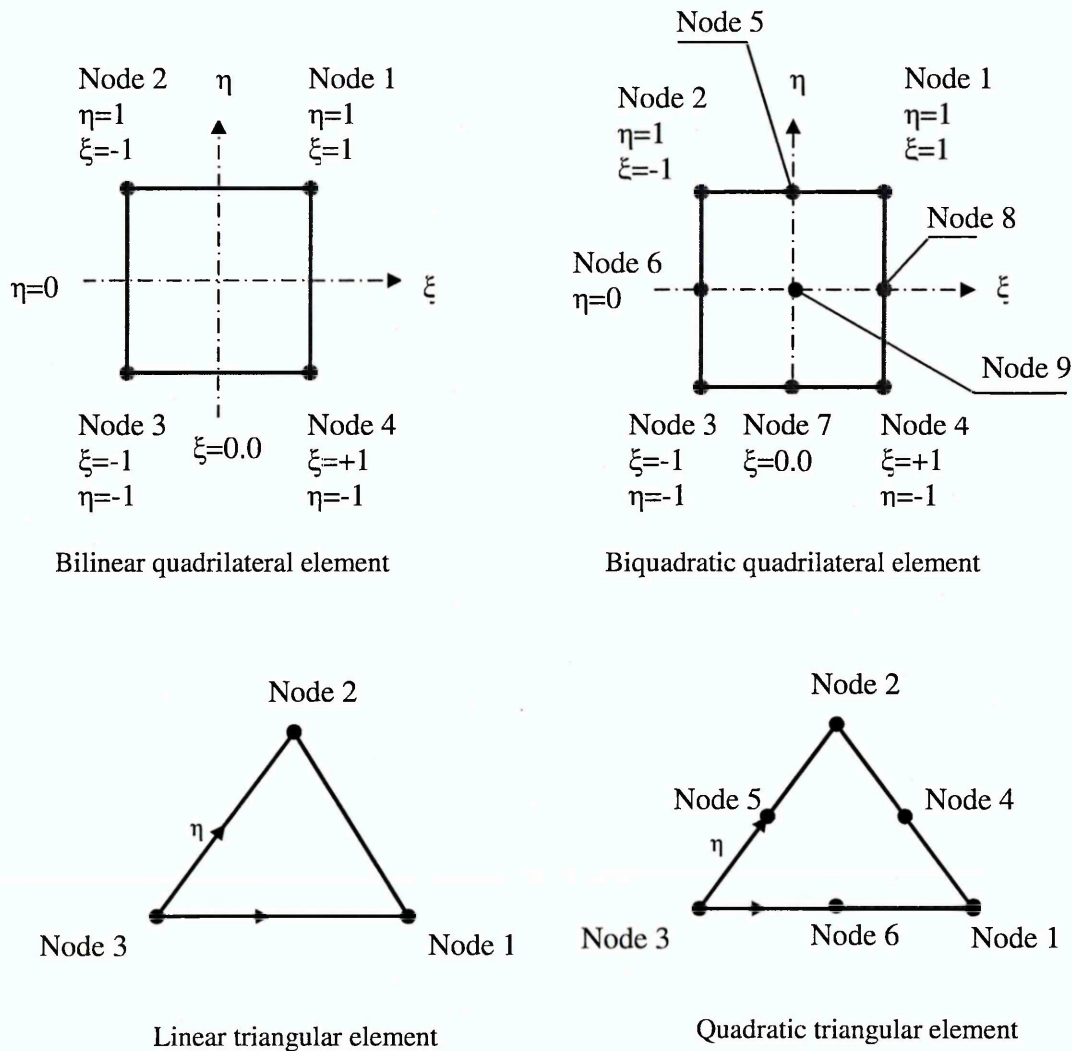


Figure 4.3 Two dimensional elements for three dimensional problems

For the cathodically protected steel-framed masonry buildings the internal point solutions play an important role to investigate the effect of joints width on the distributions of the potentials and current densities.

4.4 Boundary Conditions

The literature review has already identified the boundary conditions, as listed in Table 2.1. Normally, the types of boundary conditions allowed for are as follows:

- 1) Prescribed normal current density, for example normal current density is set to zero on insulating surface or free surface.
- 2) Prescribed potential.
- 3) A linear relationship between the potential E and current density i on the anode surface or cathode surface.
- 4) A non-linear relationship between the potential E and current density i on the anode surface or cathode surface. It may be the non-dependent or steady-state and full-time dependent or transient.

The first three of these conditions may be handed straight forwardly enough. However, the last is slightly difficult. They are analyzed below.

For a real cathodic protection system, the relationship between the potential E and current density i on the anode surface or cathode surface can be written as below:

$$\begin{aligned}
 i_a &= f_a(E_a) \\
 i_c &= f_c(E_c)
 \end{aligned}
 \tag{4.22}$$

where:

i_a = current density on the anodic surface,

E_a = potential on the anodic surface,

f_a = a function which represents the electrode kinetics and polarization on the anodic surface,

i_c = current density on the cathodic surface,

E_c = potential on the cathodic surface,

f_c = a function which represents the electrode kinetics and polarization on the cathodic surface.

The above non-linear relationship between the potential E and current density I on the anode surface or cathode surface, known as the polarisation curves, is dependent upon many factors, such as the type of metal, ionic species in the electrolyte, environment, etc. However, it can be measured in laboratory or from field data.

The experimental procedure and its measurement will be described in Chapter 5. The results of data are also included.

It should be noted that for an impressed current cathodic protection system the boundary condition on the anode surface are particularly dealt with. The details will be described in Chapter 6.

4.5 Methods and Procedure of Solution

Thanks to the non-linear nature of the boundary conditions on the anode surface or the cathode surface, an iterative procedure must be employed to solve equation (4.16).

There are two prime iterative methods. They are the Newton-Raphson method [Press etc 1992] and the method of successive approximation [Danson & Warne 1983, Strong et al 1997]. The former has been well-documented. The latter is therefore described here. There are several ways to perform the iterative procedures. One of which is described here. Its iterative process is as follow:

- Estimate the current density at the electrode interface and incorporate it into the right-hand side vector F of equation (4.16).
- Calculate the potential at the metal-to-electrolyte interface by running linear equation system (4.16).
- Evaluate the new current density using the polarisation curves of steel, which is equation (4.22) or measured polarisation data.
- Compare new current density with the previous estimate and, if the difference is outside a given tolerance, repeat the process from the second step.
- If the results are the same (with the tolerance), convergence has been achieved and the solution has been found. Then any internal point values are calculated.

Normally, the general iteration procedure is also needed. It is given in Figure 4.4 [Zamani 1986].

Usually, a number of iterations may be required, depending on the size of the problem but mostly on the slopes which are in the polarization curves. Very flat or very steep portions of the curves slow down convergence, as do sharply varying slopes in the same polarization curve, typically, convergence could be expected from a scheme as described above in 10 to 40 iterations.

A tolerance of 0.1% to 0.5% is typically used, depending on the required accuracy.

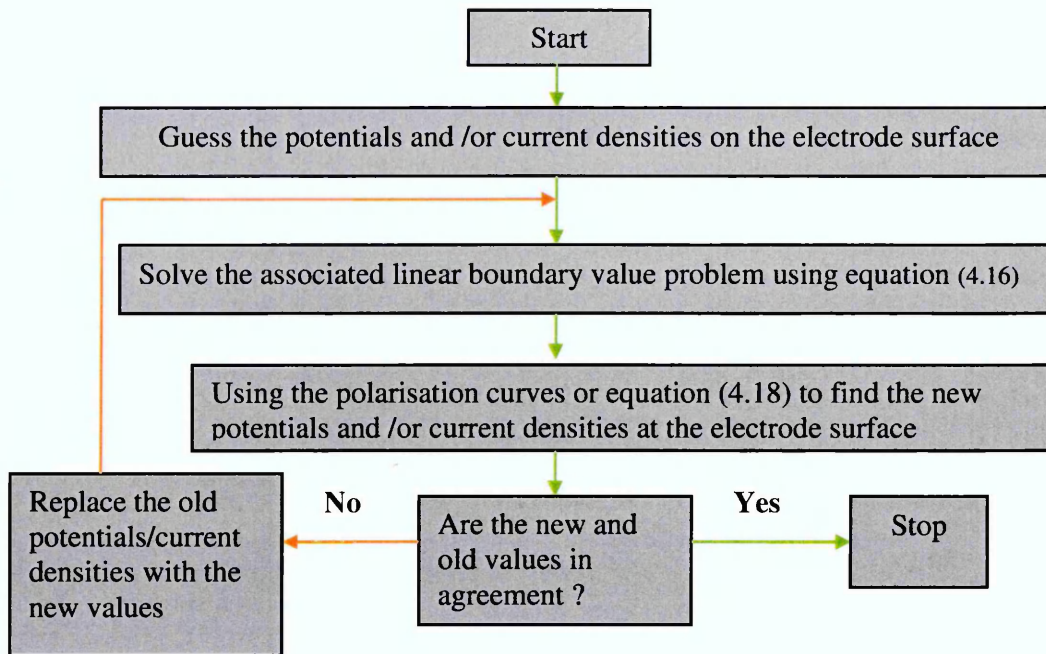


Figure 4.4: Flow chart of the general iteration procedure

4.6 Multi-regional Problems

The work described so far is only the theory and applications of boundary element method in homogeneous materials, as the fundamental solution used assumes that material properties do not change inside domain being analyzed.

There are many instances, however, where this assumption does not hold. For example, in masonry buildings, the resistivities or conductivities of the masonry, mortar, and /or concrete are not exactly the same. Therefore, the region or model under study may be divided into subregions, or zones. Further, this is mainly based on the following reasons:

- There are two or more electrolyte materials in the problem. When there are multiple electrolyte materials to be analyzed in conjunction with

each other, the only way handle this is to split the model into zones. Each zone may have only one set of materials properties, and so can be only represent one electrolyte type.

- The component being modelled is long and thin in parts. Numerical problems can arise in integrating the fundamental solutions accurately over large distances in long thin zones. By splitting the model into two or more zones, the aspect ratio of each zone is reduced, and the boundary element influence matrices can be computed more accurately.

The procedure of analysis in this problem is not very complex. The basic idea is to divide the regions or model under study into a series of subregions or zones and then the boundary element procedure can be applied to each sub-region in turn as if they were independent of each other.

The final set of equations for the whole region (electrolyte) can then be obtained by assembling the set of equations for each subregion using compatibility of potentials and current density between the common interfaces[Brebbia 1978, Brebbia & Dominguez 1989].

Consider a two zone model, for example, shown in Figure 4.5 one called Ω^1 and the other Ω^2 .

$$\begin{bmatrix} H^1 & H_t^1 \end{bmatrix} \begin{Bmatrix} E^1 \\ E_t^1 \end{Bmatrix} = \begin{bmatrix} G^1 & G_t^1 \end{bmatrix} \begin{Bmatrix} i^1 \\ i_t^1 \end{Bmatrix} \quad (4.23)$$

where E^1, i^1 are the nodal potential and normal current density at the external boundary Γ^1 . E_i^1, i_i^1 are the nodal potential and normal current density at the interface Γ_1 considering it belongs to Ω^1 .

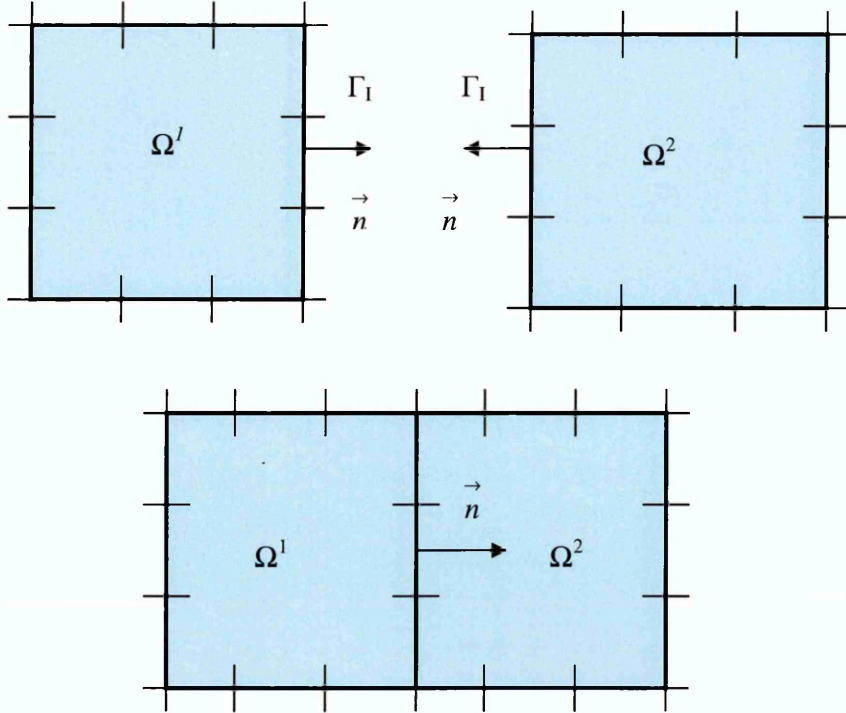


Figure 4.5: A model consisting of two zones

Similarly, the matrix equation for the zone Ω^2 may be written:

$$\begin{bmatrix} H^2 & H_i^2 \end{bmatrix} \begin{Bmatrix} E^2 \\ E_i^2 \end{Bmatrix} = \begin{bmatrix} G^2 & G_i^2 \end{bmatrix} \begin{Bmatrix} i^2 \\ i_i^2 \end{Bmatrix} \quad (4.24)$$

where E^2, i^2 are the nodal potential and normal current density at the external boundary Γ^2 respectively. E_i^2, i_i^2 are the nodal potential and normal current density at the interface Γ_1 considering it belongs to Ω^2 .

The compatibility and equilibrium conditions on the interface Γ_1 can be expressed as:

$$E_1^1 = E_1^2 = E_1 \quad (4.25)$$

and:

$$i_1^1 = -i_1^2 = i_1 \quad (4.26)$$

where E_1, i_1 are potential and normal current density on the interface.

Using the above conditions in equations (4.25) and (4.26), the combined boundary element matrix equation can now be written as:

$$\begin{bmatrix} H^1 & H_1^1 & 0 \\ 0 & H_1^2 & H^2 \end{bmatrix} \begin{Bmatrix} E^1 \\ E_1 \\ E^2 \end{Bmatrix} = \begin{bmatrix} G^1 & G_1^1 & 0 \\ 0 & -G_1^2 & G^2 \end{bmatrix} \begin{Bmatrix} i^1 \\ i_1 \\ i^2 \end{Bmatrix} \quad (4.27)$$

As E_1 and i_1 are unknown at the interface the above system is also written as:

$$\begin{bmatrix} H^1 & H_1^1 & -G_1^1 & 0 \\ 0 & H_1^2 & G_1^2 & H^2 \end{bmatrix} \begin{Bmatrix} E^1 \\ E_1 \\ i_1 \\ E^2 \end{Bmatrix} = \begin{bmatrix} G^1 & 0 \\ 0 & G^2 \end{bmatrix} \begin{Bmatrix} i^1 \\ i^2 \end{Bmatrix} \quad (4.28)$$

This gives a matrix equation which is very similar to the original single zone equation (4.14). By applying the relevant boundary conditions, the equation can be solved.

It is interesting to note that the above method is important for accurately analysing cathodically protected steel-framed structures as the different types

of electrolyte materials, such as brickwork, Portland stone, faience, mortar, and concrete that can be encountered. Furthermore, even for the same type of material the resistivity or conductivity will vary due to its composition or location, for example, brick on the interior and exterior of a wall.

4.7 Implementation of Computer Programs

The previous sections discussed the theory and application of the boundary element method in cathodic protection work. In this section, the boundary element method is employed to produce two computer programs for the modelling of cathodic protection systems as follows:

- two-and three dimensional analysis of cathodic protection in one region
- two-and three dimensional analysis of cathodic protection in multi-regions

These programs have been written in FORTRAN 90/95. The structure, instruction, and source code of the programs are listed in Appendix I.

4.8 Conclusions

This chapter has introduced, discussed and developed the use of the boundary element method in the modelling of cathodic protection systems, more specifically:

The theory and application of boundary element method in analysis of cathodic protection.

Use of the boundary element method to develop two computer programs for two-and three-dimensional modelling of cathodic protection in one region and multi-regions.

The computer programs that have been developed allow the following key activities to be carried out:

- Modelling of the distributions of protective potential and current
- Investigation of the influence of masonry type and joints width, and
- Analysis of stray current corrosion in cathodically protected steel-framed masonry buildings.

These will be discussed fully in Chapters 6, 7 and 8, respectively.

Chapter 5:
Measurement of Steel Polarization Data
in Sand and Mortar

5.1 Introduction

The application of polarization data with respect to the corrosion and protection of metals in particular environments is very widespread. It is useful not only in predicting the amount of galvanic corrosion and current demand for cathodic protection in various electrolytes for the materials involved but also in the development of computer models that can predict the distribution of galvanic corrosion, stray current corrosion and cathodic protection currents.

The polarisation data and curves for commonly used materials in seawater have been well documented [Hack 1995]. Further, the polarization data and curves of steel in soil have also been summarized [Orazem & Carson 1995]. Steel polarization in concrete has also been studied [Page & Treadaway 1982, Cigna et al 1992].

This data has been widely used for the investigation of galvanic corrosion, the modelling of cathodic protection and the analysis of stray current corrosion induced by the interference of conventional impressed current cathodic protection systems.

In the present study, the polarization data for steel in sand and various mortars are investigated and measured as information in this area has so far not been reported in the literature.

The main aim of this aspect of the work is to assist in the modelling of the cathodic protection of steel and the analysis of stray current corrosion in these media using laboratory obtained polarization data.

5.2 Materials and Test Specimens

5.2.1 Materials

The four types of materials selected for use in this study are as follows:

- Low carbon steel
- Dry medium grain sand (ZONE M SAND)
- Ordinary Portland Cement (RUGBY)
- Common lime (calcium hydroxide)

These materials are commercially available.

5.2.2 Test Specimens

5.2.2.1 Specimens for Measuring Polarization Data of Steel in Sand

Based on the resistivity of the sand and the mix proportions of water (by weight), three types of test specimens have been employed. Each test specimen is produced from the same source of sand and contains two steel bars, one of which is used as the working electrode and the other for the counter electrode. The ratio of dry sand and water for each test specimen are detailed below:

- Specimen A: dry medium grain sand with 5 % water (by weight)
- Specimen B: dry medium grain sand with 10 % water (by weight)
- Specimen C: dry medium grain sand with 15 % water (by weight)

The sand and water were mixed until apparently homogeneous. The mixed sand for each specimen was then placed and tamped in several layers into a rectangular electrically insulating plastic box, 100mm width X 100mm length X 100mm height. The thickness of each layer was about 20mm. Each specimen

contained two steel bars 6mm diameter and a copper/copper sulphate reference electrode, all located in parallel longitudinally with the centre of the plastics box. The centre-to-centre distance between the electrodes was 25mm. A schematic diagram of the test specimen is shown in Figure 5.1. Once produced, the specimens were maintained at a constant 20°C and 60% relative humidity in a controlled environment room.

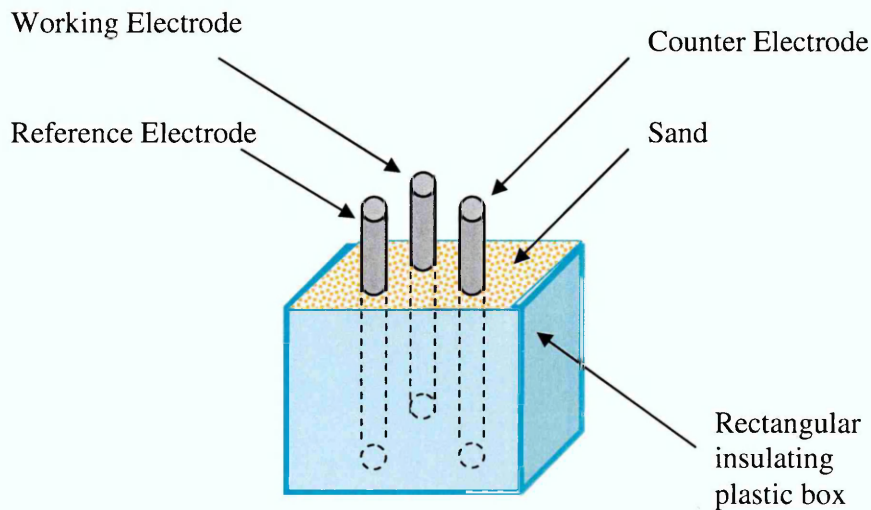


Figure 5.1 Test specimen for measuring polarization data of steel in sand

5.2.2.2 Specimens for Measuring Polarization Data of Steel in Mortar

A further three test specimens were used to repeat the polarization studies for three mortars of varying mix proportions. Each mortar test specimen again contained two steel bars of which one was the working electrode and the other the counter electrode. The proportions of the mortar mixes used for the test specimen were as follows:

- Mortar Specimen D: Mix proportions (by weight) of 1: 3 (cement: sand) with a water-cement ratio of 0.5

- Mortar Specimen E: Mix proportions (by weight) of 1 : 5 (cement: sand) with a water-cement ratio of 0.5
- Mortar Specimen F: Mix proportions (by weight) of 1 : 2 : 9 (cement: lime: sand) with a water-cement ratio of 0.5

The mixed materials for each specimen were then cast into standard rectangular steel cube moulds, 100mm width X 100mm length X 100mm height, in several layers and vibrated to achieve the optimum compaction.

Each specimen contained two steel bars 6mm in diameter and an embeddable reference electrode located in parallel longitudinally with the centre of the steel mould. The centre-to-centre distance between the electrodes was 25mm. A schematic diagram of the mortar test specimen is shown in Figure 5.2.

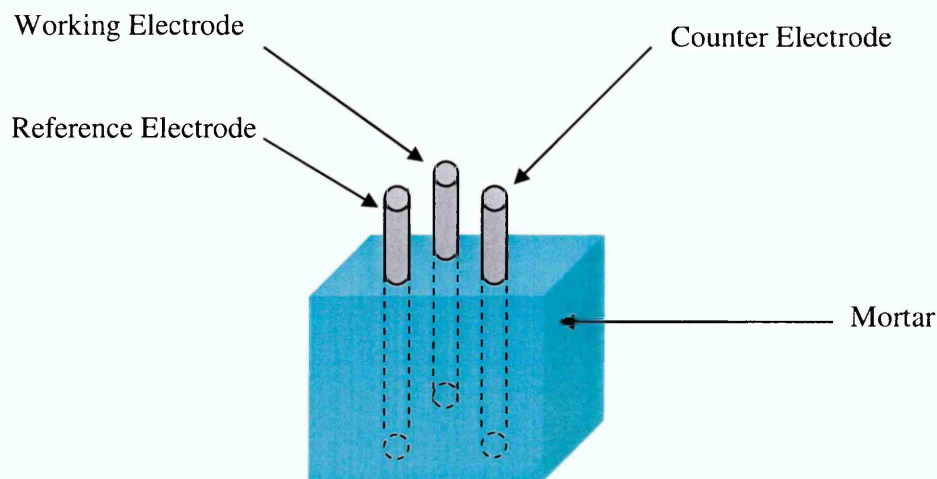


Figure 5.2 Test specimen for measuring polarization data of steel in mortar

After casting the specimens were stored in a mist curing room overnight. The specimens were demoulded after 24 hours, and cured in a water tank for six days at a constant 20⁰C.

5.3 Test Method and Procedure

5.3.1 Resistivity

The characteristics of polarization curves are dependent upon many factors, such as metal alloy type, ionic species in the electrolyte, exposure environment, etc. The resistivity of the mortar or masonry can therefore become one of the most important factors in determining the nature of the polarization response and ideally should be determined prior to obtaining polarization curves for any combination of metal and electrolyte.

In practice, the four-probe resistivity meter (Wenner) and simpler two probe systems have been widely used for measuring the resistivity of soil and concrete and operate on a similar principal [Broomfield 1997]. The resistivity of a material, ρ , can be obtained from the following equation:

$$\rho = \frac{SV}{aI} \quad (5.1)$$

where S is the surface area of the electrode, a is the electrode spacing, I is the applied current across the two electrodes, and V is the measured potential difference between two electrodes. The method of measurement using a two probe system is illustrated schematically in Figure 5.3.

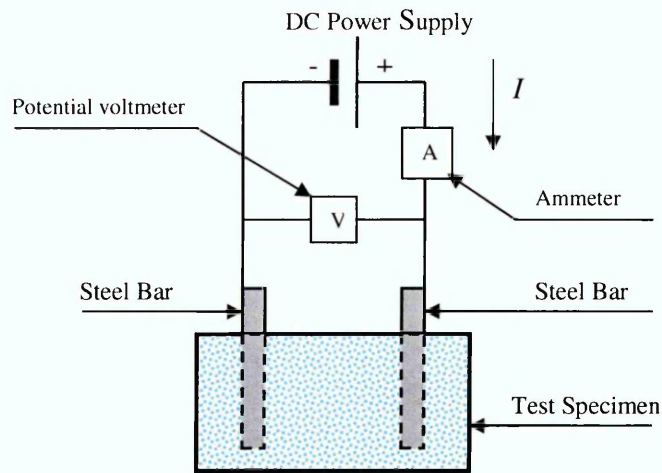


Figure 5.3: Schematic illustration two probe resistivity measurement

After measuring the potential difference V , for a specific applied current I , the resistivity of the specimen is then calculated by using equation (5.1). For the specimens to be used for obtaining polarization data of steel in sand, the resistivities determined by the method shown above are listed in Table 5.1.

Table 5.1: Resistivity of Sand

Test Specimens	Resistivity, ρ
A (dry sand with 5% water)	42.32 K .cm
B (dry sand with 10% water)	14.61 K .cm
C (dry sand with 15% water)	6.41 K .cm

For those specimens used for obtaining polarization data for steel in various mortars, the resistivities are listed in Table 5.2.

Using the results from Table 5.2, the relationship between the resistivity of specimen D, E and F and exposure time can be seen in Figure 5.4 and is discussed in Section 5.5.1.

Table 5.2: Resistivity of Mortar (Specimens D, E and F)

Exposure Times (hours)	Resistivity, ρ (K Ω .cm)		
	Specimen D	Specimen E	Specimen F
0.00	1.67	1.72	0.55
24.00	2.39	3.51	0.69
48.00	2.73	6.81	1.17
72.00	2.95	11.30	1.94
96.00	3.30	53.39	3.06
120.00	3.42	124.85	4.39
144.00	3.56		5.57
168.00	3.69		6.99
192.00	3.93		9.01
216.00	4.10		10.50
240.00	4.33		12.22
264.00	4.37		14.27
288.00	4.53		15.07
312.00	4.57		15.45
336.00	4.65		16.39
360.00	4.76		18.14
384.00	4.87		19.47
408.00	5.41		20.23
432.00	5.79		21.99
456.00	5.67		24.92
480.00	5.49		17.31
504.00	5.10		17.80

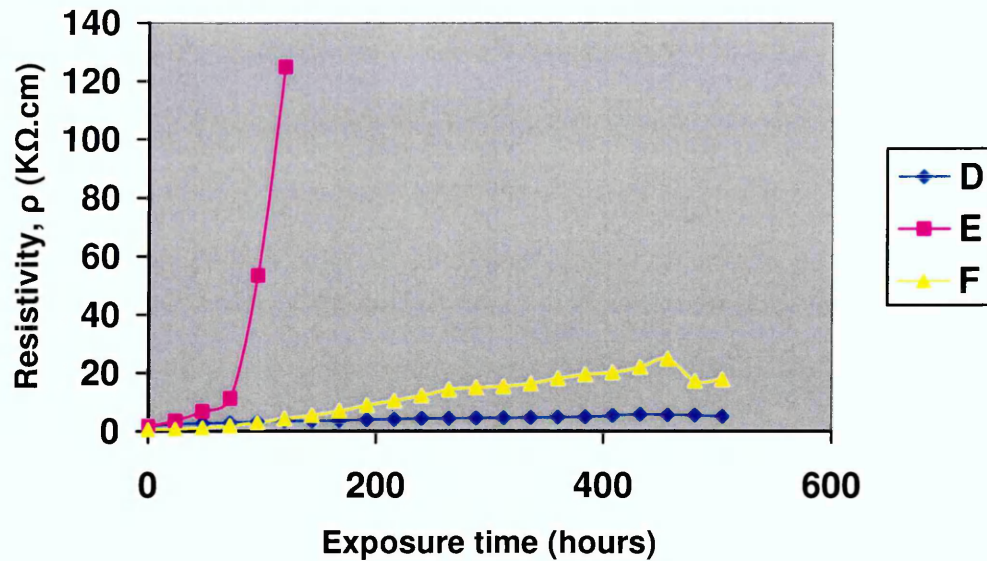


Figure 5.4: Relationship between resistivity and exposure time

5.3.2 Apparatus and Procedure of Measurements

For each specimen, the polarization test is undertaken immediately following the determination of resistivity as described above. The experimental conditions during the measurements were 20°C and 60% relative humidity. The test set-up and individual components are illustrated in Figures 5.5 and 5.6.

A ramp controlled 'Ministat' potentiostat manufactured by Thompson Electrochem Ltd. was used to determine the polarization curves (see Figure 5.6). It accurately monitors the current flowing between the working electrode and the counter or auxiliary electrode and the potential between the reference electrode and the working electrode.

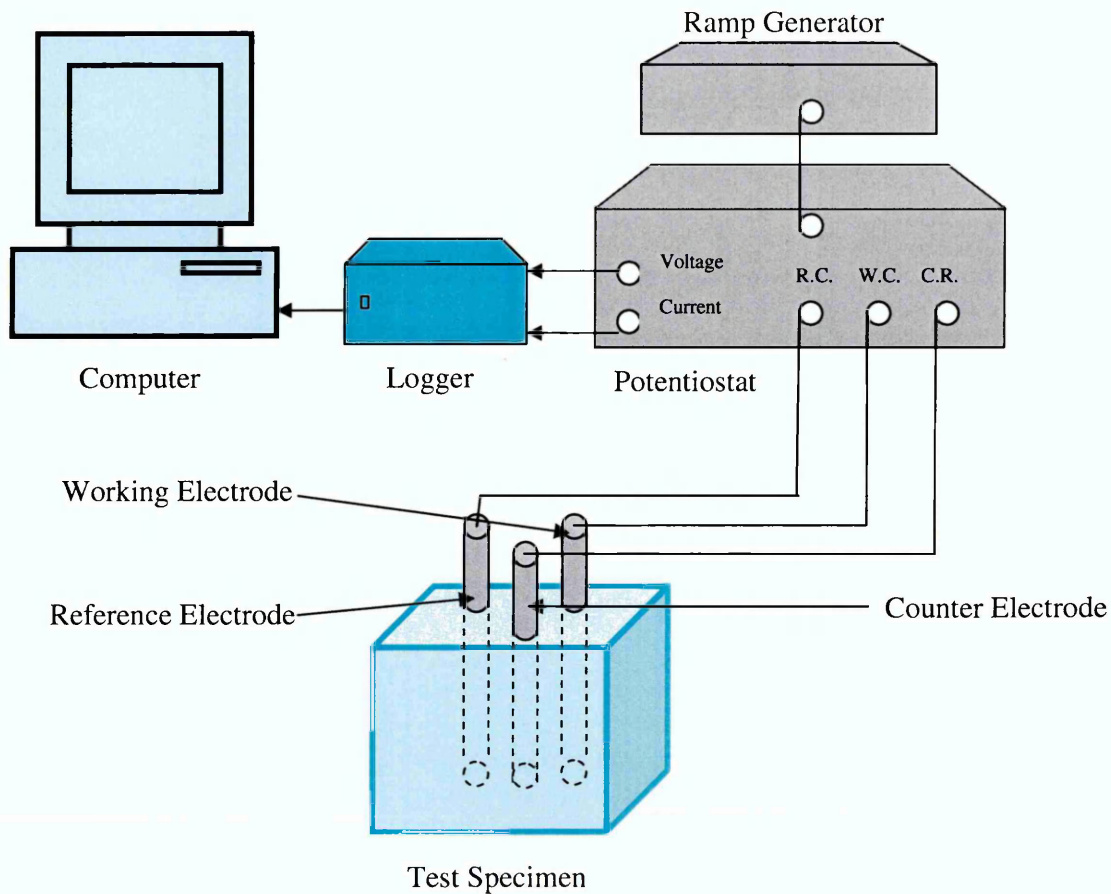


Figure 5.5: Schematic illustration of test facility

The sweep, controlled by the ramp generator, is from the rest or free potential to -1500mV more negative than the rest potential, as it is only this cathodic part of the scan that is required. The values of impressed potential and resultant current are logged on a Grant 'Squirrel' meter/logger.

Prior to commencing the sweep, the cell is held at $\pm 0\text{mV}$ with respect to the rest potential. A sweep rate of 10mV/Sec is used for the test. It is controlled by a 'Precision' 16 bit Ramp Generator (BRG16) manufactured by Thompson Electrochem Ltd (see Figure 5.6).

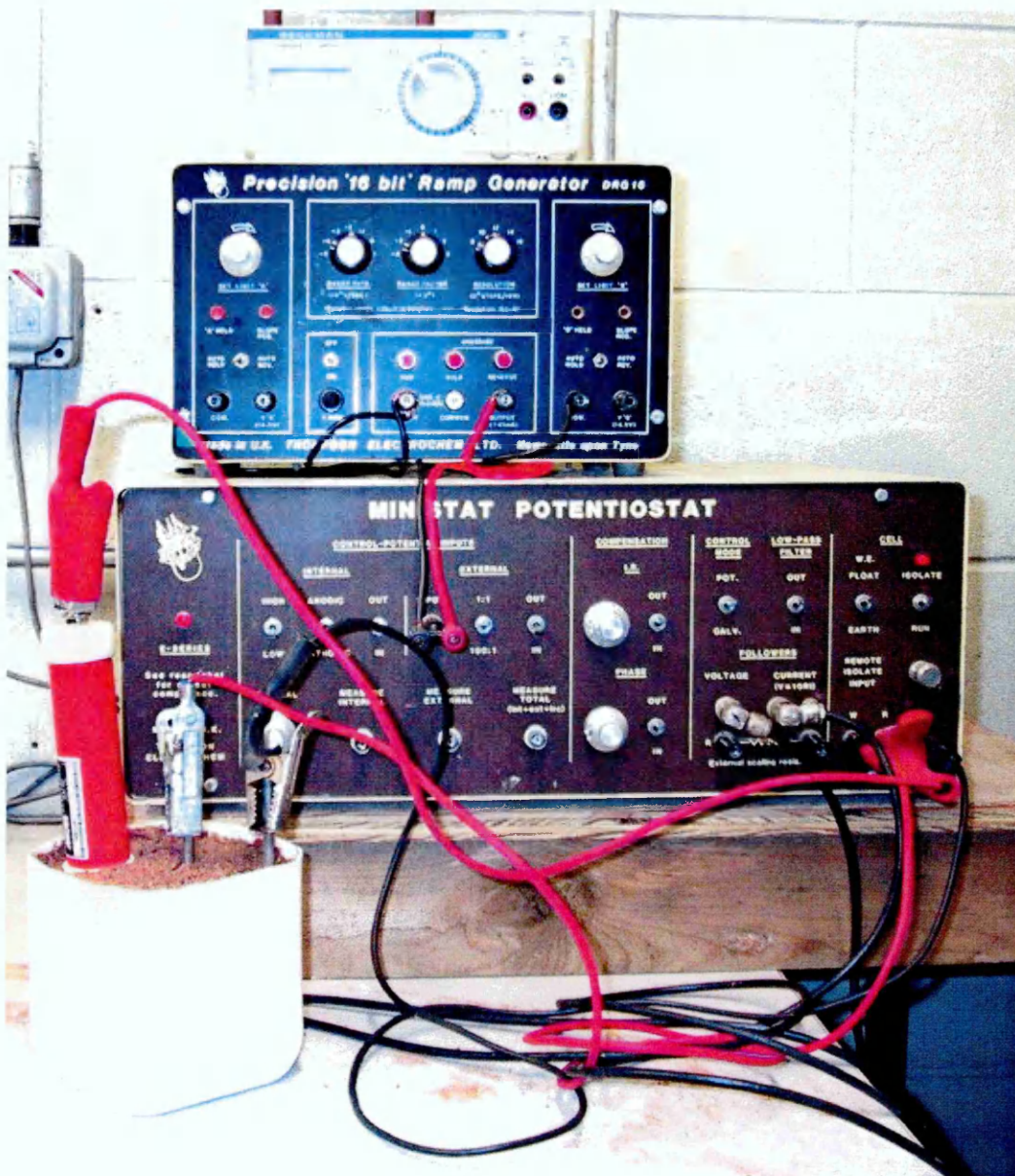


Figure 5.6: Test apparatus - potentiostat and ramp generator

Using this sweep rate, the computer automatically completes a sweep from the rest potential to -1500mV more negative than the rest potential. At the end of each sweep, the data is downloaded from the meter/logger to a computer for further analysis and plotting.

5.4 Results

5.4.1 The Polarization Data of Steel in Sand

Polarization data for steel was measured with the three different sand resistivities relating to three moisture contents. The data from generated by the polarization experiment are potential and current, however, the current density is more commonly used to express the reaction rate in electrochemistry. This is obtained by calculating the current per unit area of exposed working electrode. The results are then used to plot the polarisation curves.

The polarisation curves of steel in sand at three resistivities are shown in Figure 5.7.

5.4.2 Polarization Data for Steel in Mortar

As the resistivity of each mortar test specimen as been shown to have an element of time-dependency, a series of polarization curves for steel in each specimen different resistivities was measured. The results from these tests are again used to plot the polarisation curves.

For specimen D, the polarization curves of steel at the different resistivities are shown in Figures 5.8 to 5.13 respectively. For specimen E, the polarization curves are shown in Figure 5.14. Figure 5.15 to 5.19 show the polarization curves of steel in Specimen F.

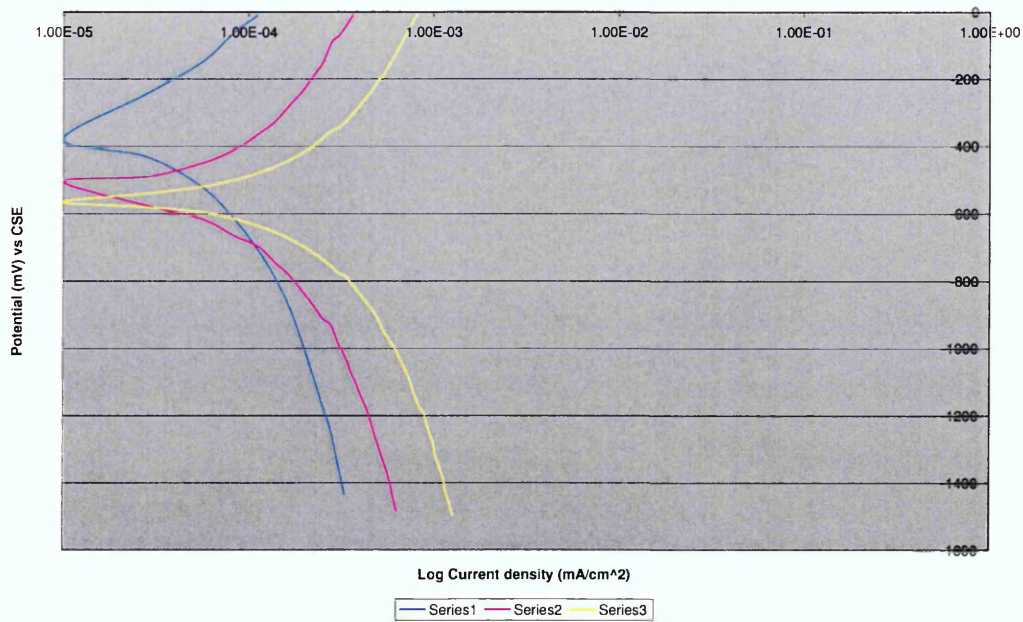


Figure 5.7: Polarization curves of steel in sand

(Series 1: Resistivity=42.32 K .cm; Series 2: Resistivity=14.61 K .cm;
Series 3: Resistivity=6.41 K .cm)

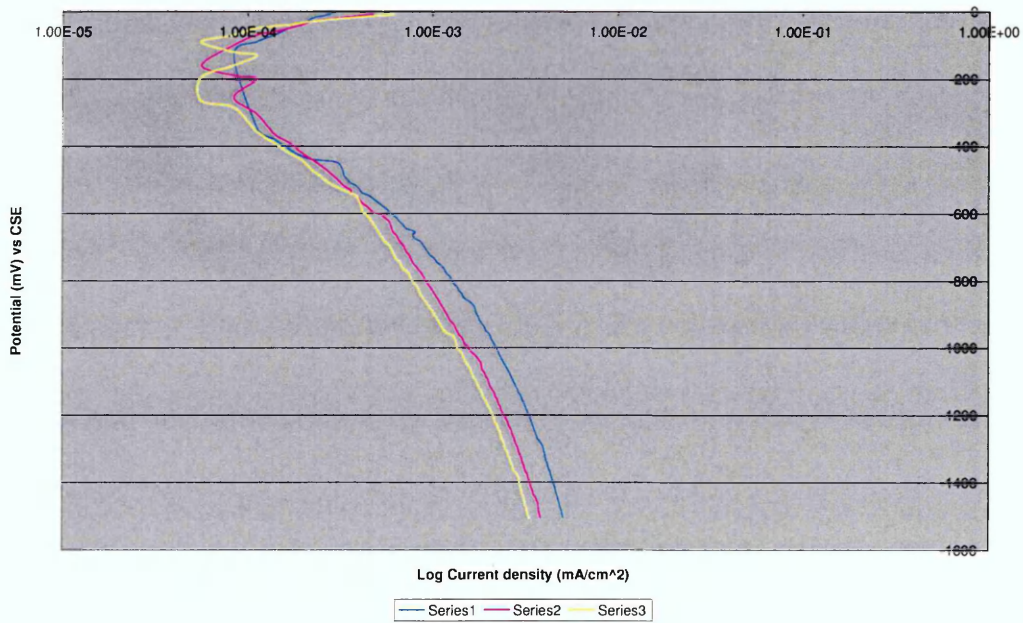


Figure 5.8: Polarization curves of steel in mortar (Specimen D)

(Series 1: Resistivity=1.67K .cm; Series 2: Resistivity=2.39 K .cm;
Series 3: Resistivity=2.73 K .cm)

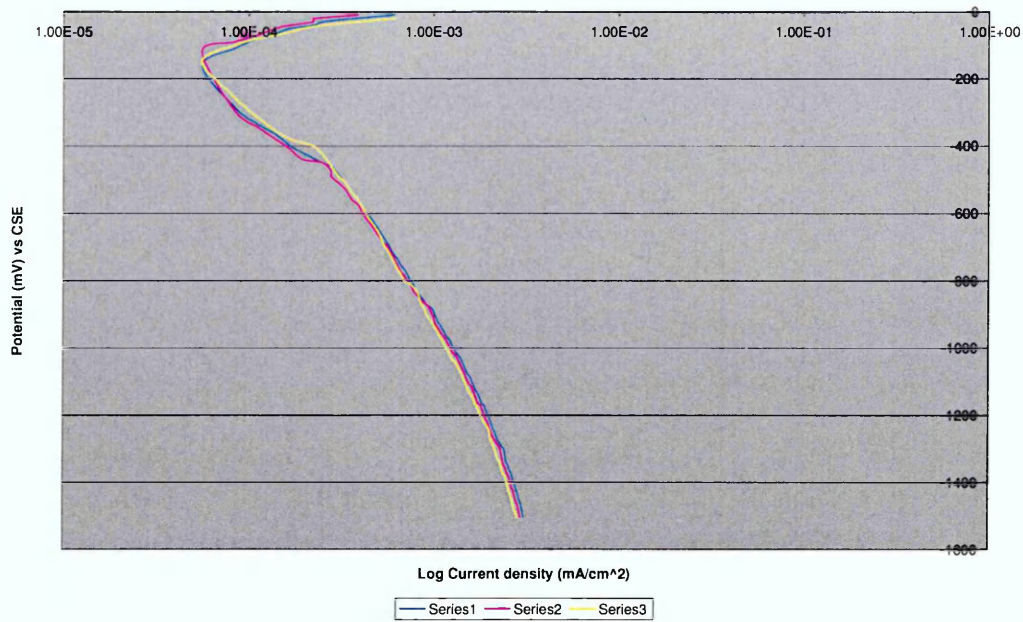


Figure 5.9: Polarization curves of steel in mortar (Specimen D)

(Series 1: resistivity=2.95K Ω .cm; Series 2: resistivity=3.30 K Ω .cm;
Series 3: resistivity=3.42 K Ω .cm)

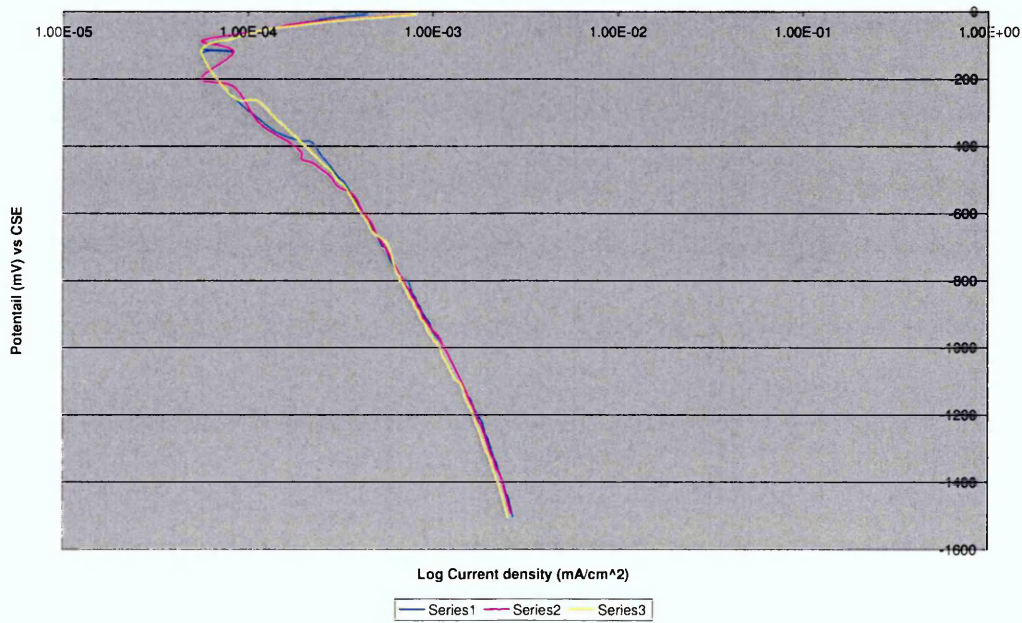


Figure 5.10: Polarization curves of steel in mortar (Specimen D)

(Series 1: Resistivity=3.56K Ω .cm; Series 2: Resistivity=3.69 K Ω .cm;
Series 3: Resistivity=3.93 K Ω .cm)

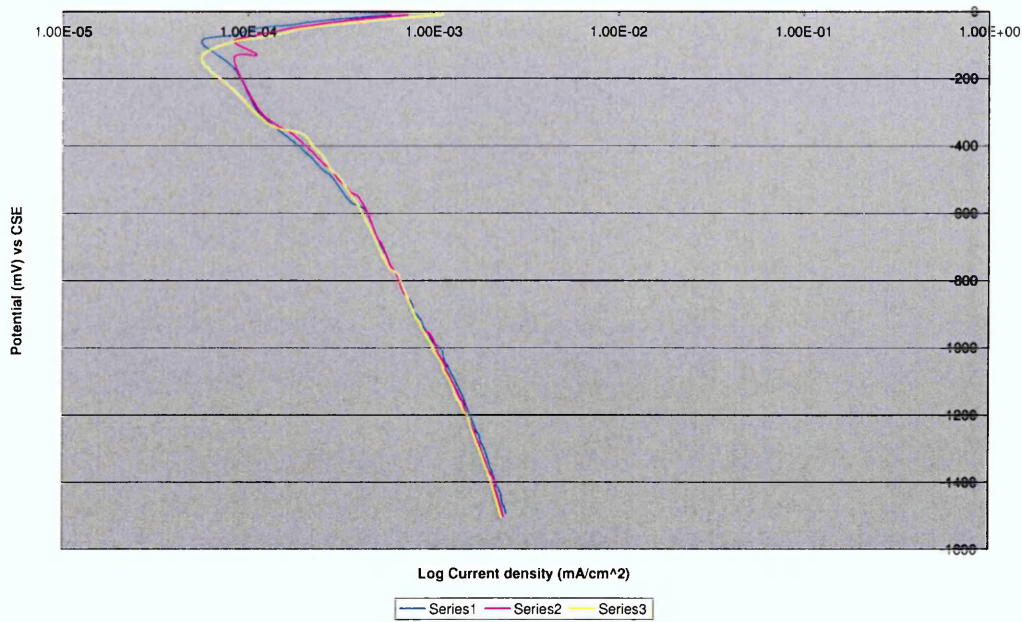


Figure 5.11: Polarization curves of steel in mortar (Specimen D)
 (Series 1: Resistivity=4.10K .cm; Series 2: Resistivity=4.33 K .cm;
 Series 3: Resistivity=4.37 K .cm)

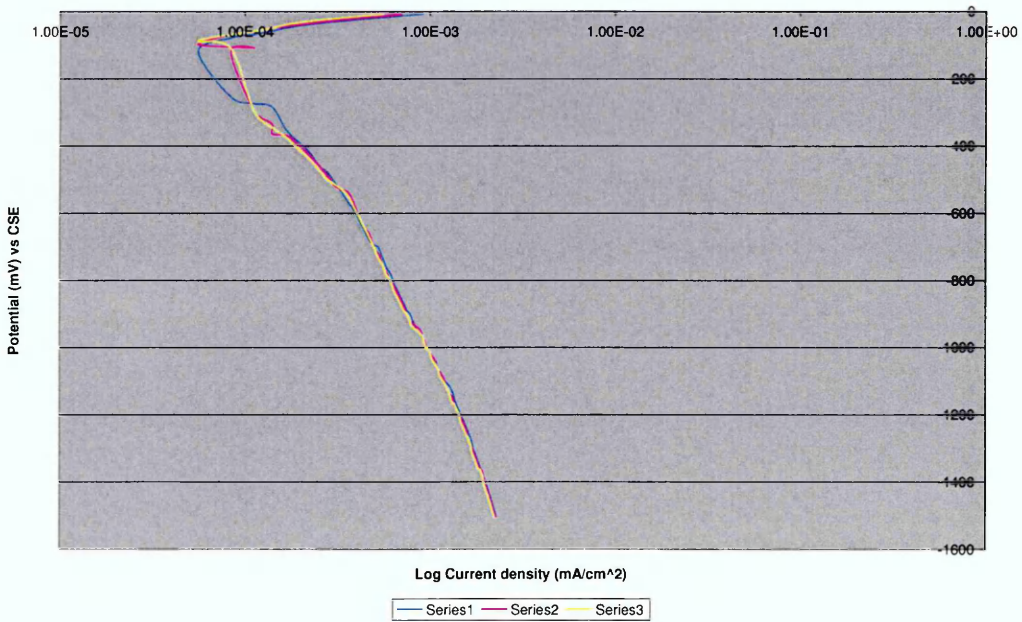


Figure 5.12: Polarization curves of steel in mortar (Specimen D)
 (Series 1: Resistivity=4.53K .cm; Series 2: Resistivity=4.57 K .cm;
 Series 3: Resistivity=4.65 K .cm)

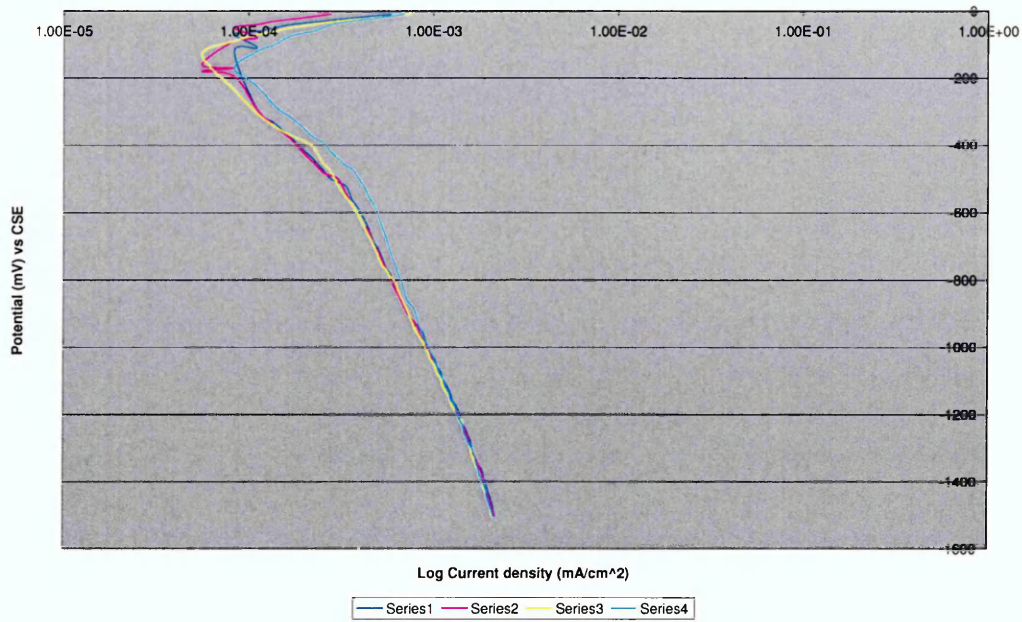


Figure 5.13: Polarization curves of steel in mortar (Specimen D)

(Series 1: Resistivity=4.76K .cm; Series 2: Resistivity=4.87 K .cm;
Series 3: Resistivity=4.41 K .cm; Series 4: Resistivity=5.79 K .cm)

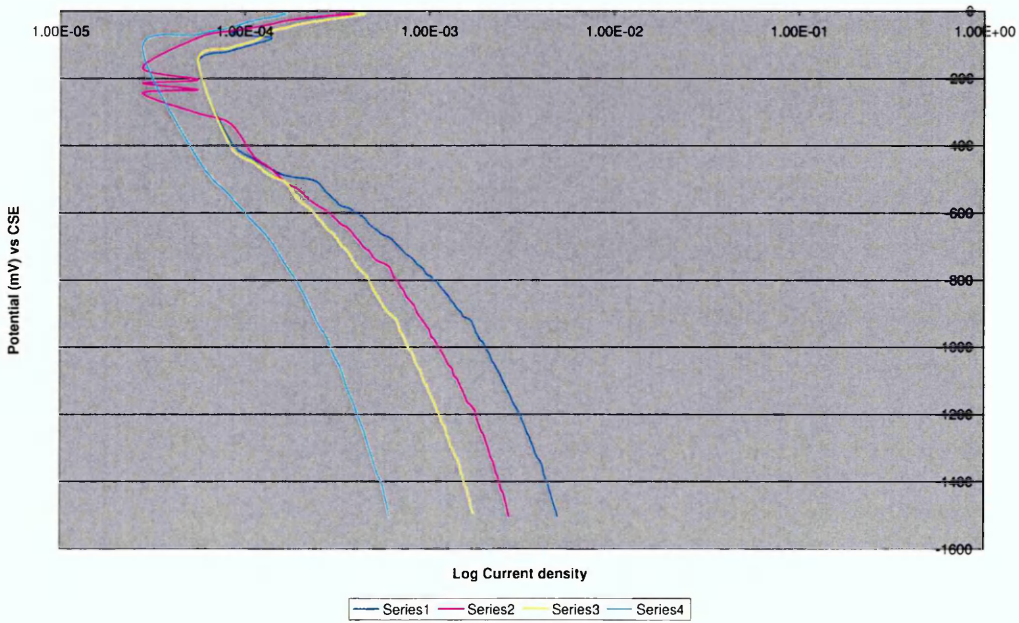


Figure 5.14: Polarization curves of steel in mortar (Specimen E)

(Series 1: Resistivity=1.72K .cm; Series 2: Resistivity=3.51 K .cm;
Series 3: Resistivity=6.81 K .cm; Series 4: Resistivity=124.85 K .cm)

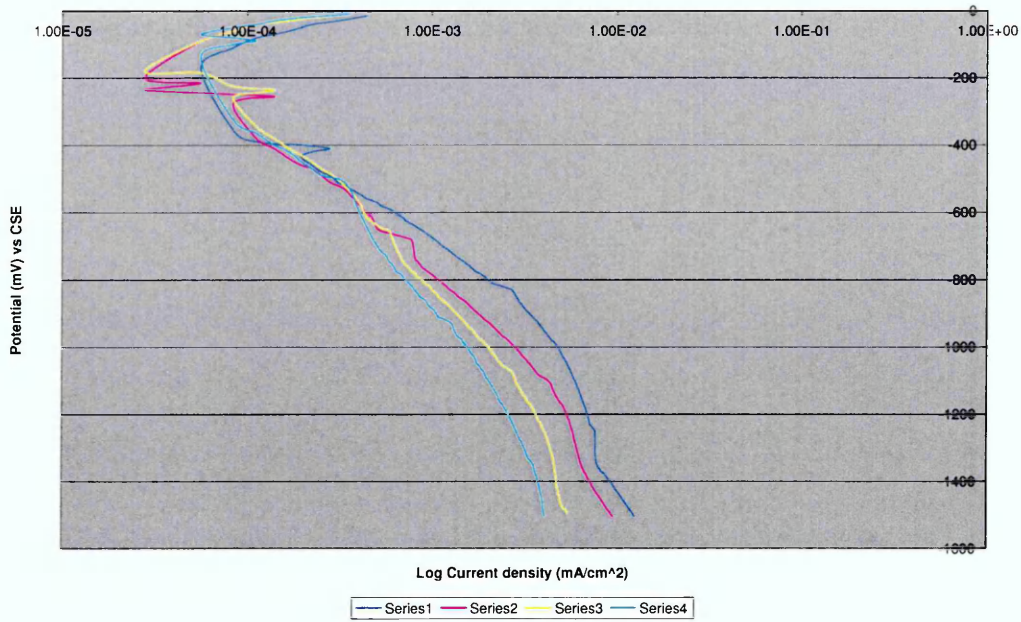


Figure 5.15: Polarization curves of steel in mortar (Specimen F)

(Series 1: Resistivity=0.55K .cm; Series 2: Resistivity=0.69 K .cm;
 Series 3: Resistivity=1.17 K .cm; Series 4: Resistivity=1.94 K .cm)

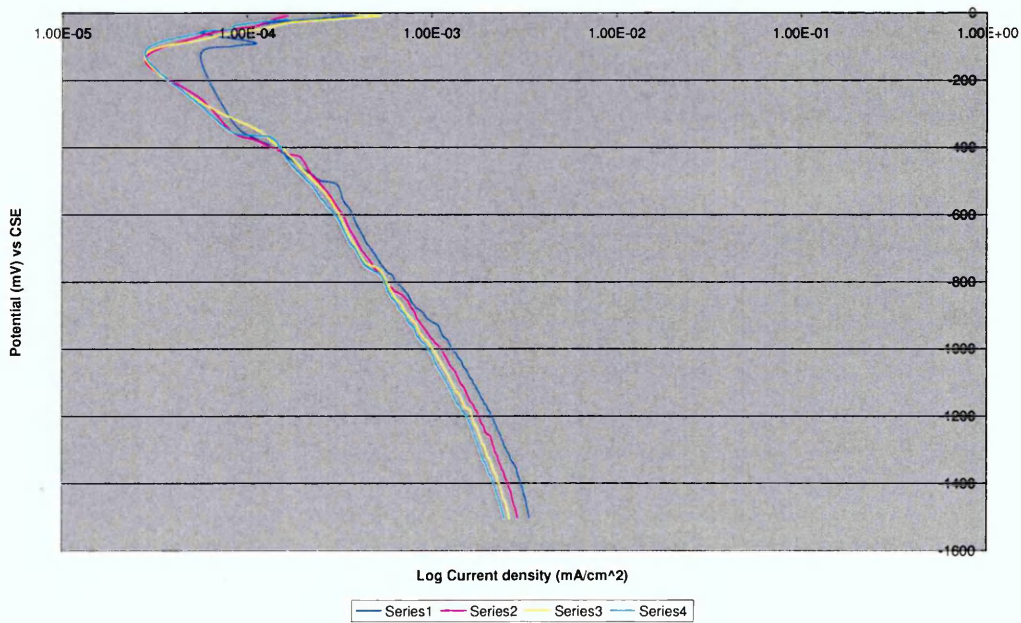


Figure 5.16: Polarization curves of steel in mortar (Specimen F)

(Series 1: Resistivity=3.06K .cm; Series 2: Resistivity=4.39 K .cm;
 Series 3: Resistivity=5.57 K .cm; Series 4: Resistivity=6.99 K .cm)

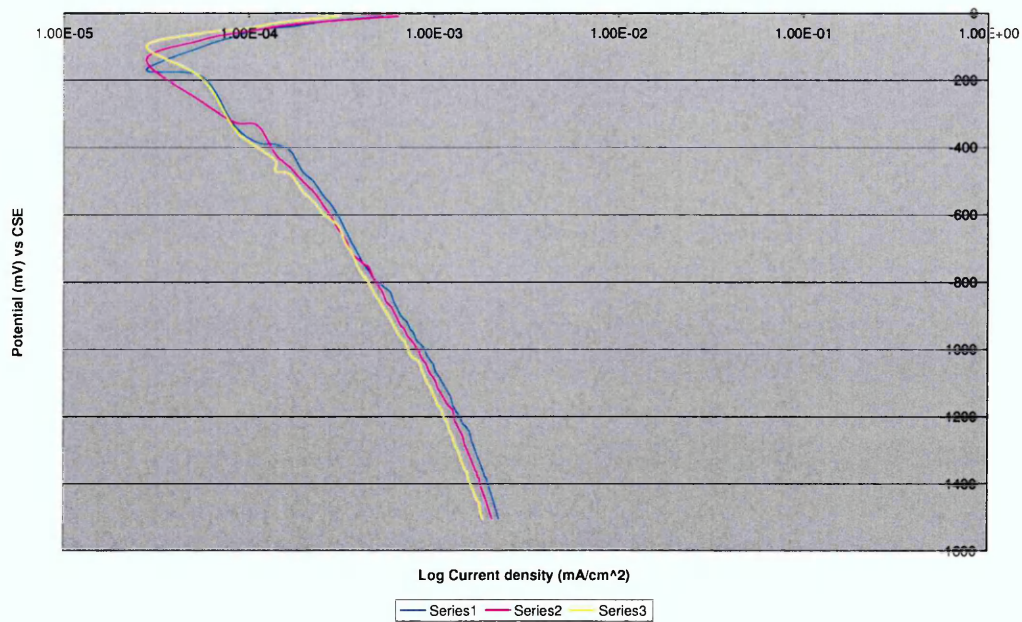


Figure 5.17: Polarization curves of steel in mortar (Specimen F)

(Series 1: Resistivity=9.01K .cm; Series 2: Resistivity=10.50 K .cm;
Series 3: Resistivity=12.22 K .cm)

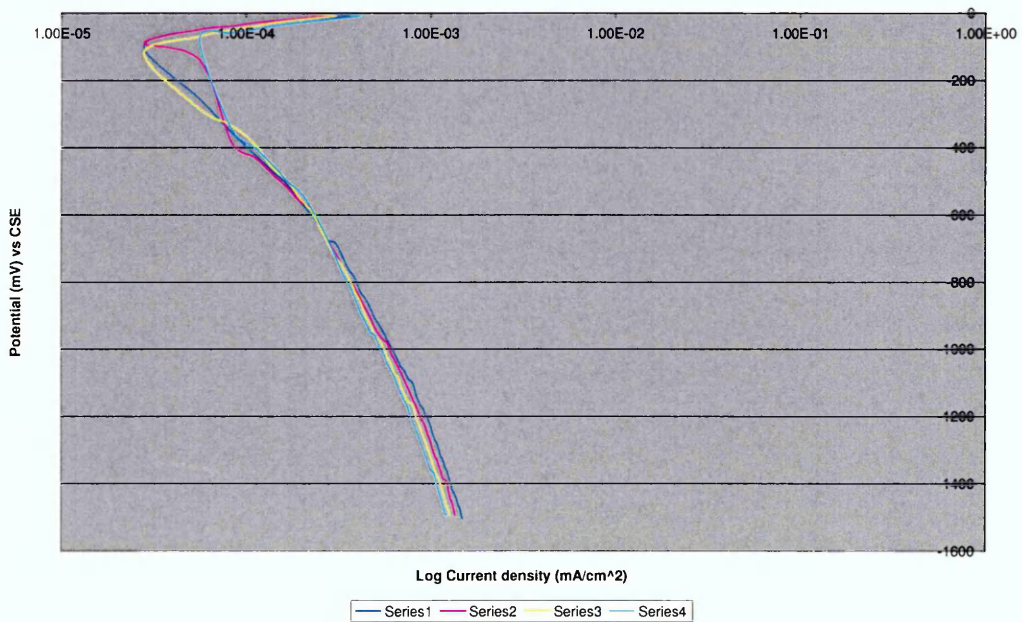


Figure 5.18: Polarization curves of steel in mortar (Specimen F)

(Series 1: Resistivity=15.07K .cm; Series 2: Resistivity=15.45 K .cm;
Series 3: Resistivity=16.39 K .cm; Series 4: Resistivity=18.14 K .cm)

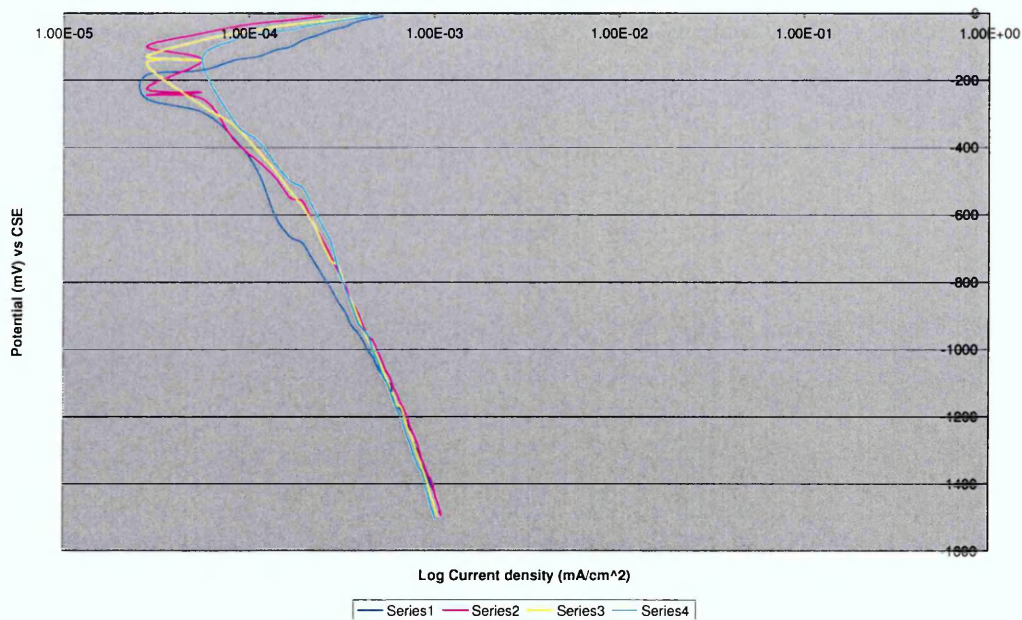


Figure 5.19: Polarization curves of steel in mortar (Specimen F)

(Series 1: Resistivity=19.47K .cm; Series 2: Resistivity=20.23 K .cm;
 Series 3: Resistivity=21.99 K .cm; Series 4: Resistivity=24.92 K .cm)

5.5.1 Discussion and Conclusion

In this part of the study the resistivities of sand with three different ratios of water and mortars based on three different mixes giving a range of resistivities have been investigated. In addition, the polarization curves of steel in these specimens were measured.

Table 5.1 shows that the resistivity of sand, which in this case is used as analogous to masonry, is not directly proportion to the ratio of dry sand and water. For example, dry medium grain sand with 5 % water (by weight), had a resistivity of 42.32 K .cm while dry medium grain sand with 10 % water (by weight) was 14.61 K .cm.

Figure 5.4 shows that the resistivities of the mortars examined in this work are apparently time-dependent under constant environmental condition. It has also been shown that the resistivity change of each composition of mortar varies with time.

Initially the resistivity of each mortar gradually increases. However, the resistivity of Specimen E, which has mix proportions (by weight) of 1: 3 (cement: sand) and a water-cement ratio of 0.5, quickly increases after 72 hours while the resistivities of Specimens D and F, which have mix proportions (by weight) of 1: 5 (cement: sand) with a water-cement ratio of 0.5 and mix proportions (by weight) of 1: 2 : 9 (cement: lime: sand) with a water-cement ratio of 0.5 respectively gradually increase (see Figure 5.4).

Eventually all the samples stabilise, suggesting that the change in resistivity could be due to the movement of charged ions between the two electrodes which eventually reach a steady flux under the applied field. On a practical basis, it would indicate the need to allow the resistivity to stabilise prior to taking a reading as this may better represent the condition of the media under a prolonged applied field, such as would be the case with cathodic protection.

From Figure 5.13 to Figure 5.19, it can be seen that the higher the resistivity of the sand and mortar, the more positive the corrosion potential of steel which could be consistent with the higher resistivity impeding corrosion processes within the damp sand.

The polarization results obtained in this part of the work play a very important role in the development of a viable model for determining the behaviour of

steel in masonry subject to cathodic protection. The boundary conditions or electrode kinetics on the surface of the anode and cathode (the polarization data), express the non-linear relationship between the potential E and current density i on the anode surface or cathode surface.

These values are subsequently employed for modelling the cathodic protection systems of steel-frame masonry structures, investigating the effects of masonry types and joints width on the distribution of the protective potential and current, and analysing the stray current corrosion resulted from cathodic protection interference in such structures.

These aspects of the work are described in Chapters 6, 7 and 8,

Chapter 6:
Distribution of Current/Potential of
Impressed Current Cathodic Protection Systems

6.1 Introduction

The various theories, prior knowledge and experimental results detailed in the preceding chapters are now employed to analyse and model the distribution of protective potential and current of two representative impressed current cathodic protection systems with variations in anode location and resistivity of the electrolyte. The work presented in this chapter consists of both experimental measurements and boundary element modelling. Finally, a discussion and conclusions are included.

6.2 Experimental Procedure

6.2.1 Test Design of Impressed Current Cathodic Protection Systems

The principle of impressed current cathodic protection systems has been described in Chapter 2 (See Figure 2.9). In its normal form, such a system may consist of the following basic components:

- DC power supply (distributed rectifier system).
- Inert anode, such as catalyzed titanium ribbon meshes or titanium\titania rods.
- Electrical continuity bonding of steel components (cathode)
- Electrolyte.
- DC wiring between the anode, steel (cathode) and rectifier.
- Monitoring probes, generally embedded reference electrodes.
- Remote monitoring and control system.

Based on the above, two ICCP systems for steel-framed masonry structures have been constructed for analyzing the distribution of the protective potential and current. The main components of DC power supply, inert anode and electrolyte, are described as follows:

- DC power supply: a CPI manual power supply system, provided by Cathodic Protection International Aps.
- Discrete anodes: The anode is one of the most critical components for a cathodic protection. As discussed in Section 3.2, the discrete anodes

employed ('Ebonex' titanium oxide anodes) have been provided by Fosroc.

- Steel sections (cathode): Two differently dimensioned 'I' section steel specimens, designated steel sections A and B respectively, are employed as the cathodes. Their dimensions are given in Figures 6.1 and 6.2.
- Sand (electrolyte): Two sandboxes, 1000mm in length, 1000mm in width and 250mm in height, have been used to represent the surrounding masonry (see Figure 6.3). On completion of the sandbox work, further testing was carried out with mortar and brick encasement as described in Chapter 7.

Dependent upon the type of steel section, two impressed current cathodic protection systems (ICCP) have been constructed. For ICCP System A, where the cathode is steel section A representing a stanchion, the test facility and its components are shown in Figures 6.4 and 6.5.

ICCP system B, for which steel section B was used as the cathode, was similar in set-up to ICCP A. However, steel section B is totally buried in sand representing a beam and two anodes are installed in ICCP System B. Figure 6.6 shows the arrangement of steel section B and the anodes. The completed sandbox is shown in Figure 6.7.

Following installation of all the components of ICCP, each system was connected to the power and monitoring equipment and powered up. In general there are two methods of controlling ICCP systems. One is that the output voltage is kept constant and the current is allowed to alter in order to maintain the set potential.

The alternative method is to fix the current and allow the potential to float. In this work, the more commonly employed former system of fixed potential was employed. Once the output current become stable, the distribution of protective potential could be measured. The details are discussed in Section 6.2.2.

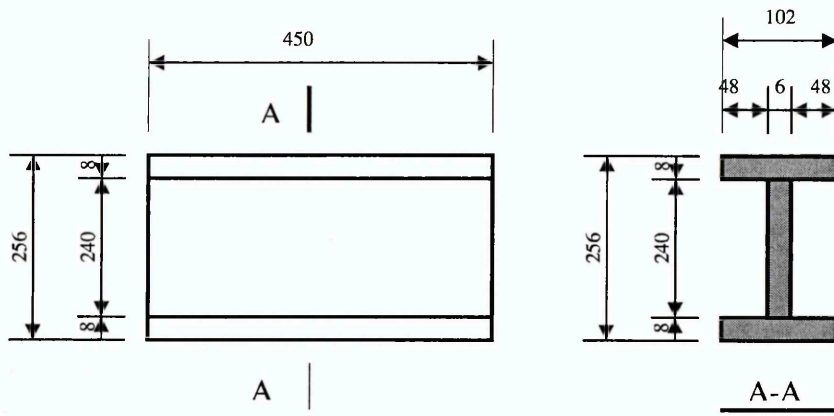


Figure 6.1: Steel Section A (unit: mm)

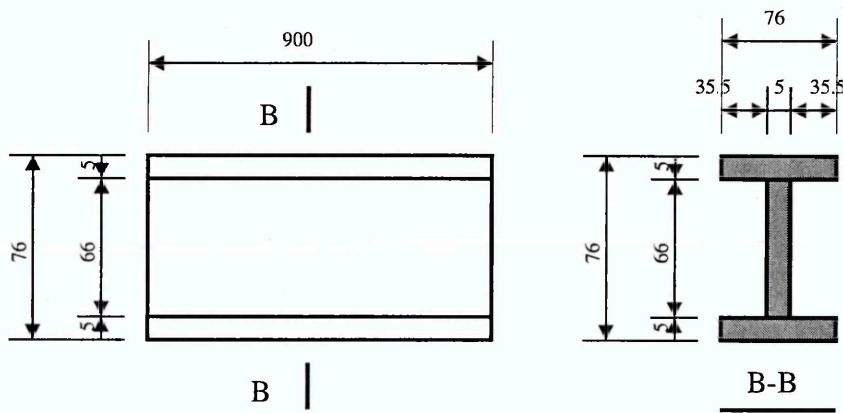


Figure 6.2: Steel Section B (unit: mm)

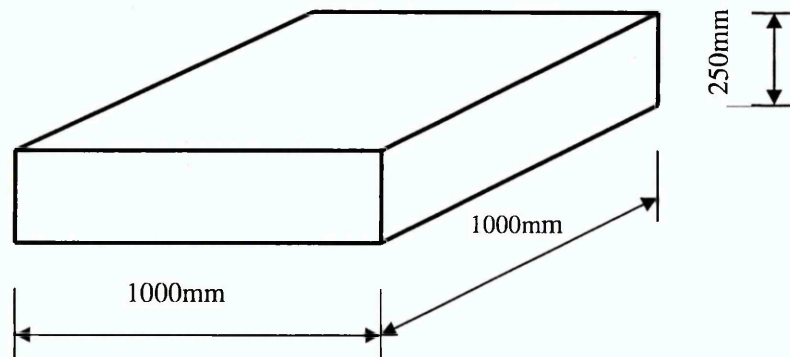


Figure 6.3: Dimensions of the large sandbox

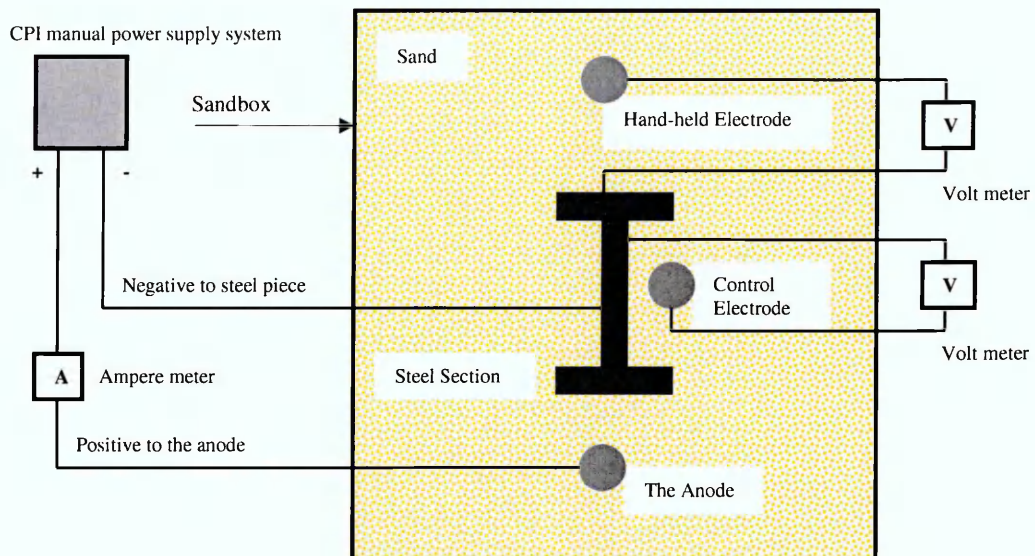


Figure 6.4: Schematic illustration of test facility (ICCP System A)

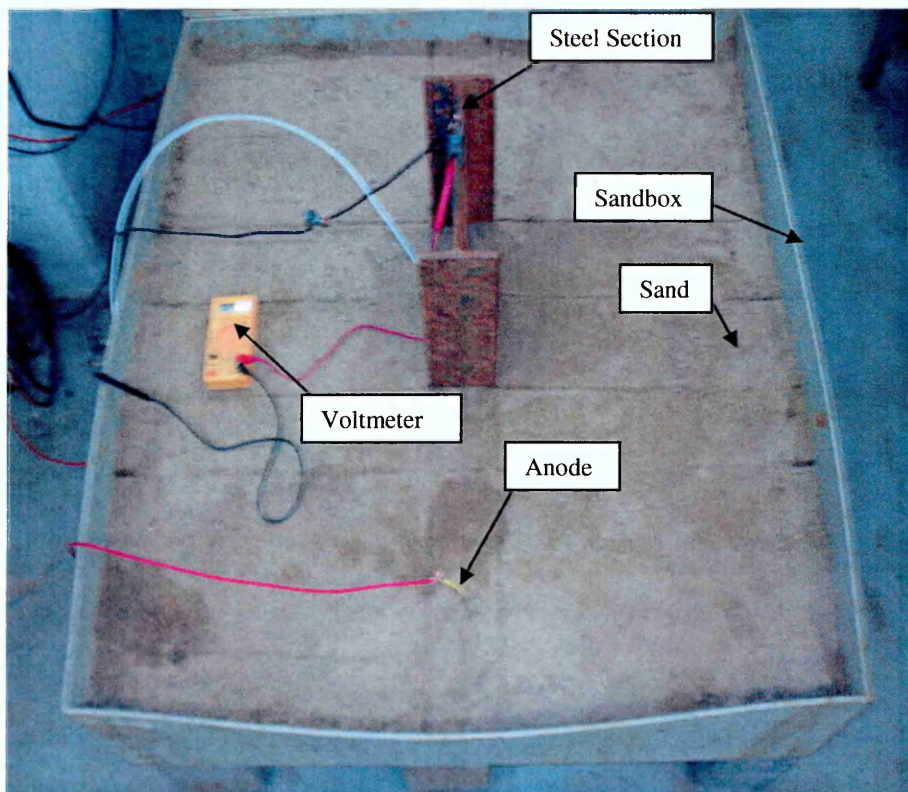


Figure 6.5: Components of ICCP System A

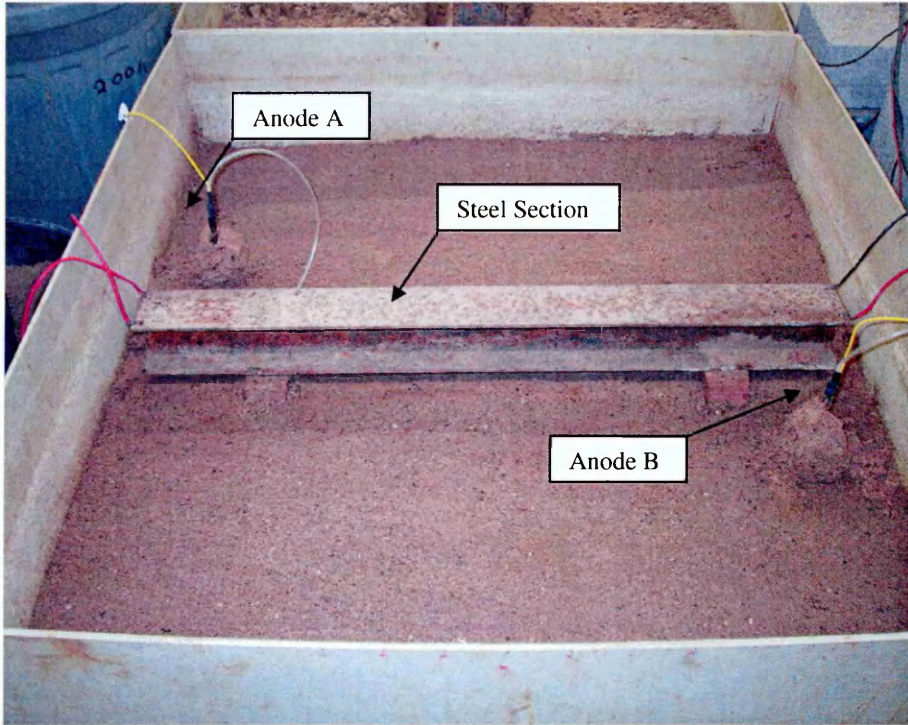


Figure 6.6: Buried steel section B and the Anodes A and B

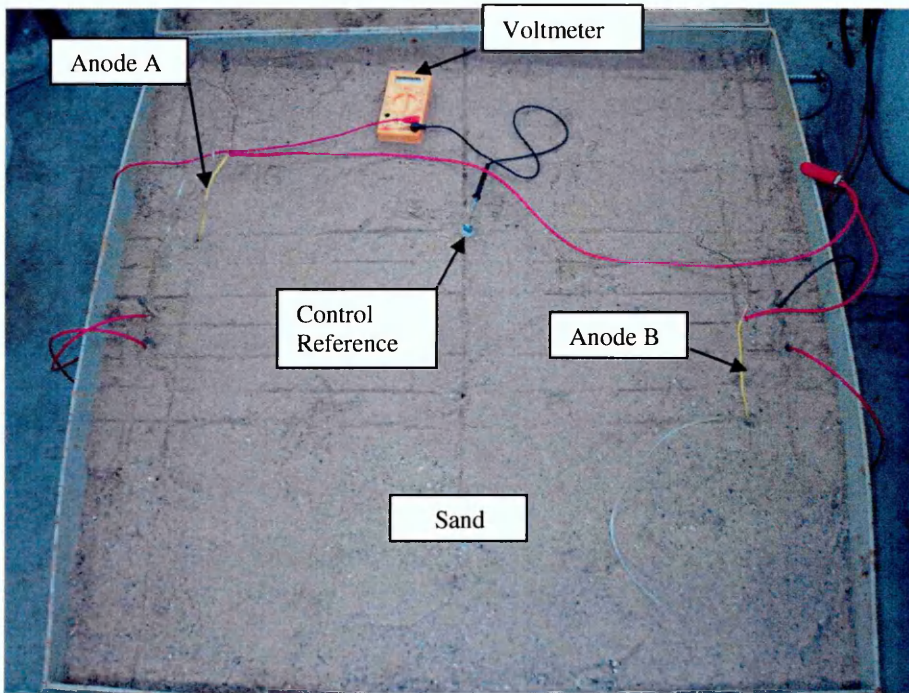


Figure 6.7: Components of ICCP System B

6.2.2 Measurement of Protective Potential

The potential distribution on a grid of sandbox free surface was measured under a range of test conditions, including the various anode coordinates, sand resistivities and output currents, by moving a hand-held copper/copper sulphate reference electrode. For ICCP System A, Figure 6.8 gives the measurement results under the following test conditions:

- Applied current density at the anode: 7.952×10^{-3} mA/cm².
- Average value of sand resistivity: 14.61 KΩ.cm.
- Anode coordinates: the bottom coordinate of the anode axis is P₁ (X₁=50.0cm, Y₁=30.0cm, Z₁=6.0cm) and the top coordinate is P₂ (X₂=50.0cm, Y₂=30.0cm, Z₂=16.0cm).

For ICCP System B, Figure 6.9 gives the measurement results for the following test conditions:

- Applied current density at the anode: 1.60×10^{-2} mA/cm².
- Average value of sand resistivity: 14.61 KΩ.cm.
- Anode coordinates:

Anode A: the bottom coordinate of the anode axis is P₁ (X₁=36.2cm, Y₁=10.0cm, Z₁=6.0cm) and the top coordinate is P₂ (X₂=36.2cm, Y₂=10.0cm, Z₂=16.0cm).

Anode B: the bottom coordinate of the anode axis is P₃ (X₃=63.8cm, Y₃=90.0cm, Z₃=6.0cm) and the top coordinate is P₄ (X₄=63.8cm, Y₄=90.0cm, Z₄=16.0cm).

However, such measured potentials do not represent the actual protective potential values on the surface of steel section. They incorporate a potential drop or IR_{Ω} value. In order to obtain the value of the IR_{Ω} -free CP protective potential on the surface of steel piece, the instant-off potential method is employed, whereby the current is briefly interrupted and a value of potential taken immediately afterwards while no current is flowing. The power is then

reapplied. The value of potential is therefore obtained when no current is flowing and there is subsequently no drop due to resistance.

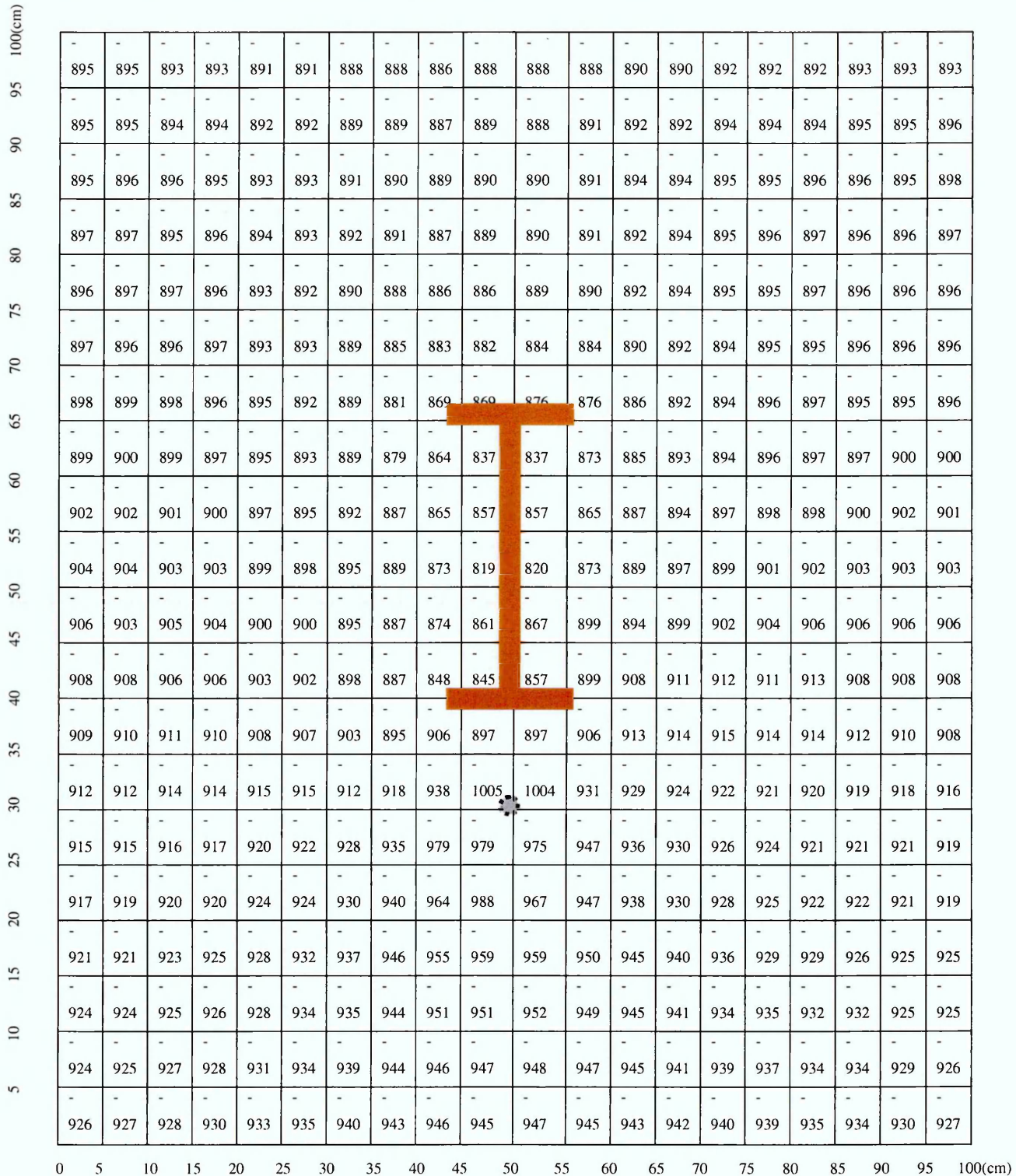


Figure 6.8: Distribution of Protective Potential (mV, vs CSE) on the free surface of the sandbox, Z=22.0cm, ICCP System A.

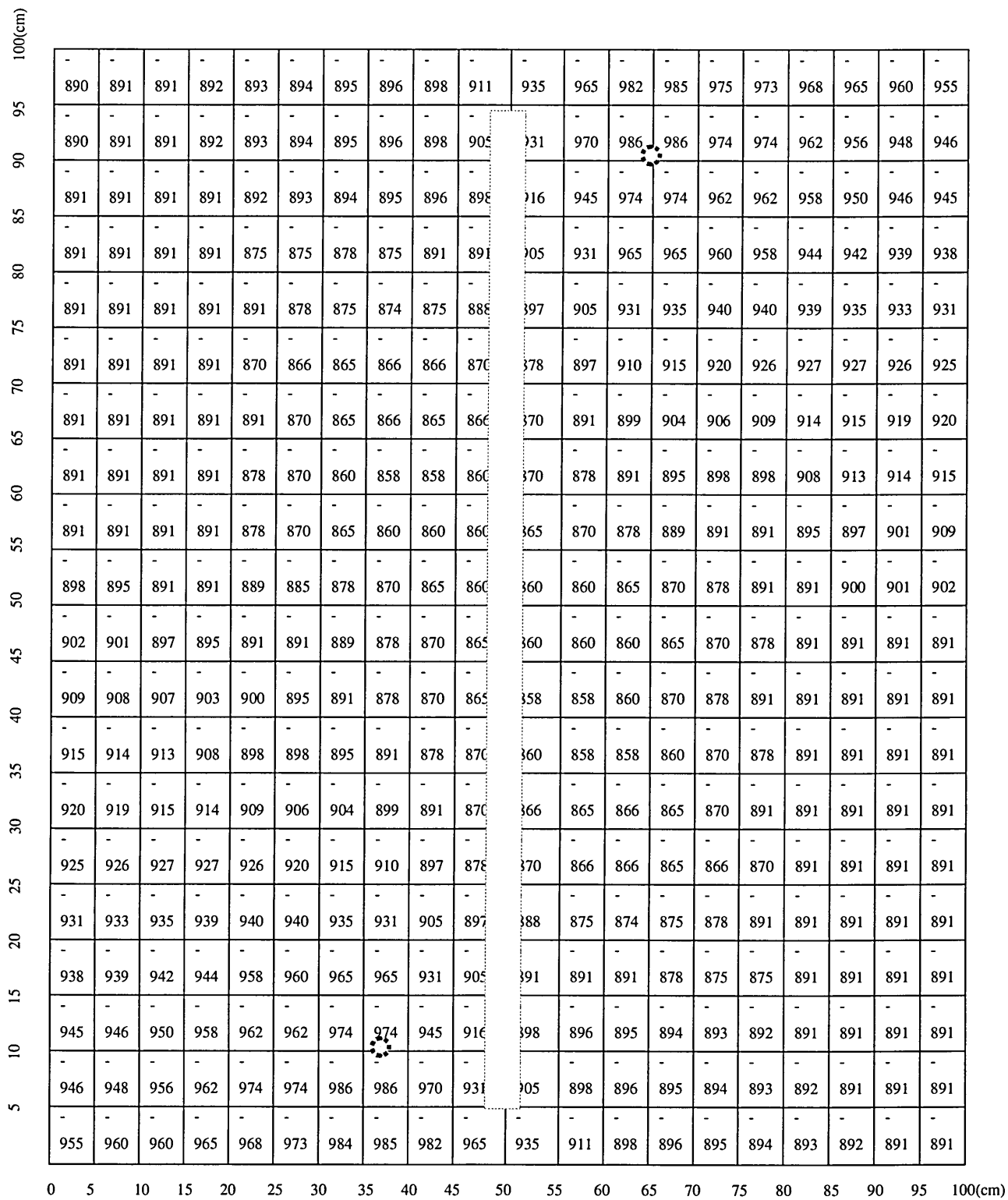


Figure 6.9: Distribution of Protective Potential (mV vs. CSE) on the free surface of sandbox, Z=22.0cm, of ICCP System B.

As the steel section has a very complex geometry it is not possible to accurately measure every point on steel surface. Due to this limitation, only the protective potential at selected points of top surface of steel section have been measured.

6.3 Modelling of Boundary Element of ICCP System A and B

The theory of the boundary element method for cathodic protection system has been discussed in Chapter 4. The polarisation curves of steel in sand were studied in Chapter 5. In this section, the knowledge and theory obtained described in these two chapters are used to model the two representative ICCP systems.

6.3.1 Discussion of Boundary Conditions

The boundary conditions of cathodic protection systems have been discussed in Section 4.4. However, for a special impressed current cathodic system such as would be employed for a steel frame application, there are some significant differences. Below are described the boundary conditions of the two systems employed in this study.

The sandbox domain, for the solution of the Laplace equation, is bounded by the following surface:

- One free surface.
- Four insulating walls and one insulated bottom surface of the sandbox.
- The surface of the discrete anode.
- The surface of steel section (cathode).

The boundary conditions on these surfaces are as follows:

- (i) On the free surface and insulating surfaces, normal current density is equal to zero:

$$k \frac{\partial E}{\partial n} = 0 \quad (6.1)$$

- (ii) At any point on the anode surface, the normal current density has a constant value i_a :

$$k \frac{\partial E}{\partial n} = i_a \quad (6.2)$$

As an alternative to defining the normal current density at an anode, the potential at an anode can be defined as a constant:

$$E = E_a \quad (6.3)$$

It should be noted that the ICCP system is evaluated under steady-state conditions. The anode is not treated as a charge source but as a fixed boundary condition. In this approach the current level of an anode is fixed and no variation is allowed. The current level at an anode will vary with time and operating conditions during the life of an ICCP system.

Therefore separate solutions must be performed for various times during the life of the system when this approach is taken.

- (iii) The normal current density at any point on the steel section (cathode) is :

$$i_c = f_c(E_c) \quad (6.4)$$

This is the same as equation (4.22). It is the experimentally determined polarisation curves which describe the non-linear relationship between the potential and the current density on the cathode surface or the cathode electrode kinetics.

The measurement of polarisation curves of steel in sand under the conditions of the different resistivities has been performed in Chapter 5. The results are directly applicable to the present modelling.

6.3.2 Boundary Element Analysis of ICCP System A

The potential and current density distributions of ICCP System A are analyzed under the following conditions:

- The average values of sand resistivity studied are 42.32 KΩ-cm, 14.61 KΩ-cm and 6.41 KΩ-cm, respectively. The aim is to investigate the effect of the resistivity on the distributions of protective potential and current density.
- One anode is placed separately on the three different coordinates. The goal is to study the effect of the anode locations on the distributions of protective potential and current density.

Initially, the bottom coordinate of the anode axis is P₁ (X₁=50.0cm, Y₁=30.0cm, Z₁=6.0cm) and the top coordinate is P₂ (X₂=50.0cm, Y₂=30.0cm, Z₂=16.0cm).

Secondly, the bottom coordinate of the anode axis is P₃ (X₃=50.0cm, Y₃=15.0cm, Z₃=6.0cm) and the top coordinate is P₄ (X₄=50.0cm, Y₄=15.0cm, Z₄=16.0cm).

Finally, the bottom coordinate of the anode axis is P₅ (X₁=35.0cm, Y₅=52.8cm, Z₅=6.0cm) and the top coordinate is P₆ (X₆=35.0cm, Y₆=52.8cm, Z₆=16.0cm).

- The applied current density on the anodes is: $7.952 \times 10^{-3} \text{ mA/cm}^2$.
- The boundary conditions on the surface of the cathode or steel section have been described in Section 6.3.1.

The total boundary element mesh used for the analysis is shown in Figure 6.10.

For clarity, the boundary element mesh on the surface of sandbox and steel piece is further shown in Figures 6.11 and 6.12. The modelling results and discussion are shown in Figures 6.13 to 6.30 and discussed in Section 6.4.

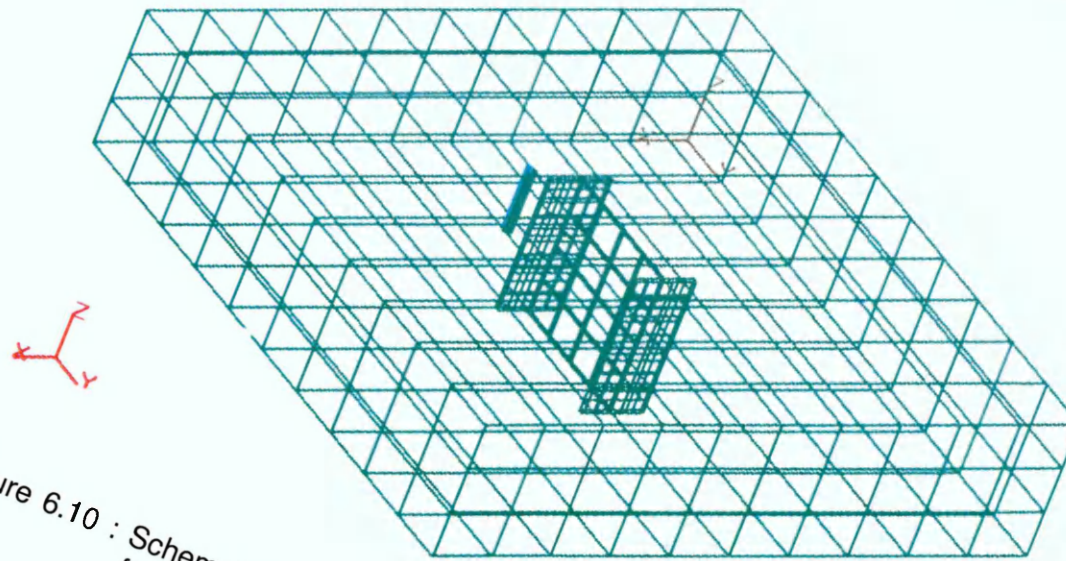


Figure 6.10 : Schematic representation of the total boundary element mesh for ICCP System A

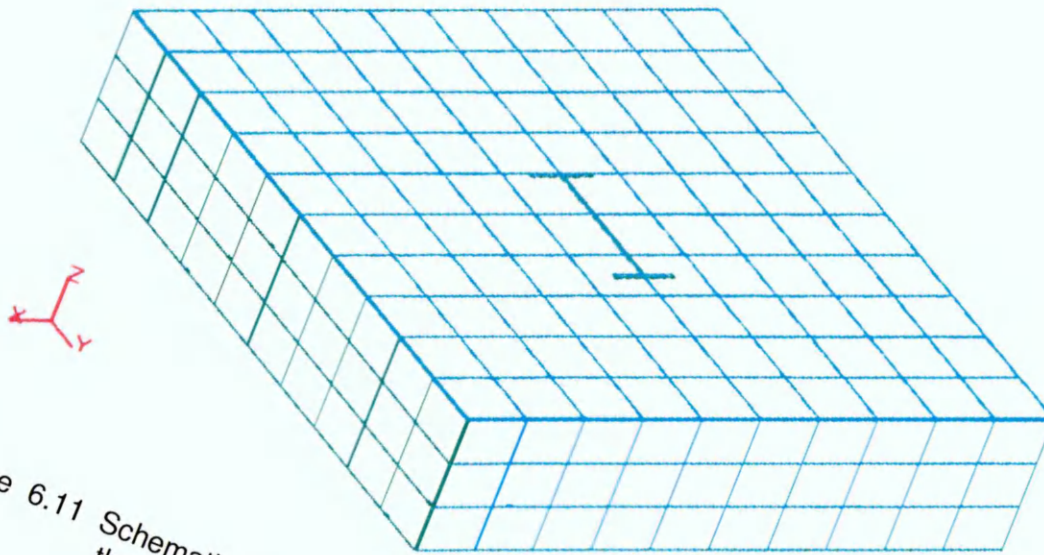


Figure 6.11 Schematic representation of the boundary element mesh on the surface of sandbox for ICCP System A

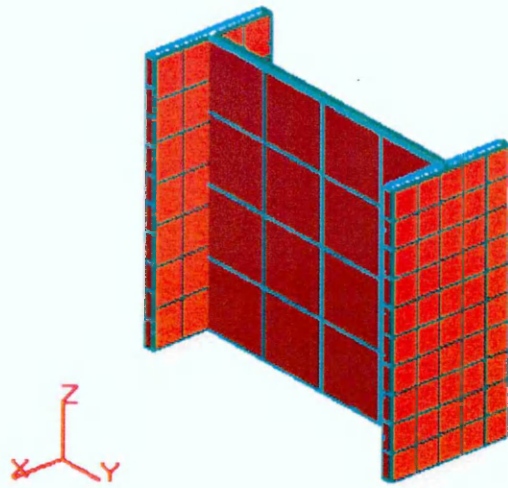


Figure 6.12: Schematic representation of the boundary element mesh on the surface of Steel Section A of ICCP System A

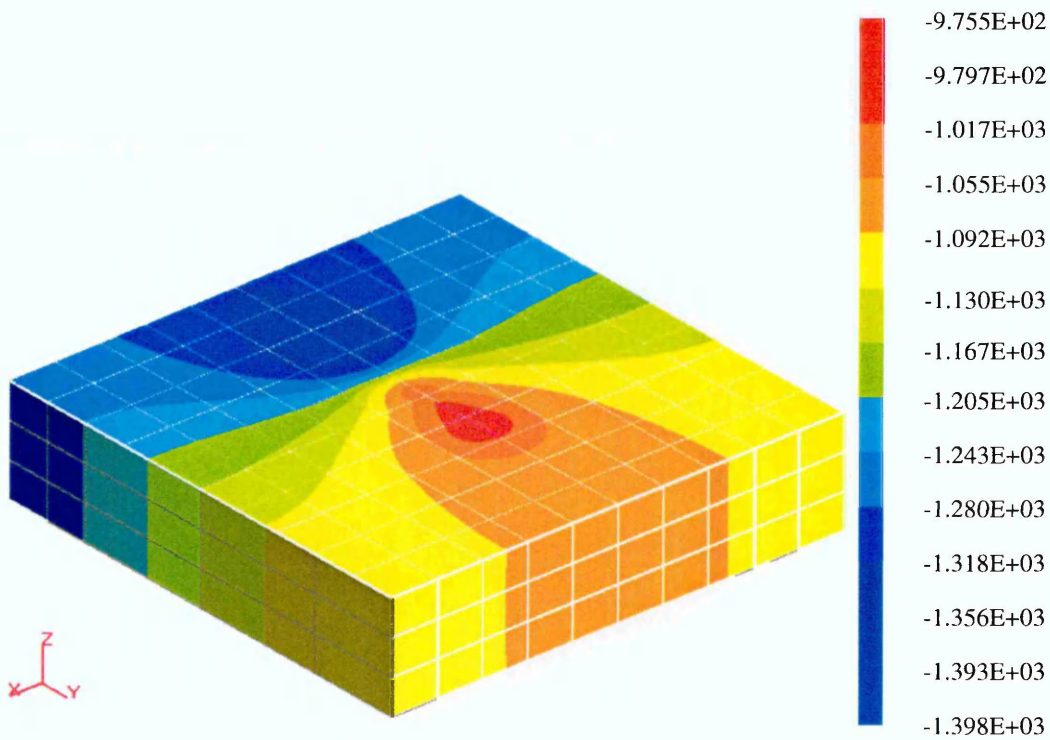


Figure 6.13: Potential distributions on the surface of sandbox of ICCP System A (mV, vs CSE)

- The applied current density at the anode: $7.952 \times 10^{-3} \text{ mA/cm}^2$.
- The average value of sand resistivity: $42.32 \text{ K} \cdot \text{cm}$.
- The anode coordinates: the bottom coordinate of the anode axis is P_1 ($X_1=50.0\text{cm}$, $Y_1=30.0\text{cm}$, $Z_1=6.0\text{cm}$) and the top coordinate is P_2 ($X_2=50.0\text{cm}$, $Y_2=30.0\text{cm}$, $Z_2=16.0\text{cm}$).

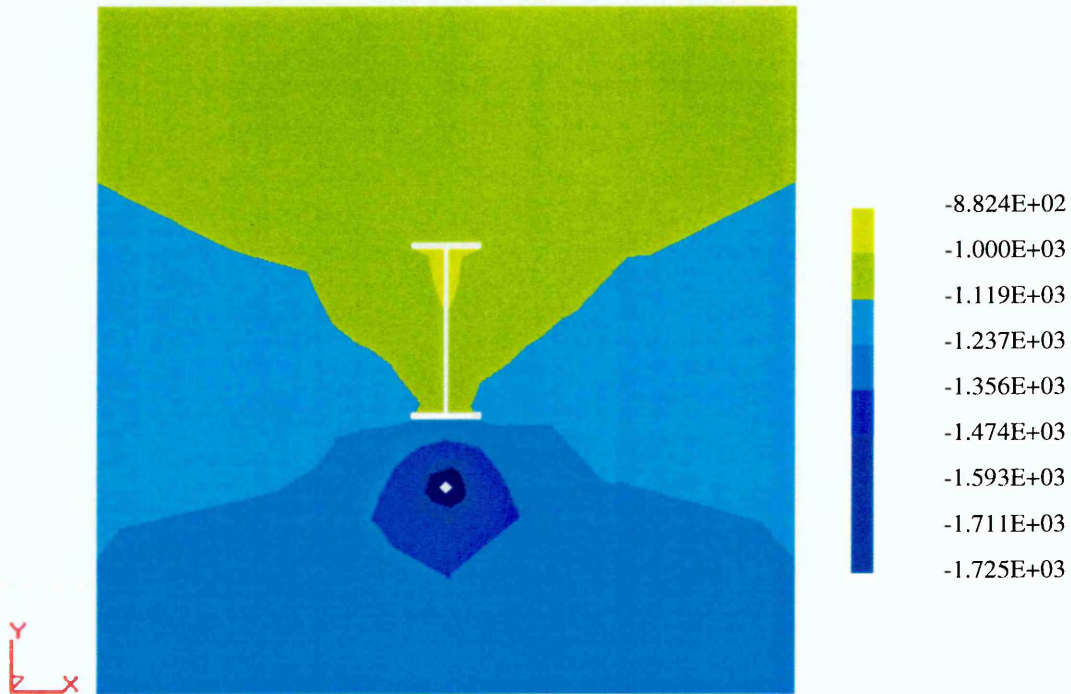


Figure 6.14: Potential distribution at Z=11.0cm of ICCP System A (mV, vs SCE)

- The applied current density at the anode: $7.952 \times 10^{-3} \text{ mA/cm}^2$.
- The average value of sand resistivity: $42.32 \text{ K} \cdot \text{cm}$.
- The anode coordinates: the bottom coordinate of the anode axis is P_1 ($X_1=50.0\text{cm}$, $Y_1=30.0\text{cm}$, $Z_1=6.0\text{cm}$) and the top coordinate is P_2 ($X_2=50.0\text{cm}$, $Y_2=30.0\text{cm}$, $Z_2=16.0\text{cm}$).

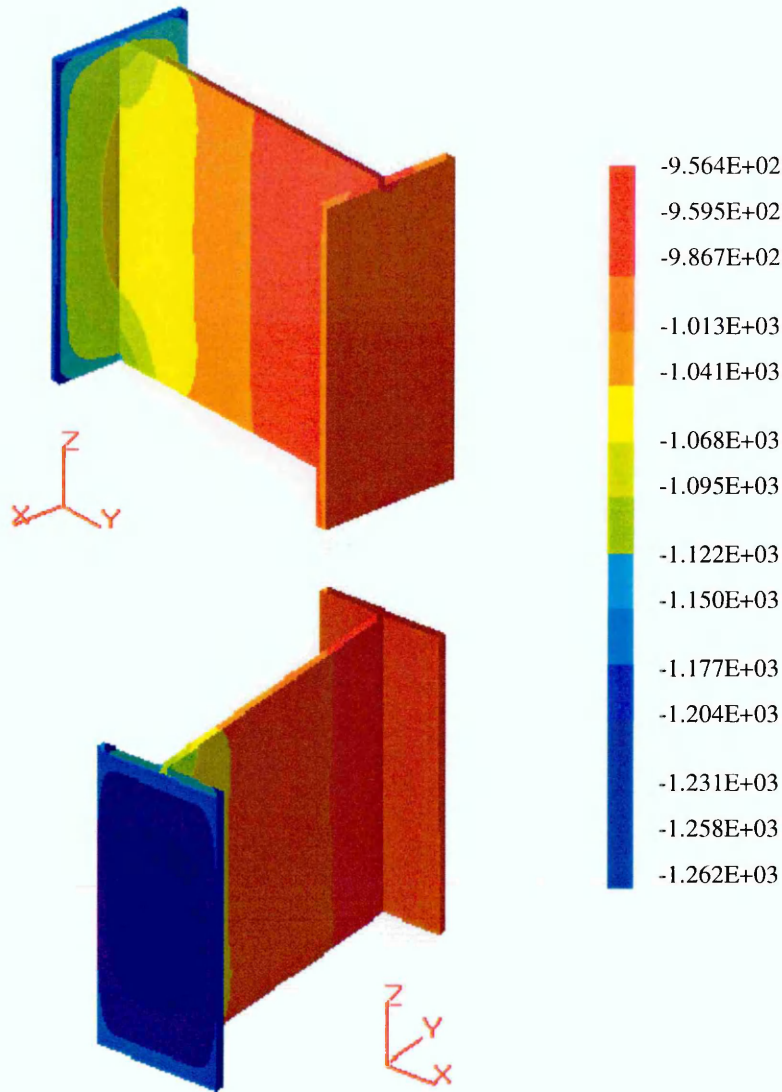


Figure 6.15: Potential distribution on the surface of Steel Section A of ICCP System A (mV, vs CSE)

- The applied current density at the anode: $7.952 \times 10^{-3} \text{ mA/cm}^2$.
- The average value of sand resistivity: $42.32 \text{ K } \cdot \text{cm}$.
- The anode coordinates: the bottom coordinate of the anode axis is P_1 ($X_1=50.0\text{cm}$, $Y_1=30.0\text{cm}$, $Z_1=6.0\text{cm}$) and the top coordinate is P_2 ($X_2=50.0\text{cm}$, $Y_2=30.0\text{cm}$, $Z_2=16.0\text{cm}$).

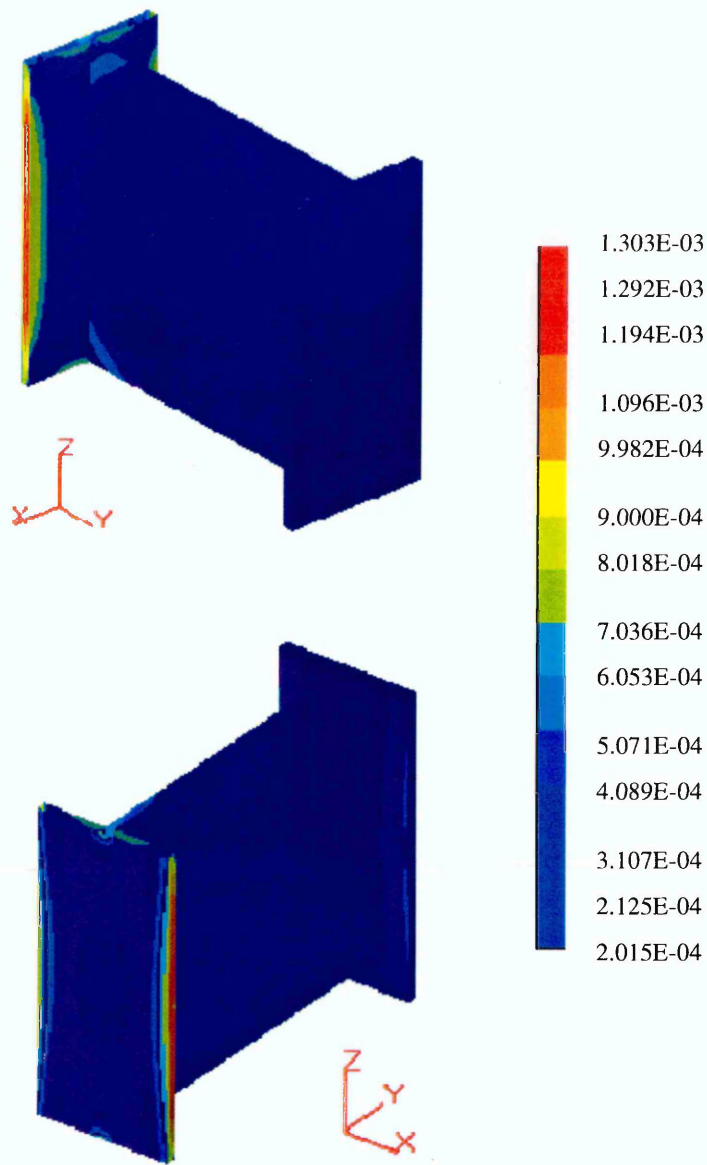


Figure 6.16: Current distribution on the surface of Steel Section A of ICCP System (mA)

- The applied current density at the anode: $7.952 \times 10^{-3} \text{ mA/cm}^2$.
- The average value of sand resistivity: $42.32 \text{ K } \Omega\text{-cm}$.
- The anode coordinates: the bottom coordinate of the anode axis is P_1 ($X_1=50.0\text{cm}$, $Y_1=30.0\text{cm}$, $Z_1=6.0\text{cm}$) and the top coordinate is P_2 ($X_2=50.0\text{cm}$, $Y_2=30.0\text{cm}$, $Z_2=16.0\text{cm}$).

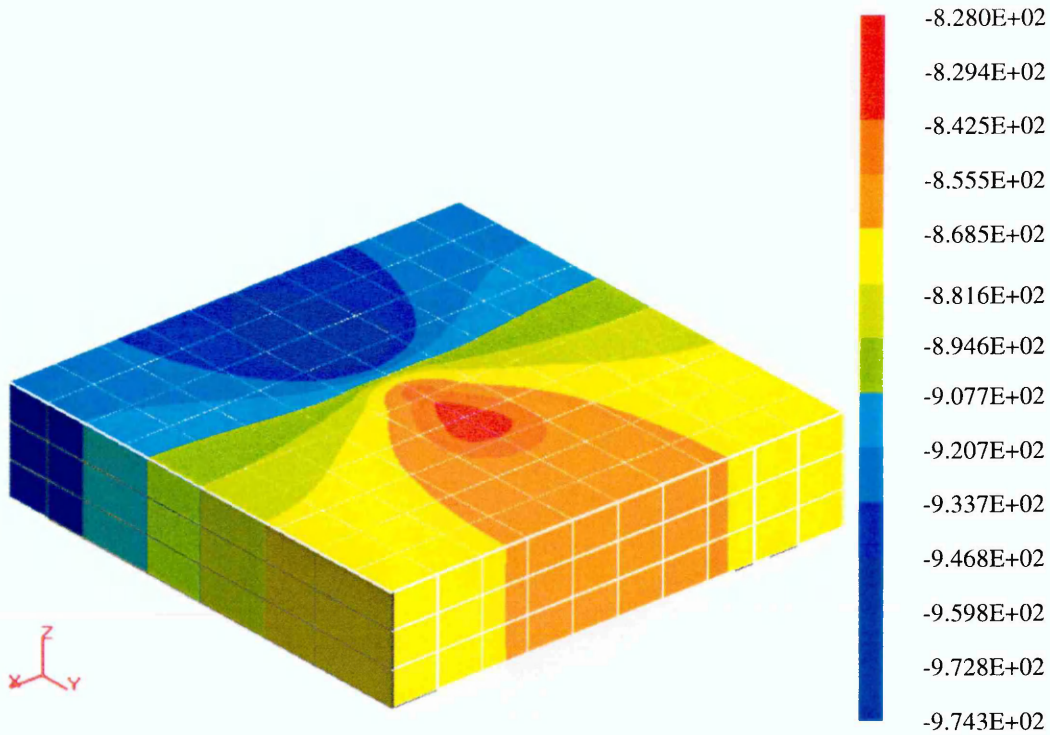


Figure 6.17: Potential distribution at the free surface of sandbox of ICCP System A (mV, vs CSE)

- The applied current density at the anode: $7.952 \times 10^{-3} \text{ mA/cm}^2$.
- The average value of sand resistivity: $14.61 \text{ K } \Omega\text{-cm}$.
- The anode coordinates: the bottom coordinate of the anode axis is P_1 ($X_1=50.0\text{cm}$, $Y_1=30.0\text{cm}$, $Z_1=6.0\text{cm}$) and the top coordinate is P_2 ($X_2=50.0\text{cm}$, $Y_2=30.0\text{cm}$, $Z_2=16.0\text{cm}$).

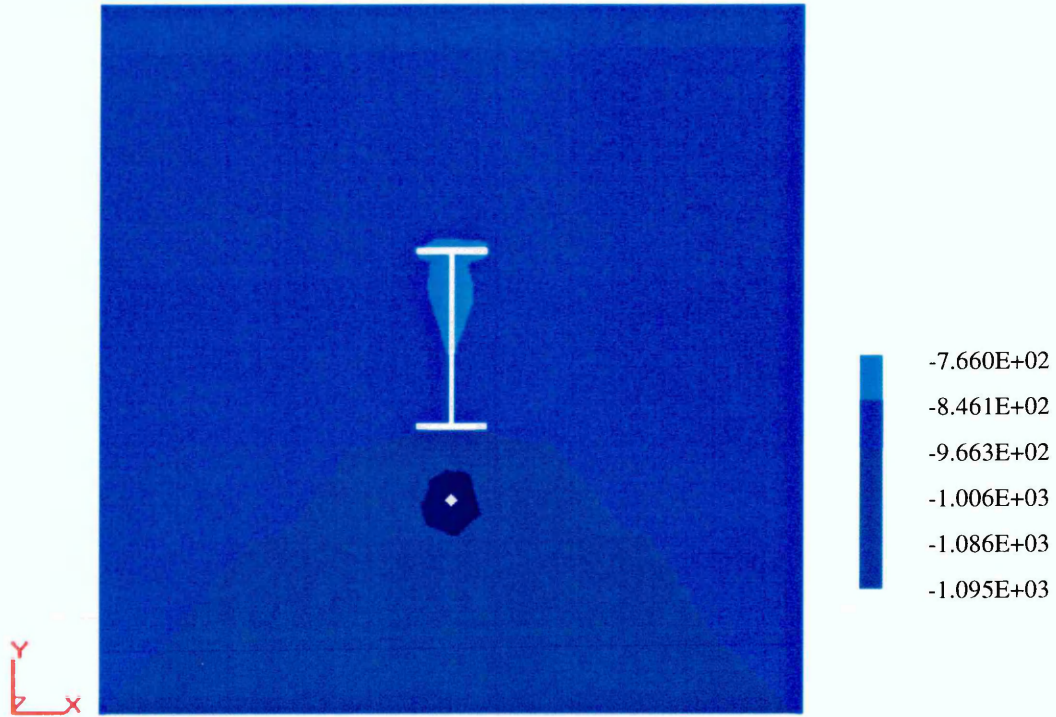


Figure 6.18: Potential distribution at Z=11.0cm of ICCP System A (mV, vs SCE)

- The applied current density at the anode: $7.952 \times 10^{-3} \text{ mA/cm}^2$.
- The average value of sand resistivity: $14.61 \text{ K } \Omega\text{-cm}$.
- The anode coordinates: the bottom coordinate of the anode axis is P_1 ($X_1=50.0\text{cm}$, $Y_1=30.0\text{cm}$, $Z_1=6.0\text{cm}$) and the top coordinate is P_2 ($X_2=50.0\text{cm}$, $Y_2=30.0\text{cm}$, $Z_2=16.0\text{cm}$).

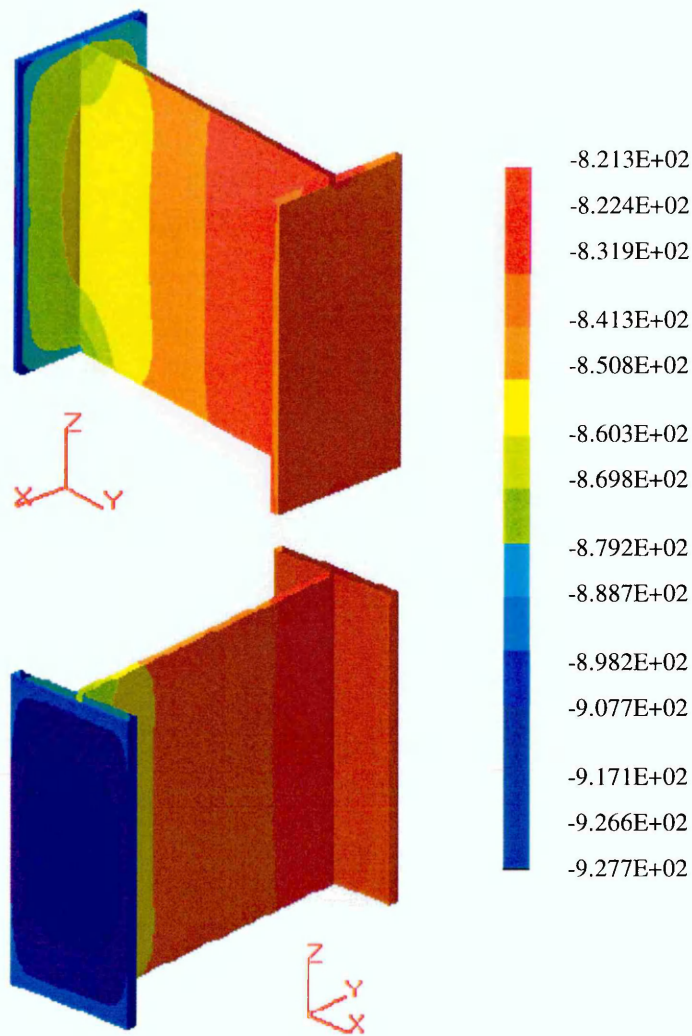


Figure 6.19: Potential distribution on the surface of Steel Section A of ICCP System A (mV, vs SCE)

- The applied current density at the anode: $7.952 \times 10^{-3} \text{ mA/cm}^2$.
- The average value of sand resistivity: $14.61 \text{ K } \Omega\text{-cm}$.
- The anode coordinates: the bottom coordinate of the anode axis is P_1 ($X_1=50.0\text{cm}$, $Y_1=30.0\text{cm}$, $Z_1=6.0\text{cm}$) and the top coordinate is P_2 ($X_2=50.0\text{cm}$, $Y_2=30.0\text{cm}$, $Z_2=16.0\text{cm}$).

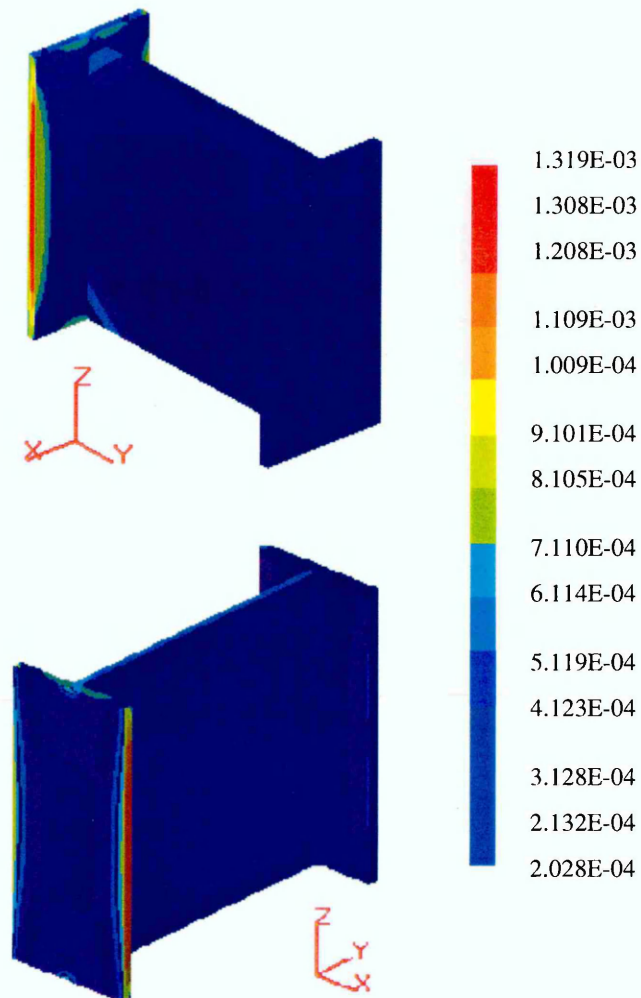


Figure 6.20: Current distribution on the surface of Steel Section A of ICCP System A (mA)

- The applied current density at the anode: $7.952 \times 10^{-3} \text{ mA/cm}^2$.
- The average value of sand resistivity: $14.61 \text{ K } \Omega\text{-cm}$.
- The anode coordinates: the bottom coordinate of the anode axis is P_1 ($X_1=50.0\text{cm}$, $Y_1=30.0\text{cm}$, $Z_1=6.0\text{cm}$) and the top coordinate is P_2 ($X_2=50.0\text{cm}$, $Y_2=30.0\text{cm}$, $Z_2=16.0\text{cm}$).

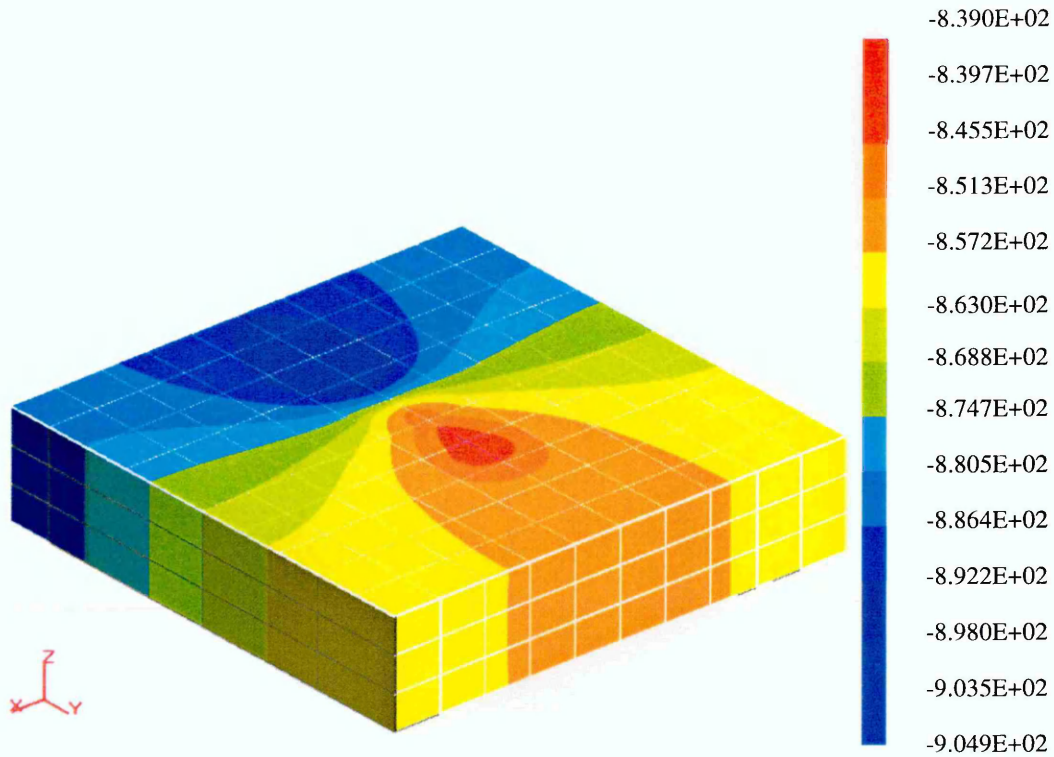


Figure 6.21: Potential distribution on the surface of sandbox of ICCP System A (mV, vs CSE)

- The applied current density at the anode: $7.952 \times 10^{-3} \text{ mA/cm}^2$.
- The average value of sand resistivity: $6.41 \text{ K } \Omega\text{-cm}$.
- The anode coordinates: the bottom coordinate of the anode axis is P_1 ($X_1=50.0\text{cm}$, $Y_1=30.0\text{cm}$, $Z_1=6.0\text{cm}$) and the top coordinate is P_2 ($X_2=50.0\text{cm}$, $Y_2=30.0\text{cm}$, $Z_2=16.0\text{cm}$).

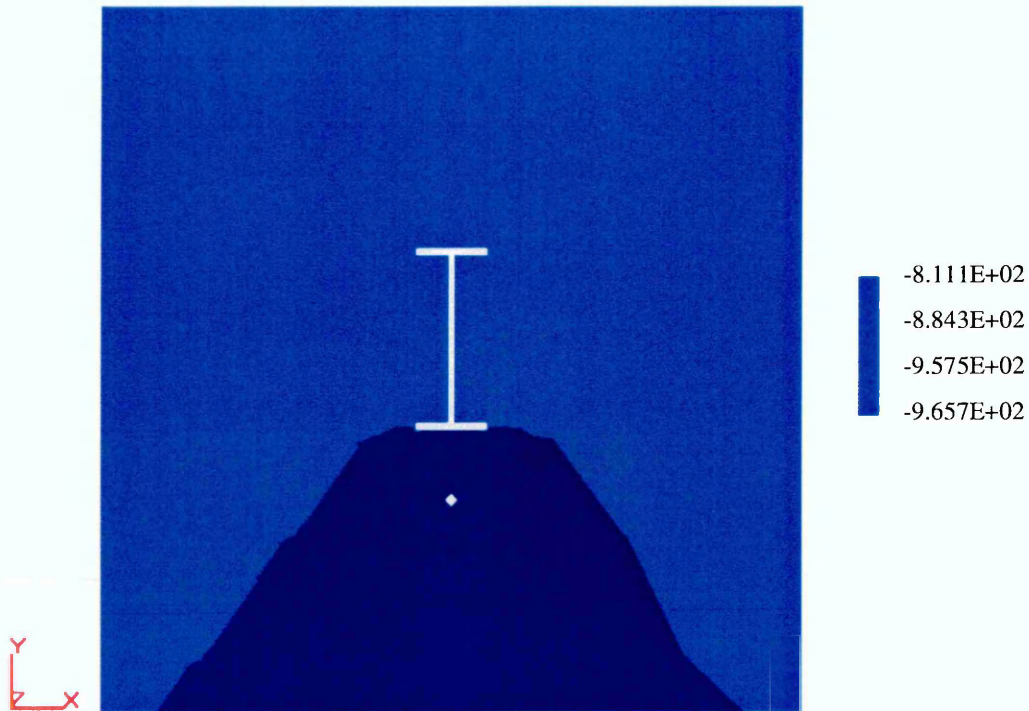


Figure 6.22: Potential distribution at Z=11.0cm of ICCP System A (mV, vs CSE)

- The applied current density at the anode: $7.952 \times 10^{-3} \text{ mA/cm}^2$.
- The average value of sand resistivity: $6.41 \text{ K } \Omega\text{-cm}$.
- The anode coordinates: the bottom coordinate of the anode axis is P_1 ($X_1=50.0\text{cm}$, $Y_1=30.0\text{cm}$, $Z_1=6.0\text{cm}$) and the top coordinate is P_2 ($X_2=50.0\text{cm}$, $Y_2=30.0\text{cm}$, $Z_2=16.0\text{cm}$).

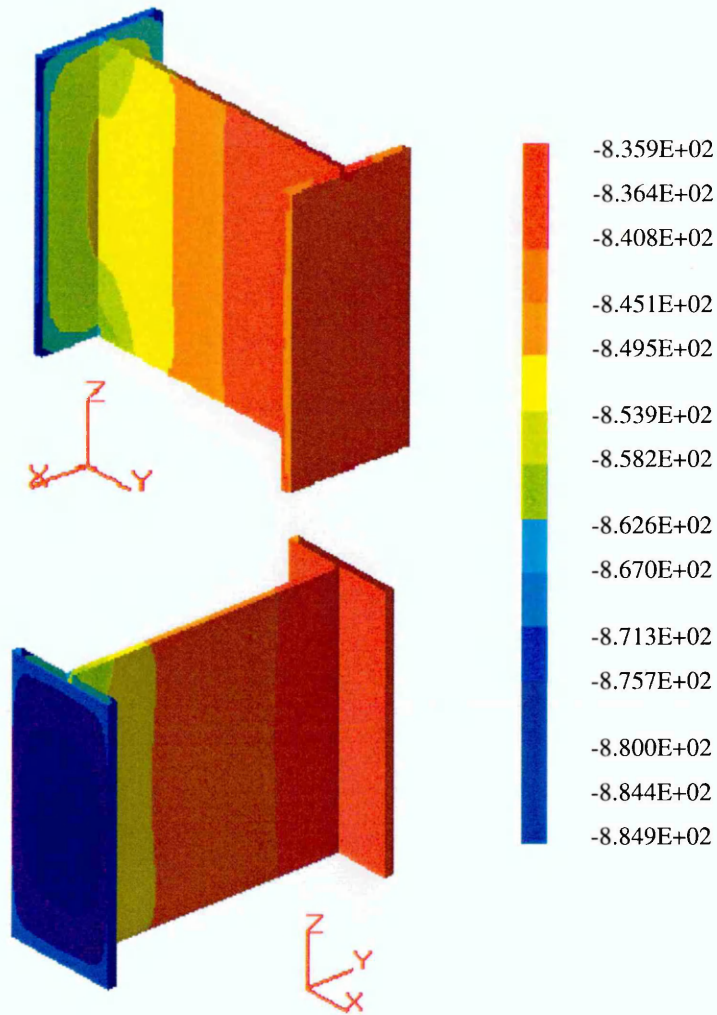


Figure 6.23: Potential distribution on the surface of Steel Section A of ICCP System A (mV, vs CSE)

- The applied current density at the anode: $7.952 \times 10^{-3} \text{ mA/cm}^2$.
- The average value of sand resistivity: $6.41 \text{ K } \Omega\text{-cm}$.
- The anode coordinates: the bottom coordinate of the anode axis is P_1 ($X_1=50.0\text{cm}$, $Y_1=30.0\text{cm}$, $Z_1=6.0\text{cm}$) and the top coordinate is P_2 ($X_2=50.0\text{cm}$, $Y_2=30.0\text{cm}$, $Z_2=16.0\text{cm}$).

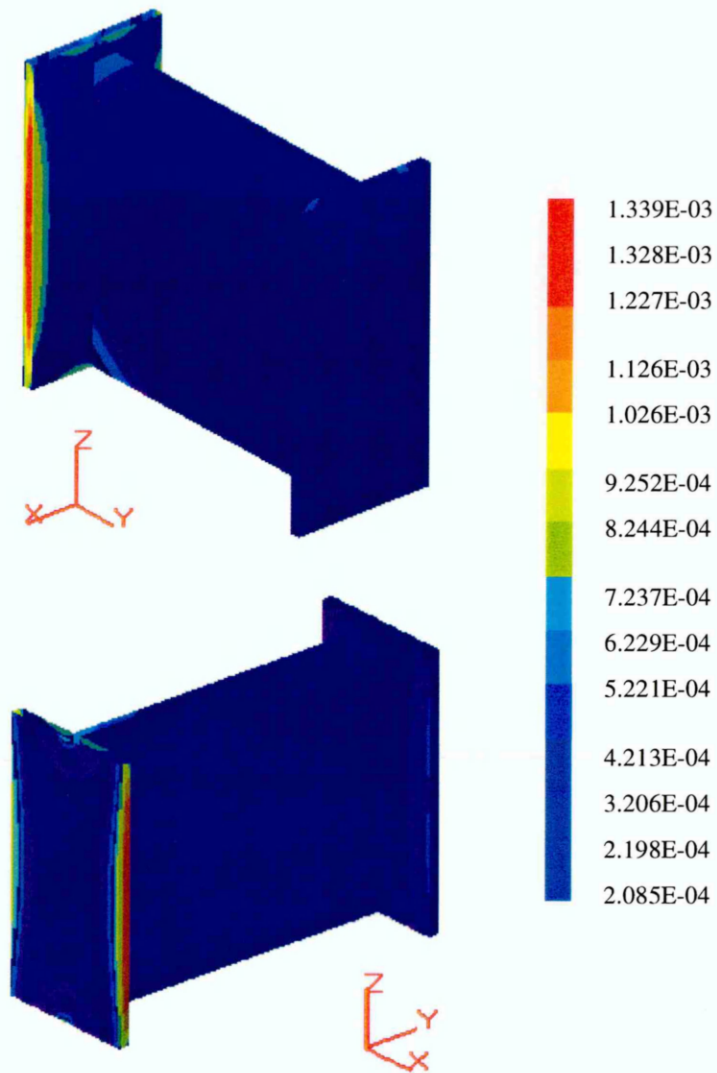


Figure 6.24: Current distribution on the surface of Steel Section A of ICCP System A (mA)

- The applied current density at the anode: $7.952 \times 10^{-3} \text{ mA/cm}^2$.
- The average value of sand resistivity: $6.41 \text{ K } \Omega\text{-cm}$.
- The anode coordinates: the bottom coordinate of the anode axis is P_1 ($X_1=50.0\text{cm}$, $Y_1=30.0\text{cm}$, $Z_1=6.0\text{cm}$) and the top coordinate is P_2 ($X_2=50.0\text{cm}$, $Y_2=30.0\text{cm}$, $Z_2=16.0\text{cm}$).

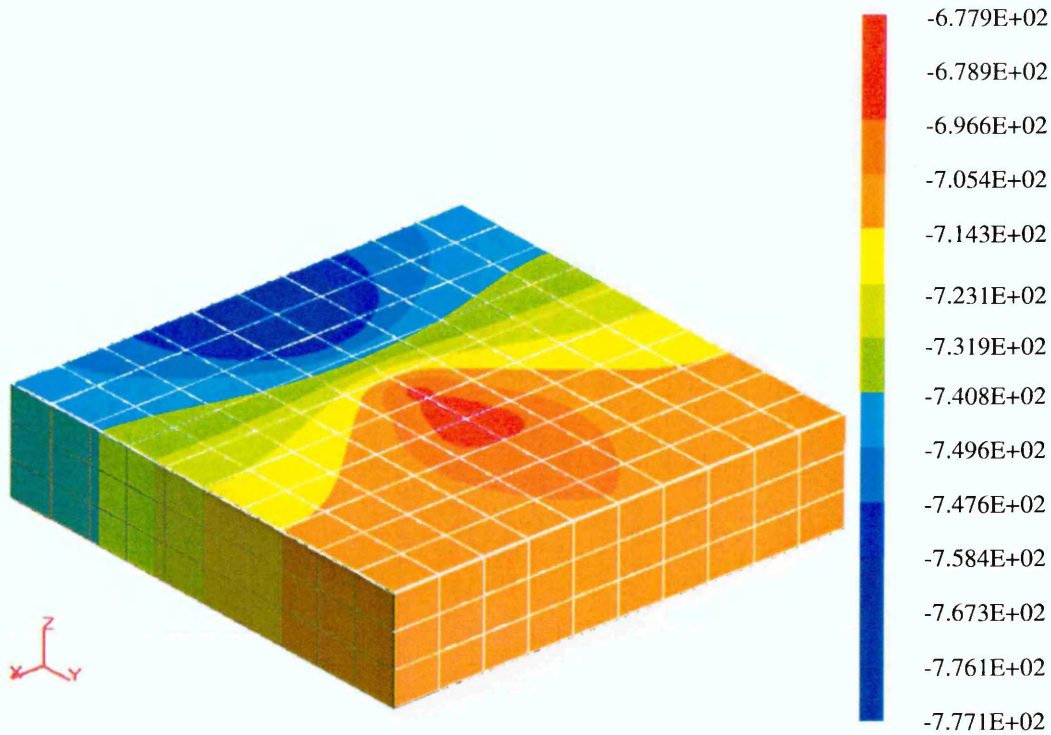


Figure 6.25: Potential distribution on the surface of sandbox of ICCP System A (mV, vs CSE)

- The applied current density at the anode: $7.952 \times 10^{-3} \text{ mA/cm}^2$.
- The average value of sand resistivity: 14.61 K Ω -cm.
- The anode coordinates: the bottom coordinate of the anode axis is P_3 ($X_3=50.0\text{cm}$, $Y_3=15.0\text{cm}$, $Z_3=6.0\text{cm}$) and the top coordinate is P_4 ($X_4=50.0\text{cm}$, $Y_4=15.0\text{cm}$, $Z_4=16.0\text{cm}$).

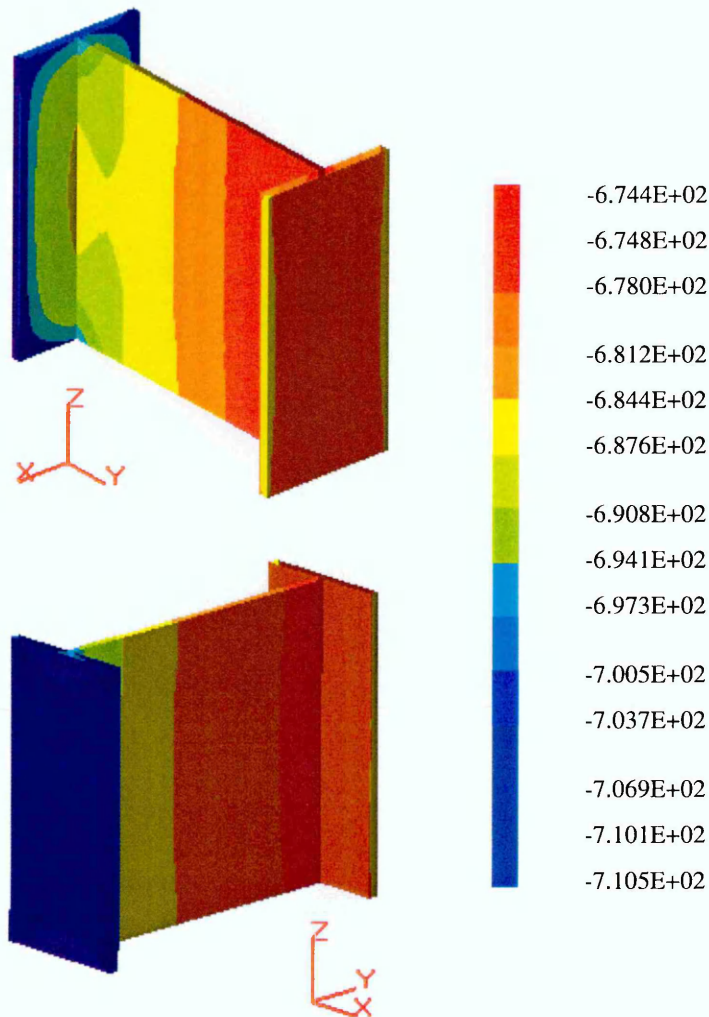


Figure 6.26: Potential distribution on the surface of Steel Section A of ICCP System A (mV, vs CSE)

- The applied current density at the anode: $7.952 \times 10^{-3} \text{ mA/cm}^2$.
- The average value of sand resistivity: $14.61 \text{ K } \Omega\text{-cm}$.
- The anode coordinates: the bottom coordinate of the anode axis is P_3 ($X_3=50.0\text{cm}$, $Y_3=15.0\text{cm}$, $Z_3=6.0\text{cm}$) and the top coordinate is P_4 ($X_4=50.0\text{cm}$, $Y_4=15.0\text{cm}$, $Z_4=16.0\text{cm}$).

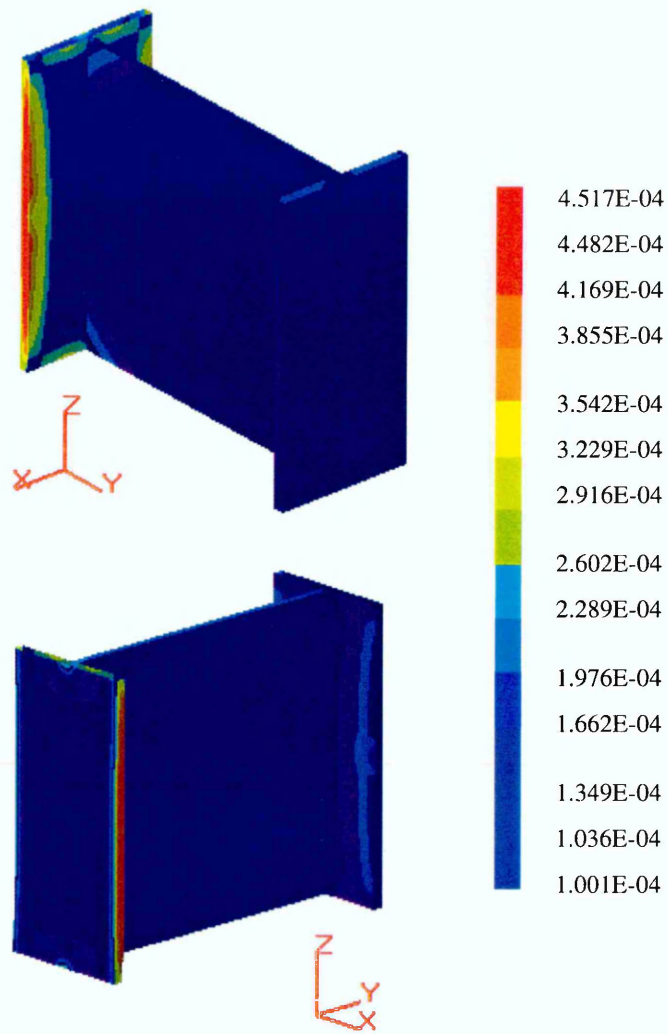


Figure 6.27: Current distribution on the surface of Steel Section A of ICCP System A (mA)

- The applied current density at the anode: $7.952 \times 10^{-3} \text{ mA/cm}^2$.
- The average value of sand resistivity: 14.61 K Ω -cm.
- The anode coordinates: the bottom coordinate of the anode axis is P_3 ($X_3=50.0\text{cm}$, $Y_3=15.0\text{cm}$, $Z_3=6.0\text{cm}$) and the top coordinate is P_4 ($X_4=50.0\text{cm}$, $Y_4=15.0\text{cm}$, $Z_4=16.0\text{cm}$).

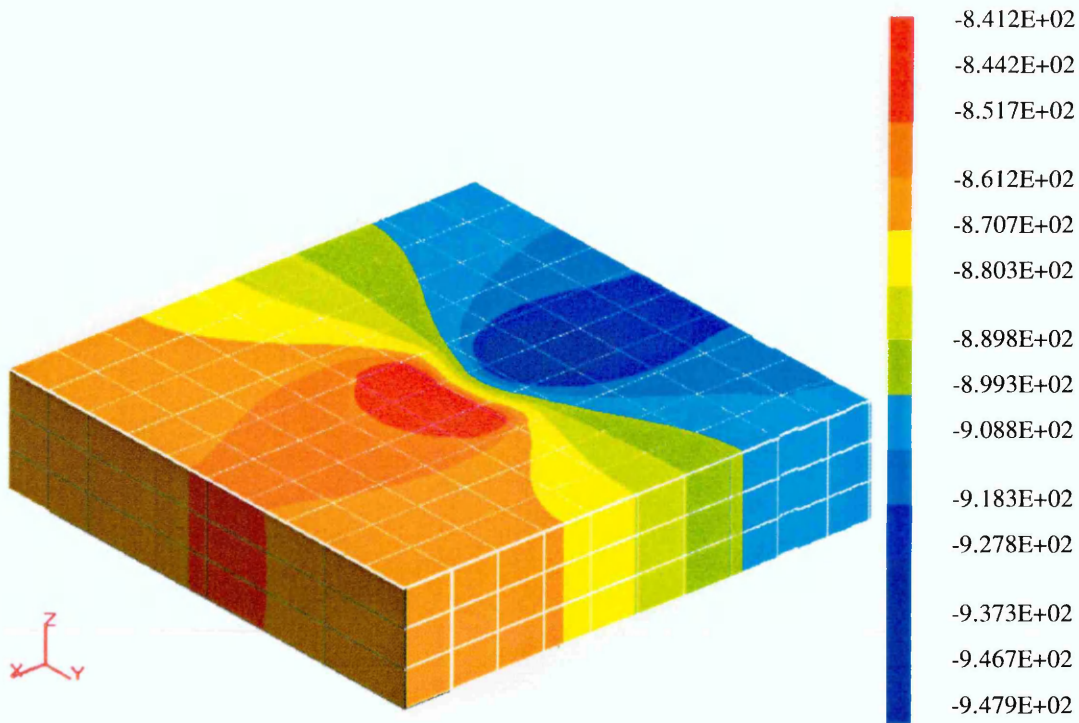


Figure 6.28: Potential distribution on the surface of sandbox of ICCP System A (mV, vs CSE)

- The applied current density at the anode: $7.952 \times 10^{-3} \text{ mA/cm}^2$.
- The average value of sand resistivity: 14.61 K Ω -cm.
- The anode coordinates: the bottom coordinate of the anode axis is P_5 ($X_5=35.0\text{cm}$, $Y_5=52.8\text{cm}$, $Z_5=6.0\text{cm}$) and the top coordinate is P_6 ($X_6=35.0\text{cm}$, $Y_6=52.8\text{cm}$, $Z_6=16.0\text{cm}$).

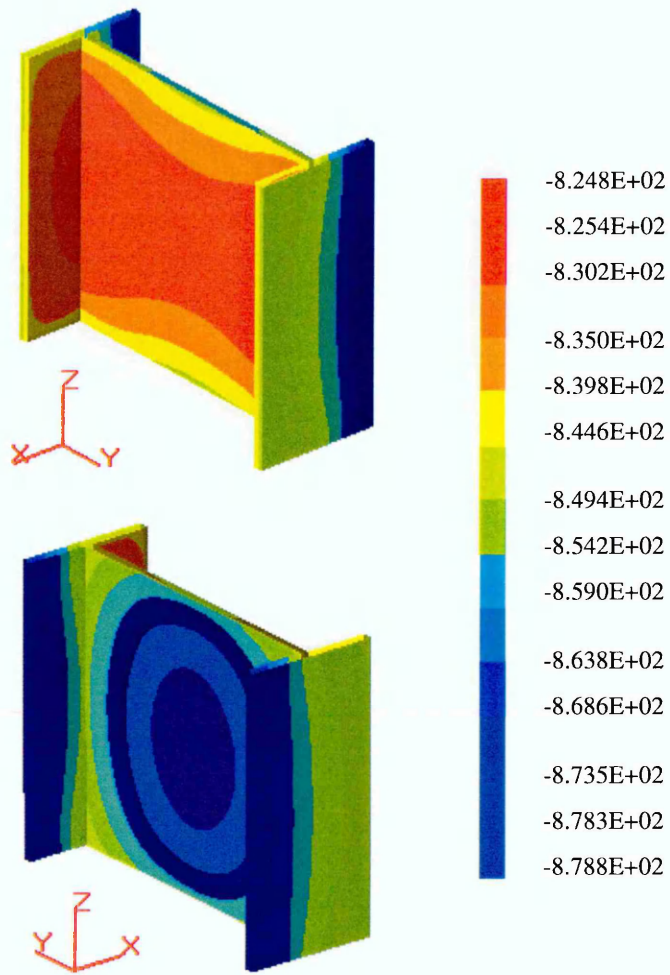


Figure 6.29: Potential distribution on the surface of Steel Section A of ICCP System A (mV, vs CSE)

- The applied current density at the anode: $7.952 \times 10^{-3} \text{ mA/cm}^2$.
- The average value of sand resistivity: 14.61 K -cm.
- The anode coordinates: the bottom coordinate of the anode axis is $P_5 (X_5=35.0\text{cm}, Y_5=52.8\text{cm}, Z_5=6.0\text{cm})$ and the top coordinate is $P_6 (X_6=35.0\text{cm}, Y_6=52.8\text{cm}, Z_6=16.0\text{cm})$.

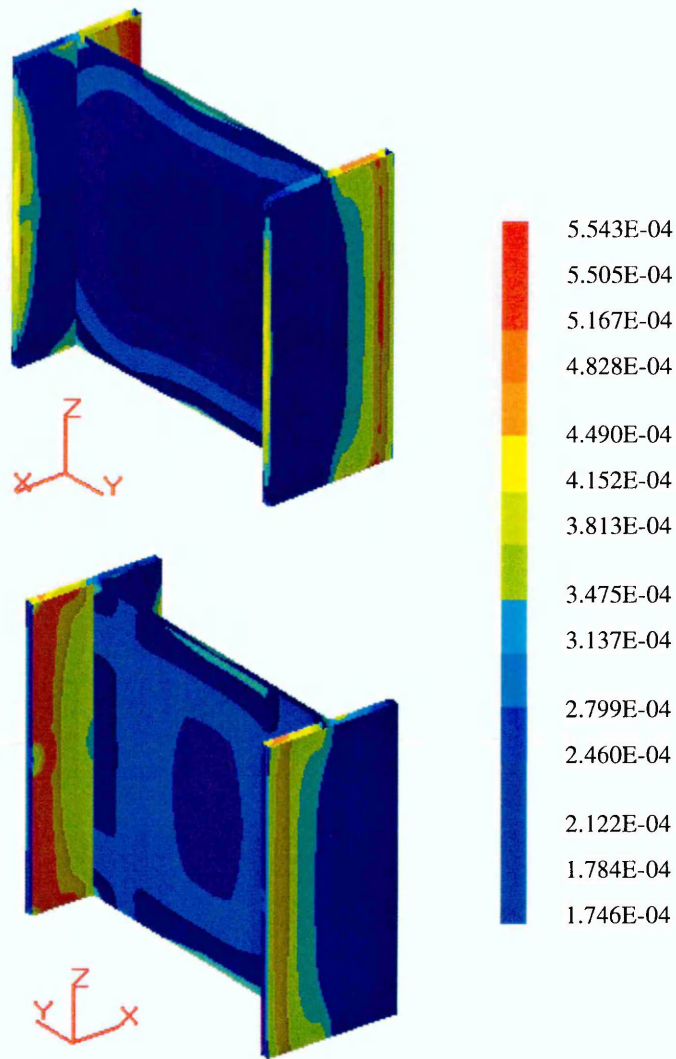


Figure 6.30: Current distribution on the surface of Steel Section A of ICCP System A (mA)

- The applied current density at the anode: $7.952 \times 10^{-3} \text{ mA/cm}^2$.
- The average value of sand resistivity: 14.61 K Ω -cm.
- The anode coordinates: the bottom coordinate of the anode axis is P_5 ($X_5=35.0\text{cm}$, $Y_5=52.8\text{cm}$, $Z_5=6.0\text{cm}$) and the top coordinate is P_6 ($X_6=35.0\text{cm}$, $Y_6=52.8\text{cm}$, $Z_6=16.0\text{cm}$).

6.3.3 Boundary Element Analysis of ICCP System B

The potential and current density distribution of ICCP system B are analyzed under the following conditions:

- The average values of sand resistivity studied are 42.32 K Ω -cm, 14.61 K Ω -cm and 6.41 K Ω -cm, respectively. The aim is to investigate the effect of the resistivity on the distributions of protective potential and current density.
- Two anodes are placed respectively on the two different coordinates. The goal is to study the effect of the anode locations on the distributions of protective potential and current density. The initial coordinates of the anodes are as follows:

Anode A: the bottom coordinate of the anode axis is P₁ (X₁=36.2cm, Y₁=10.0cm, Z₁=6.0cm) and the top coordinate is P₂ (X₂=36.2cm, Y₂=10.0cm, Z₂=16.0cm).

Anode B: the bottom coordinate of the anode axis is P₃ (X₃=63.8cm, Y₃=90.0cm, Z₃=6.0cm) and the top coordinate is P₄ (X₄=63.8cm, Y₄=90.0cm, Z₄=16.0cm).

After performing the analysis of ICCP System B with three resistivity values of sand, the anodes are moved to the following location for further analysis.

Anode A: the bottom coordinate of the anode axis is P₅ (X₅=21.2cm, Y₅=10.0cm, Z₅=6.0cm) and the top coordinate is P₆ (X₆=21.2cm, Y₆=10.0cm, Z₆=16.0cm).

Anode B: the bottom coordinate of the anode axis is P₇ (X₇=78.8cm, Y₇=90.0cm, Z₇=6.0cm) and the top coordinate is P₈ (X₈=78.8cm, Y₈=90.0cm, Z₈=16.0cm).

- The applied current density on the anodes is: 1.6X10⁻² mA/cm².

- The boundary conditions on the surface of the cathode or steel section have been described in Section 6.3.1.

The total boundary element mesh used for the analysis is shown in Figure 6.31. For clarity, the boundary element mesh on the surface of sandbox and steel piece is further shown in Figures 6.32 and 6.33. The modelling results are shown in Figures 6.33 to 6.51 and discussed in Section 6.4.

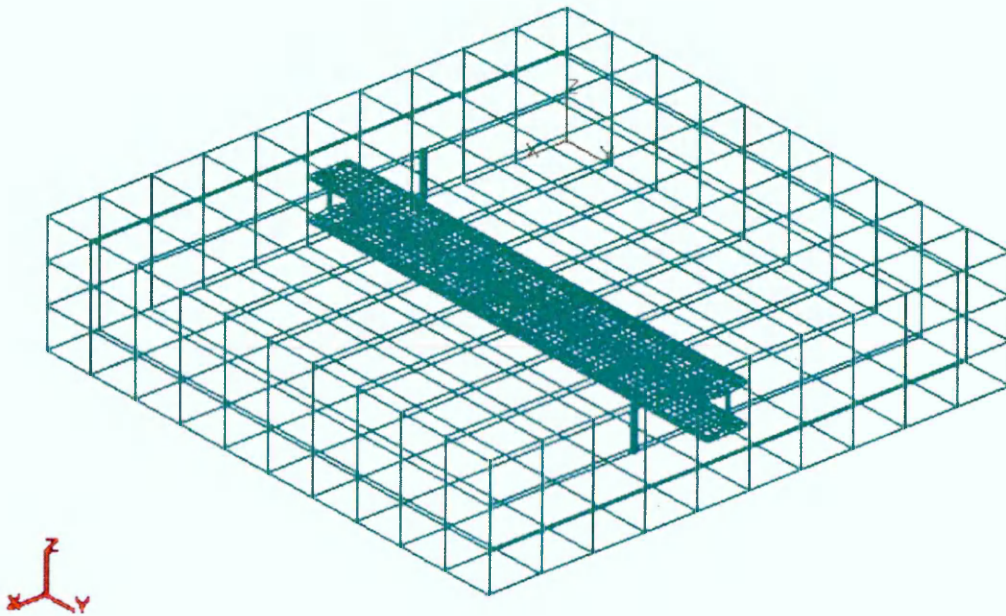


Figure 6.31: Schematic representation of the total boundary element mesh for ICCP System B

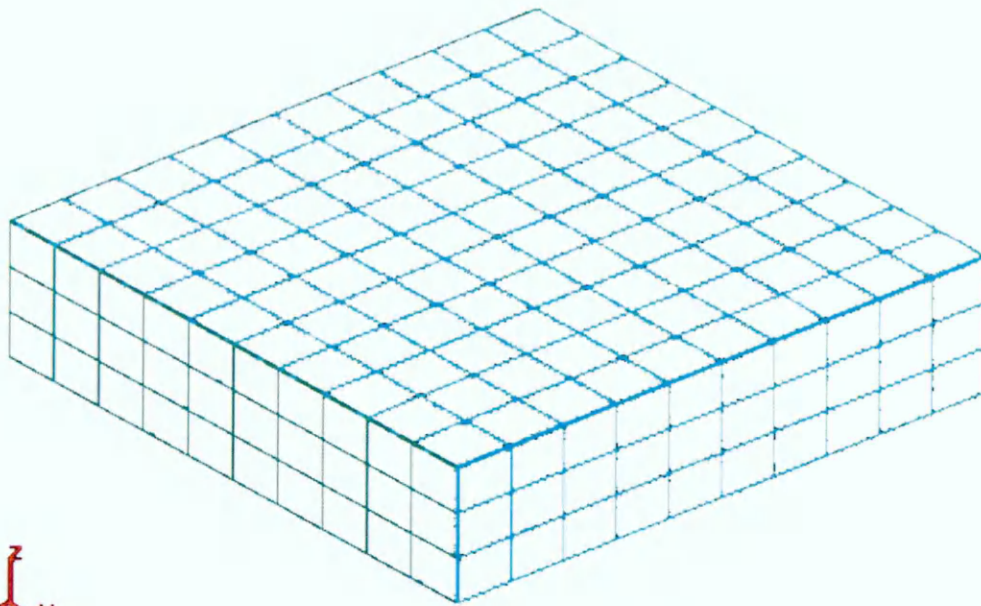


Figure 6.32: Schematic representation of the boundary element mesh on the surface of sandbox for ICCP System B

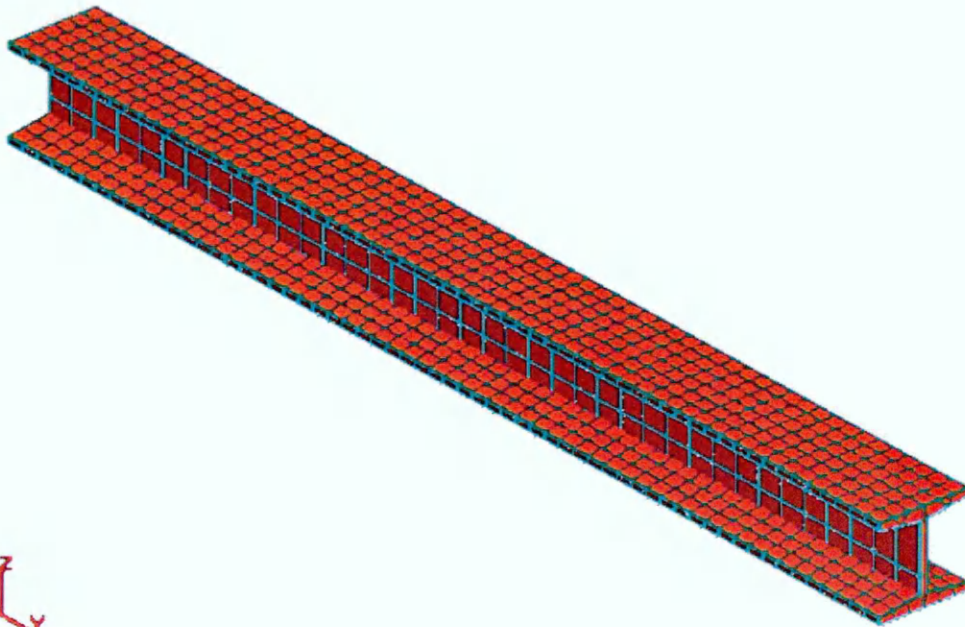


Figure 6.33: Schematic representation of the boundary element mesh on the surface of Steel Section B of ICCP System B

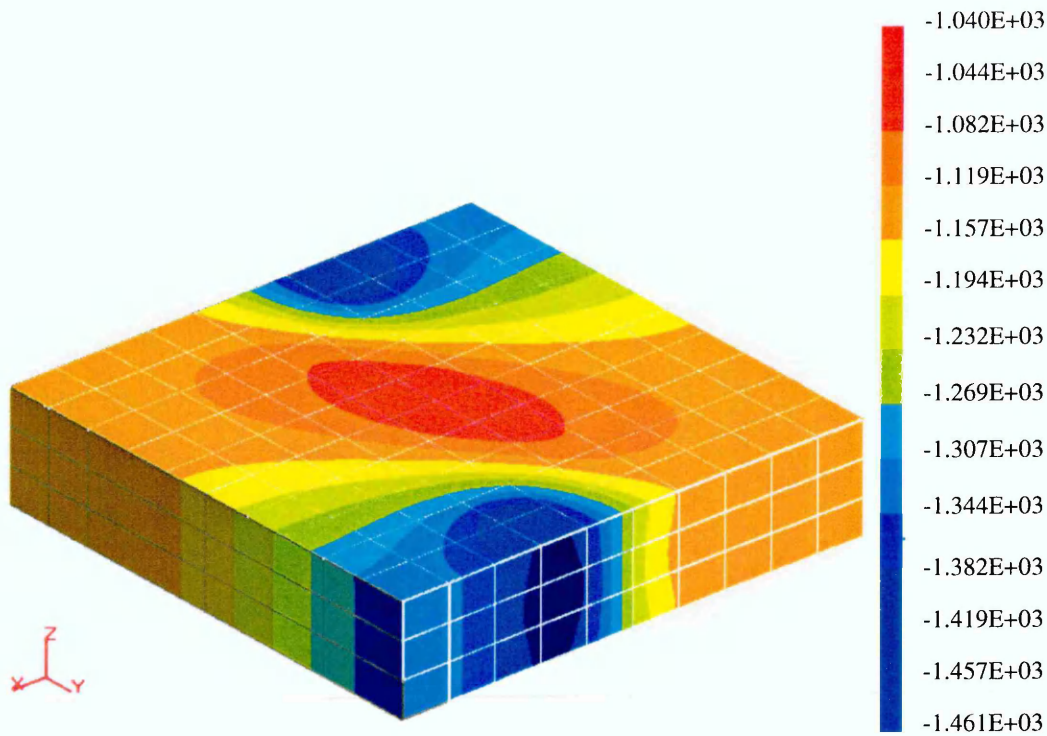


Figure 6.34: Potential distributions on the surface of sandbox of ICCP System B (mV, vs CSE)

- The applied current density at the anode: $1.60 \times 10^{-2} \text{ mA/cm}^2$.
- The average value of sand resistivity: $42.32 \text{ K } \Omega\text{-cm}$.
- The anode coordinates:

Anode A: the bottom coordinate of the anode axis is $P_1 (X_1=36.2\text{cm}, Y_1=10.0\text{cm}, Z_1=6.0\text{cm})$ and the top coordinate is $P_2 (X_2=36.2\text{cm}, Y_2=10.0\text{cm}, Z_2=16.0\text{cm})$

Anode B: the bottom coordinate of the anode axis is $P_3 (X_3=63.8\text{cm}, Y_3=90.0\text{cm}, Z_3=6.0\text{cm})$ and the top coordinate is $P_4 (X_4=63.8\text{cm}, Y_4=90.0\text{cm}, Z_4=16.0\text{cm})$

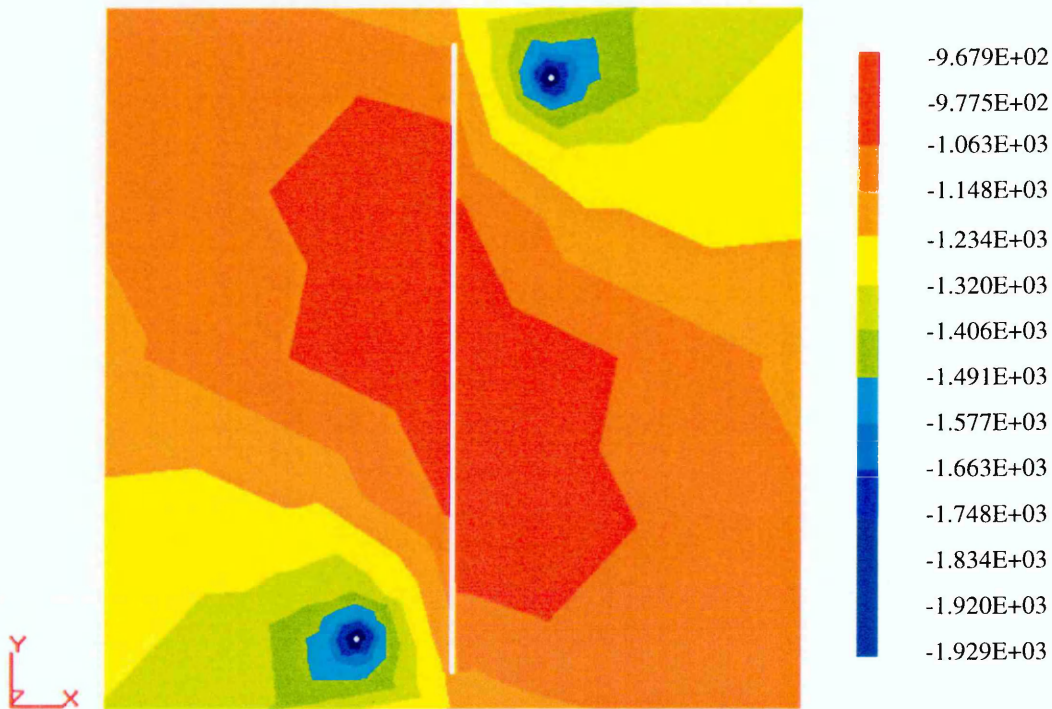


Figure 6.35: Potential distribution at Z=11.0cm of ICCP System B (mV, vs SCE)

- The applied current density at the anode: $1.60 \times 10^{-2} \text{ mA/cm}^2$.
- The average value of sand resistivity: 42.32 K -cm.
- The anode coordinates:

Anode A: the bottom coordinate of the anode axis is P_1 ($X_1=36.2\text{cm}$, $Y_1=10.0\text{cm}$, $Z_1=6.0\text{cm}$) and the top coordinate is P_2 ($X_2=36.2\text{cm}$, $Y_2=10.0\text{cm}$, $Z_2=16.0\text{cm}$)

Anode B: the bottom coordinate of the anode axis is P_3 ($X_3=63.8\text{cm}$, $Y_3=90.0\text{cm}$, $Z_3=6.0\text{cm}$) and the top coordinate is P_4 ($X_4=63.8\text{cm}$, $Y_4=90.0\text{cm}$, $Z_4=16.0\text{cm}$)

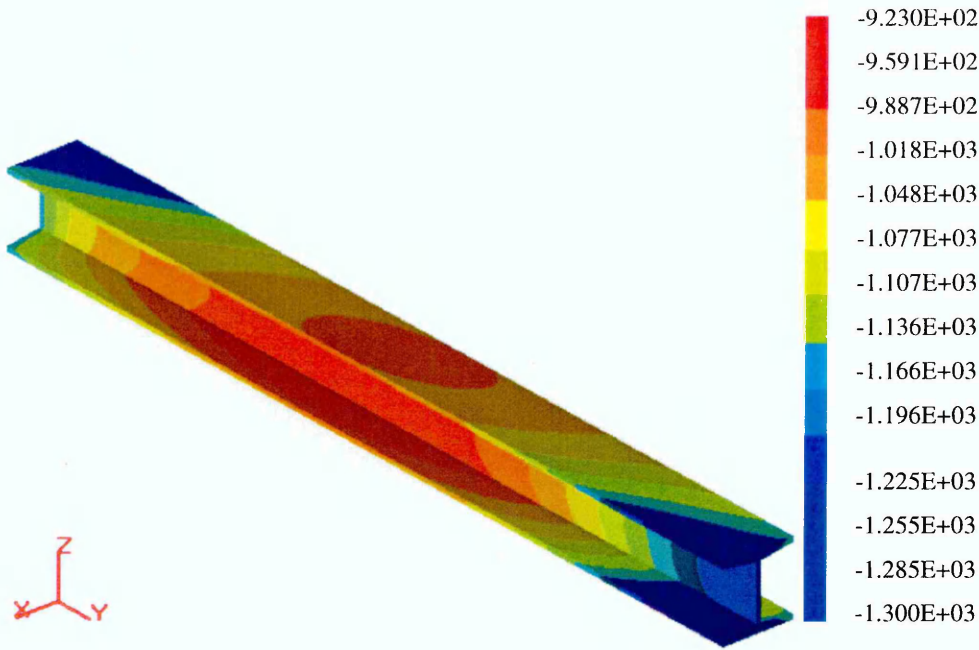


Figure 6.36: Potential distribution on the surface of Steel Section B of ICCP System B (mV, vs CSE)

- The applied current density at the anode: $1.60 \times 10^{-2} \text{mA/cm}^2$.
- The average value of sand resistivity: 42.32 K -cm.
- The anode coordinates:

Anode A: the bottom coordinate of the anode axis is P_1 ($X_1=36.2\text{cm}$, $Y_1=10.0\text{cm}$, $Z_1=6.0\text{cm}$) and the top coordinate is P_2 ($X_2=36.2\text{cm}$, $Y_2=10.0\text{cm}$, $Z_2=16.0\text{cm}$)

Anode B: the bottom coordinate of the anode axis is P_3 ($X_3=63.8\text{cm}$, $Y_3=90.0\text{cm}$, $Z_3=6.0\text{cm}$) and the top coordinate is P_4 ($X_4=63.8\text{cm}$, $Y_4=90.0\text{cm}$, $Z_4=16.0\text{cm}$)



Figure 6.37 Details of potential distribution on ZY plane of steel (mV) (the potential values are the same as in Figure 6.36)

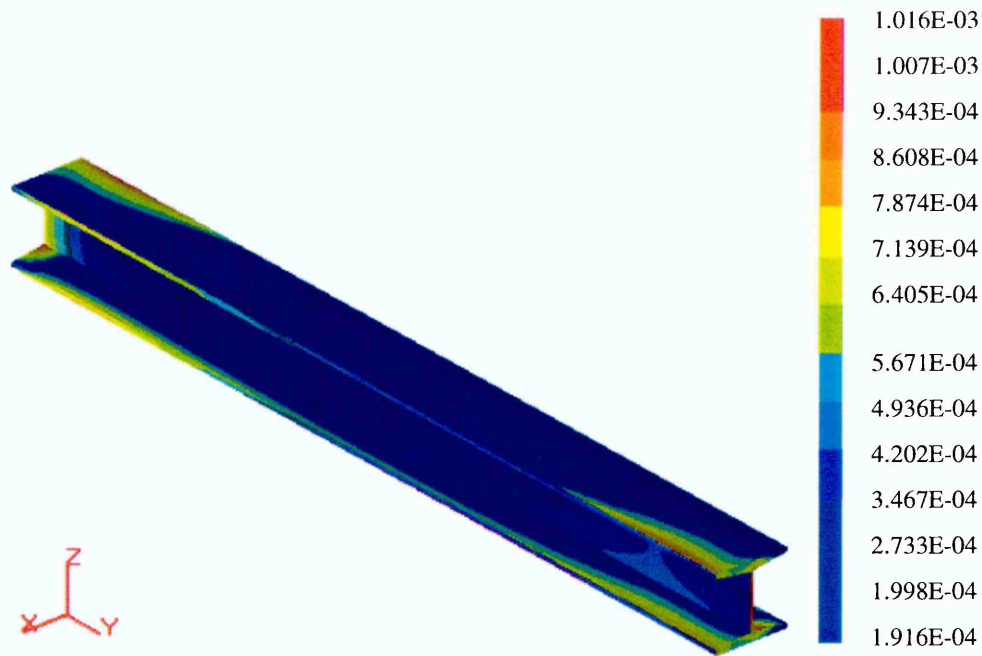


Figure 6.38: Current distribution on the surface of Steel Section B of ICCP System B (mA)

- The applied current density at the anode: $1.60 \times 10^{-2} \text{ mA/cm}^2$.
- The average value of sand resistivity: 42.32 K Ω -cm.
- The anode coordinates:

Anode A: the bottom coordinate of the anode axis is P_1 ($X_1=36.2\text{cm}$, $Y_1=10.0\text{cm}$, $Z_1=6.0\text{cm}$) and the top coordinate is P_2 ($X_2=36.2\text{cm}$, $Y_2=10.0\text{cm}$, $Z_2=16.0\text{cm}$)

Anode B: the bottom coordinate of the anode axis is P_3 ($X_3=63.8\text{cm}$, $Y_3=90.0\text{cm}$, $Z_3=6.0\text{cm}$) and the top coordinate is P_4 ($X_4=63.8\text{cm}$, $Y_4=90.0\text{cm}$, $Z_4=16.0\text{cm}$)

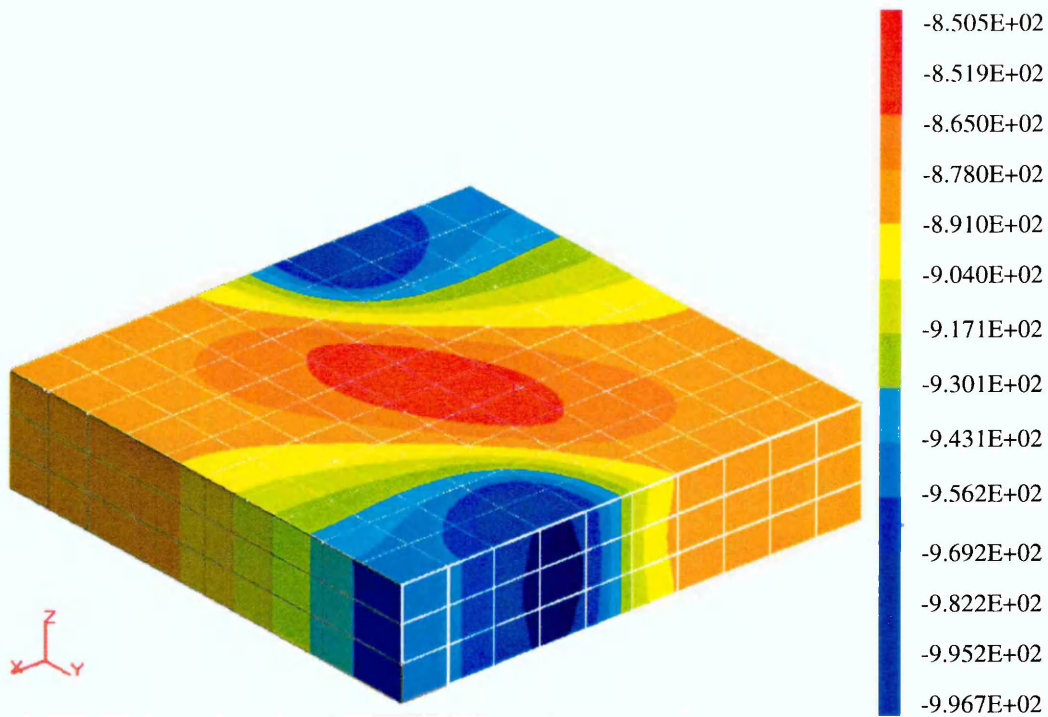


Figure 6.39: Potential distribution on the surface of sandbox of ICCP System B (mV, vs CSE)

- The applied current density at the anode: $1.60 \times 10^{-2} \text{ mA/cm}^2$.
- The average value of sand resistivity: 14.61 K -cm.
- The anode coordinates:

Anode A: the bottom coordinate of the anode axis is $P_1 (X_1=36.2\text{cm}, Y_1=10.0\text{cm}, Z_1=6.0\text{cm})$ and the top coordinate is $P_2 (X_2=36.2\text{cm}, Y_2=10.0\text{cm}, Z_2=16.0\text{cm})$

Anode B: the bottom coordinate of the anode axis is $P_3 (X_3=63.8\text{cm}, Y_3=90.0\text{cm}, Z_3=6.0\text{cm})$ and the top coordinate is $P_4 (X_4=63.8\text{cm}, Y_4=90.0\text{cm}, Z_4=16.0\text{cm})$

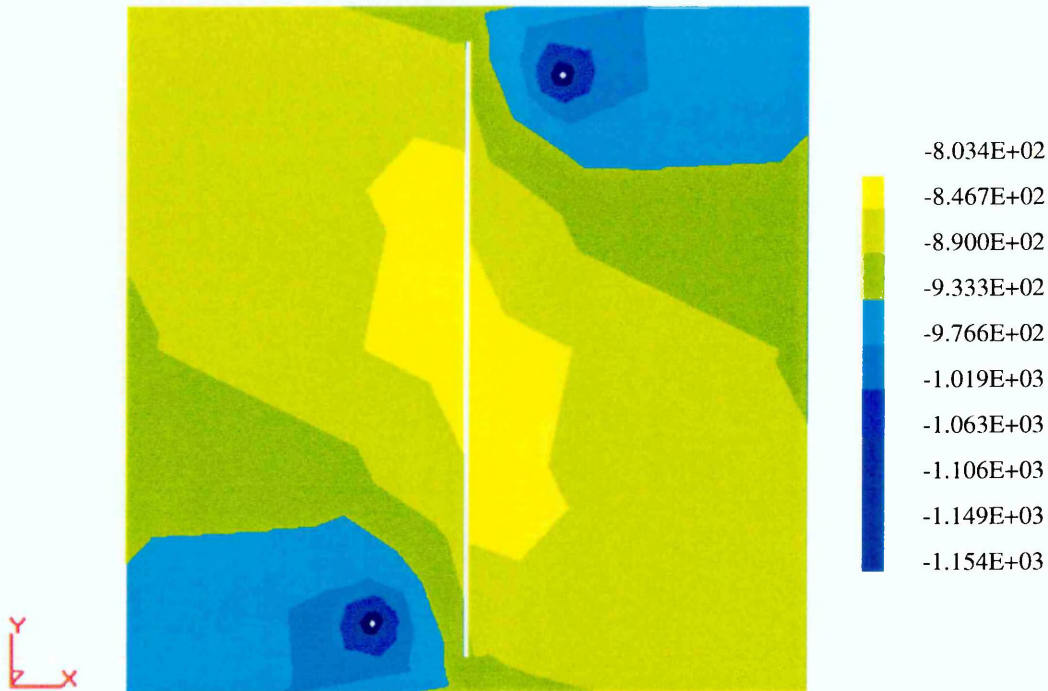


Figure 6.40: Potential distribution at Z=11.0cm of ICCP System B (mV, vs CSE)

- The applied current density at the anode: $1.60 \times 10^{-2} \text{ mA/cm}^2$.
- The average value of sand resistivity: 14.61 K -cm.
- The anode coordinates:

Anode A: the bottom coordinate of the anode axis is P_1 ($X_1=36.2\text{cm}$, $Y_1=10.0\text{cm}$, $Z_1=6.0\text{cm}$) and the top coordinate is P_2 ($X_2=36.2\text{cm}$, $Y_2=10.0\text{cm}$, $Z_2=16.0\text{cm}$)

Anode B: the bottom coordinate of the anode axis is P_3 ($X_3=63.8\text{cm}$, $Y_3=90.0\text{cm}$, $Z_3=6.0\text{cm}$) and the top coordinate is P_4 ($X_4=63.8\text{cm}$, $Y_4=90.0\text{cm}$, $Z_4=16.0\text{cm}$)

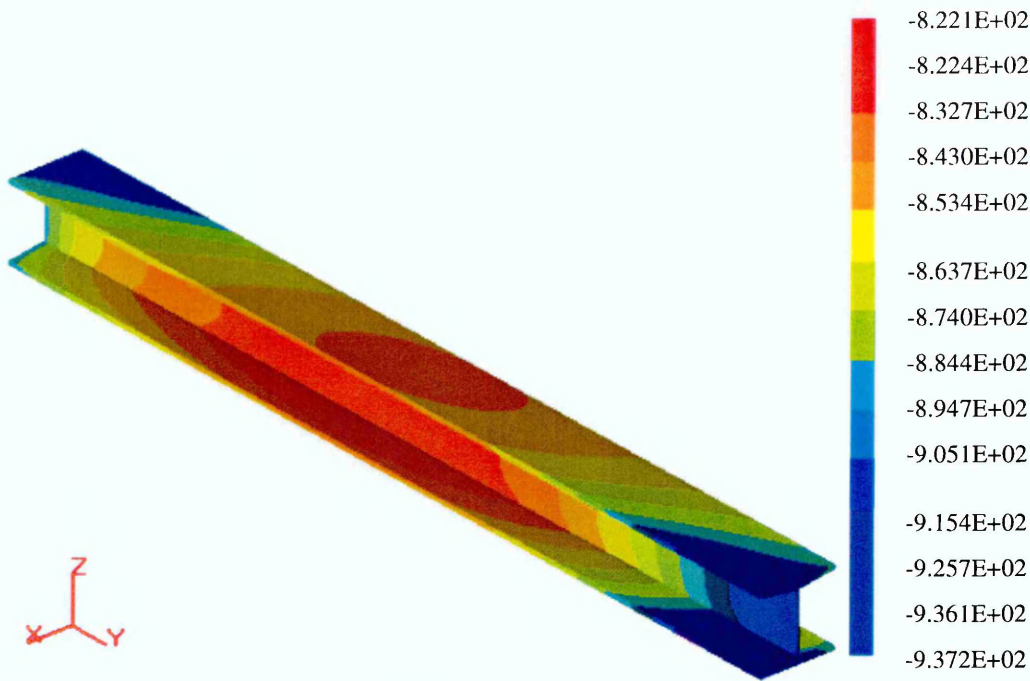


Figure 6.41: Potential distribution on the surface of Steel Section B of ICCP System B (mV, vs CSE)

- The applied current density at the anode: $1.60 \times 10^{-2} \text{mA/cm}^2$.
- The average value of sand resistivity: 14.61 K Ω -cm.
- The anode coordinates:

Anode A: the bottom coordinate of the anode axis is P_1 ($X_1=36.2\text{cm}$, $Y_1=10.0\text{cm}$, $Z_1=6.0\text{cm}$) and the top coordinate is P_2 ($X_2=36.2\text{cm}$, $Y_2=10.0\text{cm}$, $Z_2=16.0\text{cm}$)

Anode B: the bottom coordinate of the anode axis is P_3 ($X_3=63.8\text{cm}$, $Y_3=90.0\text{cm}$, $Z_3=6.0\text{cm}$) and the top coordinate is P_4 ($X_4=63.8\text{cm}$, $Y_4=90.0\text{cm}$, $Z_4=16.0\text{cm}$)



Figure 6.42: Details of the potential distribution on ZY plane of steel of ICCP System B (mV) (potential values are the same as Figure 6. 41)

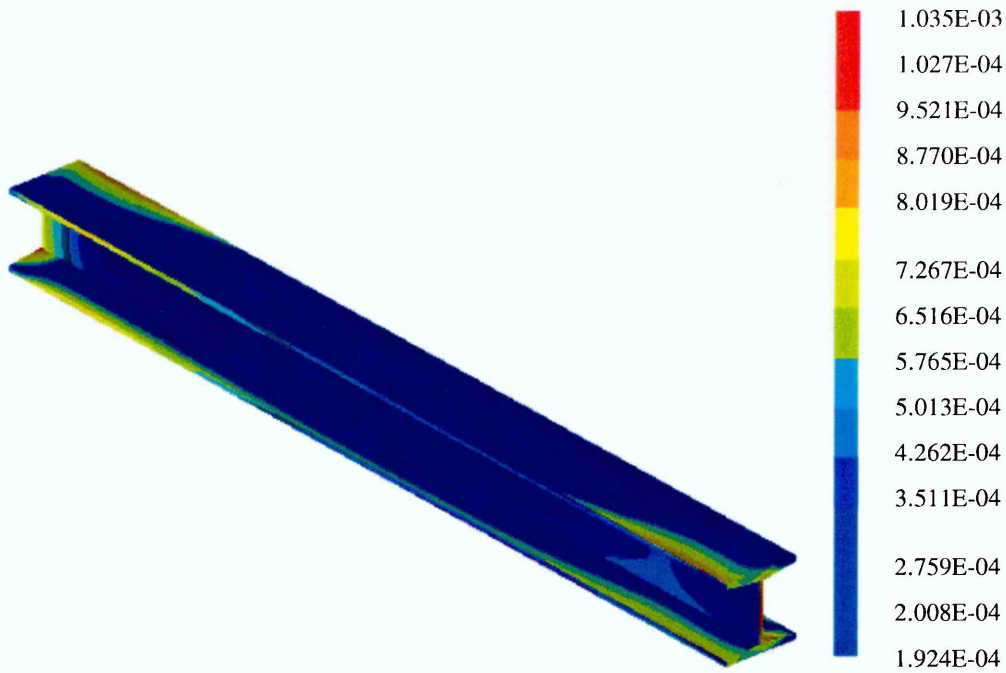


Figure 6.43: Current distribution on the surface of Steel Section B of ICCP System B (mA)

- The applied current density at the anode: $1.60 \times 10^{-2} \text{mA/cm}^2$.
- The average value of sand resistivity: 14.61 K Ω -cm.
- The anode coordinates:

Anode A: the bottom coordinate of the anode axis is P_1 ($X_1=36.2\text{cm}$, $Y_1=10.0\text{cm}$, $Z_1=6.0\text{cm}$) and the top coordinate is P_2 ($X_2=36.2\text{cm}$, $Y_2=10.0\text{cm}$, $Z_2=16.0\text{cm}$)

Anode B: the bottom coordinate of the anode axis is P_3 ($X_3=63.8\text{cm}$, $Y_3=90.0\text{cm}$, $Z_3=6.0\text{cm}$) and the top coordinate is P_4 ($X_4=63.8\text{cm}$, $Y_4=90.0\text{cm}$, $Z_4=16.0\text{cm}$)

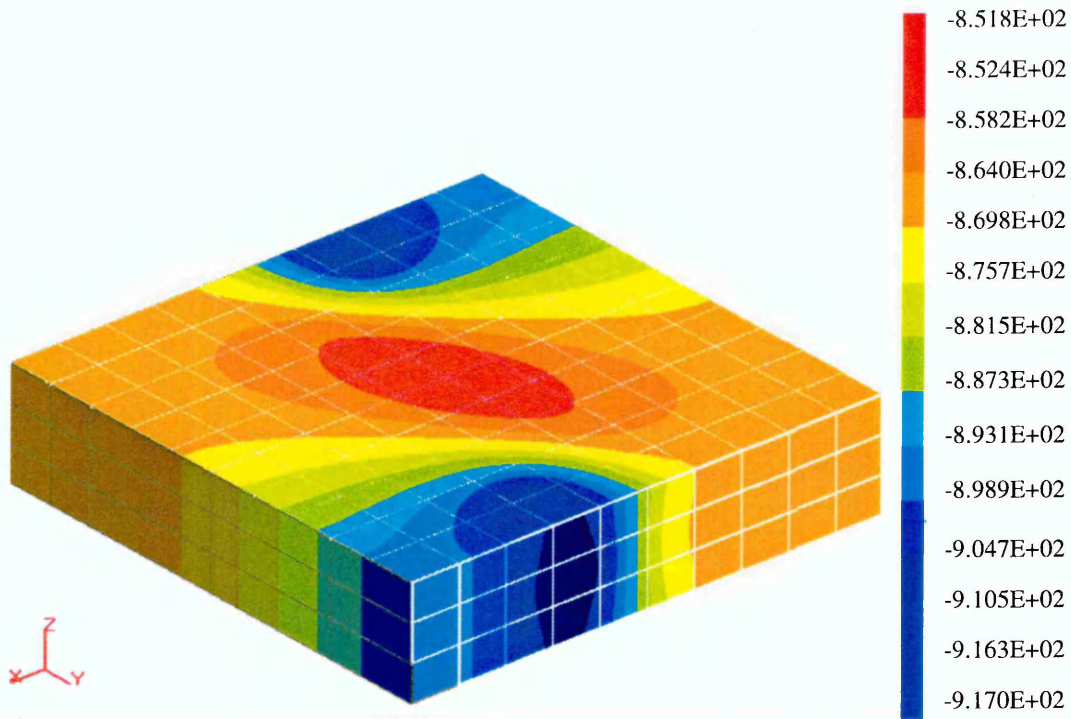


Figure 6.44 : Potential distribution on the surface of sandbox of ICCP System B (mV, vs CSE)

- The applied current density at the anode: $1.60 \times 10^{-2} \text{ mA/cm}^2$.
- The average value of sand resistivity: 6.41 K Ω -cm.
- The anode coordinates:

Anode A: the bottom coordinate of the anode axis is P_1 ($X_1=36.2\text{cm}$, $Y_1=10.0\text{cm}$, $Z_1=6.0\text{cm}$) and the top coordinate is P_2 ($X_2=36.2\text{cm}$, $Y_2=10.0\text{cm}$, $Z_2=16.0\text{cm}$)

Anode B: the bottom coordinate of the anode axis is P_3 ($X_3=63.8\text{cm}$, $Y_3=90.0\text{cm}$, $Z_3=6.0\text{cm}$) and the top coordinate is P_4 ($X_4=63.8\text{cm}$, $Y_4=90.0\text{cm}$, $Z_4=16.0\text{cm}$)

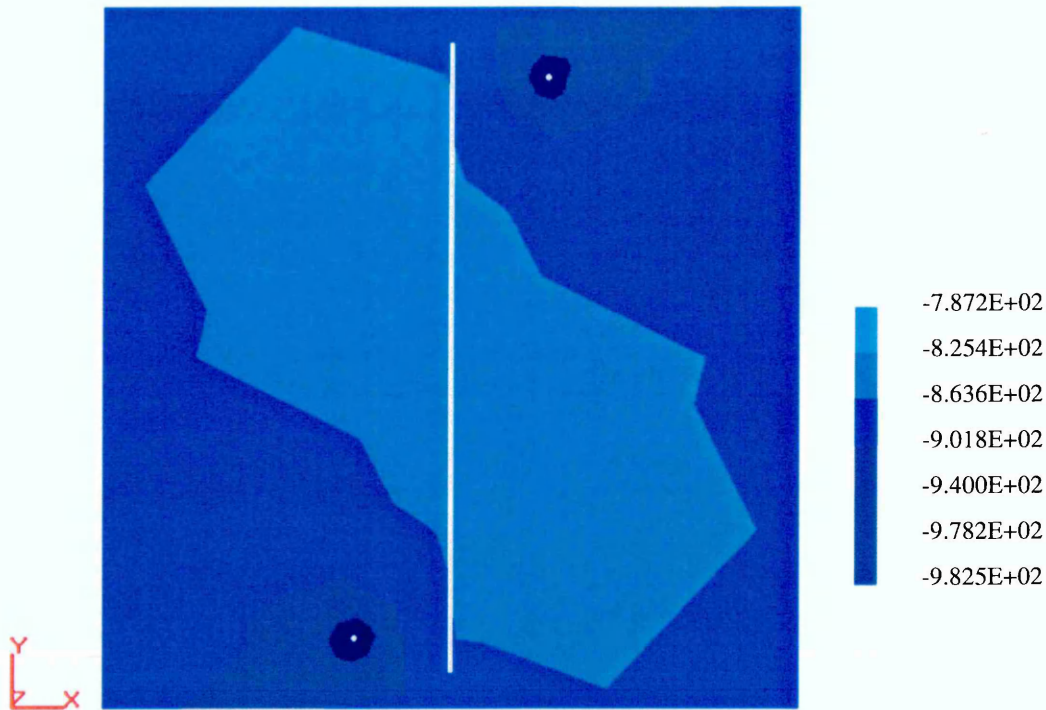


Figure 6.45: Potential distribution at Z=11.0cm of ICCP System B (mV, vs CSE)

- The applied current density at the anode: $1.60 \times 10^{-2} \text{mA/cm}^2$.
- The average value of sand resistivity: 6.41 K Ω -cm.
- The anode coordinates:

Anode A: the bottom coordinate of the anode axis is P₁ (X₁=36.2cm, Y₁=10.0cm, Z₁=6.0cm) and the top coordinate is P₂ (X₂=36.2cm, Y₂=10.0cm, Z₂=16.0cm)

Anode B: the bottom coordinate of the anode axis is P₃ (X₃=63.8cm, Y₃=90.0cm, Z₃=6.0cm) and the top coordinate is P₄ (X₄=63.8cm, Y₄=90.0cm, Z₄=16.0cm)

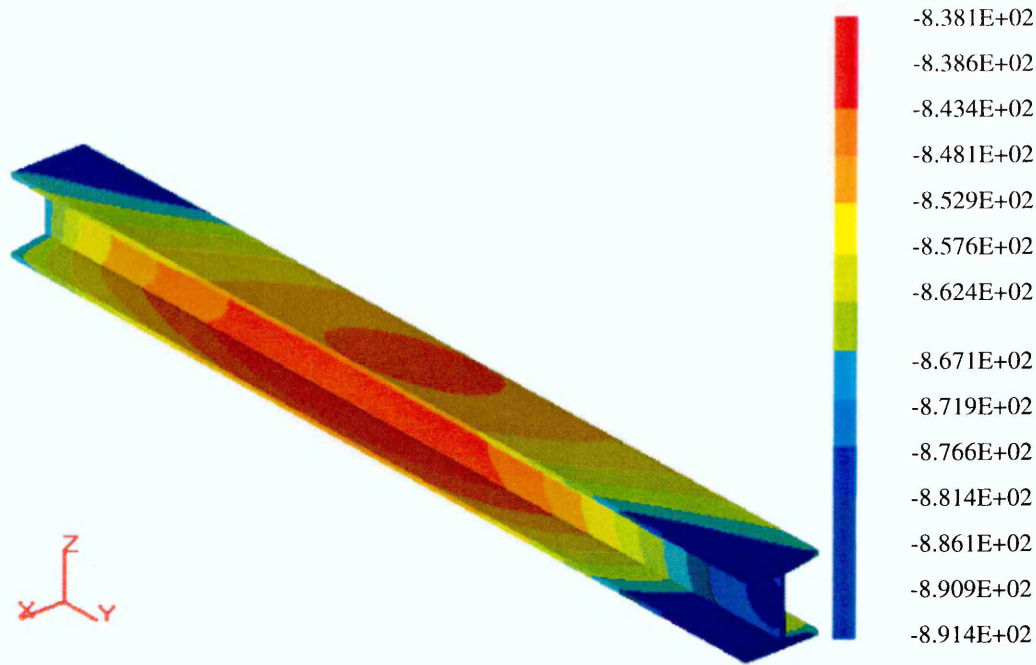


Figure 6.46: Potential distribution on the surface of Steel Section B of ICCP System B (mV, vs CSE)

- The applied current density at the anode: $1.60 \times 10^{-2} \text{mA/cm}^2$.
- The average value of sand resistivity: 6.41 K Ω -cm.
- The anode coordinates:

Anode A: the bottom coordinate of the anode axis is P_1 ($X_1=36.2\text{cm}$, $Y_1=10.0\text{cm}$, $Z_1=6.0\text{cm}$) and the top coordinate is P_2 ($X_2=36.2\text{cm}$, $Y_2=10.0\text{cm}$, $Z_2=16.0\text{cm}$)

Anode B: the bottom coordinate of the anode axis is P_3 ($X_3=63.8\text{cm}$, $Y_3=90.0\text{cm}$, $Z_3=6.0\text{cm}$) and the top coordinate is P_4 ($X_4=63.8\text{cm}$, $Y_4=90.0\text{cm}$, $Z_4=16.0\text{cm}$)



Figure 6.47: Details of potential distribution on ZY plane of steel of ICCP System B (mV) (potential values same as in Figure 6. 46)

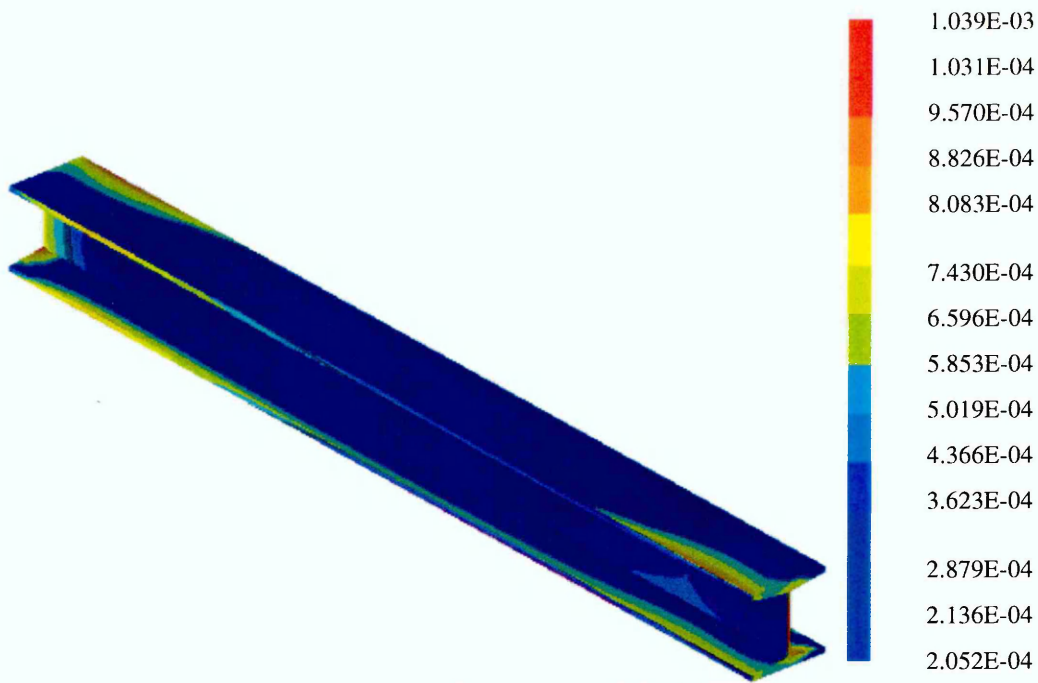


Figure 6.48: Current distribution on the surface of Steel Section B of ICCP System B (mA)

- The applied current density at the anode: $1.60 \times 10^{-2} \text{mA/cm}^2$.
- The average value of sand resistivity: 6.41 K Ω -cm.
- The anode coordinates:

Anode A: the bottom coordinate of the anode axis is P_1 ($X_1=36.2\text{cm}$, $Y_1=10.0\text{cm}$, $Z_1=6.0\text{cm}$) and the top coordinate is P_2 ($X_2=36.2\text{cm}$, $Y_2=10.0\text{cm}$, $Z_2=16.0\text{cm}$)

Anode B: the bottom coordinate of the anode axis is P_3 ($X_3=63.8\text{cm}$, $Y_3=90.0\text{cm}$, $Z_3=6.0\text{cm}$) and the top coordinate is P_4 ($X_4=63.8\text{cm}$, $Y_4=90.0\text{cm}$, $Z_4=16.0\text{cm}$)

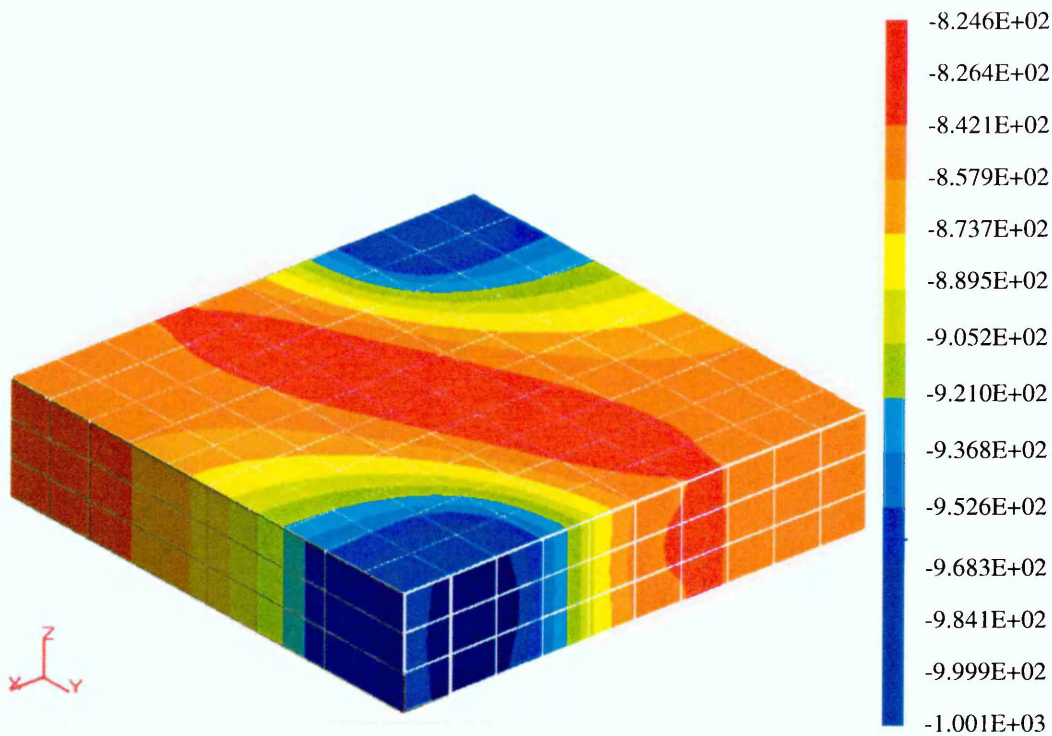


Figure 6.49: Potential distribution on the surface of sandbox of ICCP System B (mV, vs. CSE)

- The applied current density at the anode: $1.60 \times 10^{-2} \text{ mA/cm}^2$.
- The average value of sand resistivity: 14.61 K Ω -cm.
- The anode coordinates:

Anode A: the bottom coordinate of the anode axis is P_5 ($X_5=21.2\text{cm}$, $Y_5=10.0\text{cm}$, $Z_5=6.0\text{cm}$) and the top coordinate is P_6 ($X_6=21.2\text{cm}$, $Y_6=10.0\text{cm}$, $Z_6=16.0\text{cm}$)

Anode B: the bottom coordinate of the anode axis is P_7 ($X_7=78.8\text{cm}$, $Y_7=90.0\text{cm}$, $Z_7=6.0\text{cm}$) and the top coordinate is P_8 ($X_8=78.8\text{cm}$, $Y_8=90.0\text{cm}$, $Z_8=16.0\text{cm}$)

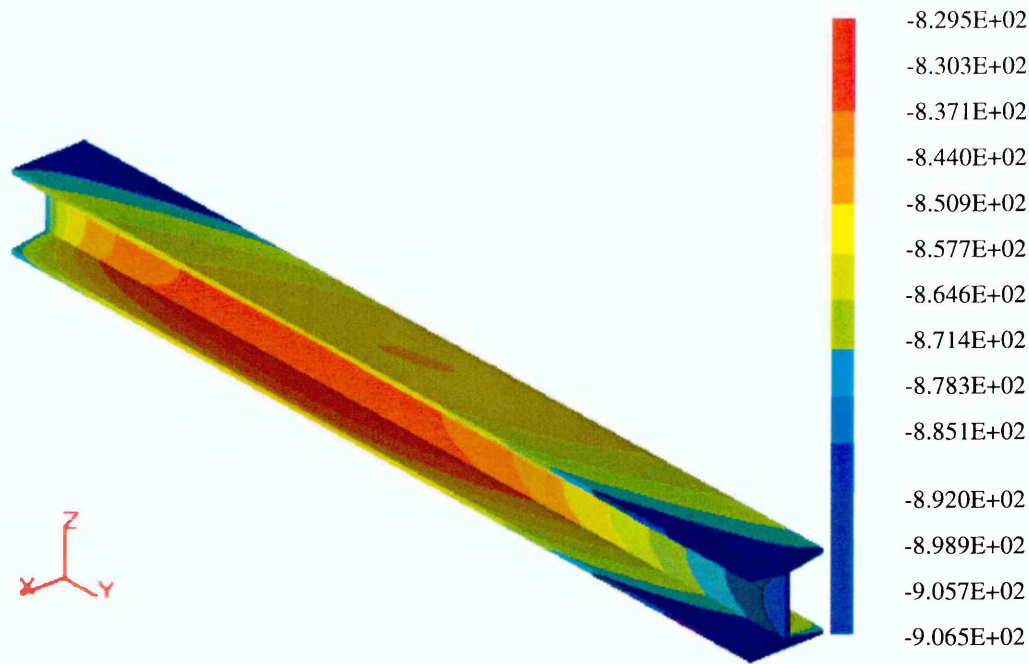


Figure 6.50: Potential distribution on the surface of Steel Section B of ICCP System B (mV, vs. CSE)

- The applied current density at the anode: $1.60 \times 10^{-2} \text{mA/cm}^2$.
- The average value of sand resistivity: 14.61 K Ω -cm.
- The anode coordinates:

Anode A: the bottom coordinate of the anode axis is P_5 ($X_5=21.2\text{cm}$, $Y_5=10.0\text{cm}$, $Z_5=6.0\text{cm}$) and the top coordinate is P_6 ($X_6=21.2\text{cm}$, $Y_6=10.0\text{cm}$, $Z_6=16.0\text{cm}$)

Anode B: the bottom coordinate of the anode axis is P_7 ($X_7=78.8\text{cm}$, $Y_7=90.0\text{cm}$, $Z_7=6.0\text{cm}$) and the top coordinate is P_8 ($X_8=78.8\text{cm}$, $Y_8=90.0\text{cm}$, $Z_8=16.0\text{cm}$)

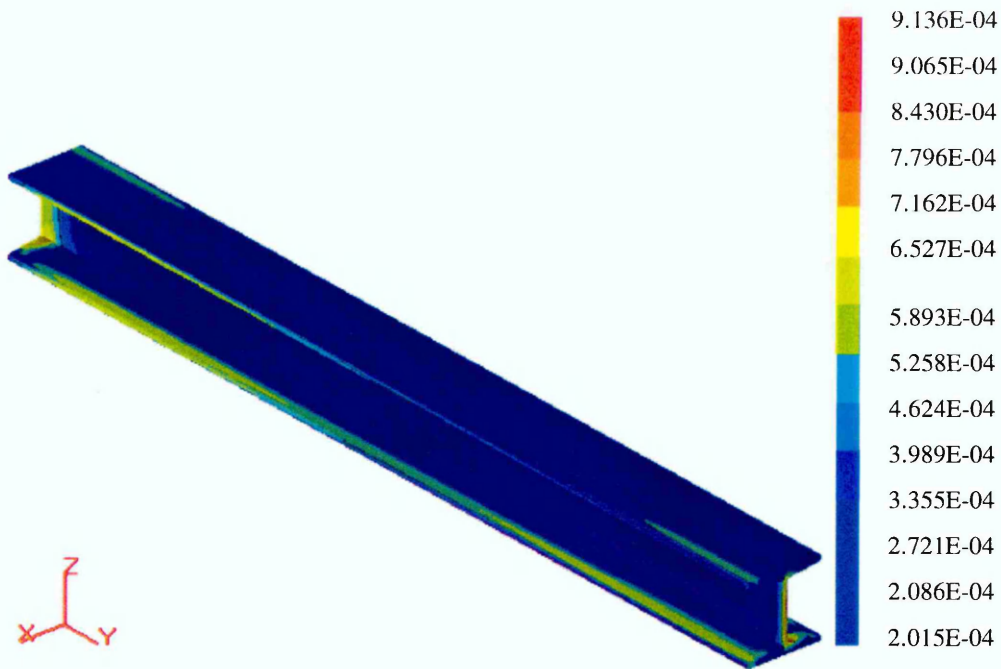


Figure 6.51: Current distribution on the surface of Steel Section B
ICCP System B (mA)

- The applied current density at the anode: $1.60 \times 10^{-2} \text{ mA/cm}^2$.
- The average value of sand resistivity: 14.61 K Ω -cm.
- The anode coordinates:

Anode A: the bottom coordinate of the anode axis is P_5 ($X_5=21.2\text{cm}$, $Y_5=10.0\text{cm}$, $Z_5=6.0\text{cm}$) and the top coordinate is P_6 ($X_6=21.2\text{cm}$, $Y_6=10.0\text{cm}$, $Z_6=16.0\text{cm}$)

Anode B: the bottom coordinate of the anode axis is P_7 ($X_7=78.8\text{cm}$, $Y_7=90.0\text{cm}$, $Z_7=6.0\text{cm}$) and the top coordinate is P_8 ($X_8=78.8\text{cm}$, $Y_8=90.0\text{cm}$, $Z_8=16.0\text{cm}$)

6.4 Modelling Results and Discussion

6.4.1 The Effect of Resistivity on Potential & Current Density Distribution

For ICCP System A, the potential and current density distributions are shown in Figures 6.13 to 6.30. For ICCP System B, the potential and current density distributions are shown in Figures 6.34 to 6.51. Under the conditions of the same applied current density and the same anode coordinate, Figures 6.15, 6.19, 6.23, 6.36, 6.41 and 6.46 indicate that a higher electrolyte resistivity results in a less negative protective potential on the surface of steel section.

It also is clear that a higher resistivity of electrolyte results in a lower protective current density on the surface of steel piece which is illustrated in Figures 6.16, 6.20, 6.24, 6.38, 6.43 and 6.48. Therefore, for a higher resistivity electrolyte, a higher applied current density is needed to maintain the protective potential at any set level.

It should be noted that there is a significant variation of protective potential and current density in different regions of the steel surface. This variation is related to not only the resistivity of sand but also the geometry of steel section.

Analysis of the results shows that the distribution of the protective potential and current density is more uniform in low resistivity of sand compared with a high resistivity under the same conditions of applied current density and the same anode coordinates.

6.4.2 Relationship between Potential Distribution and Anode Location

In this section, the relationship between potential / current density distribution and anode location has been studied. For ICCP System A, the bottom coordinate of the anode axis is moved to P_3 ($X_3=50.0\text{cm}$, $Y_3=15.0\text{cm}$, $Z_3=6.0\text{cm}$) and the top coordinate is P_4 ($X_4=50.0\text{cm}$, $Y_4=15.0\text{cm}$, $Z_4=16.0\text{cm}$). Finally, the bottom coordinate of the anode axis is P_5 ($X_5=35.0\text{cm}$, $Y_5=52.8\text{cm}$, $Z_5=6.0\text{cm}$) and the top coordinate is changed to P_6 ($X_6=35.0\text{cm}$, $Y_6=52.8\text{cm}$,

$Z_6=16.0\text{cm}$). The results of modelling are shown in Figures 6.25 to 6.30 for 14.61 K Ω .cm sand.

For ICCP System B, the anodes have been moved to the following locations. For Anode A, the bottom coordinate of the anode axis is P_5 ($X_5=21.2\text{cm}$, $Y_5=10.0\text{cm}$, $Z_5=6.0\text{cm}$) and the top coordinate is P_6 ($X_6=21.2\text{cm}$, $Y_6=10.0\text{cm}$, $Z_6=16.0\text{cm}$). For Anode B, the bottom coordinate of the anode axis is P_7 ($X_7=78.8\text{cm}$, $Y_7=90.0\text{cm}$, $Z_7=6.0\text{cm}$) and the top coordinate is P_8 ($X_8=78.8\text{cm}$, $Y_8=90.0\text{cm}$, $Z_8=16.0\text{cm}$).

The results are given in Figure 6.49 to 6.51 for a 14.61 K Ω .cm sand.

As can be seen from these plots, the potential and current density distributions along the surface of steel section is more uniform as the anode distance from the steel increases. Therefore, the positioning of the anodes in an ICCP system is fundamental to achieve an adequate level of protection over the entire structure.

6.4.3 Comparison of Boundary Element Modelling with the Experiments and Discussion

The results of the boundary element modelling in Figures 6.17 and 6.28 are compared with the experimental measurements in Figures 6.8 and 6.9. It is shown that there is good agreement between the experimental measurement and the calculation of the boundary element method. However, there are some differences between them, as discussed below. The cause for this variation could be related to one or all of the following three reasons:

- The resistivity of sand: In boundary element modelling, the sand resistivity is assumed to be uniform and have the same value. But, in reality, the sand resistivity will not be precisely the same in each experiment and there will be some variation between different areas of the sandbox.
- The polarisation curves: The experimentally measured polarisation curves may contain some inaccuracies. As the most important factor in

the determination of boundary condition on the steel section, any errors or variations could result in such differences.

- The formation of a passive film: It is possible that formation of a passive film on steel section has varying kinetics during the process of cathodic protection.

The above reasons all probably exist to some extent and are not readily avoided. However, the results indicate that the boundary element method can provide sufficient accurate results to make it an effective tool for modelling such complex problems.

6.5 Conclusions

From the work carried out in the chapter, the following conclusions have been obtained:

- The distributions of CP potential and current density are related to the resistivity of electrolyte. The higher resistivity, the lower protective potential of steel at a given current.
- The anode position has a significant effect on the distribution of CP potential and current density.
- Boundary element modelling shows significant promise as a practical tool for analysing and optimising the design of cathodic protection system for steel framed masonry structures.

From this it can be concluded that a boundary element approach may be adopted for the modelling and design of cathodic protection systems for steel framed structures.

Chapter 7:

Effect of Brick Type and Joints Width on

CP Current and Potential Distribution

7.1 Introduction

Chapter 6 studied the distribution of the CP current and potential on the steel surface in a sandbox, on the assumption that the electrolyte (sand) was homogeneous and the resistivity of the sand throughout the sandbox remained the same. The results of that study showed that the CP current and potential distribution on the steel surface are related to the anode locations and sand resistivity for any given anode current density.

However, the resistivities of most masonry materials are much higher than the mortars employed in steel-framed masonry structures. The specific resistivities of the various masonry materials such as brick and Portland stone are also different. As a result, any area of low resistivity may be expected to "attract" a higher current density, with current flowing preferentially along the path of least resistance, as shown in Figure 7.1 [Roberge, 1999].

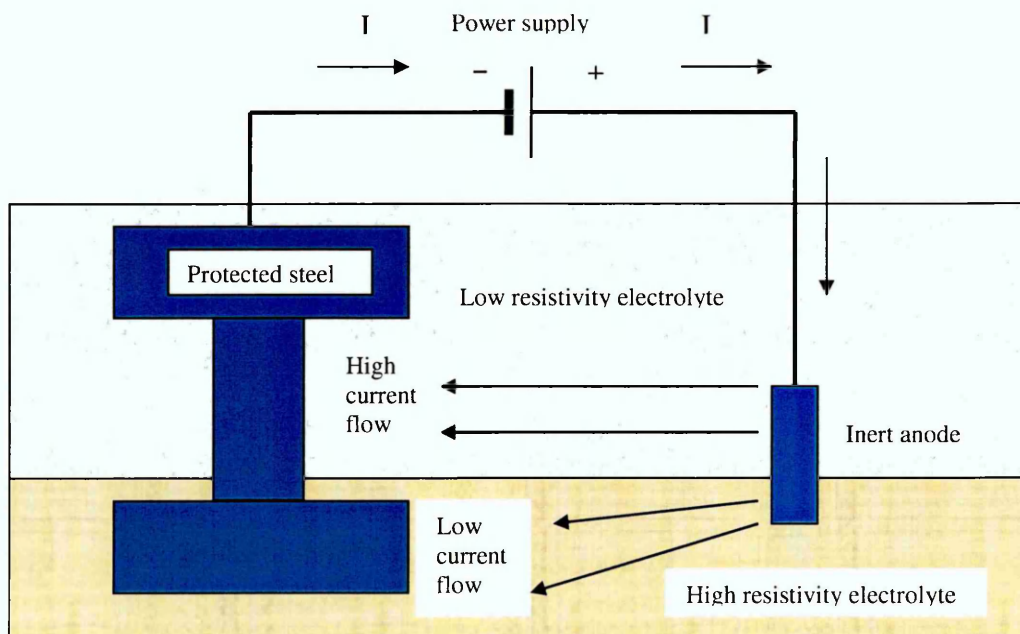


Figure 7.1 Non-uniform current distribution.

Therefore, the purpose of the work described in this chapter is to study the influence of masonry type and joint width on the CP current and potential. The work involves both experimental measurements and boundary element modelling. To complete this element of the work, a discussion and conclusion are also included.

7.2 Test Set-up

7.2.1 Basic Components

The basic components of an impressed current cathodic protection system have been described in Section 6.2.1. In the present study, a representative ICCP system has been set up so as to investigate the effect of masonry type, in this case bricks, and joints width on CP current and potential. The basic components of this system are as follows:

- DC power supply unit: A CPI manual power supply system, supplied by Cathodic Protection International Aps.
- Discrete anodes: Two discrete anodes, 10mm diameter X 100mm length, (Ebonex anodes or titanium oxide) manufactured by Fosroc.
- Steel section (cathode): An ' I ' form mild steel section has been selected as the cathode. Its dimensions are shown Figure 7.2.
- Mortar: A simple cement-lime mortar with mix proportions (by weight) of 1:2:9 (Cement: Lime: Sand) and a water/cement ratio of 0.5.
- Masonry: In the present test, fired clay 'common' brick is used. The nominal dimensions of each brick are 215mm length x 102.5mm width x 65mm height.

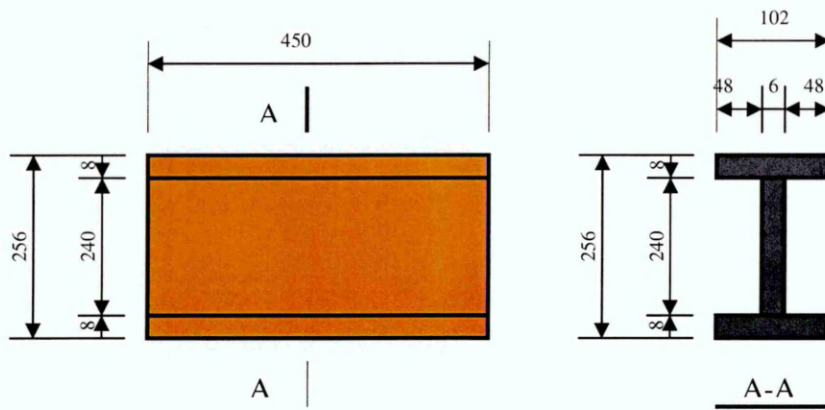


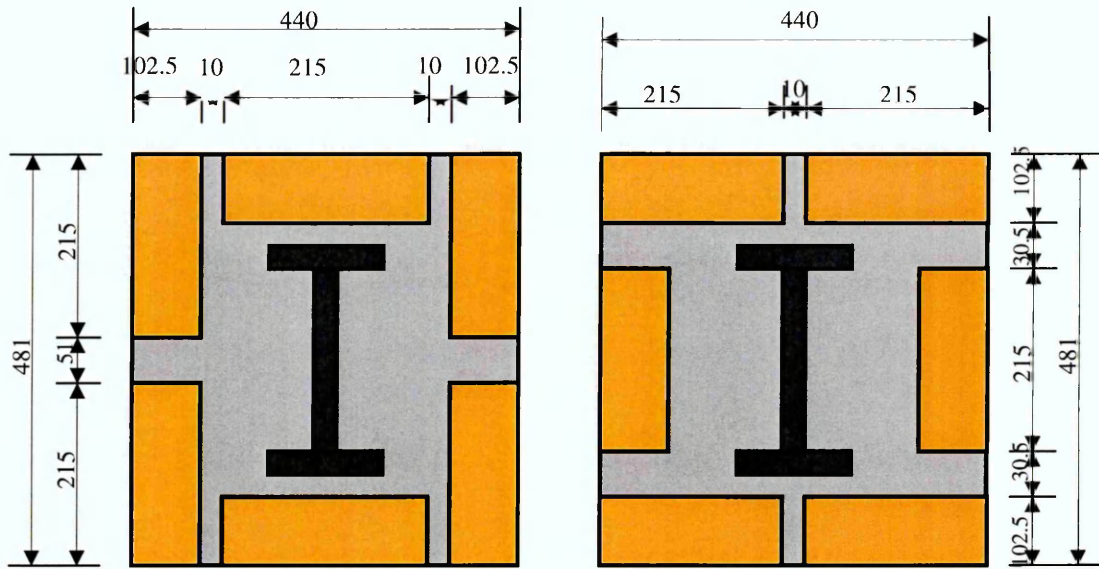
Figure 7.2: Steel section (unit: mm)

7.2.2 Test Specimen

A test specimen, 440mm width x 481mm length x 450mm height, was constructed for this study. The materials used were as described in Section 7.2.1. The details of the test specimen are illustrated in Figure 7.3.

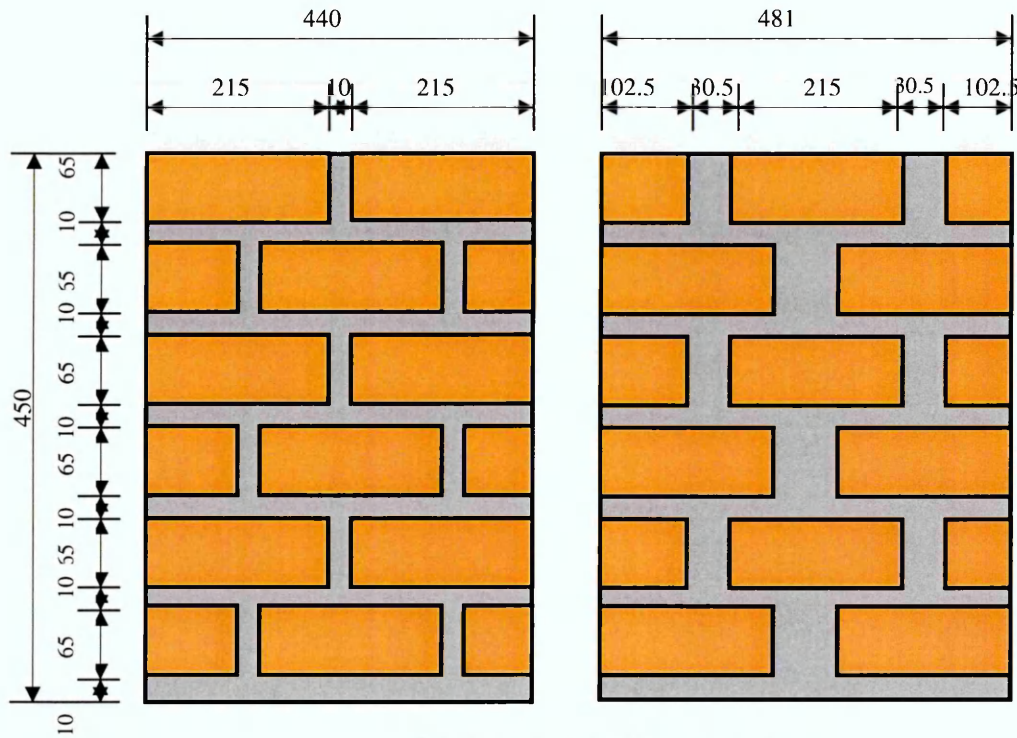
Two discrete anodes, each 10mm diameter x 100mm length, were used independently to provide the protection current. They were located between the 3rd and 4th course. Their locations are illustrated in Figure 7.4. Their coordinates are illustrated in Section 7.4.2.

To evaluate cathodic protection levels, an embedded monitoring probe (embeddable silver/silver chloride/potassium chloride reference electrode) was installed in the test specimen. The distance between the electrode axis and the steel surface is 5mm, as shown in Figure 7.4. After construction, the test specimen was cured at a constant 20°C and relative humidity of 60% for two weeks.



(a) 1st, 3rd and 5th courses

(b) 2nd, 4rd and 6th courses



(c) Height of test specimen

Figure 7.3: Layout of brick and dimension of test specimen (unit: mm)

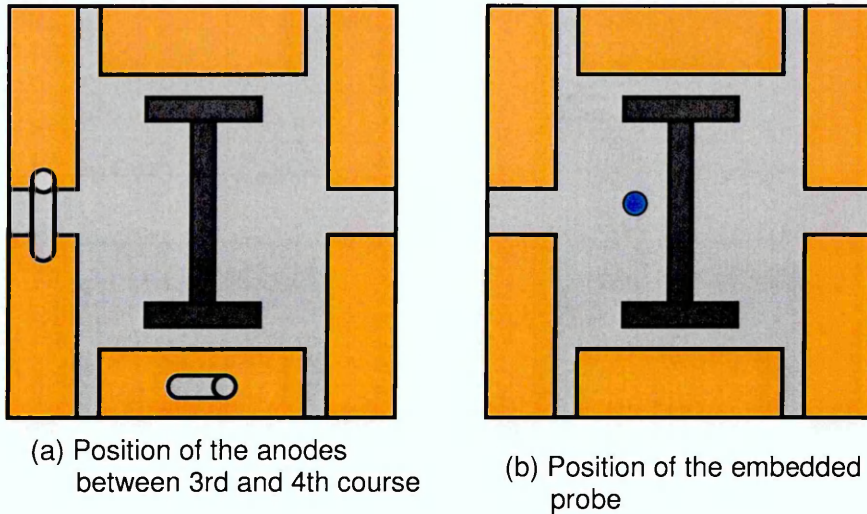


Figure 7.4: Plane view of position of the anodes (a) and embedded probe (b)

7.2.3 Resistivity of Test Specimen

There is significant variability between the resistivity of the bricks and the mortar in the test specimen. The resistivity measurements in this study were used to investigate their effect on CP protective current and potential distribution.

For the measurement of brick resistivity, two holes each 5mm diameter and 5mm in depth were drilled into the side of the brick. A commercially available 'Scribe' hand-held resistivity meter, which has 2 probes with a spacing of 50mm, was then employed to measure the resistivity.

Two methods were used for measuring the resistivity of the mortar. The first one, which is the same as the measurements for the bricks, was employed to measure the resistivity of joints mortar. The second one, which was described in Section 5.3.1, was used for measuring the resistivity of the mortar

surrounding the steel section (cathode). For this measurement, four holes 8mm diameter by 100mm depth were drilled vertically down into the top course (6th course). The spacing of between the holes was 100mm. The process measurement has previously been described in Section 5.3.1.

It should be noted that the measurement of resistivity must be carried out with the protection current switched off to avoid any interference by the CP current.

7.2.4 Installation of CP System and Power Supply

The completed CP system is shown in Figures 7.5 and 7.6.

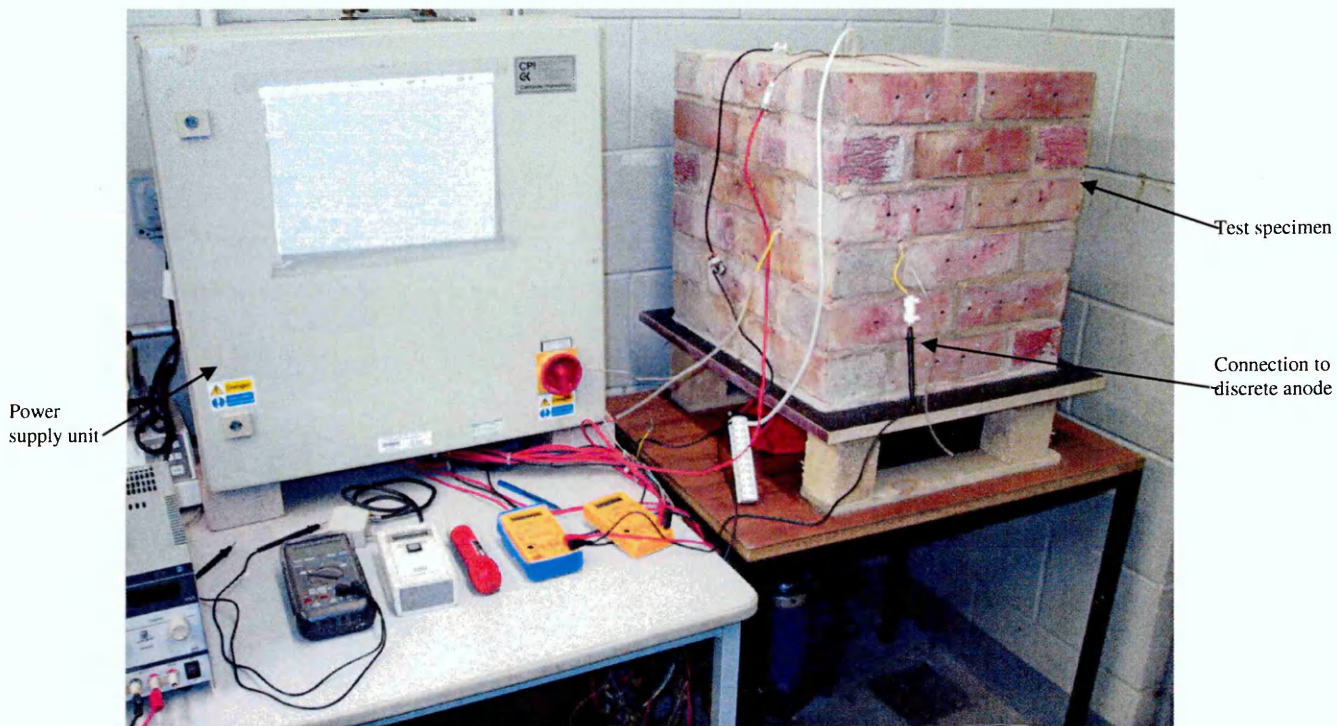


Figure 7.5: Experimental set-up of ICCP system



Figure 7.6: Test specimen plan view of ICCP system

Typically, such systems may be operated under constant current, constant voltage or potential control. In the present study, the CP system operated on a constant voltage basis, so the output current varies to suit the changes in polarisation response of steel surface and the resistivity of the bricks and mortar. The value of the constant output voltage was maintained at 7.23 V. The initial value of the output current was 8.172 mA.

7.2.5 Measurement of Protective Potential

The potential distribution on a grid of free surface of the test specimen was measured under a range of test conditions, including variations in brick and masonry resistivity and output current, by means of a hand-held potential measurement electrode, in this case a copper/copper sulphate electrode (CSE).

However, potential values obtained in this manner with the protection current on do not represent the actual potentials on the surface of steel section due to the IR_{Ω} value (IR drop). In order to obtain values of IR_{Ω} -free CP protective potential on the surface of steel section the instant-off potential method was employed, as previously described. As the steel section has a relatively complex geometry, it is not possible to accurately measure every point potential on the steel surface. Due to this limitation, only the protective potentials at selected points of steel were measured.

Table 7.1: Protective potential on steel surface

Conditions	Constant temperature					20 ⁰ C		
	Relative humidity					60%		
	Average resistivity of mortar					9.00 K Ω .cm		
	Average resistivity of brick					95.00 K Ω .cm		
	Anode axis locations (X, Y, Z) cm:					Right (X=-5, Y=42.975, Z=23). Left (X=5, Y=42.975, Z=23).		
	Applied current density on the anodes					4.20X10 ⁻² mA/cm ²		
Coordinates	(0,36.85,5)	(0,36.85,10)	(0,36.85,15)	(0,36.85,20)	(0,36.85,25)	(0,36.85,30)	(0,36.85,35)	(0,36.85,40)
Potential(V) vs. CSE	-0.74	-0.81	-0.92	-1.12	-1.33	-1.12	-0.86	-0.81

Table 7.1 lists the measured potential values of the steel surface on the line in which the planes X=0.00 cm and Y= 36.85 cm cross. The measured conditions are as follows:

- Average value of mortar resistivity: 9.00 KΩ.cm.
- Average value of brick resistivity: 95.00 KΩ.cm.
- Anode axis locations (X, Y, Z) cm: Right (X=-5, Y=42.975, Z=23).
Left (X=5, Y=42.975, Z=23).
- Applied current density on the anodes: 4.20×10^{-2} mA/cm².

The above resistivity of mortar and brick were determined by measurement, as described in Section 7.2.3. The results show the resistivity of both the mortar and individual bricks are fairly constant within themselves, as a consequence only the average values of resistivity are listed for each material. It should be noted that mortar has a significantly lower resistivity than that of the surrounding brick, which is up to ten times greater.

7.3 Monitoring of the CP System

As described in Section 7.2.2, the cathodic protection levels were evaluated by the embedded monitoring probe. The 'on' potential at the location of the probe could therefore be monitored at any time during the tests. The potential applied to the steel surface adjacent to the monitoring probe was measured by the instant off potential method at different times during the test period, starting from the initial application of power.

7.3.1 Modelling of Boundary Element of ICCP System

In Chapter 6 the boundary element method was employed to analyze the distribution of CP current and potential in two representative ICCP systems where the electrolyte was an isotropic or homogeneous electrolyte. The results show the boundary element modelling demonstrates significant

promise as a practical tool for analysing and optimising the design of such cathodic protection systems.

The boundary element method for multi-regions, as discussed in Section 4.6, was used to analyze the distribution of the CP current and potential of the masonry encased ICCP system as shown in Figure 7.5.

7.4 Discussion of Boundary Conditions

General boundary conditions for cathodic protection system have been discussed in Section 4.4. However, for an impressed current cathodic system in a multi-regional electrolyte as considered in this chapter, there are significant differences when compared to a single region as studied in Chapter 6. As such, the boundary conditions for such a system requires further consideration.

As discussed in Section 4.6, the test specimen is divided into sub-regions or zones.

The boundary conditions on these sub-regions or zones are described as follows:

- (i) On the free surface and insulating surfaces, the normal current density is equal to zero:

$$k \frac{\partial E}{\partial n} = 0 \quad (6.1)$$

- (ii) At any point on the anode surface, the normal current density has a constant value i_a :

$$k \frac{\partial E}{\partial n} = i_a \quad (6.2)$$

As an alternative to defining the normal current density at an anode, the potential at an anode can be defined as a constant:

$$E = E_a \quad (6.3)$$

It should be noted that the ICCP system is evaluated under steady-state conditions. The anode is not treated as a charge source but as a fixed boundary condition. In this approach the current level of an anode is fixed and no variation is allowed. However, under real conditions the current level at an anode will vary with time and operating conditions during the life of the ICCP system. Therefore, separate solutions must be performed for various times during the life of the system when this approach is taken.

(iii) The normal current density at any point on the steel section (cathode) is:

$$i_c = f_c(E_c) \quad (6.4)$$

This is the same as equation (4.22). It is the experimentally determined polarisation curves which describes the non-linear relationship between the potential and the current density on the cathode surface or the cathode electrode kinetics.

The measurement of polarisation curves of steel in lime mortar under the conditions of different resistivities have previously been described in Chapter 5. The results obtained are directly applicable to the present modelling.

- (iv) For each sub-region, the conditions of compatibility and equilibrium potentials and current density between the common interfaces are used. These were expressed in Equations (4.25) and (4.26).

7.4.1 Boundary Element Analysis

As described above, this is a multi-regional problem. The theory and applications of the boundary element method for such problems has been described and discussed in Section 4.6. Here it is used to analyze the laboratory brick-encased test CP system.

The resistivities of the mortar and bricks has been obtained by direct measurement. The results of these measurements show:

- The mortar has a significantly lower resistivity than that of the surrounding brick.
- The resistivity at different locations in the mortar is similar.
- The resistivity of each brick is similar.

So the whole of the mortar bed can reasonably be modelled as a zone. Each brick can also be modelled as a separate zone. There are therefore thirty-four zones in the test specimen. This appears to be a very complex problem. However, in the present work, the system is symmetrical in the $X=0$ and $Y=0$ directions. By simplifying the model in this manner it is possible to save computation time and memory requirements. Therefore, in this simplified model only twenty-two zones need to be incorporated.

The system is firstly analyzed under the following two cases which is symmetrical in the $X=0$ direction:

Case 1:

- Average value of mortar resistivity: 9.00 KΩ.cm.
- Average value of brick resistivity: 95.00 KΩ.cm.
- Anode axis locations (X, Y, Z) cm: Right (X=-5, Y=18.925, Z=23).
Left (X=5, Y=18.925, Z=23).
- Applied current density on the anodes: 4.20×10^{-2} mA/cm².

Case 2:

- Average value of mortar resistivity: 7.00 KΩ.cm.
- Average value of brick resistivity: 90.00 KΩ.cm.
- Anode axis locations (X, Y, Z) cm: Right (X=-5, Y=18.925, Z=23).
Left (X=5, Y=18.925, Z=23).
- Applied current density on the anodes: 4.50×10^{-2} mA/cm².

On completion of these two cases the anode is moved to the following location for further analysis which is symmetrical in the Y=0 direction.

Case 3:

- Average value of mortar resistivity: 9.00 KΩ.cm.
- Average value of brick resistivity: 95.00 KΩ.cm.
- Anode axis locations (X, Y, Z) cm: Right (X =16.875, Y=-5, Z=23).
Left (X=16.875, Y=5, Z=23).
- Applied current density on the anodes: 4.20×10^{-2} mA/cm².

For Case 1 and Case 2, the total boundary element mesh used for the analysis is shown in Figure 7.7. For clarity, the boundary element mesh on the surface of mortar, brick and steel test specimen is shown in Figures 7.8, 7.9 and 7.10. The modelling results and discussion are given in Section 7.4.2.

For Case 3, the total boundary element mesh used for the analysis is shown in Figure 7.23. For clarity, the boundary element mesh on the surface of the mortar, brick and steel test specimen is shown in Figures 7.24, 7.25 and 7.26. The modelling results and discussion are given in Section 7.4.3.

7.4.2 Modelling Results and Discussion

For Case 1, the potential and current density distributions are illustrated in Figures to 7.16. For Case 2, the results of the modelling are shown in Figures 7.17 to 7.22. Figures 7.27 to 7.32 show the results of the modelling in Case 3.

Figure 7.13 (Case 1), Figure 7.19 (Case 2) and Figure 7.29 (Case 3) show that there is a significant range in the potential distribution between the maximum and minimum values on the steel surface which is up to 48.75 %, 48.53 % and 40.2%, respectively. Similarly, the change of current density distribution is also large. The range of the difference between maximum and minimum values is 88.58 % (Case 1), 89.43% (Case 2) and 87.31% (Case 3). Therefore, it is apparent that, for this sample arrangement, the distribution of potential and current density on the surface of steel is noticeably non-uniform.

Figures 7.15 and 7.16 (Case 1), Figures 7.21 and 7.22 (Case 2), and Figures 7.31 and 7.32 illustrate the potential distribution in the electrolyte (brick and mortar). It can be seen that the potential distribution in the electrolyte is not

continuous. This may be due to the differences in resistivity between the brick and mortar having an effect on the distribution of potential and current density throughout the whole electrolyte. A further discussion of this effect is in Section 7.4.3.

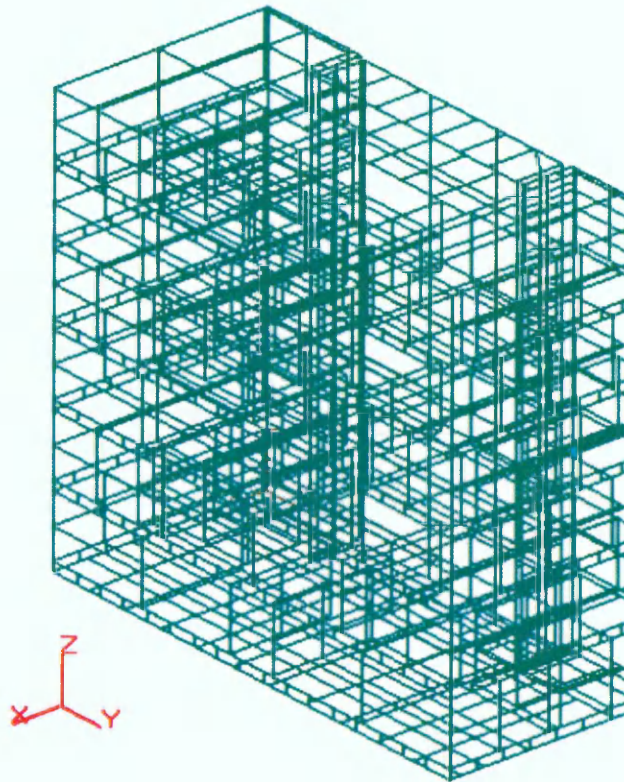


Figure 7.7: Schematic representation of the total boundary element mesh on the surface of the encased specimen (Case 1 and Case 2)

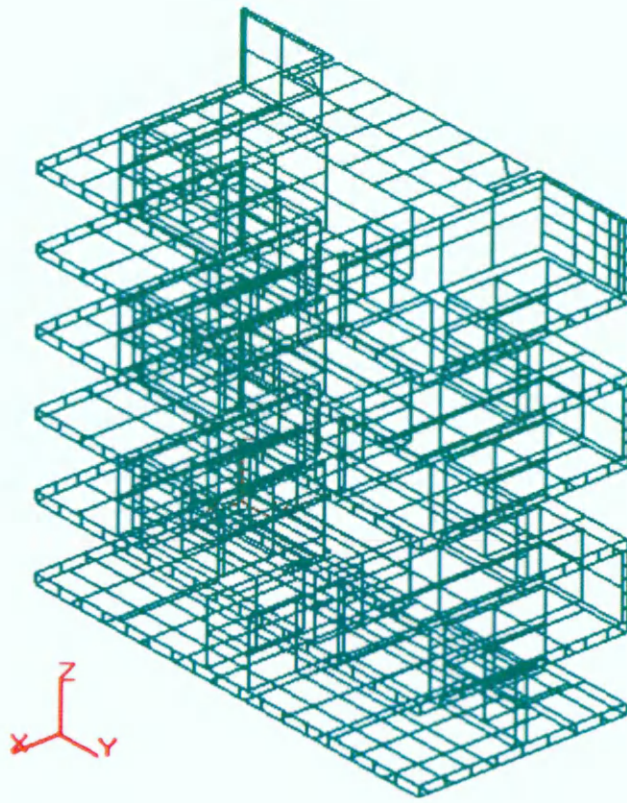


Figure 7.8 Schematic representation of the boundary element mesh for the mortar beds (Case 1 and Case 2)

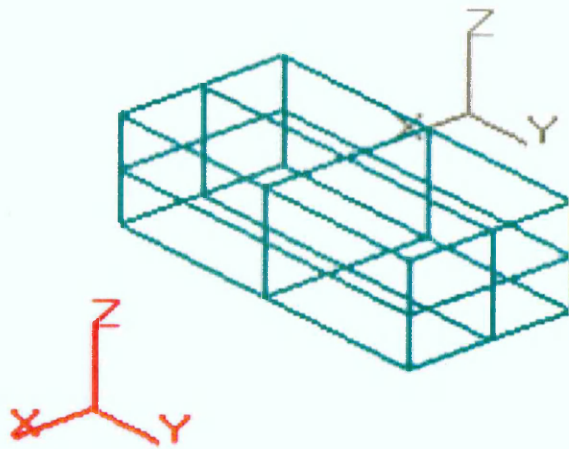


Figure 7.9: Schematic representation of the boundary element mesh on the surface of each brick (Case 1 and Case 2)

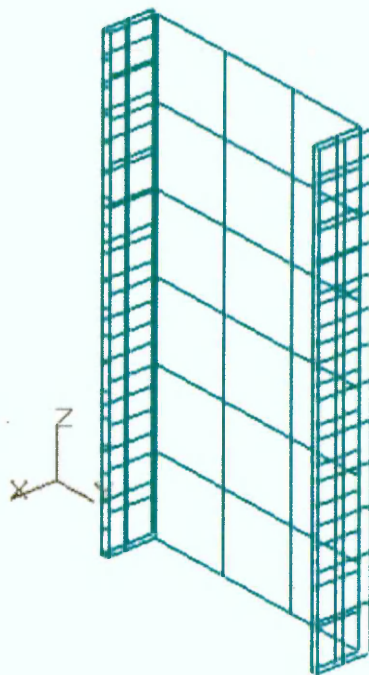


Figure 7.10: Schematic representation of the boundary element mesh on the surface of steel section (Case 1 and Case 2, symmetric in plane $X=0$)

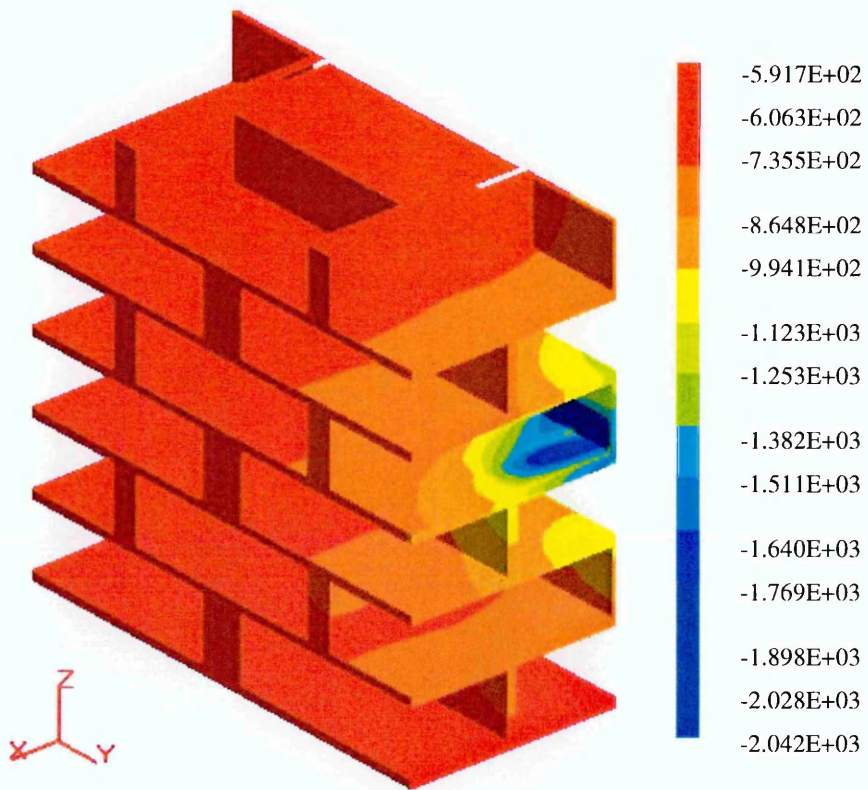


Figure 7.11: Potential distribution on the surface of mortar (mV vs CSE, symmetric in plane X=0, Case 1)

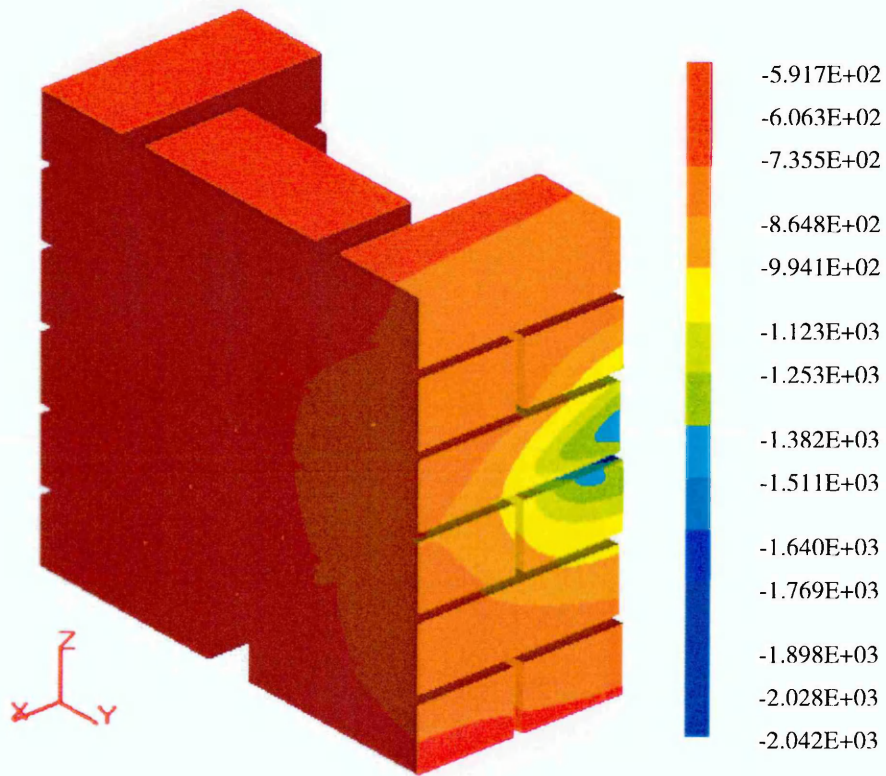


Figure 7.12: Potential distribution on the surface of brick (mV vs CSE, symmetric in plane X=0, Case 1)

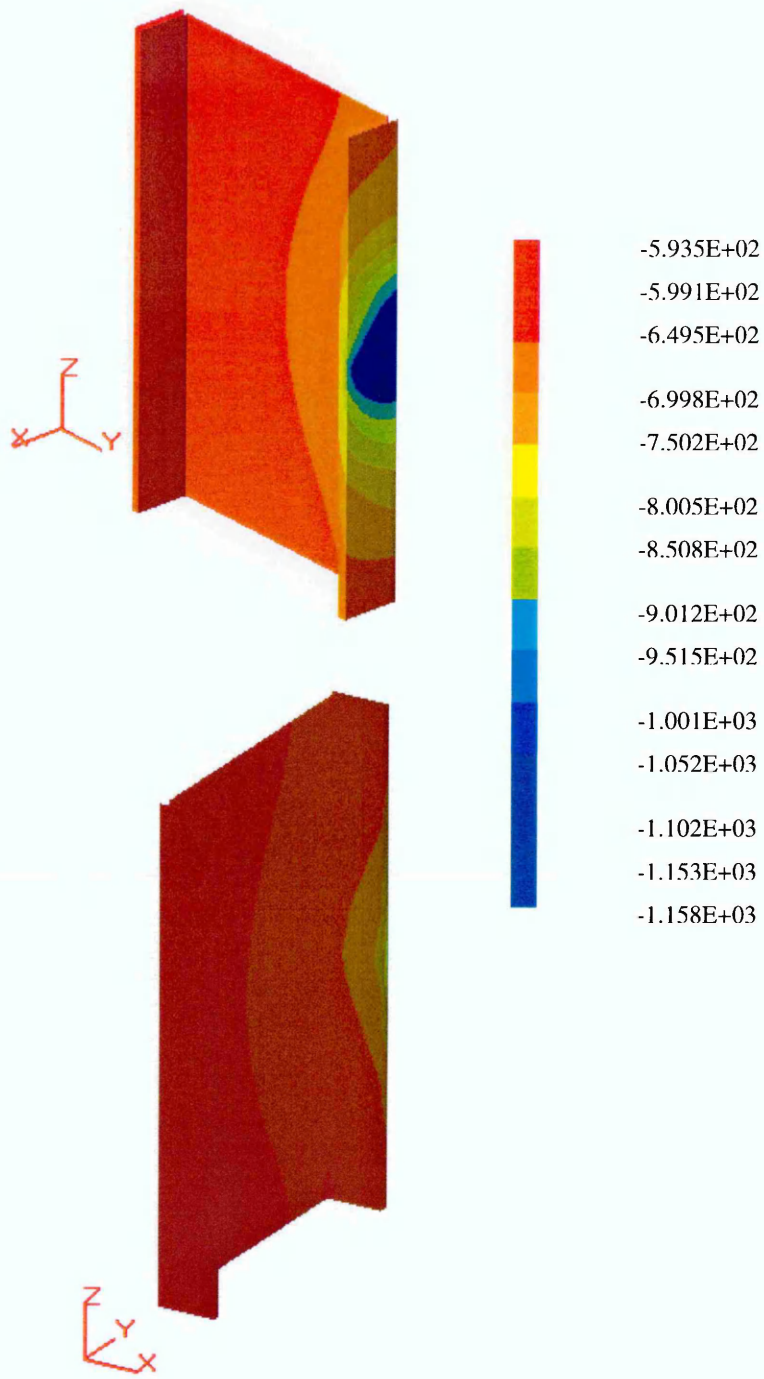


Figure 7.13: Potential distribution on the surface of steel (mV vs CSE, symmetric in plane $X=0$, Case 1)

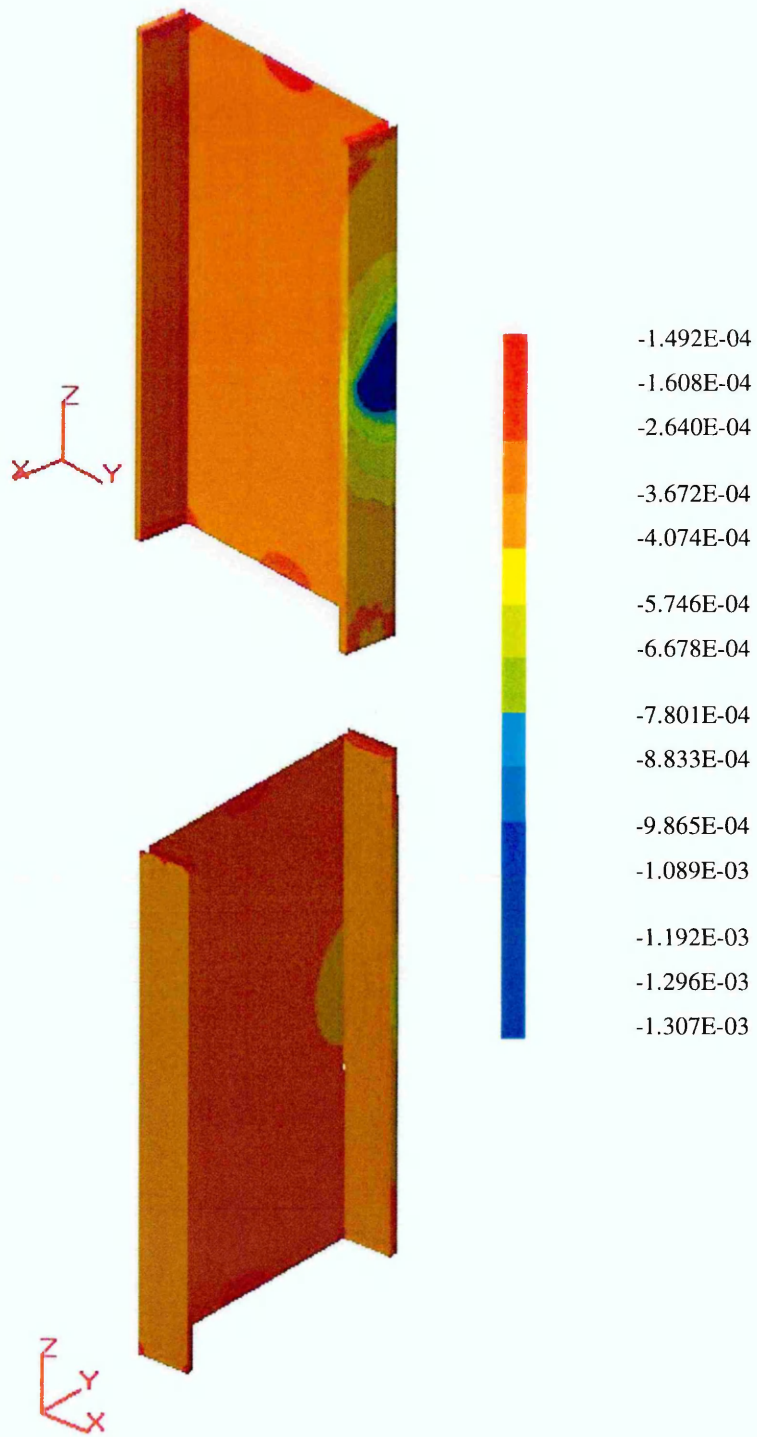


Figure 7.14: Normal current distribution on the surface of steel (mA/cm^2 , - current in, + current out, symmetric in plane $X=0$, Case 1)

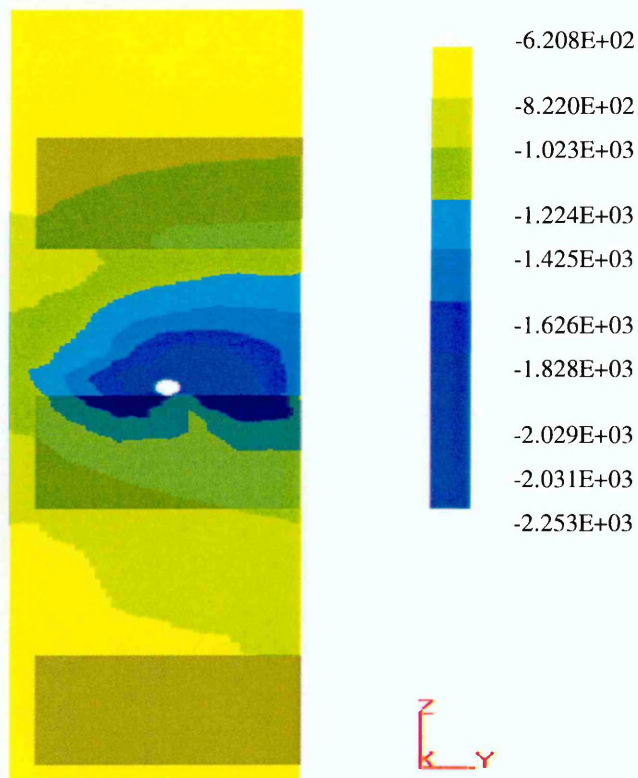


Figure 7.15: Potential distribution on the plane which is closed by $X=0.0\text{cm}$, $Y1=18.425\text{cm}$, $Y2=24.05\text{cm}$, $Z1=0$ and $Z2=45\text{cm}$ (mV vs CSE, symmetric in plane $X=0$, Case 1)

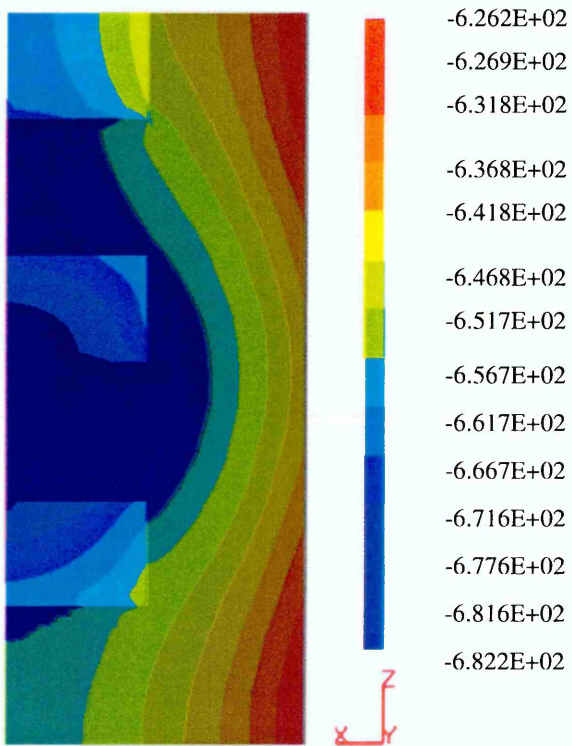


Figure 7.16: Potential distribution on the plane, $Y=0.00$,
(mV vs CSE, symmetric in plane $X=0$, Case 1)

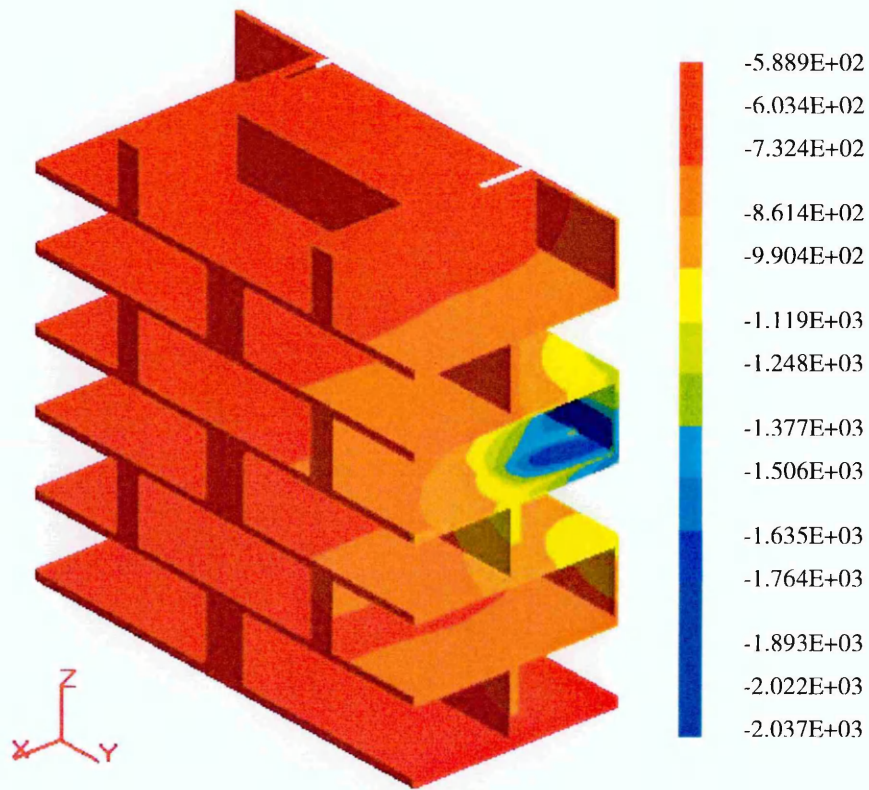


Figure 7.17: Potential distribution on the surface of mortar (mV vs CSE, symmetric in plane X=0, Case 2)

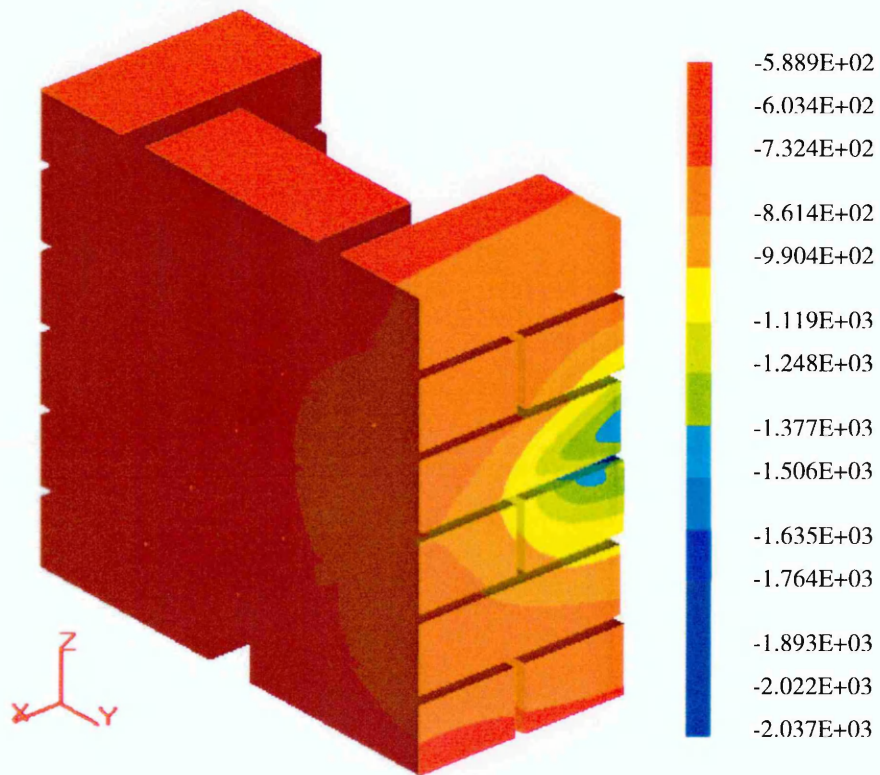


Figure 7.18: Potential distribution on the surface of brick (mV vs CSE, symmetric in plane $X=0$, Case 2)

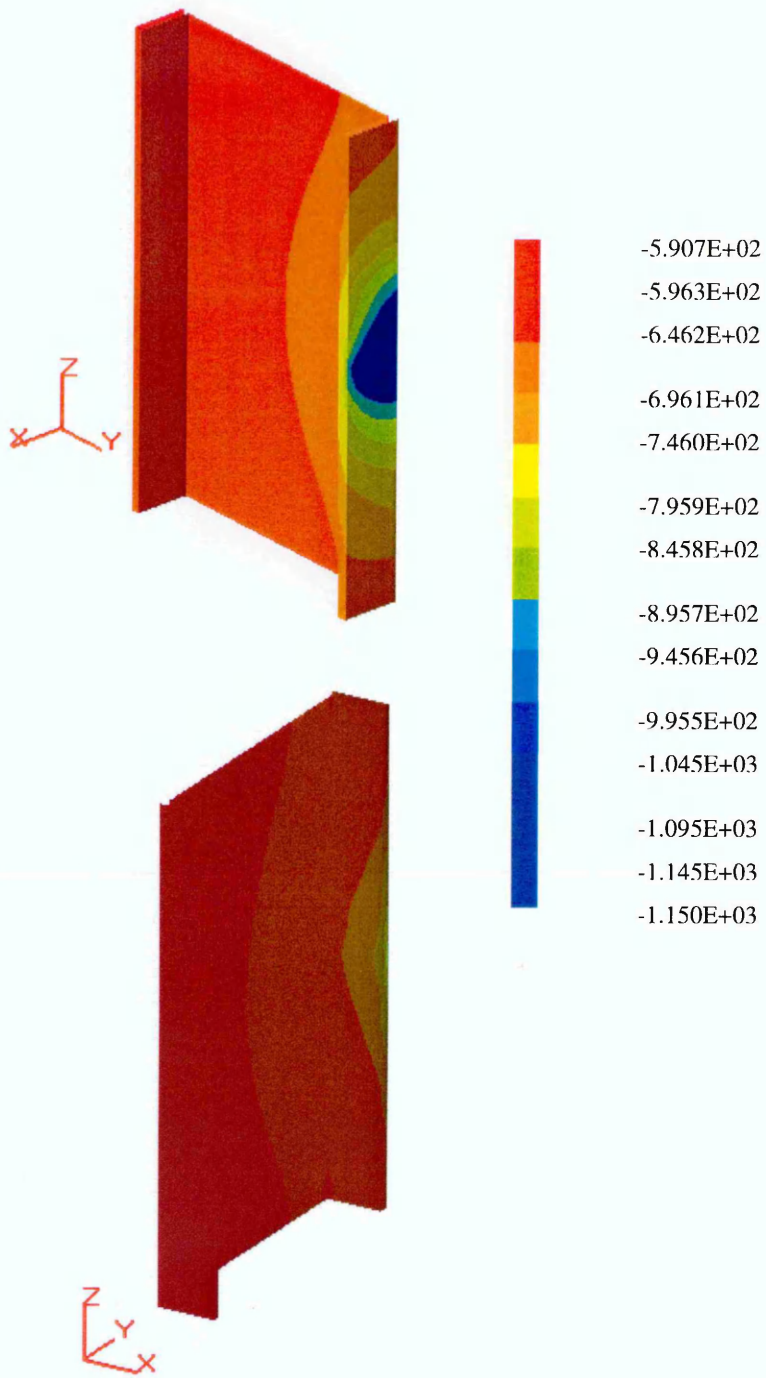


Figure 7.19: Potential distribution on the surface of steel (mV vs CSE, symmetric in plane $X=0$, Case 2)

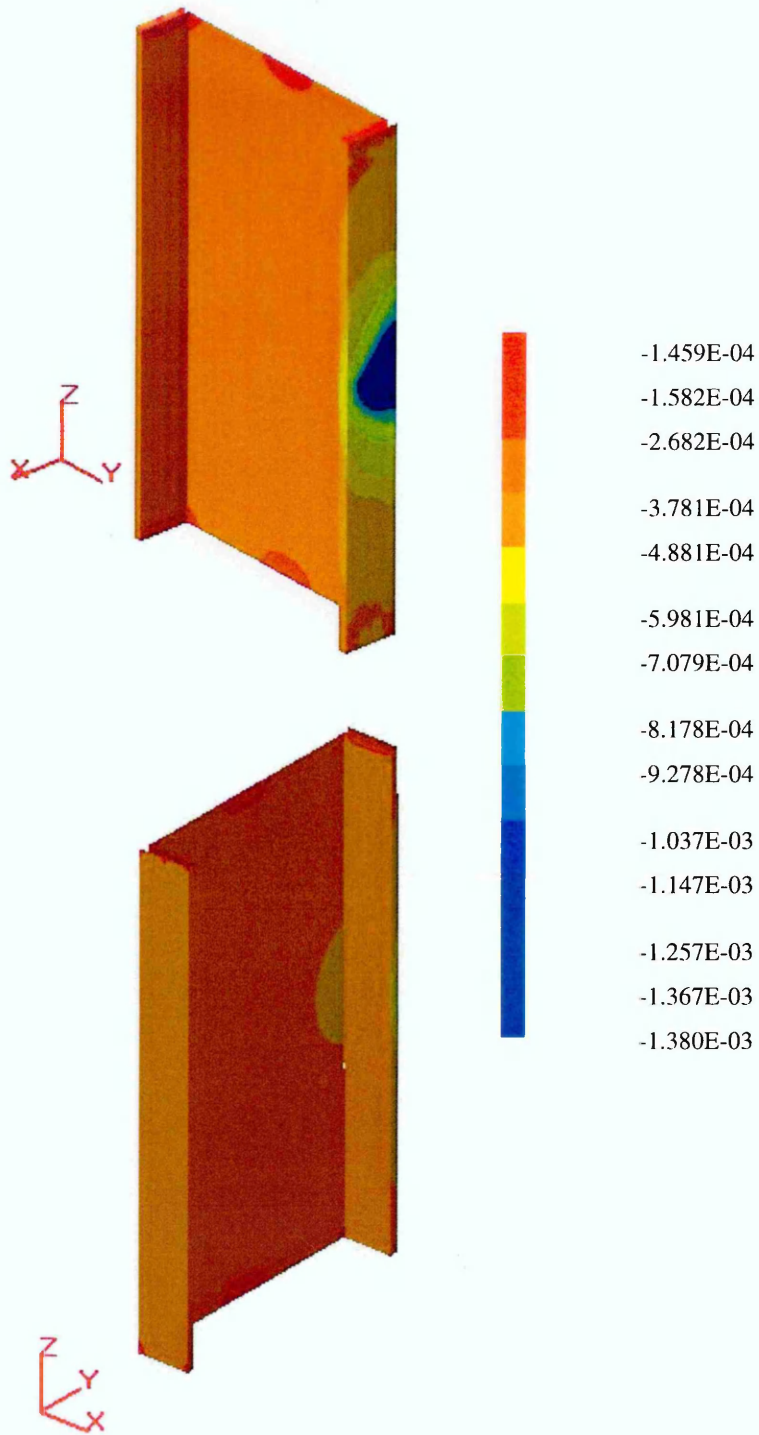


Figure 7.20: Normal current distribution on the surface of steel (mA/cm², - current in, + current out, symmetric in plane X=0, Case 2)

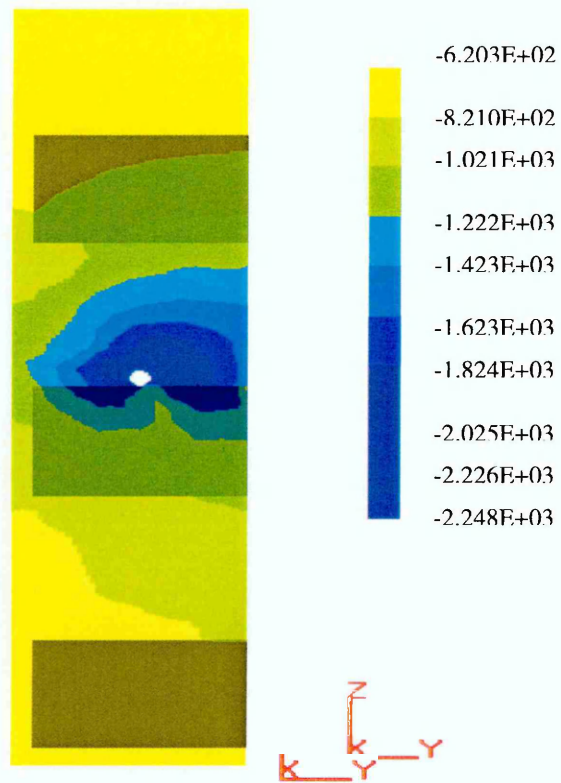


Figure 7.21: Potential distribution on the plane which is closed by the lines $X=0.0\text{cm}$, $Y_1=18.425\text{cm}$, $Y_2=24.05\text{cm}$, $Z_1=0$ and $Z_2=45\text{cm}$ (mV vs CSE, symmetric in plane $X=0$, Case 2)

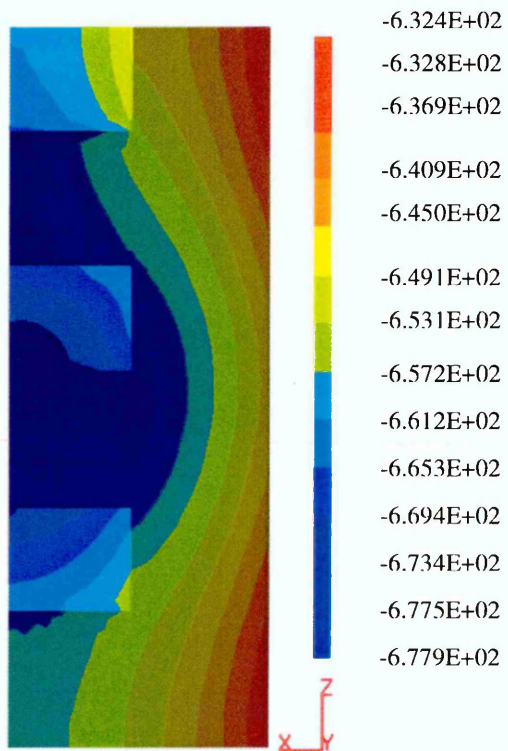


Figure 7.22: Potential distribution on the plane which is closed by the lines $X1=0.3\text{cm}$, $X2=22.0$, $Y=0.0$, $Z1=0$ and $Z2=45\text{cm}$ (mV vs CSE, symmetric in plane $X=0$, Case 2)

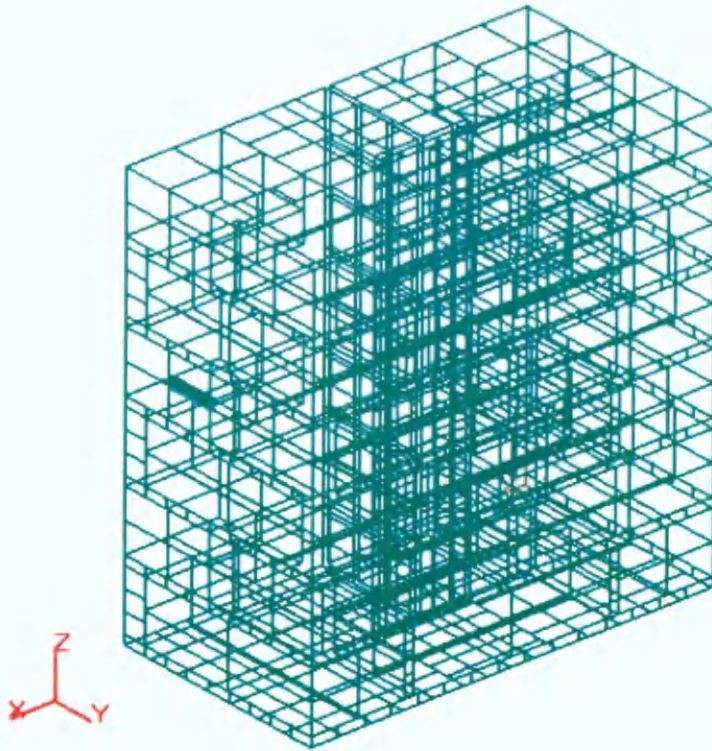


Figure 7.23: Schematic representation of the total boundary element mesh on the surface of specimen (Case 3)

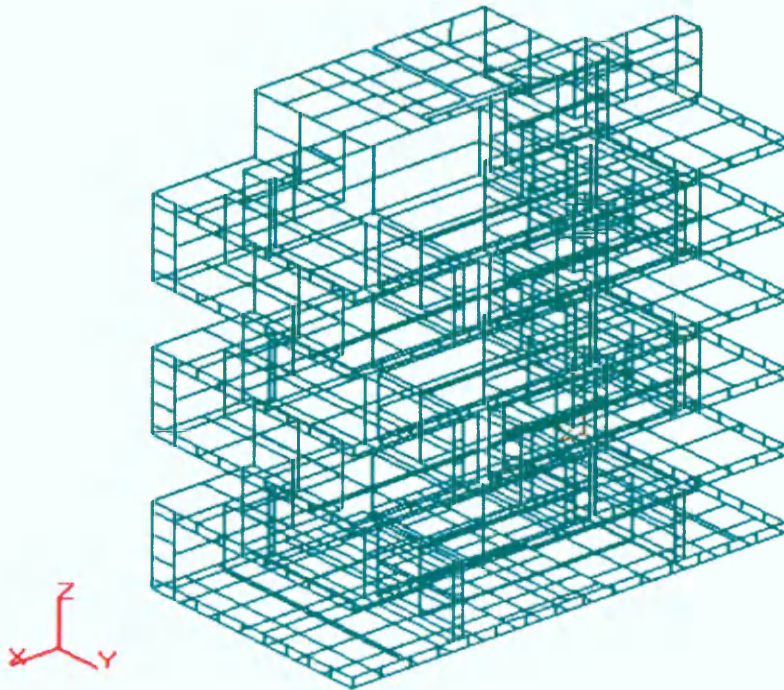


Figure 7.24: Schematic representation of the boundary element mesh on the mortar bed (Case 3)

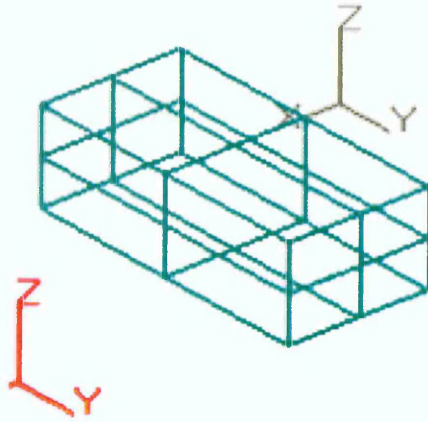


Figure 7.25: Schematic representation of details of the boundary element mesh on the surface of each brick (Case 3)

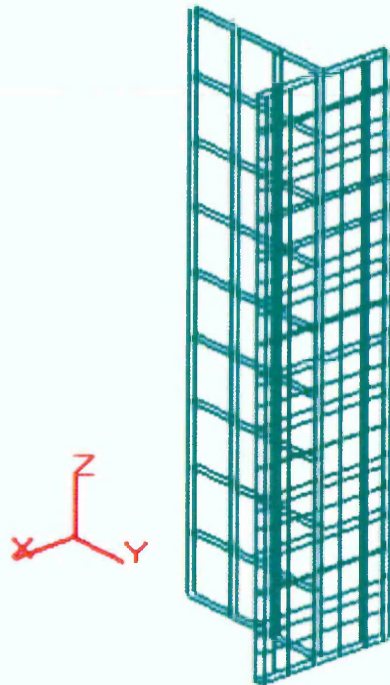


Figure 7.26: Schematic representation of the boundary element mesh on the surface of steel piece (Case 3, symmetric in plane $Y=0$)

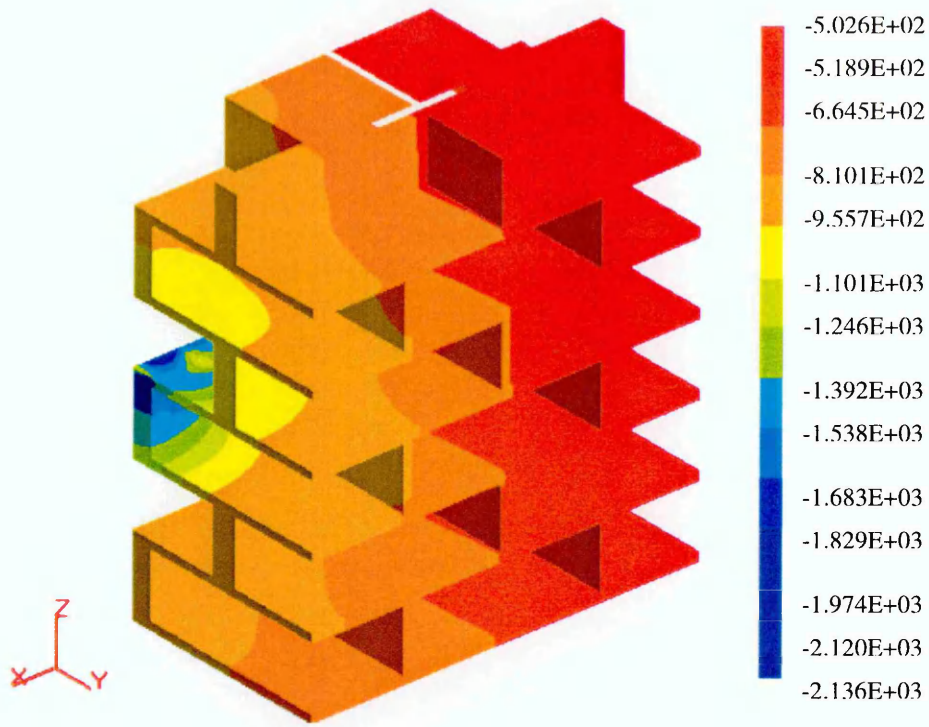


Figure 7.27: Potential distribution on the surface of mortar (mV vs CSE, symmetric in plane Y=0, Case 3)

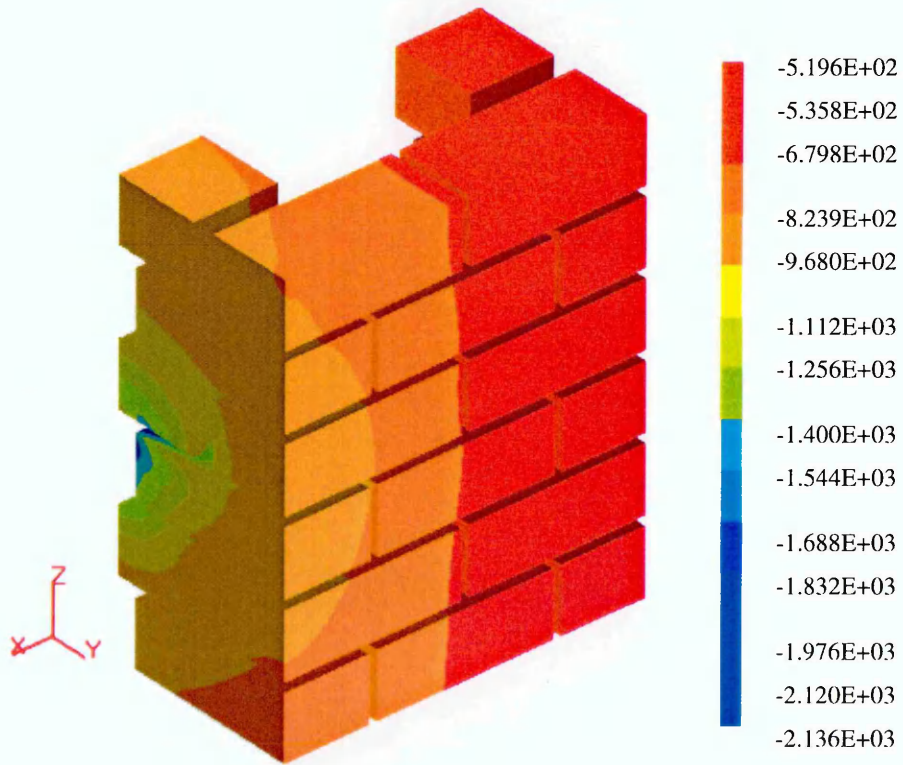


Figure 7.28: Potential distribution on the surface of brick (mV vs CSE, symmetric in plane Y=0, Case 3)

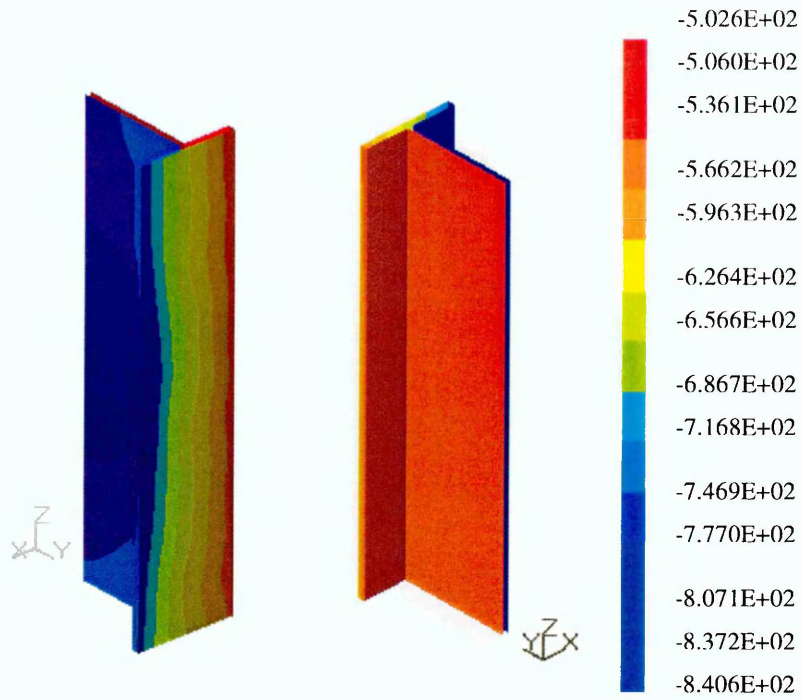


Figure 7.29: Potential distribution on the surface of steel (mV vs CSE, symmetric in plane Y=0, Case 3)

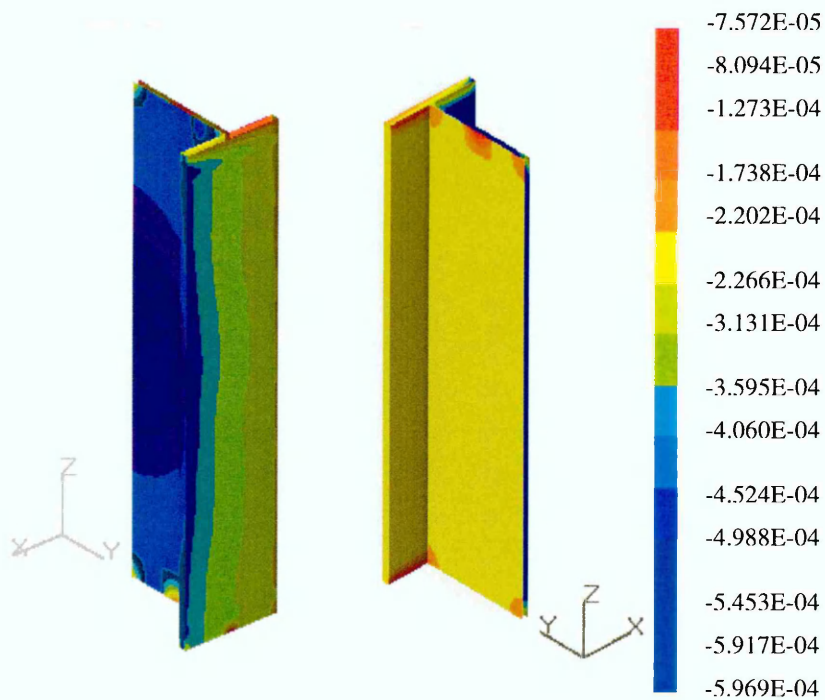


Figure 7.30: Normal current distribution on the surface of steel (mA/cm², - current in, + current out, symmetric in plane Y=0, Case 3)

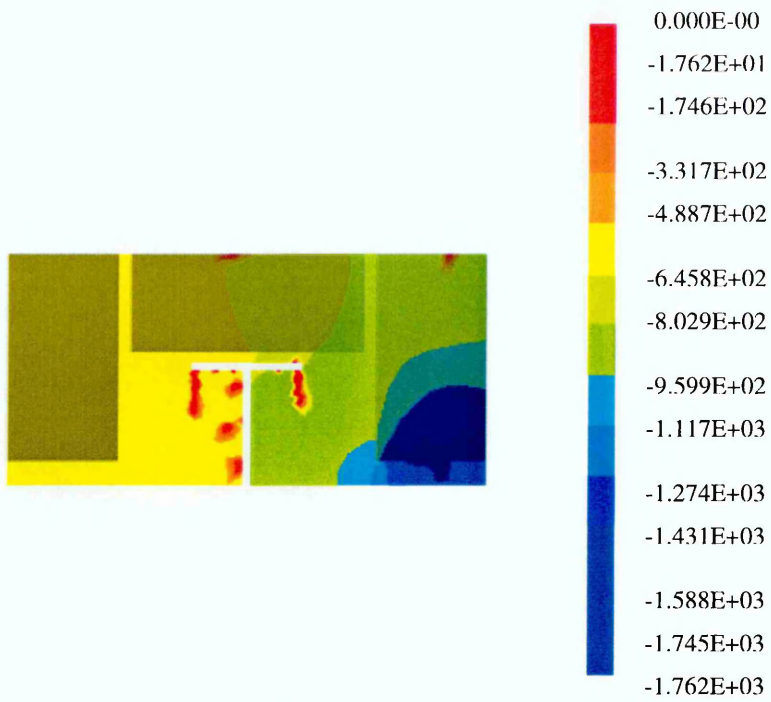


Figure 7.31: Potential distribution on the plane $Z= 20.0$ cm, (mV vs CSE, symmetric in plane $Y= 0$, Case 3)

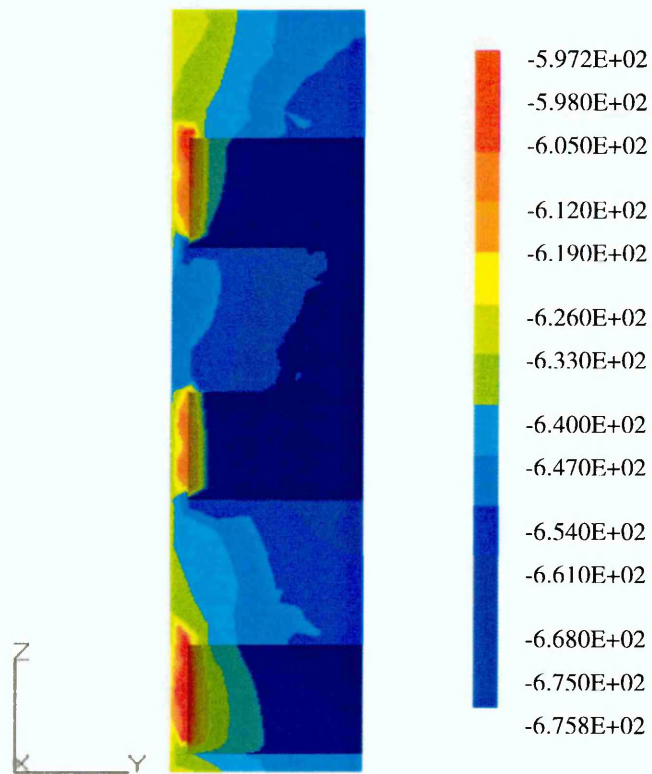


Figure 7.32: Potential distribution on the plane which is closed by the lines $X=0.0$ cm, $Y1=18.425$ cm, $Y2=24.05$ cm, $Z1=0$ and $Z2=45$ cm (mV vs CSE, symmetric in plane $Y=0$, Case 3)

Comparing the modelling results of Case 1 with Case 3, it is apparent that, for each anode location, the potential and current distribution both on the steel surface and in the electrolyte are completely different under the same modelling conditions. It therefore clearly demonstrates the key role played by the anode locations in the optimal distribution of the protective current in a CP system of this type.

7.4.3 Further Discussion of Modelling Results

In the above Section, the effect of the resistivity of brick and mortar on the distribution of potential and current density has been discussed. In order to better understand the problem, the following two cases (Cases 4 and 5) are analyzed.

Consider the situation where the bricks in Case 1 and Case 3 are removed and the steel is encased completely by mortar in both cases while the other modelling conditions are the same as Case 1 and Case 3, respectively. For ease of illustration, their details are shown below:

Case 4:

- Average value of mortar resistivity: 9.00 K Ω .cm.
- Anode axis locations (X, Y, Z) cm: Right (X=-5, Y=18.925, Z=23).
Left (X=5, Y=18.925, Z=23).
- Applied current density on the anodes: 4.20X10⁻² mA/cm².

Case 5:

- Average value of mortar resistivity: 9.00 K Ω .cm.

- Anode axis locations (X, Y, Z) cm: Right (X=16.875, Y=-5, Z=23).
Left (X=16.875, Y=5, Z=23).
- Applied current density on the anodes: 4.20×10^{-2} mA/cm².

Under such situations, the two specimens can be considered to be homogeneous. They may then be analyzed by the boundary element method.

For Case 4, the total boundary element mesh used for the analysis is shown in Figure 7.33. For clear purpose, the boundary element mesh on the surface of mortar and steel piece is further shown in Figure 7.34, Figure 7.35, separately. The results are shown from Figure 7.36 to Figure 7.40.

For Case 5, the total boundary element mesh used for the analysis is shown in Figure 7.41. For clarity, the boundary element mesh on the surface of mortar and steel specimen is shown in Figures 7.42 and 7.43. The results of the boundary element analysis are shown in Figures 7.44 to 7.48.

Comparing Case 1 with Case 4, it can be seen that the potential and current distributions on the steel surface in Case 4 are more uniform than in Case 1. Figure 7.13 (Case 1) shows the difference of potential distribution between the maximum and minimum values on the steel surface is 48.75% while this value in Case 4 is 32.23% (Figure 7.37). Figure 7.14 (Case 1) shows the difference in current distribution between the maximum and minimum values on the steel surface is 88.58% while the equivalent value for Case 4 is 77.73% (Figure 7.38).

The above trend is also apparent in Case 3 and Case 5. In Case 3 the difference of potential distribution between the maximum and minimum values

on the steel surface is 40.20 % (Figure 7.29) while this value for Case 5 is 29.19% (Figure 7.45). Similarly, Figure 7.30 (Case 3) shows the difference of current distribution is 87.31% while this value in Case 5 is 72.52 % (Figure 7.46). Therefore, it can be seen that the potential and current distribution on the steel surface is more uniform when the steel is encased only in mortar.

By comparing Figures 7.15 and 7.16 (Case 1) with Figures 7.39 and 7.40 (Case 4), it is apparent that the potential distribution in the latter case is continuous whereas the former is not. Further, the results in Figures 3.31 and 7.32 (Case 3) are compared with the results in Figures 7.47 and 7.48 (Case 5). It can also be seen that the potential distribution in the electrolyte in Case 5 (Figures 7.47 and 7.48) is continuous but in Case 3 (Figures 7.31 and 7.32) is discontinuous.

Based on the above study, it is apparent that the difference in resistivity between brick and mortar or brick type and joints widths have a significant effect on the distribution of the potential and current density on the steel surface under the conditions of a fixed anode location and a given anode current.

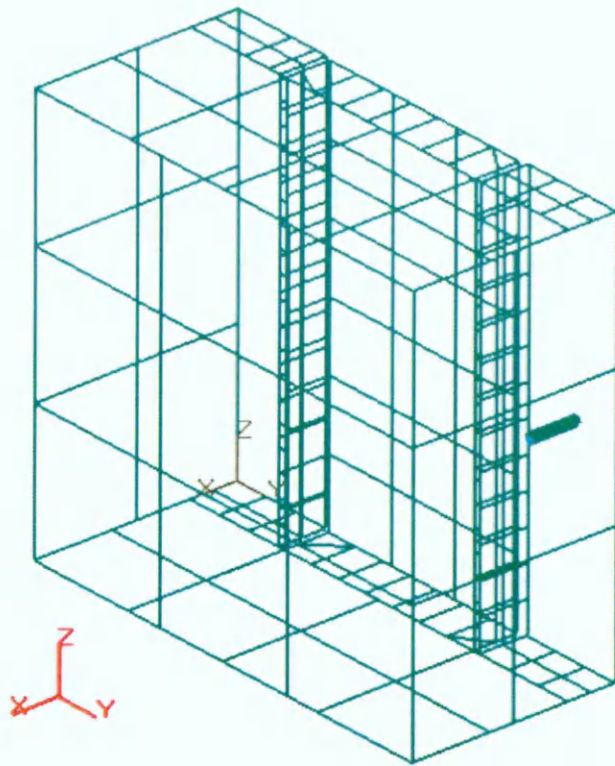


Figure 7.33: Schematic representation of the total boundary element mesh (Case 4, symmetric in plane $X=0$)

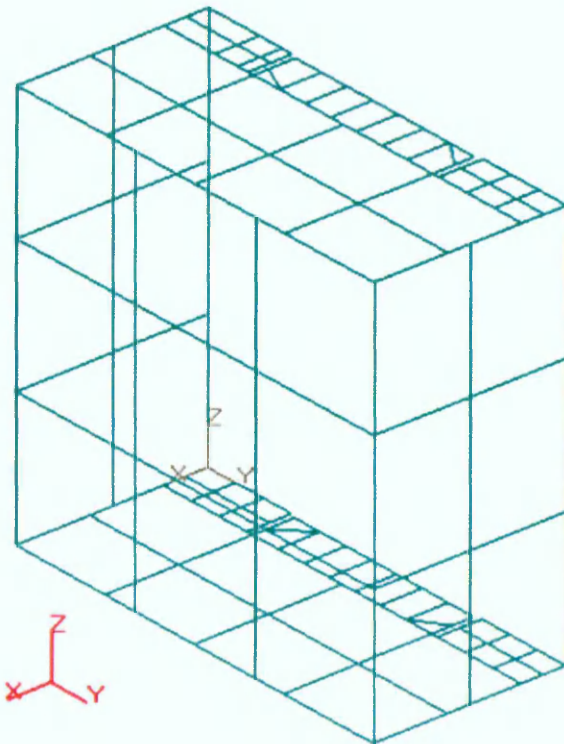


Figure 7.34: Schematic representation of details of boundary element mesh on the surface of mortar (Case 4, symmetric in the plane $X=0$)

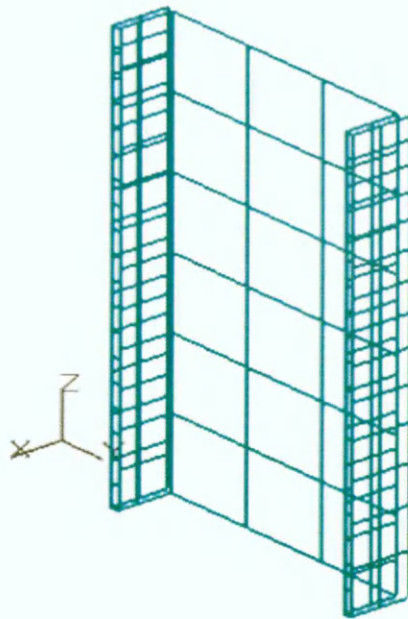


Figure 7.35: Schematic representation of the boundary element mesh on the surface of steel piece (symmetric in plane $X=0$, Case 4)

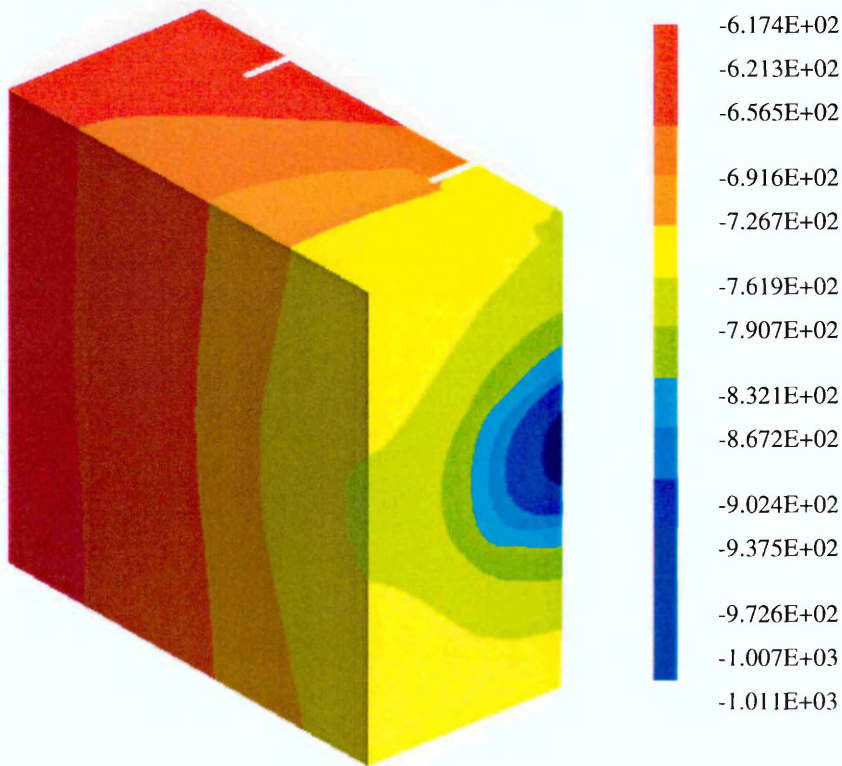


Figure 7.36: Potential distribution on the surface of mortar (mV vs CSE, symmetric in plane $X=0$, Case 4)

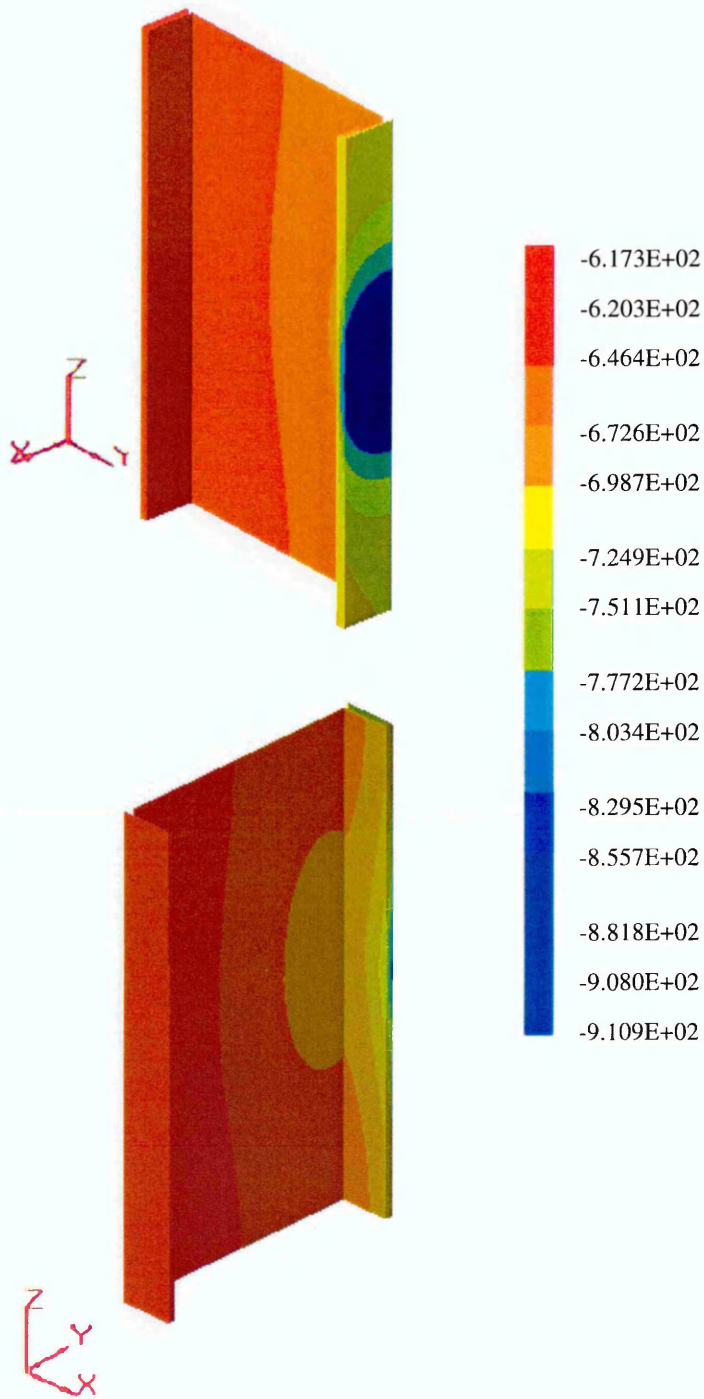


Figure 7.37: Potential distribution on the surface of steel (mV vs CSE, symmetric in plane X=0, Case 4)

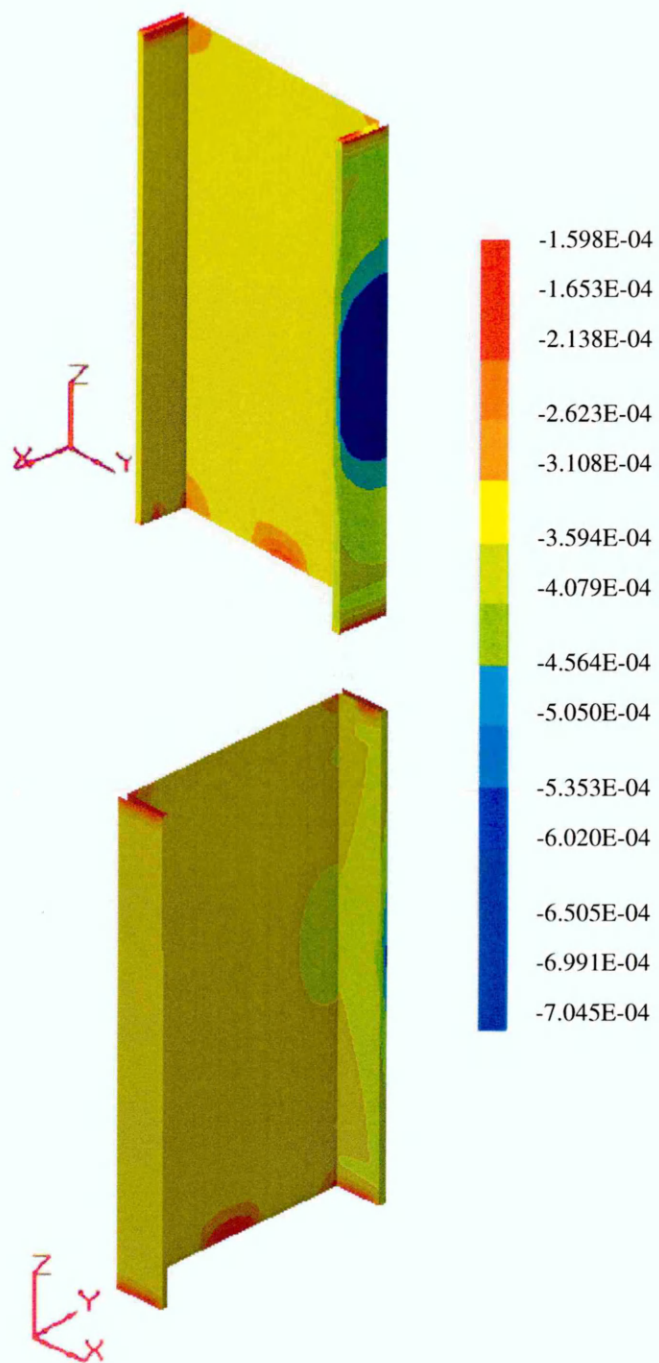


Figure 7.38: Normal current distribution on the surface of steel (mA/cm^2 , - current in, + current out, symmetric in plane $X=0$, Case 4)

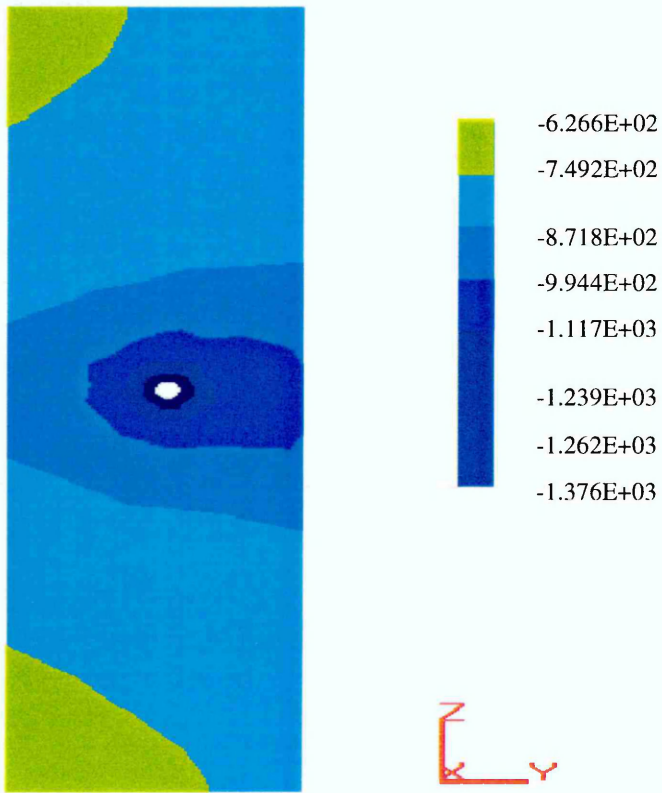


Figure 7.39: Potential distribution on the plane which is closed by the lines $X=0.0\text{cm}$, $Y_1=18.425\text{cm}$, $Y_2=24.05\text{cm}$, $Z_1=0$ and $Z_2=45\text{cm}$ (mV vs CSE symmetric in plane $X=0$, Case 4)

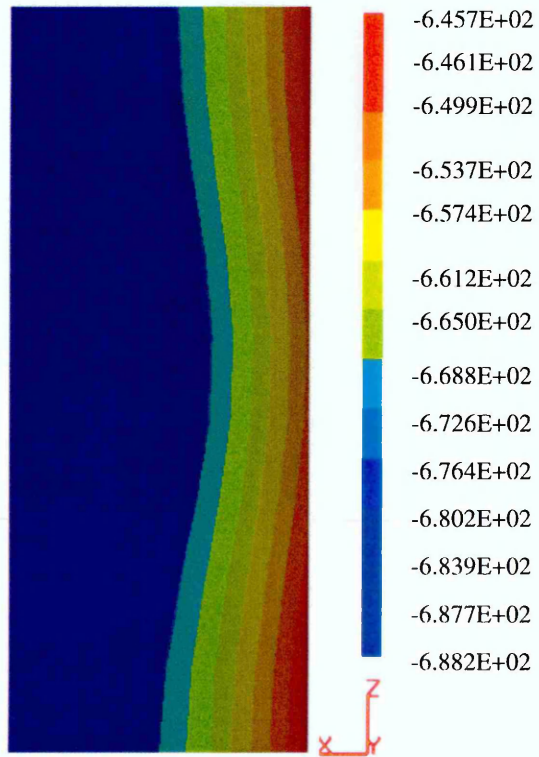


Figure 7.40: Potential distribution on the plane which is closed by the lines $X1=0.3\text{cm}$, $X2=22.0$, $Y=0.0$, $Z1=0$ and $Z2=45\text{cm}$ (mV vs CSE, symmetric in plane $X=0$, Case 4)

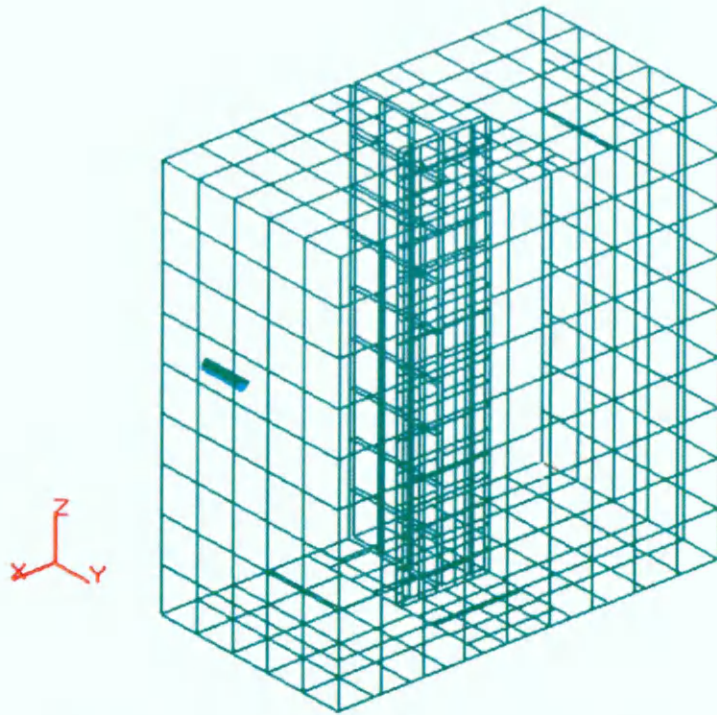


Figure 7.41: Schematic representations of the total boundary element mesh (symmetric in plane $Y=0$, Case 5)

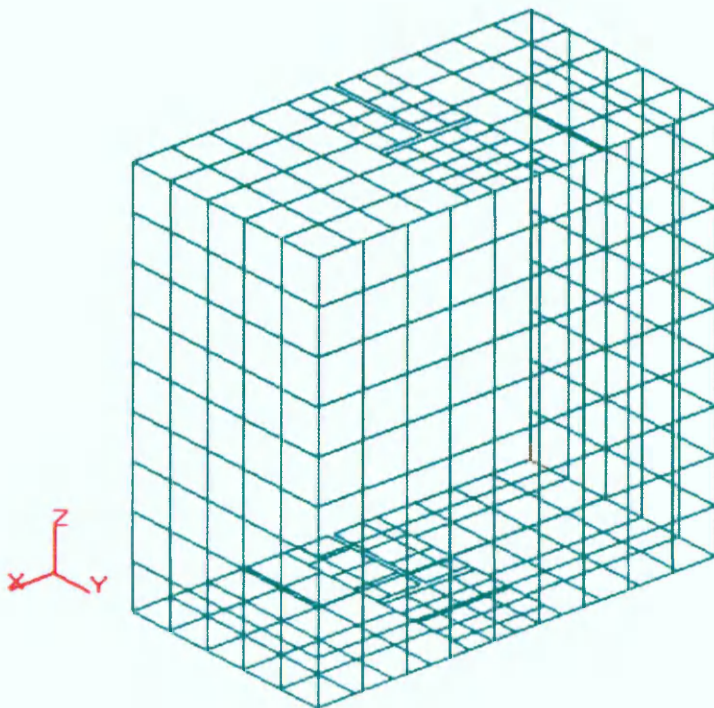


Figure 7.42: Schematic representation of boundary element mesh on the surface of mortar (Case 5, symmetric in the plane $Y=0$)

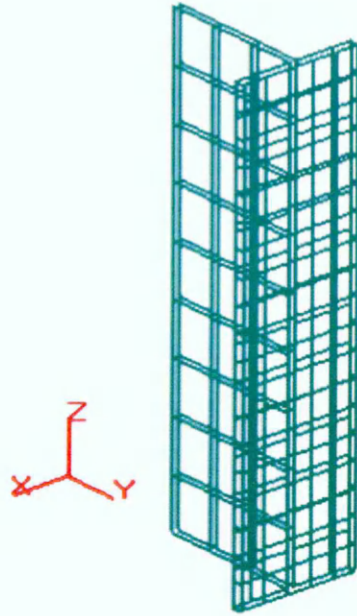


Figure 7.43: Schematic representation of the boundary element mesh on the surface of steel section (symmetric in plane $Y=0$, Case 5)

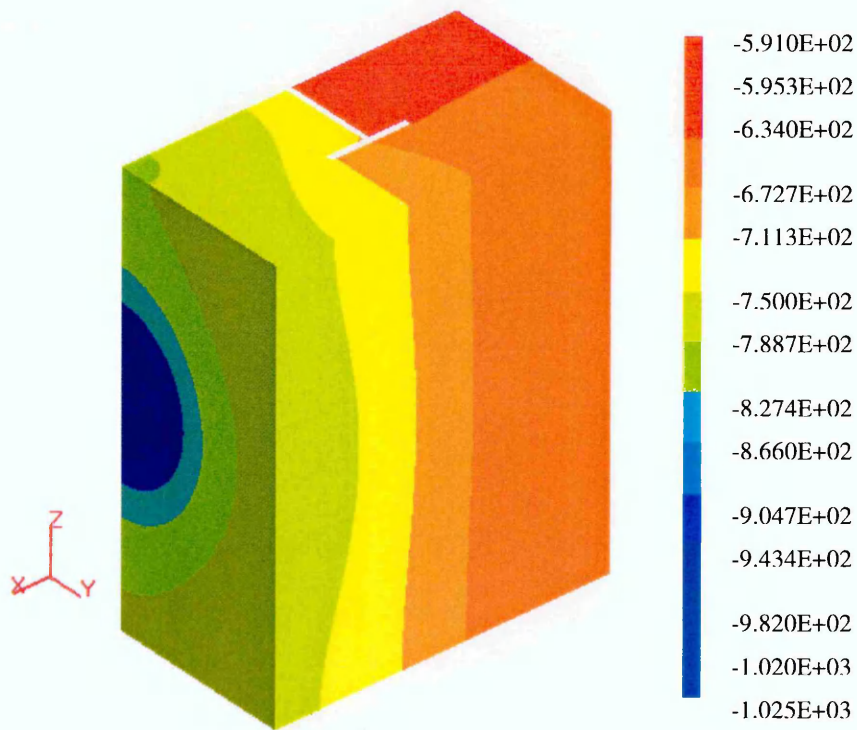


Figure 7.44: Potential distribution on the surface of mortar (mV vs CSE, symmetric in plane $Y=0$, Case 5)

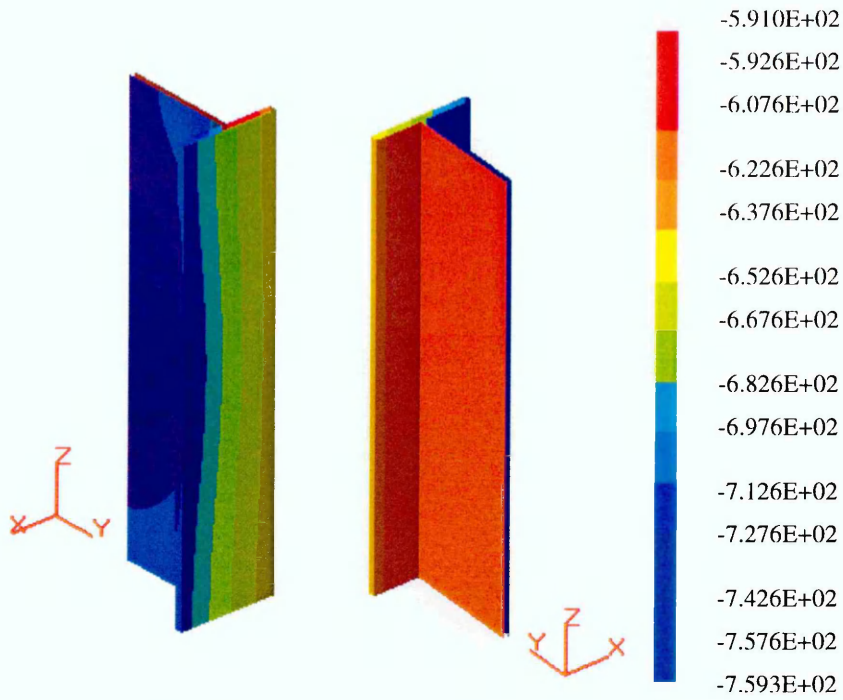


Figure 7.45: Potential distribution on the surface of steel (mV vs CSE, symmetric in plane Y=0, Case 5)

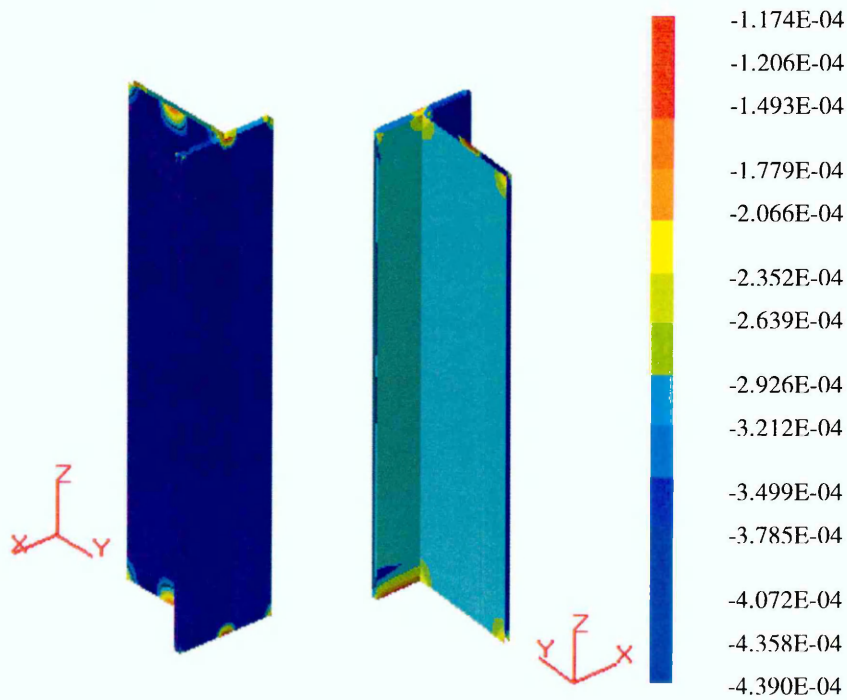


Figure 7.46: Normal current distribution on the surface of steel (mA/cm², - current in, + current out, symmetric in plane Y=0, Case 5)

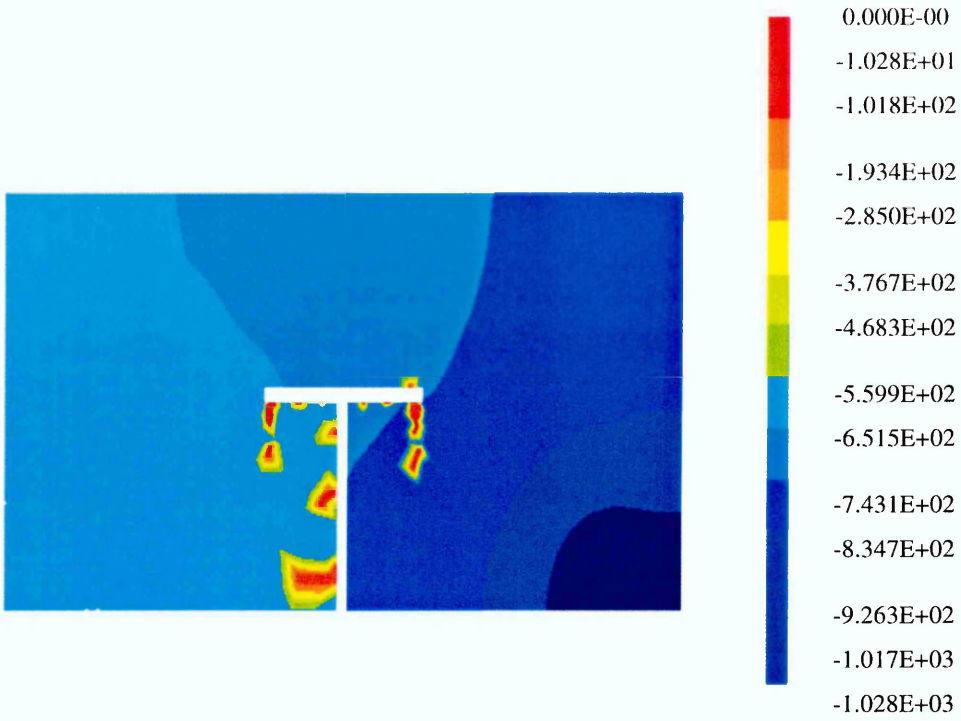


Figure 7.47: Potential distribution on the plane $Z=20.0\text{cm}$, (mV vs CSE, symmetric in plane $Y=0$, Case 5)

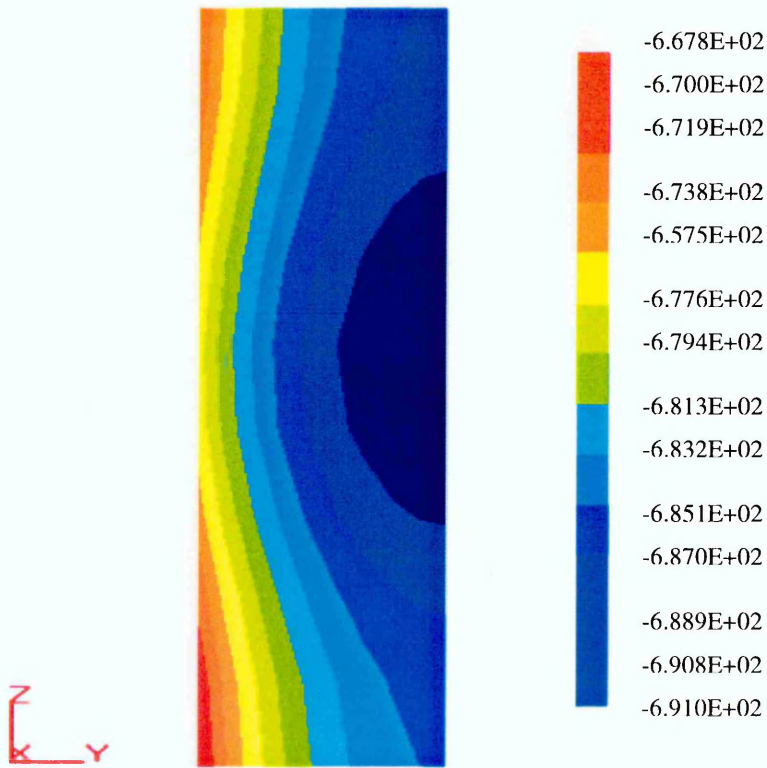


Figure 7.48: Potential distribution on the plane which is closed by the lines $X=0.0\text{cm}$, $Y1=18.425\text{cm}$, $Y2=24.05\text{cm}$, $Z1=0$ and $Z2=45\text{cm}$ (mV vs CSE, symmetric in plane $Y=0$, Case 5)

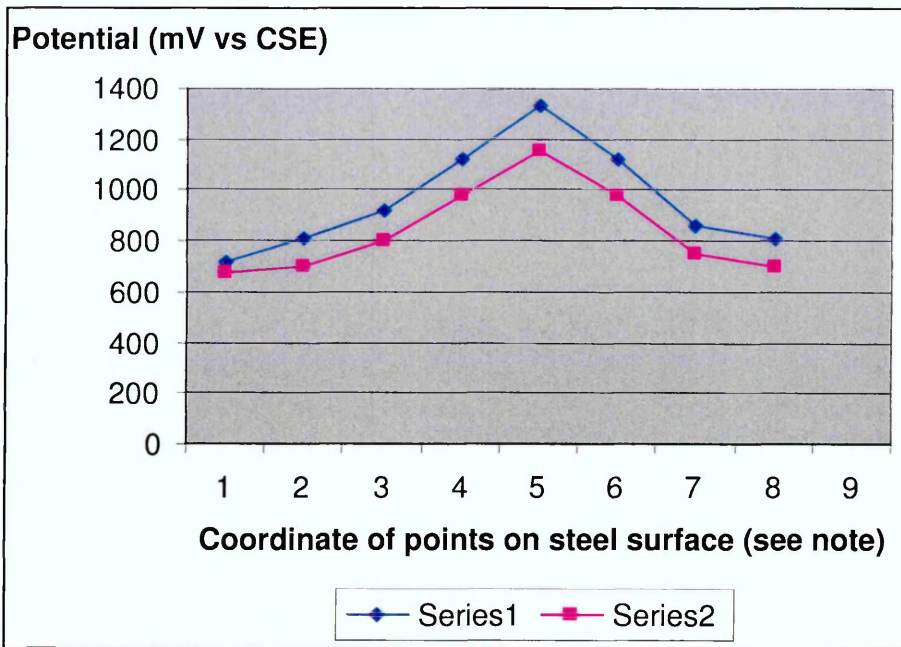


Figure 7.49: Comparison of experimental measurement of potential with boundary element solutions on the steel surface (Case 1).

Note:

- (1) Series 1: Experimental data;
- (2) Series 2: Boundary element results.

(3) Coordinate of points on steel surface:

P1(0,36.85,5); P2 (0,36.85,10);P3(0,36.85,15);P4(0,36.85,20)
P5(0,36.85,25);P6(0,36.85,30); P7(0,36.85,35); 8(0,36.85,40)

7.5 Comparison of Boundary Element Modelling with the Experiments

The results of the boundary element modelling in Case 1 may now compared with the experimental measurements in Figure 7.31. The results for both the boundary element solutions and the experimental data, as shown in Figure 7.49, generally follow the same trends, although there is a difference of around 15 % in the individual potential values.

The explanation for this difference could be associated with either the experimental procedure or the method of modelling. For example, the following reasons could result in inaccurate experimental measurement:

- Poor connections between meters and test leads.
- Miss-reading of digital displays.

In boundary element modelling, the possible causes of error include:

- The polarisation curves obtained by experimental measurement not adequately reflecting the polarisation behaviour of steel in masonry.
- Inaccurate discretisation of the element mesh.

Although there is some difference between the boundary element results and experimental data, the general trend is good and the results sufficiently accurate for design purposes.

7.6 Conclusions

The work presented in this chapter leads to the following conclusions:

- The difference in resistivity between typical mortar and brick samples is large. It has an effect on the distribution of the potential and current as measured and modelled on the steel surface. Low resistivity mortar "attracts" a higher current density, with current flowing preferentially along the path of least electrical resistance. As a result, the distribution of potential and current on the steel surface is not uniform for any given anode location and anode current.

- Boundary element modelling provides a powerful technique for analysing and optimising the design of cathodic protection system for steel framed masonry structures. The important design variables, such as the anode locations and potential distribution can be predicted with sufficient accuracy in the design optimisation process by using such a numerical technique. The optimum design can therefore be achieved and the CP system performance for steel-framed masonry buildings can be improved accordingly.

8.1 Introduction

Steel-framed masonry buildings contain a variety of metallic elements. In addition to the frame itself, the following components are commonly encountered:

- Metal window frames.
- Metal drainage pipes and gutters.
- Metal fixings such as wall ties, cramps and lintels.

Generally electrical continuity between structural members is rarely a problem [Atkins, Lambert & Coull 2002] since the structural connections are typically bolted or riveted. However, other elements are more likely to be electrically discontinuous. These must be considered before CP systems are installed.

When CP is applied to such buildings, failure to ensure the electrical continuity of all metallic elements could result in stray current interactions between the various elements of the structure, resulting in accelerated corrosion of the discontinuous items. An example of CP interference is represented in Figure 8.1.

The study described in this chapter investigates the risk and extent of stray current corrosion in such structures when subject to impressed current cathodic protection.

The objective is to allow cathodic protection systems to be optimised so that interference is minimised.

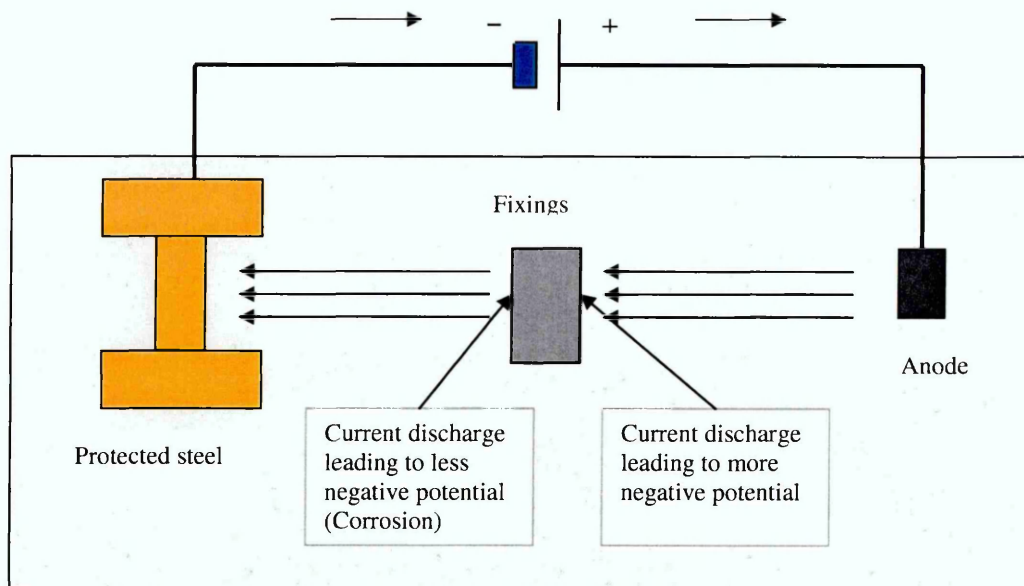


Figure 8.1: CP inducing corrosion on discontinuous metal fixings

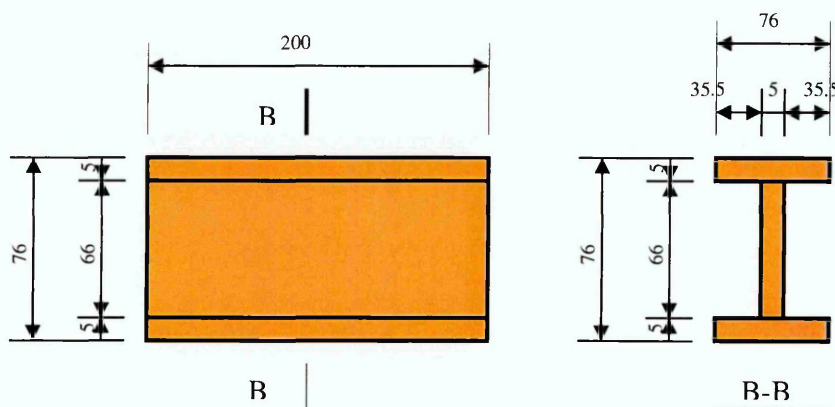


Figure 8.2: Steel Section (unit: mm)

8.2 Experimental Configuration

8.2.1 Specimen Design

A small scale representative ICCP system which incorporates two electrically discontinuous steel bar was constructed to analyze the distribution of

protective potential and current. The main components of the test set-up were as follows:

- DC power supply.
- Discrete anodes (10mm diameter X 100mm length), as discussed in Section 3.2.
- Steel section (cathode), dimension as shown in Figure 8.2
- Two steel bars (each 8mm diameter X 200mm length), employed to represent electrically discontinuous metal items.
- Sand (electrolyte), in a small sandboxes, 100mm length, 360 width and 560mm height, used to represent the surrounding masonry.

The test facility and its components are illustrated in Figure 8.3. The completed test specimen is shown in Figure 8.4. The experimental work was performed at a constant 20°C and 60% relative humidity in an environmentally controlled room.

8.2.2 Measurement of Potential

The potential distribution on a grid of the sandbox's free surface was measured under a range of testing conditions, including different sand resistivities and output currents, by moving a hand-held potential measurement electrode (CSE). Selected measurement results are listed in Table 8.1.

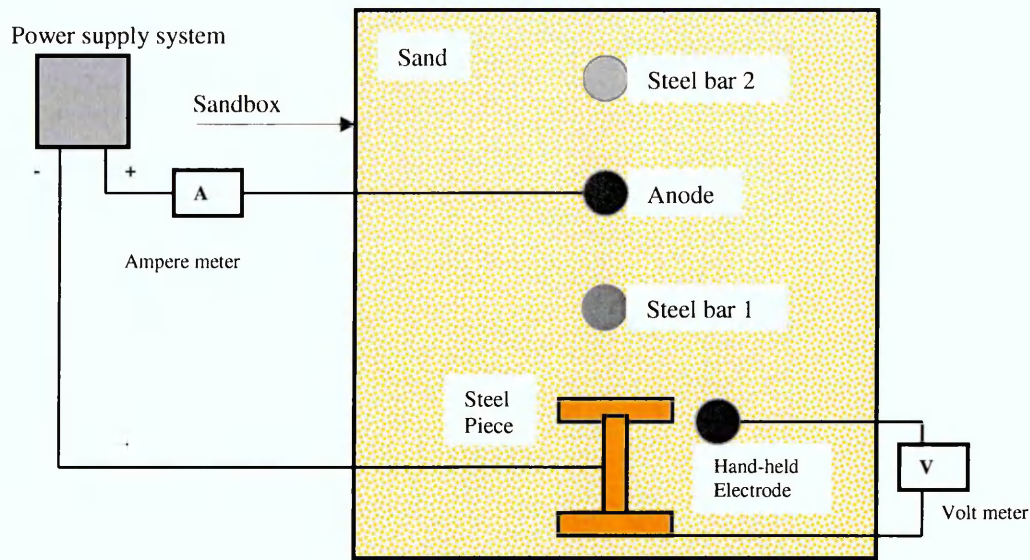


Figure 8.3: Schematic illustration of test facility

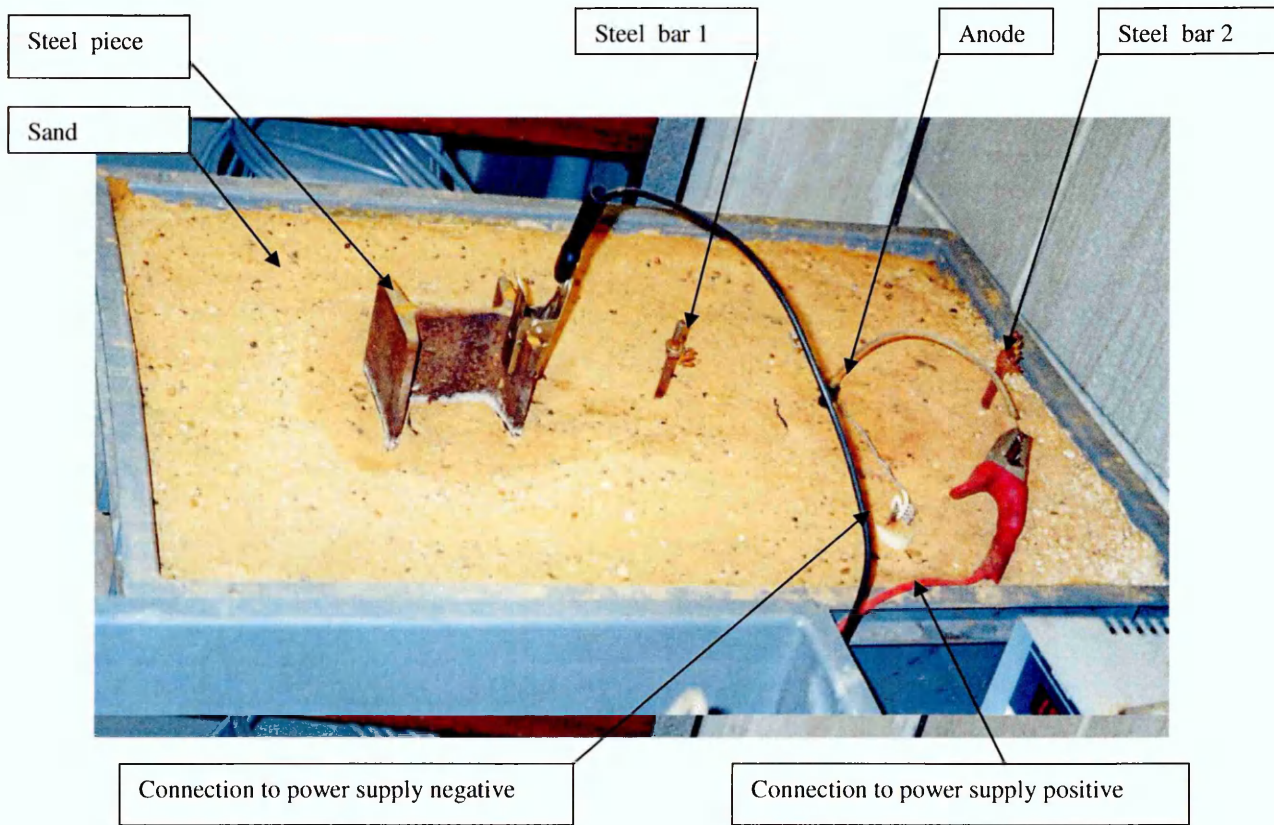


Figure 8.4: Sandbox and ICCP components

Table 8.1: Protective potential on the free surface of sandbox

Conditions	Constant temperature						20 ⁰ C
	Relative humidity						60%
	Average resistivity of sand						15.00 KΩ.cm
	Anode axis locations (X, Y, Z) cm:						Top (X=17.8, Y=43, Z=10). Left (X=17.8, Y=43, Z=0).
	Applied current density on the anodes						2.50X10 ⁻³ mA/cm ²
Coordinates	(5,10,10)	(10,10,10)	(15,10,10)	(20,10,10)	(25,10,10)	(30,10,10)	(35,10,10)
Potential(V) vs. CSE	0.91	0.89	0.88	0.88	0.89	0.91	0.91
Coordinates	(5,38,10)	(10,38,10)	(15,38,10)	(20,38,10)	(25,38,10)	(30,38,10)	(30,38,10)
Potential (V) vs. CSE	0.97	0.97	0.98	0.99	0.98	0.97	0.96
Coordinates	(5,48,10)	(10,48,10)	(15,48,10)	(20,48,10)	(25,48,10)	(30,48,10)	(35,48,10)
Potential(V) vs. CSE	0.99	0.99	0.99	1.1	1.0	0.99	0.98

8.3 Boundary Element Modelling

8.3.1 Boundary Conditions

The theory of boundary element method and its application for the modelling of cathodic protection systems have previously been described and discussed in Chapter 4. In this chapter they are applied to analyze stray current corrosion in the representative ICCP system.

Its boundary conditions may be defined as follows:

- (i) On the insulating surfaces (sandbox wall) and the free surface, the normal current density is equal to zero:

$$k \frac{\partial E}{\partial n} = 0 \quad (8.1)$$

- (ii) At any point on the anode surface, the normal current density has a constant value i_a :

$$k \frac{\partial E}{\partial n} = i_a \quad (8.2)$$

As an alternative to defining the normal current density at an anode, the potential at an anode can be defined as a constant:

$$E = E_a \quad (8.3)$$

It should be noted that the ICCP system is evaluated at steady-state conditions. The anode is not treated as a charge source but as a fixed boundary condition. In this approach the current level of the anode is fixed and no variation is allowed. In reality the current level at the anode will vary with time and operating conditions during the life of the ICCP system. Therefore, separate solutions must be performed for various times during the life of the system when this approach is taken.

- (iii) The normal current density at any point on the steel section (cathode) is:

$$i_c = f_c(E_c) \quad (8.4)$$

This is the same as Equation 4.22. Experimentally determined polarisation curves are employed to describe the non-linear relationship between the potential and the current density on the cathode surface or the cathode electrode kinetics. The measurement of polarisation curves for steel in sand under the conditions of varying resistivities was described in Chapter 5 and the results are used in the present modelling.

(iv) The normal current density at any point on the steel bar surface is :

$$i_c = f_c(E_c) \quad (8.5)$$

Similar to the normal current density at any point on the steel section, it is the experimentally determined polarisation curves which describe the non-linear relationship between the potential and the current density on the cathode surface.

8.3.2 Description of the Boundary Element Modelling

Steel Bar 1 and Steel Bar 2 were placed in the sand. The diameter of each steel bar was 8mm. As the bars are so small they can be modelled as polygons. The system was analyzed for the following two cases:

Case 1

- Average value of sand resistivity: 42.00 KΩ.cm.
- Anode axis locations (X, Y, Z) cm: Top (X=17.8, Y=43, Z=10).
Bottom (X=17.8, Y=43, Z=0).
- Axis locations of steel bar 1 (X, Y, Z) cm: Top (X=17.8, Y=33, Z=10).
Bottom (X=17.8, Y=33, Z=0).
- Axis locations of steel bar 2 (X, Y, Z) cm: Top (X=17.8, Y=53, Z=10).
Bottom (X=17.8, Y=53, Z=0).
- Applied current density on the anode: 4.84×10^{-4} mA/cm².

Case 2

- Average value of sand resistivity: 15.00 K Ω .cm.
- Anode axis locations (X, Y, Z) cm: Top (X=17.8, Y=43, Z=10).
Bottom (X=17.8, Y=43, Z=0).
- Axis locations of steel bar 1 (X, Y, Z) cm: Top (X=17.8, Y=33, Z=10).
Bottom (X=17.8, Y=33, Z=0).
- Axis locations of steel bar 2 (X, Y, Z) cm: Top (X=17.8, Y=53, Z=10).
Bottom (X=17.8, Y=53, Z=0).
- Applied current density on the anode: 2.50×10^{-3} mA/cm².

The total boundary element mesh used for the analysis is shown in Figure 8.5.

For clarity, the boundary element mesh on the surface of the steel section and steel bar is also shown in Figure 8.6.

The modelling results and discussion are given in Section 8.3.3.

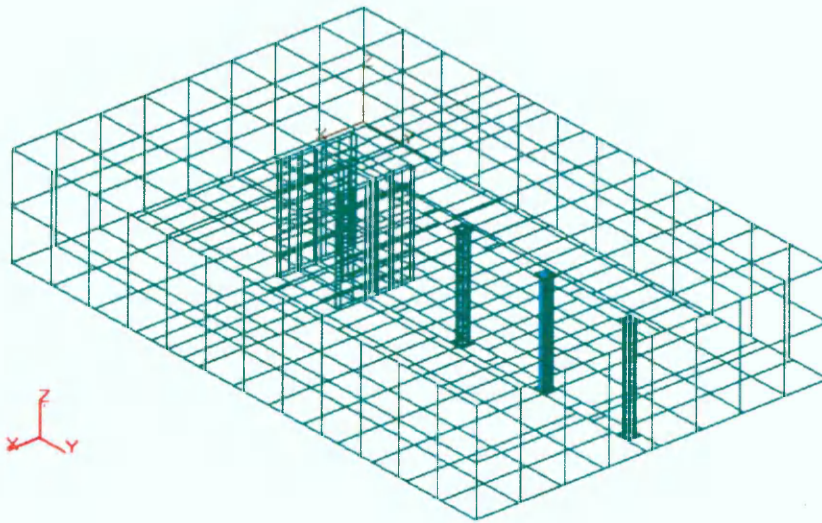


Figure 8.5: Schematic representation of the total boundary element mesh on the surface of sandbox

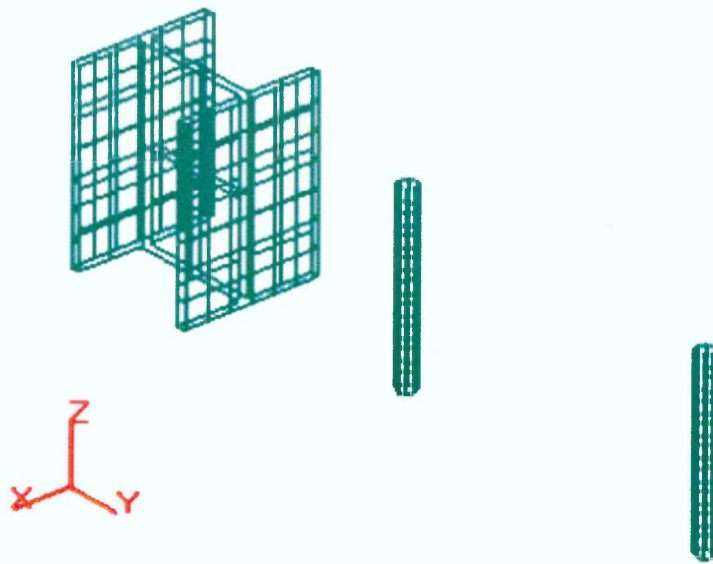


Figure 8.6: Schematic representation of the element mesh on the surface of steel piece and steel bar

8.3.3 Weight Loss of Steel

The boundary element modelling allows cathodic protection interference to be assessed in term of current density, which is directly proportional to corrosion rate. As a consequence, the weight loss of steel can be defined as [Adey and Pei Yuang Pang, 1999]:

$$w = \frac{iM}{nF} \quad (8.7)$$

Where w is the weight loss per unit time per unit area, i is the current density on the steel bar surface), M is the molecular weight of reacting species, n is the number of electrons transferred and F is Faradays.

Therefore the weight loss on discontinuous steel subject to induced stray current corrosion can be calculated based on equation (8.7) once the modelling results have been obtained.

8.3.4 Modelling Results and Discussion

For Case 1, the potential and current density distributions are illustrated in Figures 8.7 to 8.13. For Case 2, the results of the modelling are shown in Figure 8.14 to 8.20.

The results in Figure 8.7 to Figure 8.10 (Case 1) and Figure 8.14 to Figure 8.17 (Case 2) indicate that stray current corrosion cannot be simply identified by analyzing the potential distribution on the surface of the sandbox or steel. This is particularly an important in the analysis of stray current corrosion.

However, the study of normal current density distribution on the surface of Steel Bar 1 and Steel Bar 2 shows that there are two clear areas on the bars that are acting either anodically or cathodically.

In areas of both Steel Bars 1 and 2 which are closest to the anode, the measured current is negative. This means that current is being picked up at this site (cathodic behaviour).

At the same time, the current on the areas which are furthest away from the anode are positive. This reflects a current discharge (anodic behaviour). As a result, corrosion is induced at this area. This is clearly illustrated in both Case 1 (Figures 8.11 to 8.13) and Case 2 (Figures 8.18 to 8.20).

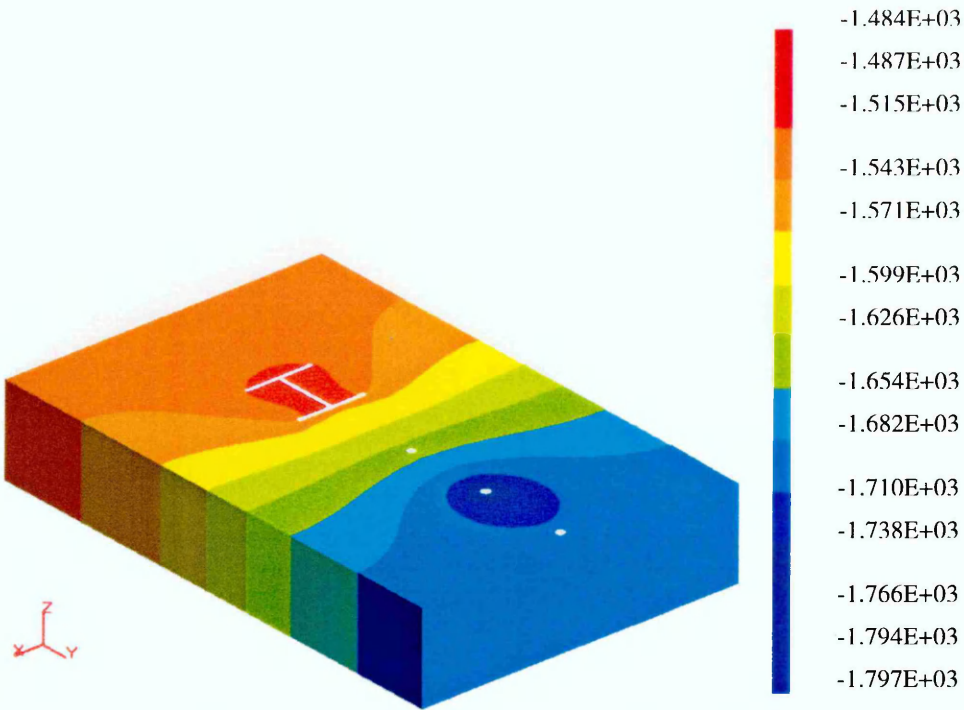


Figure 8.7: Potential distribution on the surface of sandbox (mV vs CSE, Case 1)

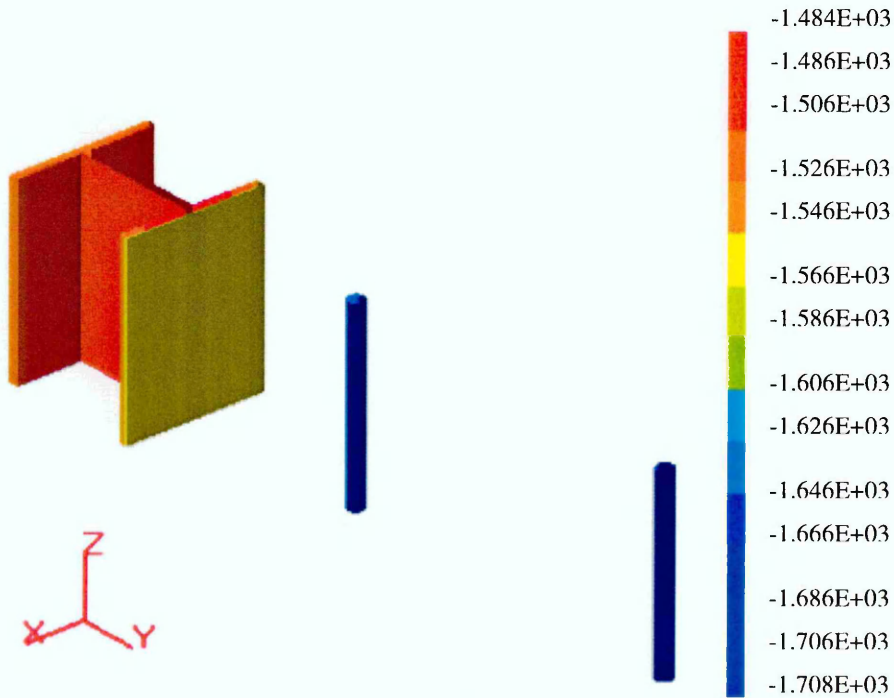


Figure 8.8: Potential distribution on the surface of the steel section and steel bars (mV vs CSE, Case 1)

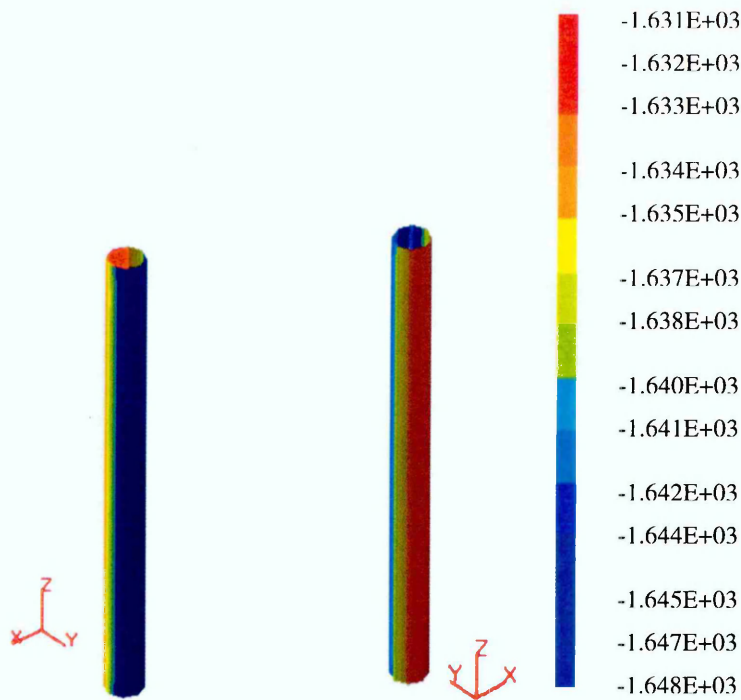


Figure 8.9: Potential distribution on the surface of Steel Bar 1 (mV vs CSE, Case 1)

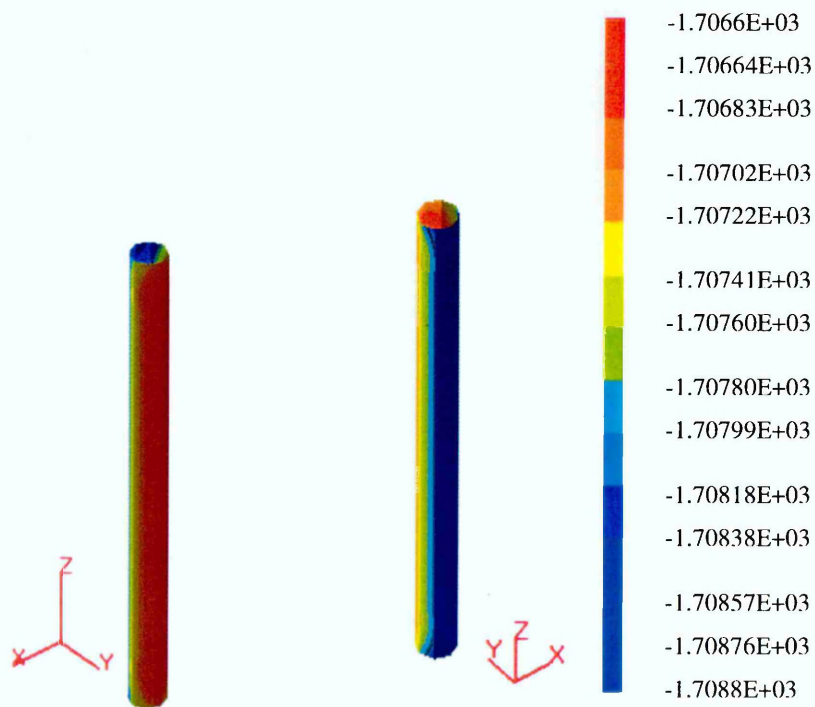


Figure 8.10 Potential distribution on the surface of Steel Bar 2 (mV vs CSE, Case 1)

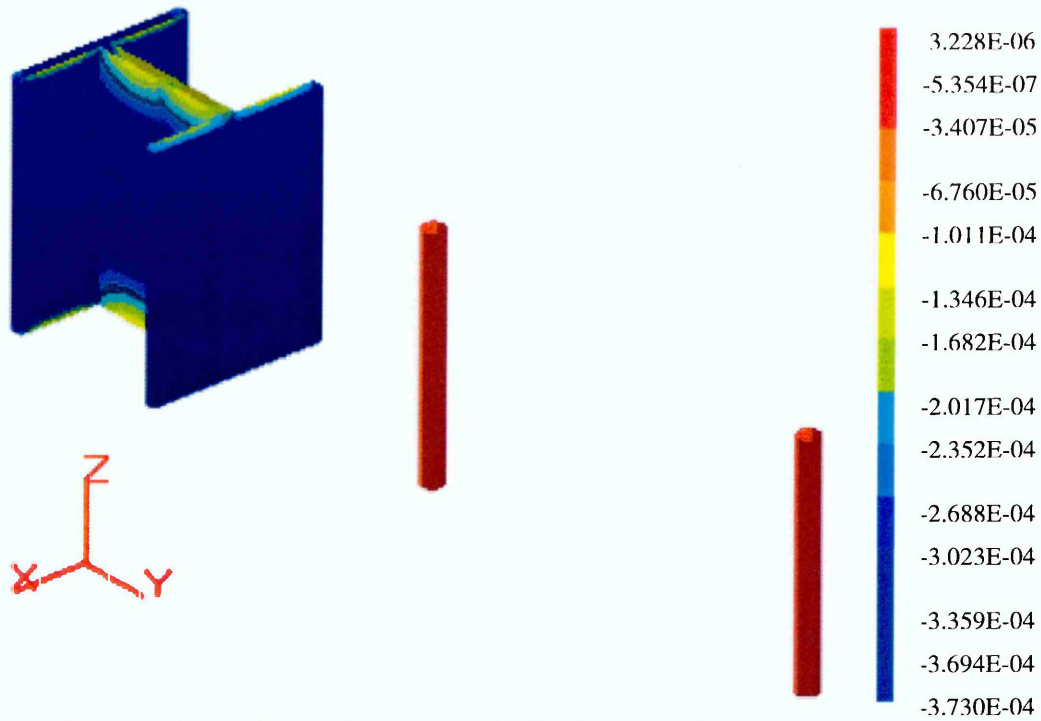


Figure 8.11: Normal current distribution on the surface of steel and steel bars (mA/cm^2 , - current in, + current out, Case 1)

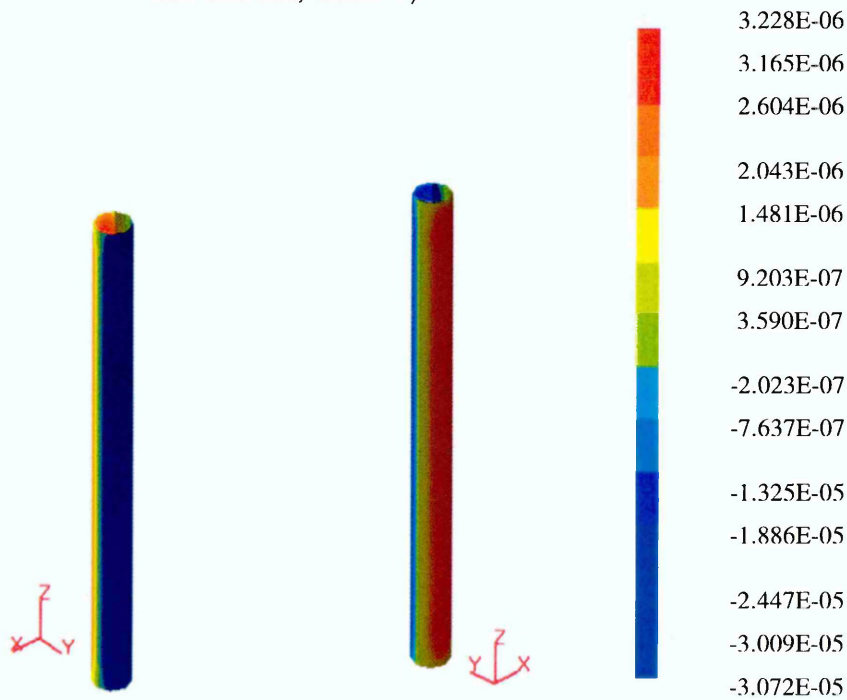


Figure 8.12: Normal current distribution on the surface of steel bar 1 (mA/cm^2 , - current in, + current out, Case 1)

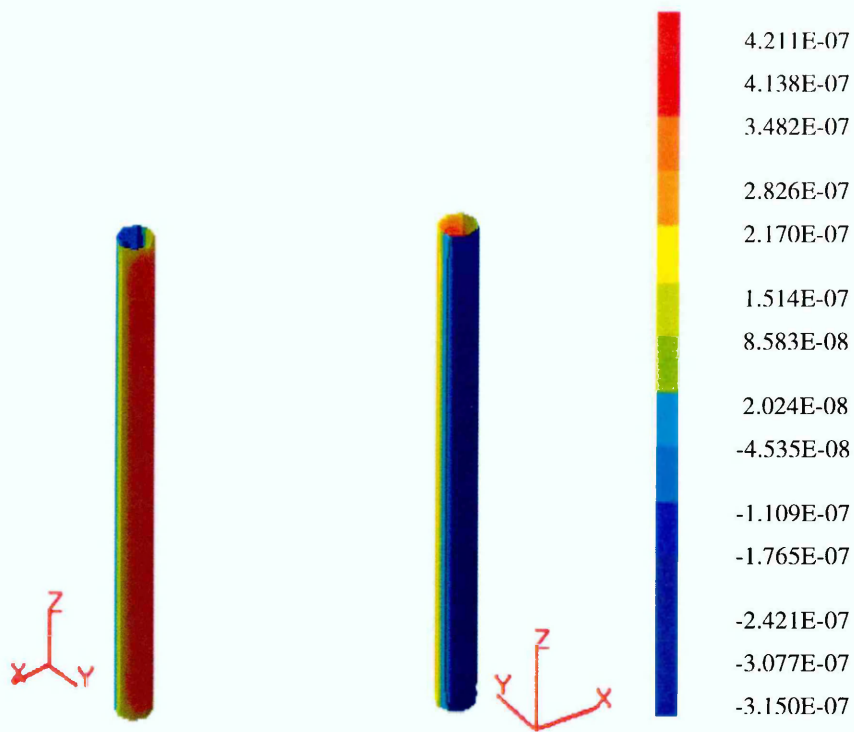


Figure 8.13: Normal current distribution on the surface of Steel Bar 2 (mA/cm², - current in, + current out, Case 1)

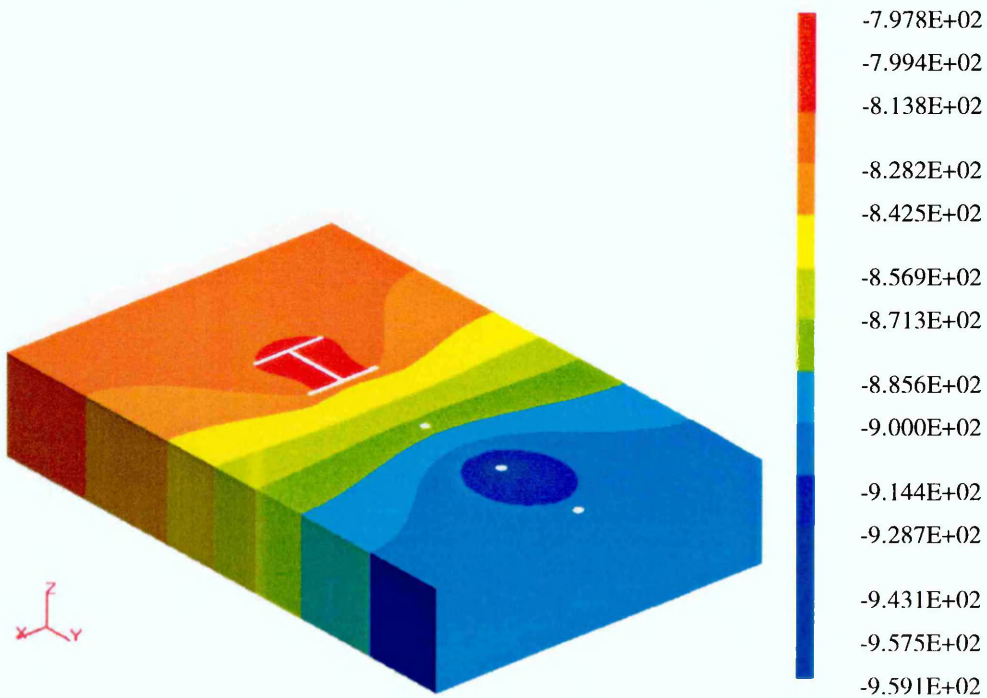


Figure 8.14: Potential distribution on the surface of the sandbox (mV vs CSE, Case 2)

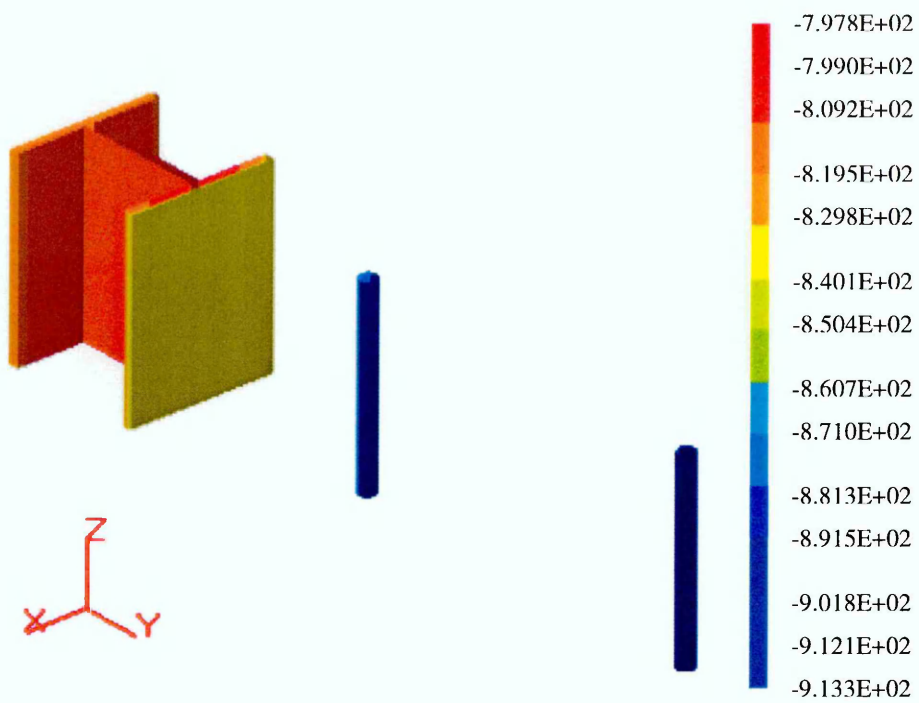


Figure 8.15 Potential distribution on the surface of steel section and steel bars (mV vs CSE, Case 2)

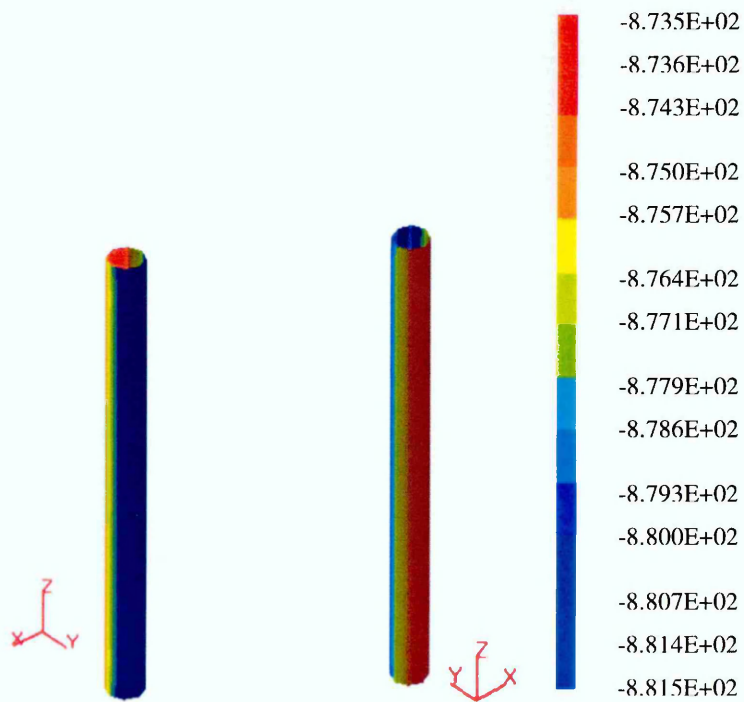


Figure 8.16: Potential distribution on the surface of Steel Bar 1 (mV vs CSE, Case 2)

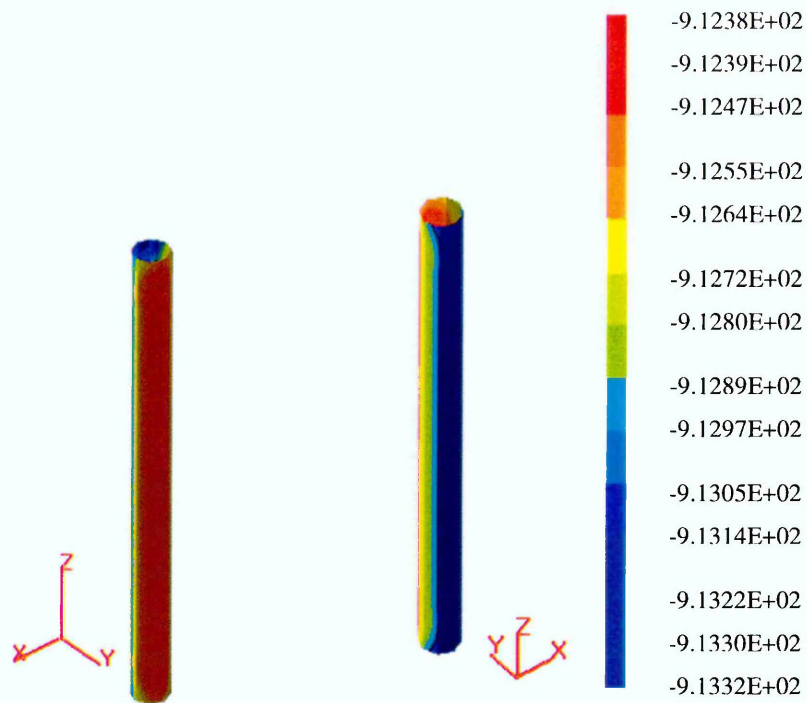


Figure 8.17: Potential distribution on the surface of Steel Bar 2 (mV vs CSE, Case 2)

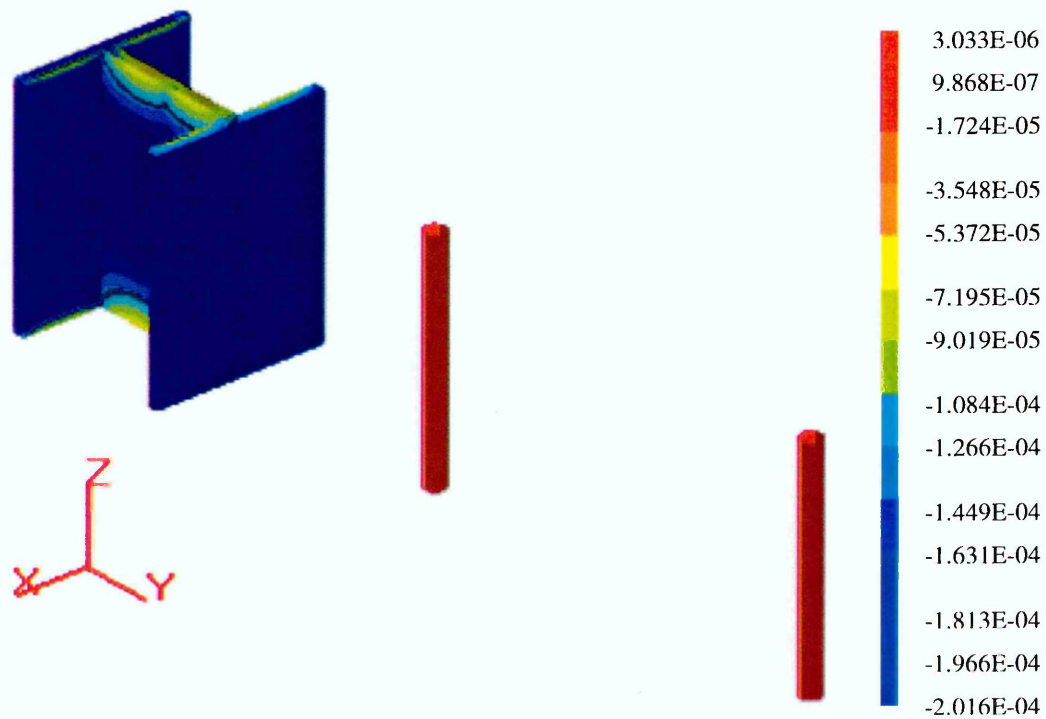


Figure 8.18: Normal current distribution on the surface of steel section and bars (mA/cm², - current in, + current out, Case 2)

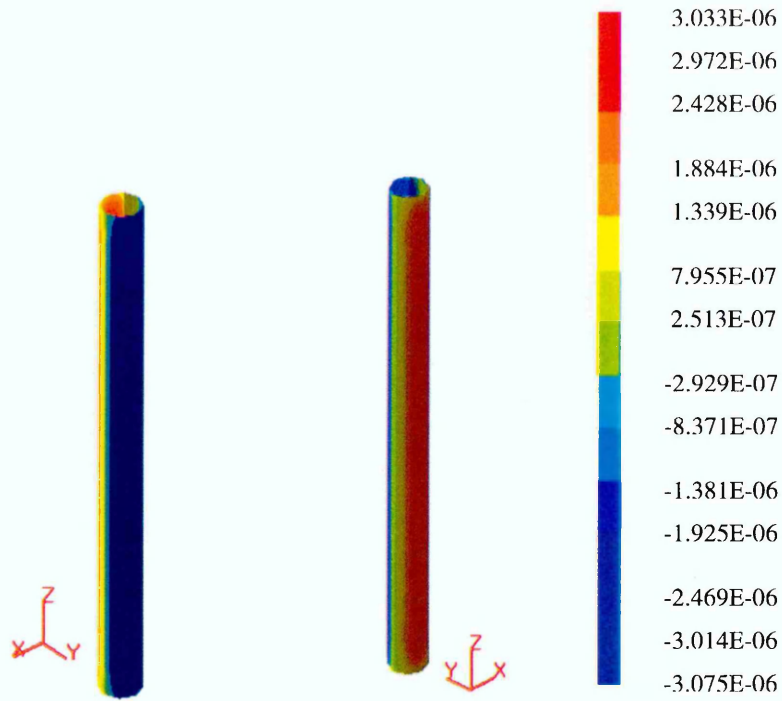


Figure 8.19: Normal current distribution on the surface of Steel Bar 1 (mA/cm², - current in, + current out, Case 2)

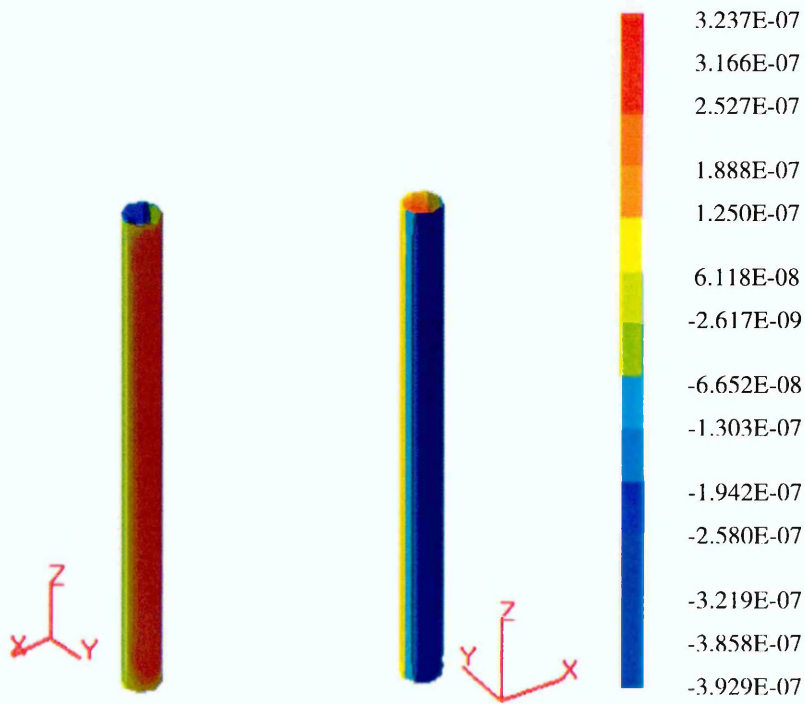


Figure 8.20: Normal current distribution on the surface of Steel Bar 2 (mA/cm², - current in, + current out, Case 2)

The stray current density on the surface of Steel Bar 1 is higher than on the Steel Bar 2 in both Case 1 and Case 2. This is clearly indicated in Figures 8.12 and 8.13 (Case 1) and Figure 8.19 and 8.20 (Case 2). Therefore, it is apparent that the effect of stray current corrosion on Steel Bar 1 is greater than that on Steel Bar 2 in the present study.

This would appear to be because Steel Bar 1 is located directly between the anode and the steel section where the greatest current may be expected to flow. Steel Bar 2, although adjacent to the anode, is not in the direct path between the anode and the steel and as a consequence the extent of current pick-up is greatly reduced.

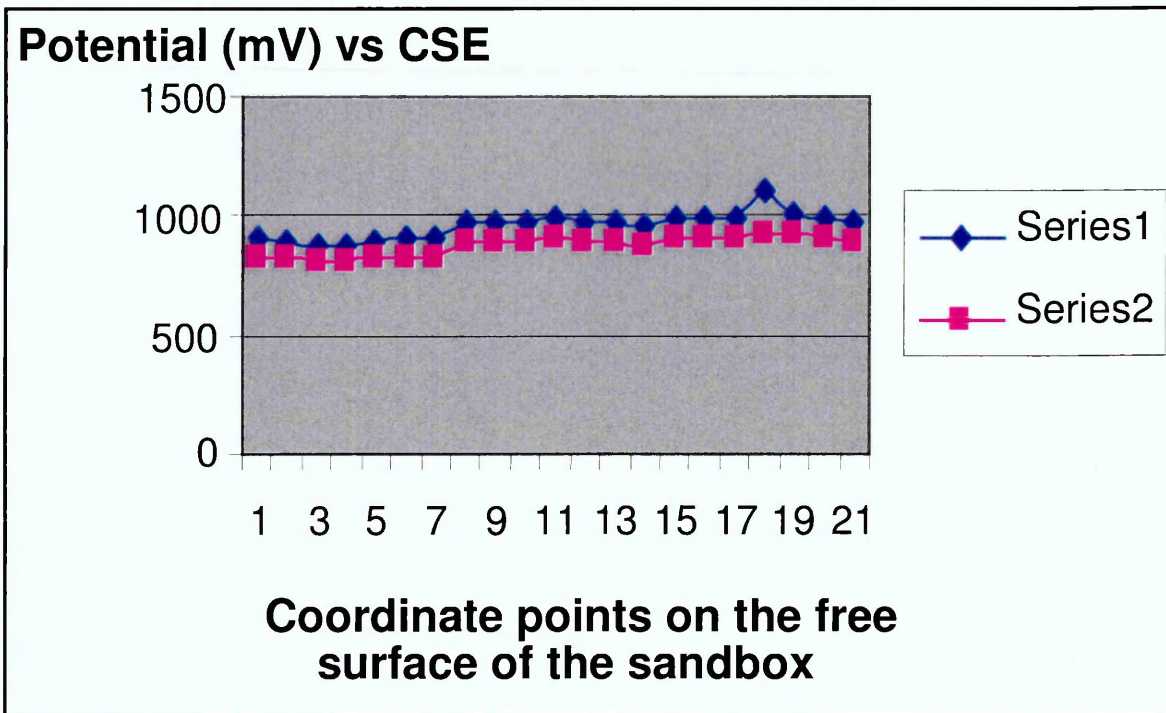


Figure 8.21 Comparison of experimental measurement of potential with boundary element solutions (Case 2).

Note:

- (1) Series 1: Experimental data.
- (2) Series 2: Boundary element results.
- (2) Coordinate of points in accordance with Table 8.1

8.4 Discussion of Boundary Element Modelling with Experimentally Obtained Values

The results of the boundary element modelling in Case 2 are now compared with the experimental measurements in Figure 8.21. While they generally follow the same trend, there is a relatively small difference of around 10 - 12 % in the potential values between the boundary element solutions and the experimental data.

8.5 Conclusions

The results demonstrate that the potential distribution cannot be used to identify or accurately illustrate the effect of stray current corrosion on electrically discontinuous steel.

The boundary element technique can however be used to model stray current corrosion induced by CP interference. It can provide information about the level of interference in terms of current density rather than potential, from which rates of metal loss can be calculated.

Boundary element modelling has therefore been shown to be a useful tool for the analysis of CP interference in steel-framed masonry buildings and may be employed to reduce or remove the risk of stray current corrosion when evaluating or designing ICCP systems for such applications.

Chapter 9:
General Conclusions
&
Recommendations for Further Research

9.1 Introduction

An investigation has been undertaken of the cathodic protection of steel framed masonry structures. The work mainly concentrates on both experiment and boundary element modelling. The findings would be expected to contribute to the development of more formal guidelines and standards for the cathodic protection of steel framed masonry buildings. The following sections outline the major contributions that have been made as well as recommendations for further work.

9.2 General Conclusions

This research programme has contributed to the knowledge base and understanding of cathodic protection of steel framed masonry structures in the following key areas.

9.2.1 Introduction of Boundary Element Technique to the Modelling Cathodic Protection of Steel Framed Masonry Structures

Prior to the present study numerical methods, including the finite difference method, finite element method and boundary element method, had not been employed for modelling the current and potential distributions of steel frame ICCP systems or for analyzing the stray current corrosion in such structures. It was therefore necessary to carry out considerable development in order to obtain an appropriate numerical technique for this relatively new field.

Based on its particular characteristics, the boundary element method was found to be the most appropriate for this type of application. Initially, its basic theory and application in the analysis of cathodic protection systems were discussed. Two computer programs for two- and three-dimensional modelling

of cathodic protection in one region and multi-regions were then developed. These programs have, in turn, allowed the three key activities of this study to be carried out. The first is the modelling of the distributions of protective potential and current. The second is the investigation of the influence of masonry type and joints widths. The final activity is the analysis of stray current corrosion in cathodically protected steel-framed masonry buildings.

This work as described in the previous chapters has shown the boundary element technique to be an effective tool for analysing cathodic protection system for steel framed masonry structures.

9.2.2 Measurement of Steel Polarization Data in Sand and Mortar

In the present study, two representative impressed current cathodic protection systems were constructed in the laboratory. The first employed a sandbox to represent the surrounding masonry. The second used a typical brick and mortar masonry encasement.

As there was no published data for the behaviour of cathodically protected steel under such conditions, it was necessary to investigate and measure polarization data for structural steel sections in sand and various mortar environments.

The experimental results presented in this study will contribute to the understanding of the polarization of steel enclosed in masonry environments. The data which expresses the non-linear relationship between the potential and current density on the anode and cathode surfaces are subsequently used as boundary conditions or electrode kinetics on the surface of steel for

modelling the cathodic protection systems of steel-frame masonry structures, investigating the effects of brick types and joints width on the distribution of the protective potential and current, and analyzing the stray current corrosion resulting from cathodic protection interference in such structures.

9.2.3 Distribution of Impressed Current & Potential of Cathodic Protection Systems

The geometry of the 'I' section beams and columns or stanchions employed in steel framed masonry structures is relatively complex. The understanding of how the protective current and potential are distributed on such element surface plays a very important role when designing the optimum cathodic protection system for such structures.

Information in this area has not been reported in the literature despite over twenty such systems having been completed and commissioned in the UK and US. Most of the knowledge is based on empirical observation and is in the hands of a very small number of specialists.

The investigation undertaken in this study addresses many aspects of the above problem. Based on the results of the experiment and boundary element modelling, the following conclusions have been obtained.

It is evident that the distributions of CP potential and current density are related to the resistivity of electrolyte. For a given current and given anode location, a higher resistivity results in a more non-uniform protective potential of the steel. In addition, the anode position has a significant and demonstrable effect on the distribution of CP potential and current density. Boundary element modelling has shown significant promise as a practical tool for

analysing and optimising the design of cathodic protection system for steel framed masonry structures.

From this it can be concluded that a boundary element approach may be adopted for the modelling and design of cathodic protection systems for remedial applications on steel framed structures.

9.2.4 Effects of Brick Type and Joint Widths on Distributions of Impressed Current and Potential

For any given anode current density, the CP protective current and potential distribution on the steel surface are related to both the anode locations and the resistivity of electrolyte materials. In steel-framed masonry structures, the resistivities of the most solid masonry materials are much higher than the mortars used to join them. The resistivities of the various masonry materials such as brick and Portland stone are also different. Therefore, the understanding of the effect of masonry type and joint width on CP current and potential is essential to the design and optimization of cathodic protection system for steel framed masonry structures.

Such factors have been studied in this work using both experimental methods and boundary element modelling. The two principal conclusions have been drawn from this part of the work. Firstly, the resistivity difference between mortar and brick has been shown to have a significant and measurable effect on the distribution of the potential and current on the steel surface. Low resistivity mortar "attracts" a higher current density, with current flowing preferentially along the path of least resistance. When compared to a homogeneous electrolyte which is assumed to have the same resistivity

throughout, the distribution of potential and current on steel surface in steel framed masonry structures is more non-uniform for a given anode location and anode current. The second conclusion is that boundary element modelling provides a powerful technique for analysing and optimising the design of cathodic protection system for steel framed masonry structures, despite the relative complexity of the structure being protected.

9.2.5 Analysis of Stray Current Corrosion

It is widely recognised that steel-framed masonry buildings contain a variety of discrete, electrically discontinuous metallic elements. The typical items include metal window frames, metal drainage pipes as well as metal fixings such as cramps, lintels and wall ties. When a cathodic protection system is installed to protect the structural members, other items which are within the fabric of the structure but are not in electrical continuity may suffer from stray current interactions, resulting in accelerated corrosion of the discontinuous items.

The results of the experimental and numerical modelling in this study have shown that the potential distribution measured on the surface cannot be accurately used to identify and quantify the effects of stray current corrosion. Modelling using the boundary element technique can provide valuable information about the level of interference in term of current density on the surface of the affected components and is therefore a useful tool for the analysis of CP interference in steel-framed masonry buildings.

9.3 Recommendations for Further Research

The findings from the investigations in this research project have identified a number of areas that could benefit from further research. The following

sections outline the areas in which it is considered additional research, complementary to the present study, could be carried.

9.3.1 Boundary Element Modelling

It is apparent that the two computer programs developed in FORTRAN 90/95 specifically for this study are effective at modelling cathodic protection systems for the steel framed masonry structures for the given anode current and the given anode locations. In order to obtain the optimum anode locations which permit the protective current and potential to be more uniformly distributed on the steel surface, the anode locations need to be manually adjusted. The modelling needs to be repeated for different anode positions until the optimum anode location is identified. Such procedures can be slow and time-consuming.

It would therefore be beneficial to further develop the computer programs so as to allow them to automatically optimise the anode locations for any given set of conditions. Such a program should be able to incorporate existing current and potential distribution data, for example from a trial CP installation, and automatically adjust the anode locations within the model until the optimum results are obtained.

9.3.2 Protection of Non-structural Metalwork

As previously discussed, steel-framed masonry buildings incorporate a variety of non-structural metallic elements such as metal window frame, metal drainage pipes and various metal fixtures and fittings. The protection of this metalwork from corrosion is one of the important tasks in maintaining such structures. Further research in the use of novel techniques such as pulsed

power supplies or electro-osmosis for the protection of electrically discontinuous metalwork while mitigating against stray current corrosion would be invaluable.

Other systems based on mortar encapsulated galvanic anodes such as are currently being employed in the protection of reinforced concrete may also prove to be worthy of further investigation in this area of structural repair.

9.4 Conclusion

This thesis has been principally concerned with improving the understanding of the cathodic protection of steel-framed masonry structures. The work covered both analysis of experimental data and the novel use of boundary element modelling for this application.

It is believed that the output from this work provides a significant contribution to knowledge in this area and will help progress the development of this technology and contribute to the development of formal guidelines and standards for the cathodic protection of steel-framed masonry buildings.

Adey, R.A., Niku, S.M., Brebbia, C.A. and Finnegan, J, Computer Aided Design of Cathodic Protection, Boundary Element Methods VII, Villa Olmo, Lake Como, Italy, Computational Mechanics Publications, Sept. 1985.

Adey, R.A. and Niku, S.M., *Comparison Between Boundary Elements and Finite Elements for CAD of Cathodic Protection Systems*, Boundary Element Technology Conference, South Australian Institute of Technology, Adelaide, Australia, Nov. 1985; Computational Mechanics Publications, Southampton. 1985.

Adey, R.A. and Niku, S.M., *Computational Modelling of Corrosion Using Boundary Element Methods*. Computer Modelling In Corrosion, ASTM STP 1154, R.S. Munn, Ed., American Society for Testing and Materials, Philadelphia, 1992, pp.248-263.

Adey, R.A., Pei Yuan Hang, *Computer Simulation as an Aid to Corrosion Control and Reduction*, Corrosion 99, San Antonio, USA NACE 1999.

Amaya, K., Aoki, S. and Kishimoto, K., *Optimum Location of Electrode in Cathodic Protection System*, Boundary Element Methods, Fundamentals and Applications. International Symposium. pp. 11-13 (1992).

Amaya, K. and Aoki, S., *Optimum Design of Cathodic Protection System by 3D BEM*, Boundary Element Technology, VII, pp.375-388 (1992).

Aoki, S. and Amaya, K., *Optimisation of cathodic protection system by BEM*, *Engineering Analysis with Boundary Elements* 19 pp. 147-156 (1997).

Amaya, K., and Aoki, K., *Effective boundary element methods in corrosion analysis*, *Engineering Analysis with Boundary Elements* 27 pp. 507-519 (2003).

Atkins, C.P., Lambert, P. and Coull, Z.L., *Cathodic Protection of Steel Framed Heritage Structures*, Proceedings of 9th International Conference on Durability of Building Materials and Components, Brisbane Convention & Exhibition Centre, Australia, 17-21 March 2002.

Baboian, R., *Environmental Conditions Affecting Transportation Infrastructure, Materials Performance*, September, 1995.

✓ Baeckmann, W. Van, Schwenk, W. and Prinz, W., *Handbook of Cathodic Corrosion Protection Theory and Practice of Electrochemical Processes*, Third Edition, Gulf Publishing Company, Houston, Texas, 1997.

Berkley K.G.C., and Pathmanaban, S., *Cathodic protection of Reinforced Steel in Concrete*, Butterworths, 1990.

Bertolini L., Elsener B., Pedferri P. and Polder R., *Corrosion of Steel in Concrete, Prevention, Diagnosis, Repair*, WILEY-VCH Verlag GmbH & Co.KgaA, Weinheim, 2004.

Brebbia, C.A., *The Boundary Element Method for Engineers*, Pentech Press, London, 1978.

Brebbia, C.A. and Dominguez, J., *Boundary Elements - An Introductory Course*, McGraw-Hill, New York, 1989.

Brebbia, C.A. and Niku, S.M., *Computational Applications of Boundary Element Methods for Cathodic Protection of Offshore Structures*, OMAE Conference, Houston, Texas, 1988.

Brebbia, C. A., Telles, J.C.F. and Wrobel, L. C., *Boundary Element Techniques, Theory and Applications in Engineering*, Springer Verlag, Berlin and Heidelberg, 1984.

Broomfield, J.P. *Corrosion of Steel in Concrete: Understanding, Investigation and Repair*, E & FN SPON, 1997.

Broomfield, J.P., Langford, P.E. and McAnoy, R., *Cathodic Protection for Reinforced Concrete: its application to buildings and marine structures, Corrosion of Metal in Concrete*, Proceedings of Corrosion/87, NACE, Houston, Texas, pp. 222-235.

Chess, P.M., *Cathodic Protection of Steel in Concrete*, E & FN Spon, 1998.

Cigna, R., Garcia, O., Rocchini, G. and Broglia, M., *Use of Polarization Curves in the Study of Corrosion Mechanism of Steel in Concrete*, Materials Science Forum, 1992, vol. 111-112, pp.667-688.

Daily, S.F. and Somerville, S., *Using Cathodic Protection to control Corrosion of Masonry Clad Steel Framed Buildings*. Corpro Companies Inc., Technical Paper.

Danson, D.J. and Warne, M.A., *Current Density/Voltage Calculations Using Boundary Element Techniques*, NACE Conference, Los Angeles, 1983.

Dawson, J.L. (1983), *Corrosion monitoring of steel in concrete*, (eds By Crane, A.P.) *Corrosion of Reinforcement in Concrete Construction*, Ellis Horwood for Society of Chemical Industry, pp. 175-192.

Decarlo, E.A., *Computer Aided Cathodic Protection Design Technique for Complex Offshore Structures*, Corrosion'82, Paper 165, 1982.

Santana Diaz, E. Adey R.A., *Optimisation of the Performance of an ICCP System by Changing Current Supplied and Position of the Anode*, Boundary Elements XXIV (2002).

Santana Diaz, E. Adey, R.A., *Optimising the Location of Anodes in Cathodic Protection Systems*, Boundary Element Technology, USA, May 2003.

Doig, P. and Flewitt, P.E.J., *A Finite Difference Numerical Analysis of Galvanic Corrosion for Semi-Infinite Linear Coplanar Electrodes*, Journal of the Electrochemical Society, Vol.125, No.12, 1979, pp.2057.

Fleck, R.N., M.Sc. Thesis, University of California, Sept. 1964.

Fontana, M.G., *Corrosion Engineering*, Third Edition, McGraw-Hill, New York, 1978.

Forest, A.W., Wu, J.W. and Biccicchi, R.T., *Validation of Finite-Element Technique for Modelling Cathodic Protection Systems*, NACE National Conference, 1980, Paper 150.

Forest, A.W. and Biccicchi, R., *Cathodic Protection of Bronze Propellers for Copper Nickel Surface Ships*, Corrosion, Vol.27, No.6, 1981, pp.349-357.

Fu, J.W. and Chen, S.K., *Cathodic Protection Design Using an Integral Equation Numerical Method*, Corrosion'82, Paper 163, 1982.

Gartland, P.O. and Johsen, R., SINTEF Report STF F85040, Trondheim, April 1985.

Gartland, P.O. and Johsen, R., COMCAPS-*Computer Modelling of Cathodic Protection Systems*, Corrosion'85. Paper 319, 1985.

Gibbs, P., *Corrosion of Masonry Clad Steel Framed Buildings, Historic Scotland, Technical Conservation Research and Education Division, Technical Advice Note 20*, June 2000.

Gibbs, P., "*Cathodic Protection of Early Steel Framed Buildings*", Corrosion Prevention Association, Monograph No. 7, 2001.

Giorgi, D., Thomas II, V.G. and Kaznoff, A.L., *Numerical Simulation of Impressed Current Cathodic Protection (ICCP) Systems Using Boundary Element Methods*. Computer Modelling In Corrosion, ASTM STP 1154, R.S. Munn, Ed., American Society for Testing and Materials, Philadelphia, 1992, pp.265-276.

Glass G.K. and Buenfeld, N.R., *Theoretical basis for designing reinforced concrete cathodic protection systems*, British Corrosion Journal, Vol.32, No.3 1997, pp.179-184.

Hack H.P., *Atlas of Polarization Diagrams for Naval Materials in Seawater*, Carderock Division, Naval Surface Warfare Centre, Survivability, Structures, and Materials Directorate Technical Report, April 1995.

Hang, P.Y. and Robert, A.A., *Boundary Elements XXI*, C.A. Brebbia. H. Power. Editors, pp.195-206 (1999).

Hassanein, A.M., Glass G.K., and Buenfeld, N.R. , *Potential Current Distribution in Reinforced Concrete Cathodic Protection Systems*, Cement & Concrete Composite, 24, 2002, pp.159-167.

Helle, H.P.E., *The Electrochemical Potential Distribution Around Ships*, The Royal Institution of Naval Architects, W8, 1980, pp.1-10.

Heuze, B., *Cathodic Protection of Steel in Prestressed Concrete. Materials Performance*, November 1965. pp. 57-62.

Holser, R. A., Prentice, G., Pond, R.B. and Guanti, R.J., *Current Distribution in Galvanically Coupled and Cathodically Protected Tubes*, Corrosion, Vol.48, No.4, 1992, pp.332-341.

Jones, D. A., *Principles and Prevention of Corrosion*, Second Edition, Prentice Hall, Upper Saddle River, New York, 1996.

Jones, G., Lambert, P., Bolton P., and Robinson, M., *Hi-Tech Heritage*, Concrete Engineering International, November/December 1999. pp 17-20.

Kasper, R.G., and Pril, M.G, *Electro-galvanic Finite Analysis of Partially Protected Marine Structures*, Corrosion'83 ,Vol.39,No. 5,1983, pp.181-188.

Kelly, R. G., Scully, J. R., Shoesmith, D. W., Buchheit, R. G., *Electrochemical Techniques in Corrosion Science and Engineering*, Marcel Dekker, Inc, New York, 2003.

Klingert, J. A. , Lynn, S. and Toblas, C. W., *Electrochimica Acta*, Vol. 9, pp. 297-311.1964.

Kuhn, R. J. ,Bureau of Standards 73B75. (1928).

Lambert, P., *Corrosion Mechanism - Introduction to Aqueous Corrosion*, Corrosion Prevention Association, Aldershot, UK, 2001.

Lambert, P., *Repairing Reinforced Concrete: An Overview from Preserving Post War Heritage*, The Care and Conservation of Mid-Twentieth Century Architecture" Donhead Publishing for English Heritage, 2001. pp116-127.

McCafferty, E., *Mathematical Analysis of Circular Corrosion Cells Having Unequal Polarization Parameters*, Naval Research Laboratory Technical Report, NRL Report 8107, 1977.

Morgan, J. H., *Cathodic Protection: Its Theory and Practice in the Prevention of Corrosion*, Leonard Hill Limited, 1959.

Munn, R.S., and Clark, J. H. , *Using of Numerical Techniques and Microcomputers to Predict Corrosion Rates on Underground Metallic Structures*. Corrosion' 83, Paper 301, 1983.

Munn, R.S., *Numerical Analysis of Galvanic Systems for Marine Cathodic Protection System Design*, Corrosion '82, Paper 71, 1982.

Munn, R.S. and Devereux, O.F., *Numerical Modelling and Solution of Galvanic Corrosion Systems*, Corrosion, Vol.47, No.8, 1991, pp.618-635.

Niku, S.M. and Adey, A. R., *A CAD System for the Analysis and Design of Cathodic Protection Systems*, Plant Corrosion: Prediction of Materials Performance, Cranfield Institute of Technology, Cranfield, Cranfield, UK, Feb. 1985.

Niku, S.M., Brebbia, C.A. and Adey, R. A. , *BEASY-CP: A CAD System for Mathematical Modelling of Galvanic Corrosion and Cathodic Protection Problems*, CADDMO'86, Washington D.C., Sept.1986; Computational Mechanics Publications, Southampton and Springer-Verlag, Berlin and NY, 1986.

Nisancioglu, K., *Modelling for Cathodic Protection*. Cathodic Protection Theory and Practice, (eds) V. Ashworth and C. Googan) Ellis Horwood Ltd, London 1993. pp.17-49.

Page C.L., Treadaway, K.W.J., *Aspects of the Electrochemistry of Steel in Concrete*, Nature, Vol. 297, No. 5862, pp. 109-115, 13 May 1982.

Parker, M. E, *Pipeline Corrosion and Cathodic Protection, a practical manual for corrosion engineers, technicians, and field personnel*. Gulf Publishing Company, Houston, Texas, 1984.

Rewerts, T., *The Epidemic of Problems in Traditional Masonry Cladding in High- Rise Buildings*, Structural Engineer, October, 2000.

Roberge, P.R., *Handbook of Corrosion Engineering*, McGraw-Hill, 1999.

Scully, J.R. and Bundy, K.J. , "*Electrochemical Methods for the Measurement of Steel Pipe Corrosion Rates in Soil*", *Materials Performance*, April 1985.

Stratful, R.F., *Experimental Cathodic Protection of a Bridge Deck*, *Transportation Research Record 550*, Transportation Research Board, Washington, DC, 1974.

Strommen, R. and Rodland, A., *Corrosion Surveillance of Submarine Pipelines by Electric Field Strength Monitoring*, *Materials Performance*, Oct. 1981, pp. 47-53.

Strommen, R. and Rodland, A., *Computerized Techniques Applied in Design of Offshore Cathodic Protection Systems*. *Materials Performance*, Vol. 20, No.4, 1981, pp.15-20.

Strommen, R., *Advances in Offshore Cathodic Protection Modelling Using Boundary Element Method*. *Materials Performance*, NACE, Feb.1987, pp.23-28.

Strommen, R., *Computer Modelling of Offshore Cathodic Protection Systems: Method and Experience*. *Computer Modelling In Corrosion*, ASTM STP 1154, R.S. Munn, Ed., American Society for Testing and Materials, Philadelphia,1992, pp.229-247.

Strong, G.E., Adey, R.A., and Rudas, R.S., *Computer Prediction of Stray Current Corrosion*, *Australian Corrosion Conference*, Melbourne, November 1997.

Symrl, W. H. and Newman,J., *Current and Potential Distributions in Plating Corrosion Systems*, *Journal of the Electrochemical Society*, Vol.123,No.1, 1976, pp.1423.

Telles, J.C.F. et al., *Boundary Elements for Cathodic Protection Problems*. Boundary Element Methods VII, Villa Olmo, Lake Como, Italy, Computational Mechanics Publications, Sept. 1985.

Trevelyan, J. and Hack, H.P.: *Analysis of Stray Current Corrosion Problems using Boundary Method*. Boundary Element Technology IX, 1994.

Uhlig, Herbert H. and Winston Revie, R., *Corrosion and Corrosion Control*, Third Edition, John Wiley & Sons, New York, 1985.

Waber, J.T., *Mathematical Studies on Galvanic Corrosion, I, Coplanar Electrodes with Negligible Polarization*. Journal of the Electrochemical Society, Vol.101, No.6, 1954, pp.271-276.

Waber, J.T. and Rosenbluth, M., *Mathematical Studies on Galvanic Corrosion, II. Coplanar Electrodes with One Electrode Infinitely Large and with Equal Polarization Parameters*. Journal of the Electrochemical Society, Vol.102, No.6, 1955, pp.344-353.

Waber, J.T., *Mathematical Studies on Galvanic Corrosion, III. Semi-Infinite Coplanar Electrodes with Equal Constant Polarization Parameters*, Journal of the Electrochemical Society, Vol.102, No.7, 1955, pp.420-429.

Waber J.T., and Fagan, B., *Mathematical Studies on Galvanic Corrosion, IV. Influence of Electrolyte Thickness on the Potential and Current Distributions over Coplanar Electrodes using Polarization Parameters*, Journal of the Electrochemical Society, Vol.103, No.1, 1956, pp.64-72.

Wagner, C., *Contribution to the Theory of Cathodic Protection*, Journal of the Electrochemical Society, Vol.99, No.1, 1952, pp.1-12.

Wagner, C., *Theoretical Analysis of Current Density Distribution in Electrolytic Cells*, Journal of the Electrochemical Society, Vol.98, No.3, 1951, pp.116-128.

Warland, EG, *Modern Practical Masonry*, Pitman, London, UK, 1924
(reprinted by Stone Federation, London, UK in 1953, 1986).

Zamani, N.G. , Porter, J.F. and Mufi, A. A., *A Survey of Computational Efforts in the Field of Corrosion Engineering*, International Journal for Numerical Methods in Engineering, Vol. 23, 1986, pp.1295-1311.

Zamani, N.G., *Boundary Element Simulation of Cathodic Protection System in Prototype Ship*, Applied Mathematics and Computation.Vol.26, No.2, 1988.
pp.118-134.

Appendix I:
FORTRAN Modelling Program
Developed for this Study

1.0 Introduction

In this project, the boundary element technique has been employed for modelling cathodic protection of steel framed masonry structures. The programs for one-region and multi-region problems are listed below. They are also listed on the enclosed disc together with the various library subroutines. These programs have been written in FORTRAN 90/95.

2.0 Pre & Post Processing System

To assist with the management and manipulation of the large amounts of data required for analysis it is common practice to use a pre-processor with a graphical interface which assists with the input of data. Similarly, a post-processor that allows the analysis results to be graphically displayed is also of benefit.

In this project the GiD pre- and post-processing package developed by the International Center for Numerical Methods in Engineering has been employed. The academic version can be freely available. It has been designed as a universal, adaptive and user-friendly graphical user interface for geometrical modelling, data input and visualisation of results for all types of numerical simulation programs, including finite element, boundary element and finite difference methods.

Further details can be found at the website <http://gid.cimne.upc.es>.

3.0 Program Developed for One-Region Problems

```
PROGRAM BEM
!-----
!   BEM program
!   for solving one region CP problems
!-----
!USE DFLIB;
USE Utility_lib ; SE Laplace_lib ;USE Integration_lib
IMPLICIT NONE
INTEGER,PARAMETER :: K7=SELECTED_INT_KIND(18)
INTEGER(K7)                :: response
INTEGER, ALLOCATABLE :: Inci(:,:)           ! Element Incidences
INTEGER, ALLOCATABLE :: BCode(:,:), NCode(:) ! Element BC's
INTEGER, ALLOCATABLE :: Ldest(:,:)         ! Element destination vector
INTEGER, ALLOCATABLE :: Ndest(:,:)         ! Node destination vector
```

```

REAL, ALLOCATABLE :: Elres_u(:, :) ! Element results , u
REAL, ALLOCATABLE :: Elres_t(:, :) ! Element results , t
REAL, ALLOCATABLE :: Elcor(:, :) ! Element coordinates
REAL, ALLOCATABLE :: xP(:, :) ! Node co-ordinates
REAL, PARAMETER :: K6=SELECTED_REAL_KIND(18,4931)
REAL(K6), ALLOCATABLE :: dUe(:, :), dTe(:, :), Diag(:, :)
REAL(K6), ALLOCATABLE :: Lhs(:, :), F(:)
REAL(K6), ALLOCATABLE :: u1(:) ! global vector of unknown
CHARACTER (LEN=80) :: Title
INTEGER :: Cdim, Node, m, n, Istat, Nodel, Nel, N dof, Toa
INTEGER :: Nreg, Ltyp, Nodes, Maxe, N dof, N d of s, ndg, NE_u, NE_t
INTEGER :: nod, nd, i, j, k, l, DoF, Pos, Isym, nsym, nsy
REAL, ALLOCATABLE :: Fac(:) ! Factors for symmetry
REAL, ALLOCATABLE :: Elres_te(:, :), Elres_ue(:)
INTEGER, ALLOCATABLE :: Incie(:) ! Incidences for one element
INTEGER, ALLOCATABLE :: Ldeste(:) ! Destination vector 1 elem
REAL :: Con, E, ny, Scat, Scad
!-----
! Read job information
!-----
OPEN (UNIT=1, FILE='INPUT', FORM='FORMATTED') ! Input
OPEN (UNIT=2, FILE='OUTPUT', FORM='FORMATTED') ! Output
Call Jobin(Title, Cdim, N dof, Toa, Nreg, Ltyp, Con, E, ny, &
    Isym, nodel, nodes, maxe)
Nsym= 2**Isym ! number of symmetry loops
ALLOCATE(xP(Cdim, Nodes)) ! Array for node coordinates
ALLOCATE(Inc(Maxe, Nodel)) ! Array for incidences
CALL Geomin(Nodes, Maxe, xP, Inc, Nodel, Cdim)
N dof = Nodel * N dof ! Total degrees of freedom of element
ALLOCATE(BCode(Maxe, N dof)) ! Element Boundary codes
ALLOCATE(Elres_u(Maxe, N dof), Elres_t(Maxe, N dof))
CALL BCinput(Elres_u, Elres_t, Bcode, nodel, n dof, n dof)
ALLOCATE(Ldest(maxe, N dof)) ! Elem. destination vector
ALLOCATE(Ndest(Nodes, N dof))

!-----
! Determine Node destination vector and Element destination vector
!-----
CALL Destination(Isym, Ndest, Ldest, xP, Inc, N d of s, nodes, N dof, Nodel, Maxe)
!-----
! Determine global Boundary code vector
!-----
ALLOCATE(NCode(N d of s))

NCode=0
DoF_o_System: &
DO nd=1, N d of s
    DO Nel=1, Maxe
        DO m=1, N dof
            IF (nd == Ldest(Nel, m) .and. NCode(nd) == 0) THEN
                NCode(nd)= NCode(nd)+BCode(Nel, m)
            END IF
        END DO
    END DO
END DO &
DoF_o_System
IF(N dof ==1)E= Con
CALL Scal(E, xP(:, :), Elres_u(:, :), Elres_t(:, :), Cdim, Scad, Scat)
!Scad=1.
!Scat=1.

ALLOCATE(dTe(N d of s, N dof), dUe(N d of s, N dof)) ! Elem. coef. matrices
ALLOCATE(Diag(N d of s, N dof)) ! Diagonal coefficients
ALLOCATE(Lhs(N d of s, N d of s), F(N d of s), u1(N d of s)) ! global arrays
ALLOCATE(Elcor(Cdim, Nodel)) ! Elem. Coordinates
ALLOCATE(Fac(N dof)) ! Factor for symmetric elements
ALLOCATE(Incie(Nodel)) ! Element incidences

```

ALLOCATE(Ldeste(Ndofe))

! Element destination

```
!-----
! Compute element coefficient matrices
!-----
Lhs(:, :) = 0.0; F(:, :) = 0.0; u1(:, :) = 0.0
Elements_1:&
DO Nel=1,Maxe
  WRITE(2,*)'Element: ',Nel
  Symmetry_loop:&
  DO nsy= 1,Nsym
    Elcor(:, :) = xP(:, Inci(Nel, :))      ! gather element coordinates
    Incie= Inci(nel, :)                  ! incidences
    Ldeste= Ldest(nel, :)                ! and destinations
    Fac(1:nodel*ndof)= 1.0
    Elres_te(:)=Elres_1(Nel, :)
    IF(Isym > 0) THEN
      CALL Mirror(Isym, nsy, Nodes, Elcor, Fac, Incie, Ldeste, Elres_te, Elres_ue &
        , nodel, ndof, Cdim)
    END IF
    IF(Cdim == 2) THEN
      IF(Ndof == 1) THEN
        CALL Integ2P(Elcor, Incie, Nodel, Nodes, xP, Con, dUe, dTe, Ndest, Isym)
      ELSE
        CALL Integ2E(Elcor, Incie, Nodel, Nodes, xP, E, ny, dUe, dTe, Ndest, Isym)
      END IF
    ELSE
      CALL Integ3(Elcor, Incie, Nodel, Nodes, xP, Ndof &
        , E, ny, Con, dUe, dTe, Ndest, Isym)
    END IF
    CALL Assembly(Lhs, F, DTe, DUe, Ldeste, BCode(Nel, :), Ncode &
      , Elres_u(Nel, :), Elres_te, Diag, Ndofe, Ndof, Nodel, Fac)
  END DO &
  Symmetry_loop

!WRITE(2,*) "DTe"
!WRITE(2, '(8F12.5)') (DTe)
!WRITE(2,*) ""
!WRITE(2,*) "DUe"
!WRITE(2, '(8F12.5)') (DUe)
!WRITE(2,*) ""

END DO &
Elements_1
!-----
! Add azimuthal integral for infinite regions
!-----
IF(Nreg == 2) THEN
  DO m=1, Nodes
    DO n=1, Ndof
      IF(Ndest(m, n) == 0) CYCLE
      k=Ndest(m, n)
      ! k=Ndof*(m-1)+n
      Diag(k, n) = Diag(k, n) + 1.0
    END DO
  END DO
END IF
!-----
! Add Diagonal coefficients
!-----
DO m=1, Ndofs      ! Loop over collocationpoints
  Nod=0
  DO n=1, Nodes
    DO l=1, Ndof
      IF (m == Ndest(n, l)) THEN
        Nod=n
        EXIT
      END IF
    END DO
  END DO
END DO
```

```

        END IF
    END DO
    IF (Nod /= 0)EXIT
END DO
DO k=1,Ndof
    DoF=Ndest(Nod,k)
    IF(DoF /= 0) THEN
        IF(NCode(DoF) == 1) THEN
            Nel=0
            Pos=0
            DO i=1,Maxe
                DO j=1,Ndofe
                    IF(DoF == Ldest(i,j))THEN
                        Nel=i
                        Pos=j
                        EXIT
                    END IF
                END DO
            END DO
            IF(Nel /= 0)EXIT
        END DO
        F(m) = F(m) - Diag(m,k) * Elres_u(Nel,Pos)
    ELSE
        Lhs(m,DoF)= Lhs(m,DoF) + Diag(m,k)
    END IF
END IF
END DO
END DO
!-----
! Solve system of equations
!-----
!DO n=1, Ndofs
! WRITE(2,'(8F12.5)') (Lhs(n,:))
!END DO
!WRITE(2,*) ""
!WRITE(2,'(8F12.5)') (F)

CALL MNEWT(Lhs,F,u1,n)
CLOSE(UNIT=2)
OPEN (UNIT=2,FILE='BERESULTS',FORM='FORMATTED')
! Gather Element results from global result vector u1
Elements_2: &
DO nel=1,maxe
    D_o_F1: &
    DO nd=1,Ndofe
        IF(Ldest(nel,nd) /= 0)THEN
            IF(NCode(Ldest(nel,nd)) == 0) THEN
                Elres_u(nel,nd) = Elres_u(nel,nd) + u1(Ldest(nel,nd))
            ELSE
                Elres_t(nel,nd) = Elres_t(nel,nd) + u1(Ldest(nel,nd))
            END IF
        END IF
    END DO &
    D_o_F1
    Elres_u(nel,:)= Elres_u(nel,:) * Scad
    Elres_t(nel,:)= Elres_t(nel,:) / Scad
    WRITE(2,'(24F12.5)') (Elres_u(nel,m), m=1,Ndofe)
    WRITE(2,'(24F12.5)') (Elres_t(nel,m), m=1,Ndofe)
END DO &
Elements_2

!response = MESSAGEBOXQQ('Program finished'C,'General Purpose Program'C, MBSICONASTERISK)
END PROGRAM

```

4.0 Program Developed for Multi-Region Problems

```

PROGRAM MRBEM
!-----
! BEM program for solving CP problems
! with multiple regions
!-----
USE Utility_lib; USE Laplace_lib; USE Integration_lib; USE Stiffness_lib
IMPLICIT NONE
INTEGER,PARAMETER ::K7=SELECTED_INT_KIND(18)
INTEGER(K7) :: response
INTEGER, ALLOCATABLE :: NCode(:,:) ! Element BC's
INTEGER, ALLOCATABLE :: Ldest_KBE(:) ! Interface destination vector for region assembly
INTEGER, ALLOCATABLE :: TypeR(:) ! Type of BE-regions (1 == finite, 2 == Infinite)
REAL, ALLOCATABLE :: Elcor(:,:) ! Element coordinates
REAL, ALLOCATABLE :: xP(:,:) ! Node co-ordinates
REAL, ALLOCATABLE :: Elres_u(:,:) ! Element results
REAL, ALLOCATABLE :: Elres_t(:,:) ! Element results
REAL,PARAMETER ::K6=SELECTED_REAL_KIND(18,4931)
REAL(K6), ALLOCATABLE :: KBE(:,,:) ! Region stiffness
REAL(K6), ALLOCATABLE :: A(:,,:) ! Results due to ui=1
REAL(K6), ALLOCATABLE :: Lhs(:,,:),Rhs(:) ! global matrices
REAL(K6), ALLOCATABLE :: uc(:) ! interface unknown
REAL(K6), ALLOCATABLE :: ucr(:) ! interface unknown (region)
REAL(K6), ALLOCATABLE :: tc(:) ! interface tractions
REAL(K6), ALLOCATABLE :: xf(:) ! free unknown
REAL(K6), ALLOCATABLE :: tcxf(:) ! unknowns of region
REAL, ALLOCATABLE :: XpR(:,:) ! Region node coordinates
REAL, ALLOCATABLE :: ConR(:) ! Conductivity of regions
REAL :: E,ny,Con !
INTEGER,ALLOCATABLE :: InciR(:,:) ! Global node numbers / region / local sequence
INTEGER,ALLOCATABLE :: Incie(:,:) ! Element incidences (global) of system
INTEGER,ALLOCATABLE :: IncieR(:,:) ! Element incidences (local) of region
INTEGER,ALLOCATABLE :: ListC(:) ! List of interface nodes
INTEGER,ALLOCATABLE :: ListEC(:,:) ! List of interface Elements / region
INTEGER,ALLOCATABLE :: ListEF(:,:) ! List of free Elements / region
INTEGER,ALLOCATABLE :: LdestR(:,:) ! Global D.o.F. numbers / region / local sequence
INTEGER, ALLOCATABLE :: Nbel(:) ! Number of Boundary Elements each region
INTEGER,ALLOCATABLE :: NbelC(:) ! Number of Interfacelements / region
INTEGER,ALLOCATABLE :: NbelF(:) ! Number of free elements / region
INTEGER, ALLOCATABLE :: Bcode(:,:) ! Boundary code for all elements
INTEGER, ALLOCATABLE :: Ldeste(:,:) ! Destination Vector global of System
INTEGER, ALLOCATABLE :: LdesteR(:,:) ! Destination Vector local of all regions
INTEGER, ALLOCATABLE :: NodeR(:) ! No. of nodes of Region
INTEGER, ALLOCATABLE :: NodeC(:) ! No. of nodes of Interface / region
INTEGER, ALLOCATABLE :: ListR(:,:) ! List of Elementnumbers each region
INTEGER, ALLOCATABLE :: Ndest(:,:)
INTEGER :: Cdim ! Cartesian dimension
INTEGER :: Nodes ! No. of nodes of System
INTEGER :: Nodel ! No. of nodes per element
INTEGER :: Ndofe ! D.o.F's of Element
INTEGER :: Ndof ! No. of degeres of freedom per node
INTEGER :: Ndofs ! D.o.F's of System
INTEGER :: NdofR ! Number of D.o.F. of region
INTEGER :: NdofC ! Number of interface D.o.F. of region
INTEGER :: NdofF ! Number D.o.F. of free nodes of region
INTEGER :: NodeF ! Number of free Nodes of region
INTEGER :: NodesC ! Total number of interface nodes of System
INTEGER :: NdofsC ! Total number of interface D.o.F. of System
INTEGER :: Nregs ! Number of regions
INTEGER :: Ltyp ! Element type(linear = 1, quadratic = 2)
INTEGER :: Isym ! Symmetry code
INTEGER :: Maxe ! Number of Elements of System
INTEGER :: nr,nb,nc,nel,nel
INTEGER :: n,node,is,nc,no,ro,co
INTEGER :: k,m,nd,nrow,ncln,DoF_KBE,DoF

```

CHARACTER(LEN=80)

:: Title

```
!-----
! Read job information
!-----
OPEN (UNIT=1,FILE='INPUT',FORM='FORMATTED') ! Input
OPEN (UNIT=2,FILE='OUTPUT',FORM='FORMATTED')! Output
Call JobinMR(Title,Cdim,Ndof,Toa,Ltyp,Isym,nodel,nodes,maxe)
Ndofs= Nodes * Ndof           ! D.O.F's of System
Ndofe= Nodel * Ndof           ! D.O.F's of Element
Isym= 0 ! no symmetry considered here
ALLOCATE(Ndest(Nodes,Ndof))
Ndest= 0
READ(1,*)Nregs
ALLOCATE(TypeR(Nregs),Nbel(Nregs),ListR(Nregs,Maxe))
IF(Ndof == 1)THEN
  ALLOCATE(ConR(Nregs))
ELSE
  ALLOCATE(ER(Nregs),nyR(Nregs))
END IF
CALL Reg_Info(Nregs,ToA,Ndof,TypeR,ConR,ER,nyR,Nbel,ListR)
ALLOCATE(xP(Cdim,Nodes)) ! Array for node coordinates
ALLOCATE(Incie(Maxe,Nodel)) ! Array for incidences
CALL Geomin(Nodes,Maxe,xp,Incie,Nodel,Cdim)
ALLOCATE(BCode(Maxe,Ndofe))
ALLOCATE(Elres_u(Maxe,Ndofe),Elres_t(Maxe,Ndofe))
CALL BCinput(Elres_u,Elres_t,Bcode,nodel,ndofe,ndof)
!-----
! Determine Element destination vector for assembly
!-----
ALLOCATE(Ldeste(Maxe,Ndofe))
Elements_of_region2:&
DO Nel=1,Maxe
  k=0
  DO n=1,Nodel
    DO m=1,Ndof
      k=k+1
      IF(Ndof > 1) THEN
        Ldeste(Nel,k)= ((Incie(Nel,n)-1)*Ndof + m)
      ELSE
        Ldeste(Nel,k)= Incie(Nel,n)
      END IF
    END DO
  END DO
END DO &
Elements_of_region2
!-----
! Detect interface elements,
! assign interface boundary conditions
! Determine number of interface nodes
!-----
ALLOCATE(ListC(Nodes))
NodesC=0
ListC=0
Elements_loop: &
DO ne=1,Maxe
  Elements_loop1: &
  DO nel=ne+1,Maxe
    IF(Match(Incie(nel,:),Incie(ne,:))) THEN
      BCode(ne,:)= 2 ; BCode(nel,:)= 2 ! assign interface BC
      Element_nodes: &
      DO n=1,nodel
        Node= Incie(nel,n)
        is= 0
        Interface_nodes: &
        DO nc=1,NodesC
          IF(Node == ListC(nc)) is= 1
        END DO
      END DO
    END IF
  END DO
END DO &
```

```

        END DO &
        Interface_nodes
        IF(is == 0) THEN
            NodesC= NodesC + 1
            ListC(NodesC)= Node
        END IF
    END DO &
    Element_nodes
    EXIT
END IF
END DO &
Elements_loop1
END DO &
Elements_loop
NdofsC= NodesC*N dof
ALLOCATE(InciR(Nregs,Nodes),InciR(Maxe,Nodel))
ALLOCATE(KBE(Nregs,NdofsC,NdofsC),A(Nregs,Ndofs,Ndofs))
ALLOCATE(Lhs(NdofsC,NdofsC),Rhs(NdofsC),uc(NdofsC),tc(NdofsC))
ALLOCATE(NodeR(Nregs),NodeC(Nregs))
ALLOCATE(ListEC(Nregs,maxe))
ALLOCATE(ListEF(Nregs,maxe))
ALLOCATE(LdesteR(Maxe,Ndofe)) ! Elem. destination vector
ALLOCATE(Ldest_KBE(Ndofs))
ALLOCATE(NCode(Nregs,Ndofs))
ALLOCATE(LdestR(Nregs,Ndofs))
ALLOCATE(NbelC(Nregs))
ALLOCATE(NbelF(Nregs))

LdesteR= 0
Ncode= 0
NbelF= 0
NbelC= 0
!-----
! Assign local (region) numbering
! and incidences of BE in local numbering
!-----
ListEC= 0
ListEF= 0
DoF_KBE= 0
Regions_loop_1: &
DO nr=1,Nregs
    node= 0
    Elements_of_region: &
    DO nb=1,Nbel(nr)
        ne= ListR(nr,nb)
        Interface_elements: &
        IF(Bcode(ne,1) == 2) THEN
            NbelC(nr)= NbelC(nr) + 1
            ListEC(nr,NbelC(nr))= ne
            Nodes_of_Elem: &
            DO n=1,Nodel
! check if node has already been entered
                is=0
                DO no=1,node
                    IF(InciR(nr,no) == Incie(ne,n)) THEN
                        is= 1
                        EXIT
                    END IF
                END DO
                IF(is == 0) THEN
                    node=node+1
                    InciR(nr,node)= Incie(ne,n)
                    IncieR(ne,n)= node
                ELSE
                    IncieR(ne,n)= no
                END IF
            END DO &
        END DO &
    END DO &
END DO &

```

```

      Nodes_of_Elem
    END IF &
    Interface_elements
  END DO &
  Elements_of_region
  NodeC(nr)= Node          ! No of interface nodes of Region nr
  N dofC= NodeC(nr)*N dof  ! D.o.F. at interface of Region nr
  Elements_of_region1: &
  DO nb=1,Nbel(nr)
    ne= ListR(nr,nb)
    Free_elements: &
    IF(Bcode(ne,1) /= 2) THEN
      NbelF(nr)= NbelF(nr) + 1
      ListEF(nr,NbelF(nr))= ne
      Nodes_of_Elem1: &
      DO n=1,Nodel
        is=0
        DO no=1,node
          IF(InciR(nr,no) == Incie(ne,n)) THEN
            is= 1
            EXIT
          END IF
        END DO
        IF(is == 0) THEN
          node=node+1
          InciR(nr,node)= Incie(ne,n)
          IncieR(nc,n)= node
        ELSE
          IncieR(nc,n)= no
        END IF
      END DO &
      Nodes_of_Elem1
    END IF &
    Free_elements
  END DO &
  Elements_of_region1
  NodeR(nr)= node        ! number of nodes per region
  !-----
  ! Determine Local Element destination vector
  !-----
  Elements:&
  DO Nel=1,Nbel(nr)
    k=0
    ne= ListR(nr,Nel)
    DO n=1,Nodel
      DO m=1,N dof
        k=k+1
        IF(N dof > 1) THEN
          LdesteR(ne,k)= ((InciR(ne,n)-1)*N dof + m)
        ELSE
          LdesteR(ne,k)= IncieR(ne,n)
        END IF
      END DO
    END DO
  END DO &
  Elements
  !-----
  ! Determine Local Node destination vector
  !-----
  n= 0
  DO no=1, NodeR(nr)
    DO m=1, N dof
      n= n + 1
      LdestR(nr,n)= (InciR(nr,no)-1) * N dof + m
    END DO
  END DO

```

```

!-----
! Determine global Boundary code vector for assembly
!-----
      N dofR= NodeR(nr)*N dof                      ! Total degrees of freedom of region
      DoF_o_System: &
      DO nd=1,N dofR
        DO Ncl=1,N bel(nr)
          ne=ListR(nr,Ncl)
          DO m=1,N dof
            IF (nd == LdesteR(ne,m) .and. NCode(nr,nd) == 0) THEN
              NCode(nr,nd)= NCode(nr,nd)+BCode(ne,m)
            END IF
          END DO
        END DO
      END DO &
      DoF_o_System
END DO &
Regions_loop_1

Regions_loop_2: &
DO nr=1,N regs
!-----
! allocate coordinates in local(region) numbering
!-----
      ALLOCATE(XpR(Cdim,NodeR(nr)))
      Region_nodes: &
      DO Node=1,NodeR(nr)
        XpR(:,Node)= Xp(:,InciR(nr,node))
      END DO &
      Region_nodes
!-----
! Determine interface destination vector for region assembly
!-----
      No_o_Interfaceelements:&
      DO n=1, N belC(nr)
        ne= ListEC(nr,n)
        DoF_o_Element:&
        DO m=1, N dof
          DoF= Ldeste(ne,m)
          IF(Ldest_KBE(DoF) == 0)THEN
            DoF_KBE= DoF_KBE + 1
            Ldest_KBE(DoF)= DoF_KBE
          END IF
        END DO DoF_o_Element
      END DO No_o_Interfaceelements
      N dofR= NodeR(nr)*N dof                      ! Total degrees of freedom of region
      N dofC= NodeC(nr)*N dof                      ! D.o.F. of interface of Region nr
      E=ER(nr)
      ny=nyR(nr)
CALLStiffness_BEM(nr,XpR,Nodel,N dof,N dof,NodeR,Ncode(nr,:),N dofR,N dofC,&
KBE(nr,:,:),A(nr,:,:),tc,Cdim,Elres_u,Elres_t,InciR,LdesteR,N bel,ListR,TypeR,Bcode&
,Con,E,ny,N dest,Isym)
      DO ro=1,N dofC
        DoF= LdestR(nr,ro)
        Nrow= Ldest_KBE(DoF)
        Rhs(Nrow)= Rhs(Nrow) + tc(ro)
        DO co=1, N dofC
          DoF= LdestR(nr,co)
          Ncln= Ldest_KBE(DoF)
          Lhs(Nrow,Ncln)= Lhs(Nrow,Ncln) - KBE(nr,ro,co)
        END DO
      END DO
      DEALLOCATE (XPR)
END DO &
Regions_loop_2
DEALLOCATE(tc)
!-----

```

```

! solve for interface unknown
!-----
CALL Solve(Lhs,Rhs,uc)
!-----
! compute and add effect of interface displ.
!-----
Regions_loop_3: &
DO nr=1,Nregs
! gather region interface displacements
N dofC= NodeC(nr)*N dof
  ALLOCATE(ucr(N dofC))
Interface_dof: &
  DO n=1,N dofC
    DoF= LdestR(nr,n)
    ucr(n)= uc(Ldest_KBE(DoF))
  END DO &
Interface_dof
!-----
! Store Interfacedisplacements into Elres_u
!-----
Interface_DoF1:&
DO nd=1, N dofC
  DO n=1, Nbel(nr)
    ne=ListR(nr,n)
    DO m=1, N dofe
      IF(nd == Ldester(ne,m))THEN
        Elres_u(ne,m)= Elres_u(ne,m) + ucr(nd)
      END IF
    END DO
  END DO
END DO Interface_DoF1
! effects of interface displacement in local (region) numbering
N dofR= NodeR(nr)*N dof
N dofF= (NodeR(nr) - NodeC(nr))*N dof ! d.o.F , free nodes
ALLOCATE(tc(N dofC),xf(N dofF),tcxf(N dofR))
tc= 0.0; xf= 0.0; tcxf= 0.0
tc= Matmul(KBE(nr,1:N dofC,1:N dofC),ucr)
xf= Matmul(A(nr,1:N dofF,1:N dofC),ucr)
tcxf(1:N dofC)= tc
tcxf(N dofC+1:N dofR)= xf
!-----
! Store Interfacetractions into Elres_t
!-----
DO nd=1, N dofC
  DO n=1, NbelC(nr)
    ne=ListEC(nr,n)
    DO m=1, N dofe
      IF(nd == Ldester(ne,m))THEN
        Elres_t(ne,m)= Elres_t(ne,m) + tcxf(nd)
      END IF
    END DO
  END DO
END DO
!-----
! Store Results of free nodes into Elres_u or Elres_t
!-----
DO nd=N dofC+1, N dofR
  DO n=1, NbelF(nr)
    ne=ListEF(nr,n)
    DO m=1, N dofe
      IF(nd == Ldester(ne,m))THEN
        IF(Ncode(nr,nd) == 0)THEN
          Elres_u(ne,m)= Elres_u(ne,m) + tcxf(nd)
        ELSE IF(Bcode(ne,m) == 1)THEN
          Elres_t(ne,m)= Elres_t(ne,m) + tcxf(nd)
        END IF
      END IF
    END IF
  END IF
END IF

```

```

        END DO
    END DO
END DO
Elements_of_region3: &
DO nb=1,Nbel(nr)
    ne= Listr(nr,nb)
    Element_Dofr: &
    DO nd=1,Ndofe
        IF(Ncode(nr,LdesteR(nc,nd)) == 2) THEN
            Elres_t(ne,nd)= Elres_t(ne,nd) + tcxf(LdesteR(ne,nd))
        ELSE IF(Ncode(nr,LdesteR(ne,nd)) == 1) THEN
            Elres_t(ne,nd)= Elres_t(nc,nd) + tcxf(LdesteR(nc,nd))
        ELSE IF(Ncode(nr,LdesteR(ne,nd)) == 0) THEN
            Elres_u(ne,nd)= Elres_u(ne,nd) + tcxf(LdesteR(ne,nd))
        END IF
    END DO &
    Element_Dofr
END DO &
Elements_of_region3
    DEALLOCATE(tc,xf,tcxf,ucr)
END DO &
Regions_loop_3
!-----
! Print out results
!-----
CLOSE(UNIT=2)
OPEN(UNIT=2,FILE= 'BERESULTS',FORM='FORMATTED')
Elements_all: &
DO nel=1,Maxe
    WRITE(2,*) ' Results, Element ',nel
    WRITE(2,*) 'u=' , (Elres_u(nel,m), m=1,Ndofe)
    WRITE(2,*) 't=' , (Elres_t(nel,m), m=1,Ndofe)
END DO &
Elements_all
END PROGRAM MRBEM

```

The listings of these programs, plus the associated library sub-routines, are available on the enclosed disc.

Appendix II:
Reprint of Peer-Reviewed Paper from the Proceedings of the
Second International Conference on Maritime Heritage,
April 2005, Barcelona, Spain.

Electrochemical methods for the preservation of masonry clad structural frames

P. Lambert & Y-Y. Wu

*Centre for Infrastructure Management,
Sheffield Hallam University, United Kingdom*

Abstract

A large number of historic structures incorporate wrought iron or early steel components within the masonry. Generally these were incorporated at the time of construction or in later refurbishments to enhance the structural integrity or fire resistance of the buildings. With time and in the presence of moisture and oxygen, the ferrous component starts to corrode and the voluminous corrosion products cause cracking and spalling of the surrounding masonry.

The traditional method of dealing with such problems has been to remove the affected masonry and treat or replace the corroded metalwork prior to reinstatement. This is not only expensive but involves the removal of large amounts of original masonry which may have to be replaced with modern equivalents. A more effective and sensitive option is available through the use of electrochemical treatments, specifically cathodic protection which was originally developed by Sir Humphry Davy in the early 19th century for the preservation of naval vessels.

This paper discusses the development of the technology from early naval trials to recent development for use on heritage buildings and introduces the numerical methods for modelling of cathodic protection systems that assist in the design optimisation of such systems for protecting historically sensitive structures with the minimum of physical disruption. A number of existing and developing electrochemical approaches to corrosion control are also discussed. The work is being undertaken at the Centre for Infrastructure Management, Sheffield Hallam University with support from the Royal Society.

Keywords: corrosion, masonry, steel frame, cathodic protection, galvanic or sacrificial anodes, impressed current, numerical modelling.

1 Introduction

The identification of "Regent Street Disease" in the United Kingdom in the late 1970's highlighted the problems of the corrosion of iron and steel frames and other structural components in historically sensitive buildings [1]. This has resulted in serious consequences with respect to serviceability, safety, aesthetics and heritage.

Cathodic protection, originally developed by Humphry Davy and later employed widely on buried and submerged structures, was first considered for reinforced concrete in the late 1950's. It was not until the development of improved anode systems based on catalysed titanium and titanium oxide in the early 1980's and the considerable advances in digital operating systems that it became a serious commercial solution.

The transfer to steel-framed buildings was somewhat slower and it was not until 1997 that the first full structure was protected by such a system. Even now, with several sizeable installations in the UK, there are no formal guidelines for the design, installation and operation of such systems and much of the knowledge is based on empirical observation.

2 Corrosion of iron & steel

Metal corrosion is the destructive result of chemical or electrochemical reaction between a metal or metal alloy and its environment. When moisture and oxygen are present, steel rusts. In its simplest form the corrosion process can be represented by two dissimilar metals in an aqueous electrolyte, joined to allow electrons to pass from anode to cathode. In reality, when a metal corrodes, anodic and cathodic areas can be formed on a single metal surface in contact with the aggressive aqueous environment. As a result, corrosion can occur at a large number of sites over the surface of the metal. Dissolved ions react with hydroxyl ions to form corrosion products [3]. The reactions occurring at anodic and cathodic sites can be represented as follows:

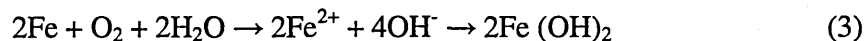
At anodic areas the following oxidation reaction (anodic reaction) takes place:



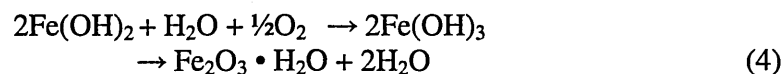
In well aerated neutral and alkaline environments, the following reduction reaction (cathodic reaction) takes place at cathodic areas:



Dissolved iron ions react with hydroxyl ions to form corrosion products. The reaction can be obtained by combining (1) and (2):



Ferrous hydroxide precipitates from solution. However, this compound is unstable in oxygenated solutions and is oxidized to the ferric salt, the final product being commonly referred to as rust:



The rate and nature of the corrosion process mainly depends on a number of factors including alloy composition, environmental factors and design. The relative humidity of an environment in particular has a profound effect on the rate of corrosion of steel [1].

3 Corrosion of steel framed masonry structures

3.1 Steel frame corrosion and damage mechanism

There has been increasing awareness over the last 50 years that many high-profile iron and steel-framed masonry structures may be prone to extensive damage as a result of corrosion of the steel frame.

The problems of corrosion of the steel-framed masonry buildings are related to the original designs and the form of construction at a time when the technology of corrosion protection was still largely undeveloped.



Figure 1: Early example of frame corrosion, as reported in 1947. [6]

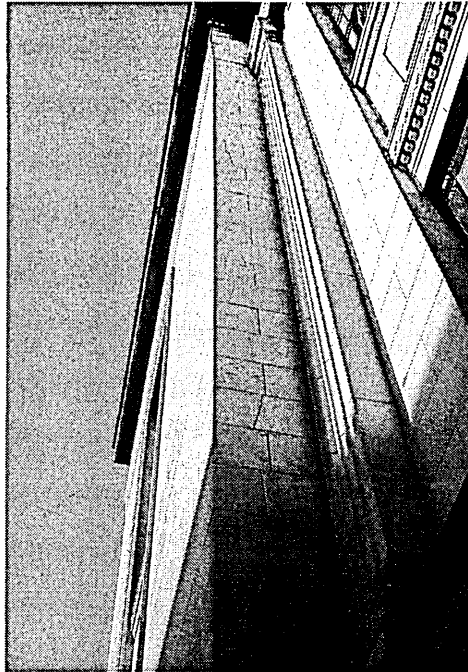


Figure 2: Cracking of Portland stone resulting from frame corrosion.

The external masonry of the buildings was often tightly packed around the iron or steel frame and cavities in-filled with mortar, brick, or other porous rubble [4]. The porous masonry and in-fill materials allow moisture entering the structures to come into contact with steelwork. Moisture can also enter the structures through a variety of routes including open joints, cracks or through poorly maintained gutters and pipework. As a result, corrosion becomes inevitable. As expansive corrosion products are formed, the tremendous stresses act on the surrounding mortar and masonry. These result in cracking, spalling and displacement of masonry, further opening up joints and cracks and permitting greater access to water. Thus, the rate of degradation tends to accelerate. Thermal movements that aggravate the opening of joints will also lead to an acceleration of the damage, as typically observed on the weather-exposed corners of such buildings [1].

The time at which corrosion initiates largely depends upon location, aspect and level of previous maintenance. The rate at which corrosion progresses largely depends upon availability to moisture and oxygen, the type of environment, and the variability of the environment. The intimacy of the contact between the corroding steel and the cladding also influences the extent and timing of the damage as gaps between steel and cladding can accommodate extensive corrosion with no visible damage. Corrosion damage not only destroys the integrity of these structures, but also could pose a serious public hazard and liability issue for the owner.

3.2 Types of corrosion in iron and steel framed structures

There are two major types of corrosion that can typically affect masonry clad steel frame buildings; uniform or general corrosion and pitting corrosion.

Uniform attack appears as an even layer of rust on the steel surface. This is the most common form of corrosion that is found in perimeter steel of masonry clad steel framed building. Uniform corrosion is generally due to electrochemical reaction, which occurs from the presence of oxygen and moisture. Under certain conditions the water or moisture that is in contact with the steel, may have extremely low values of pH due to acidic pollutants from rainfall (acid rain) and surveys have shown that acid precipitation at pH of 2 is not uncommon, especially during the initial period of snow or rain.

Carbonation, another contributor to corrosion, is a process by which carbon dioxide enters into the masonry. Carbon dioxide combines with the pore water in the mortar to form carbonic acid, which reduces the pH of the mortar to approximately 8 or 9. At these levels the protective oxide film at the steel surface is no longer stable and, with adequate supply of oxygen and moisture, corrosion will start. The penetration of masonry by carbonation is a slow process, the rate of which is determined by the porosity, permeability and moisture content of mortar.

Pitting corrosion, which is a localized form of attack, can lead to significant loss of steel section. This form of attack is most commonly found in be found in coastal and maritime buildings where air borne salts have penetrated through the porous cladding to the steel surface. The role of chloride ion in inducing corrosion of steel in concrete is well documented. If chlorides are present in sufficient quantity, they disrupt the passive film and subject the iron and steel members to corrosion even when the metal is encased in good quality mortar or concrete (see Figure 3).

4 Cathodic protection of metallic structural components

4.1 Background to cathodic protection

The principles of cathodic protection were identified by Sir Humphry Davy and reported as early as 1824 [5]. Davy was responding to a request from the Royal Navy to problems they encountered with the copper sheathing applied to the wood hulls of ships to prevent marine fouling attack by wood boring organisms. A mechanism, that would later be recognised as galvanic or bimetallic corrosion, resulted in the less noble iron nails corroding preferentially to the more corrosion resistant copper sheet resulting in the sheathing becoming detached. Davy recognised that by attaching a third metal that was more liable to corrosion than either the iron or the copper, then this would corrode preferentially and 'sacrifice' itself thus protecting both the copper and the nails.

This approach, using zinc, aluminium or magnesium as the 'sacrificial' metal, is still widely used today in a wide range of buried and submerged applications. In many ways, Davy's original solution was too successful and prevented the copper from corroding which in turn prevented it from acting as an effective anti-fouling system and it has been suggested that the resulting complaints and ridicule lead to Davy's early death following a stroke.

After Davy's discovery, Faraday examined the corrosion of cast iron in sea water and found that it corrodes faster near the water surface than deeper down. In 1834 he identified the quantitative connection between corrosion weight loss and electric current. With this discovery he firmly established the scientific foundation of

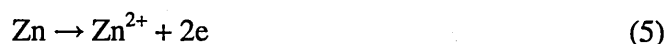
electrolysis and the principles of cathodic protection. There are two basic types of cathodic protection systems commonly used; galvanic and impressed current [6].

4.1.1 Impressed current cathodic protection (ICCP)

Consider iron corroding in well aerated neutral and alkaline environments. Impressed current cathodic protection works through the provision of a small direct current (DC) from a permanent anode fixed on to the surface or placed into the electrolyte of the protected steel. The anodes employed in the protection of steel-framed structures are generally made from titanium with a mixed metal oxide coating (MMO) or from a titanium oxide ceramic. In either case, the requirement is for the material to pass a large cumulative current without a significant loss of mass. The DC power supply passes sufficient current from the anode to the protected steel to force the anodic reaction (1) to stop, and to make the cathodic reaction (2) the only one occurring on the protected surface. This would typically be a few tens of milliamps per square metre of metal surface, running at little more than 10 or 12 volts.

4.1.2 Galvanic (sacrificial) cathodic protection

In a galvanic system the protected steel is connected to sacrificial or galvanic anode such as zinc without using a power supply. As in Davy's original system, the anode corrodes preferentially, liberating electrons with the same overall effect as the impressed current system, for example:



4.1.3 Cathodic protection of reinforced concrete

The first reference of cathodic protection of reinforced concrete is in the 1950's [7]. The work that had been carried out up to the late 1970's emphasized the limitations of the techniques and materials then available but the last few years have seen major anode developments which allowed a significant expansion of these methods of corrosion prevention. In 1973 and 1974 the first commercial cathodic protection system for reinforced concrete was applied to the top deck of Sly Park Crossing Bridge Deck in California, USA [8].



Figure 3: Corrosion of rolled steel section, circa 1900.



Figure 4: Example of conservation of a listed heritage structure by cathodic protection (1997).

Since those first systems were applied in the 1970s systems have been developed and applied to bridge deck, substructure and other elements, buildings, wharves, and every conceivable type of reinforced steel. Anodes have been developed in the form of conductive coatings, conductive meshes embedded in concrete overlays, conductive concrete overlays and probes drilled into concrete.

4.1.4 Cathodic protection of iron and steel framed masonry

Cathodic protection systems for iron and steel-framed masonry buildings have only been developed relatively recently [1]. The first cathodic protection system for the prevention of steel corrosion in a masonry structure was installed in 1991. The system protects the entrance colonnade at Royal College of Science, Dublin; a limestone structure containing two parallel structural 'I' beam members. Regular remote monitoring and annual visual inspections have confirmed corrosion has been arrested. Further applications in the early 1990s involved historically protected sites, with the protection of iron cramps in the Inigo Jones Gateway, Chiswick House, London, and iron staircase supports embedded in the brickwork of Kenwood House, Hampstead.

It was not until 1997 that the first full steel-framed structure was protected by a cathodic protection system (Gloucester Road Underground Station, see figure 4). At the present time more than twenty systems have been completed in the United Kingdom. Examples include Lloyds Bank, Lombard Street, London; Arkwright House and House of Fraser in Manchester; St Andrew House, Edinburgh and Putney Boathouse, London. However, despite several sizeable installations in the United Kingdom and considerable overseas interest, there remain no formal guidelines for the design, installation and operation of such systems.

4.2 Numerical methods for modelling of cathodic protection systems

4.2.1 Background and mathematical model

The employment of an appropriate current and potential distribution is one of the important parameters determining the effectiveness of cathodic protection systems. Both under-protection and over-protection are undesirable. Under-protection of a structure clearly does not adequately prevent corrosion while over-protection can significantly reduce the life of the system components and result in other undesirable side effects. To avoid these problems, proper anode location to produce uniform current and potential distributions is essential. This can also help minimise the current required to achieve the protection criterion, thus reducing the cost and improving the life of the system components.

To determine the optimum anode distributions, the current and potential distributions of cathodically protected structures need to be calculated as part of a design. Traditionally, such designs have mainly relied on empirical methods and experience. These methods have been used for a long time and have been an adequate tool for most conventional applications. However, for new applications of cathodic protection, the accuracy of these methods becomes uncertain. Hence, the current and potential distribution prediction of cathodic protection systems is not only useful but necessary when extending the technique to more sensitive or technically challenging applications.

For a uniform isotropic electrolyte, the flow of current can be shown to obey the Laplace equation. The equation is written in term of the electrical potential [9],

$$k\nabla^2 E(p) = 0 \quad p \in \Omega \quad (6)$$

Where E is the potential at any $p(x, y, \text{ and } z)$ of domain
 k is the conductivity of electrolyte
 Ω is the problem domain

together with the following relationship between the current density and potential:

$$i = -k \frac{\partial E}{\partial n} \quad (7)$$

where i is current density at the electrode surface, n is the normal vector to the electrode surface. This is the governing partial differential equation for potential distributions in electrochemical cells. The problem in cathodic protection is to solve the above Laplace equation subject to certain boundary conditions. They can be presented in Table 1 [10]:

Table 1 : Boundary Conditions

Type	Boundary Condition	Comment
Anodically polarized electrode	$-k \frac{\partial E}{\partial n} = i_0 f(E - E_{eq})$	Anodic branch if experimental polarization curve used
Cathodically polarized electrode	$-k \frac{\partial E}{\partial n} = i_0 f(E - E_{eq})$	Cathodic branch if experimental polarization curve used
Painted surface	$\frac{\partial E}{\partial n} = 0$	
Non-polarized	$E = \text{fixed value}$	For E consult EMF series
Impressed current	$-k \frac{\partial E}{\partial n} = \text{fixed value}$	Current density output

Combining the boundary conditions, the Laplace equation is solved and the potential distributions in electrochemical cells are given.

4.2.2 Numerical solutions

Except for some special problems, it is widely accepted that such a system in practice cannot be solved solely by analytical methods. The numerical methods have therefore been employed. The three major numerical approaches used for cathodic protection analyses are the finite difference method (FDM), finite element method (FEM) and boundary element method (BEM). Comprised with the finite difference method and

the finite element method, the advantages of boundary element method for analysis of cathodic protection are as follows [11]:

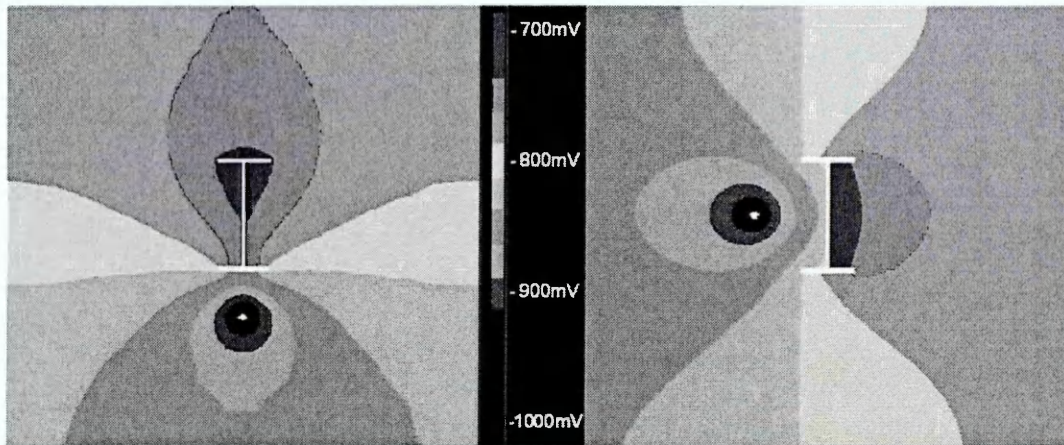


Figure 5: Numerical modelling of potential distribution between discrete anode (white dot) and stanchion (H-section) for two anode configurations.

- The meshes are only on the surface, hence only one or two-dimensional elements are required. It therefore reduces the number of nodes required to model a particular system and minimises data preparation.
- Boundary element methods give the solutions on the boundary and, only if required, at specified internal points. Since for analysis of cathodic protection the solution is only required on the surfaces, it is far easier to analyze the results than the finite element method which automatically gives results for all nodes (internal or boundary).
- Boundary element methods are very effective and accurate for modelling infinite domains.

Therefore, it is this approach that is considered most applicable for the modelling and optimisation of cathodic protection systems for the preservation of iron and steel elements in masonry structures. Using this method it is possible to predict potential distributions for the different anode locations, as shown in Figure 5.

5 Alternatives to cathodic protection

In addition to cathodic protection a number of alternative approaches are available for the treatment and control of corrosion to iron and steel structural elements encased within masonry. Corrosion inhibitors, generally based on amino alcohols, have been used extensively for the short to medium term protection of exposed surfaces and hollow sections. They can be incorporated in to protective wax coatings or blown as powder into enclosed spaces and have the advantage of being totally reversible.

More recently, low viscosity liquids have been developed that can be painted or sprayed onto the surface of concrete and masonry, allowing the active inhibitor group to permeate through the cover and attach to the surface of buried metal components [3].

It is also possible to employ temporary cathodic protection systems that take advantage of the side effects of the treatment and are optimised to either remove

chloride ions from the surrounding masonry (chloride extraction) or enhance the level of alkalinity in the vicinity of the buried metal (re-alkalisation) [6]. Such treatments have been employed for reinforced concrete but should be equally applicable to iron or steel components within masonry. The advantage of this approach from a heritage viewpoint is that once the treatment is completed, all the equipment is removed. Further techniques in use on reinforced concrete such as electro-osmosis are currently under evaluation for masonry applications.

References

- (1) Atkins, C. P., Lambert, P. and Coull, Z. L. , Cathodic Protection of Steel Framed Heritage Structures, *Proc. of 9th Int. Conf. on Durability of Building Materials and Components*, Australia, 11pp., 2002.
- (2) Lambert,P., *Corrosion Mechanisms - An Introduction to Aqueous Corrosion*, Monograph No.2, Corrosion Prevention Association, Aldershot, UK, 4pp., 2001.
- (3) Jones, G., Lambert, P., Bolton P., and Robinson, M., Hi-Tech Heritage, *Concrete Engineering International*, 6, pp.17-20, 1999.
- (4) Department of Scientific and Industrial Research, *Report of the Building Research Board*, His Majesty's Stationery Office, London, UK, 1947.
- (5) Davy, H. 'On the corrosion of copper sheeting by seawater, and on methods of preventing this effect, and on their application to ships of war and other ships'. *Proceedings of the Royal Society*, 114, pp.151-246, 1824 and 115, pp.328-346, 1825.
- (6) Drewett, J. *An Introduction to Electrochemical Rehabilitation Techniques*, Monograph No.5, Corrosion Prevention Association, Aldershot, UK, 4pp., 1998.
- (7) Heuze, B., Cathodic Protection of Steel in Prestressed Concrete. *Materials Performance*, 11, pp.57-62, 1965.
- (8) Stratfull, R. F., *Experimental Cathodic Protection of a Bridge Deck*, Transportation Research Record 500, Transportation Research Board, Washington DC, USA, 1974.
- (9) Adey, R. A., Niku, S.M., Brebbia, C.A. and Finnegan, J, Computer Aided Design of Cathodic Protection, *Boundary Element Methods VII*, Villa Olmo, Lake Como, Italy, 1985.
- (10) Zamani, N.G., Boundary Element Simulation of Cathodic Protection System in Prototype Ship, *Applied Mathematics and Computation*. 26, (2), pp.118-134, 1986.
- (11) Adey, R.A. and Niku, S.M., Computational Modelling of Corrosion Using Boundary Element Methods, *Computer Modelling In Corrosion*, STP 1154, ASTM, Philadelphia, USA, pp.248-263, 1992.